2 Misf

NASA TECHNICAL MEMORANDUM

NASA TM X-62,237

NASA TM X-62,237

AERODYNAMIC AND NOISE MEASUREMENTS ON A QUASI-TWO DIMENSIONAL AUGMENTOR WING MODEL WITH LOBE-TYPE NOZZLES

Thomas N. Aiken

Ames Research Center
Moffett Field, Calif. 94035

September 1973

NOTATION

a	nozzle lower slot thickness, cm (in)(see figure 2(e))
A	gross augmentation ratio, measured augmentor thrust/measured nozzle thrust
A_e	augmentor exit area, sq m (sq ft)
A_n	nozzle area, sq m (sq ft) or sq cm (sq in)
A_t	augmentor throat area, sq m (sq ft)
b	model span, m (ft) or cm (in) or nozzle lobe thickness, cm (in) (see figure 2(e))
c	wing chord, m (ft) or nozzle lobe spacing, cm (in) (see figure 2(e))
C_D	drag coefficient, $\frac{\text{drag}}{qS}$
C_{J_n}	jet thrust coefficient, $\frac{\text{measured nozzle thrust}}{qS}$
C_L	lift coefficient, $\frac{\text{lift}}{qS}$
C_P	pressure coefficient, $\frac{P-P_\infty}{q}$
C_V	nozzle velocity coefficient, measured thrust/isentropic thrust with measured mass flow
d	nozzle lobe height, cm (in) (see figure 2(e))
ℓ	flap length, cm (in) (see figure 2(c))
ℓ_f	horizontal distance between nozzle lip and flap/coanda reference point, cm (in) (see figure 2(c)
ℓ_s	distance from nominal position of shroud trailing edge which is in line with flap trailing edge, cm (in) (see figure 2(c)
NAR	nozzle area ratio, $\frac{d \times b}{A_n}$

OASPL	overall sound pressure level, dB
P	local static pressure, N/sq m (lb/sq ft)
P_∞	free stream static pressure, N/sq m (lb/sq ft)
PR	measured plenum pressure ratio, $\frac{\text{plenum total pressure}}{P_\infty}$
q	tunnel freestream dynamic pressure, N/sq m (lb/sq ft)
S	model planform area, sq m (sq ft)
t	equivalent slot nozzle thickness, $\frac{A_n}{b}$, cm (in)
T	nozzle thrust, N (lb)
T_1	nozzle 1 thrust, N (lb)
V	velocity, m/sec (ft/sec)
V_I	isentropic velocity based on plenum pressure, m/sec (ft/sec)
V_1	velocity at center span rake, m/sec (ft/sec)
V_2	velocity at quarter span rake, m/sec (ft/sec)
x	chordwise distance, m (ft)
y	distance from flap upper surface at exit, measured perpendicular to augmentor centerline, cm (in) (see figure 2(c)
Z_f	vertical distance between nozzle lip and flap reference, cm (in) (see figure 2(c))
α	model angle of attack, referenced to chord line deg
δ_{ID}	intake door angle, deg (see figure 2(c))
δ_f	augmentor flap angle, deg (see figure 2(c))
δ_{SL}	slat angle, deg (see figure 2(b))
δ_T	turning angle difference between flap angle, δ_f, and nozzle cant angle, deg

MODEL AND APPARATUS

The model is shown installed in the wind tunnel in figure 1. Also shown are several of the nozzles tested. Figure 2 shows geometric details of the model. A schematic of the noise measurement and data reduction apparatus is shown in figure 3. Table 1 gives geometric details of the nozzles.

Basic Model

The photographs of figure 1 and the two-view of figure 2(a) show the general arrangement of the model. The air for the augmentor nozzle enters the spar from below and expands rearward through the nozzle. The end plates are connected directly to the wing section. Three blowing BLC nozzles are installed on the inside surface of each end plate to provide increased effective aspect ratio (see figure 2(a)). The front BLC nozzle is 7.62 cm (3 in) long while the back two are 12.70 cm (5.0 in) long. All BLC nozzles have a .0508 cm (.020 in) gap. The front two BLC nozzles are normal to the airfoil surface at 2 and 50% chord. The rear BLC nozzle is canted 50° aft and the bottom is 6.35 cm (2.5 in) above the chord plane. The air for the BLC nozzles is separate from the air for the augmentor nozzle and enters through the tubes visible on the top and bottom of the model.

Wing Section

The basic wing section is shown in figure 2(b), and the augmentor section in figure 2(c). The slat was set at $\delta_{SL} = 50°$ throughout the test. The flap and shroud were mounted on their own end plates as shown in figure 1. This allowed them to be moved independently of the main wing and each other. The flap and shroud were attached to each other with movable brackets for rigidity. When ℓ_f was set at 2.54 cm (1.0 in) or less, the tertiary gap was essentially closed. The intake door could be moved manually and fixed with brackets shown in figures 1(a) and 1(b). During static tests the intake door is fitted with an inlet bellmouth (figure 2(b)). During wind-on tests the bellmouth is removed and the intake door is moved to conform to the local streamlines.

Nozzles

The geometry and dimensions of the nozzles tested are given in Table 1 and figures 2(d) and 2(e). As shown in figure 1(e), the top part of the basic nozzle is removable. The lower lip can be moved vertically to vary the proportion of slot blowing. Shims were used to set the desired slot gap. The nozzle thrust axes were canted 30° below the chord plane to give maximum thrust at a takeoff flap setting.

Instrumentation

The entire model was connected to the wind tunnel balance.

Augmentor exit pressures were measured by 2 pressure rakes at quarter and mid-span. The rakes also measured part of the flow over the shroud depending on the particular augmentor exit area. Surface static pressures were measured on all surfaces by a chordwise row of orifices at mid-span. Total pressure and temperature in the plenum were measured. The primary mass flow was measured with a sharp-edged, flat plate orifice. The pressure and temperature probes were placed such that the velocity coefficients of the nozzles are not representative of the nozzles efficiency. The plenum pressure ratio and the velocity coefficient are used as reference only.

The sound data acquisition system is shown schematically in figure 3. The microphone was located in the mid-span plane.

TESTS

Static

During the static tests, the tunnel was blocked 3.05 m (10 ft) forward of the model and 3.05 m (10 ft) wide wind tunnel doors on the underside of the model opened (see figure 1(f)). Normal test procedure consisted primarily of varying the flap and shroud positions while maintaining constant pressure ratio and 0° angle-of-attack. Flap deflections varied from 30° to 75°. The intake door was set at 25° and the inlet bellmouth was on, unless noted. A constant end plate BLC nozzle setting was used throughout the static and wind-on tests. The augmentor nozzle and BLC nozzle thrust were measured statically.

Wind-On

Two procedures were used during wind-on testing. The first consisted of varying angle-of-attack while maintaining constant augmentor geometry and pressure ratio. The second procedure varied augmentor geometry at 0° angle-of-attack and constant pressure ratio. The pressure ratio used during the test was 1.53 unless otherwise noted. The dynamic pressures used to obtain the various C_{J_n}'s are as follows:

Nozzle \ C_{J_n}	0.5 N/sq m (lb/sq ft)	1.0	1.5
1	890 (18.6)	445 (9.3)	297 (6.2)
3b	747 (15.6)	374 (7.8)	249 (5.2)
5c	920 (19.2)	460 (9.6)	306 (6.4)

The Reynolds number, based on the wing chord, ranged from 1.05 million to 2.03 million.

The intake door was set by visually observing which setting delayed shroud flow separation to the highest q. The shroud flow was separated to some extent at all flap settings of 60° and 75°, even when the shroud was moved to the low setting (ℓ_S = 5.08 cm (2.0 in)).

Noise

Noise data were taken at static conditions. The test procedure used was the same as in the static tests except that for each configuration, the microphone boom was rotated in an arc to obtain acoustic directivity. Data were obtained for flap settings of 30° and 60°.

DATA REDUCTION

Model lift and drag are the only force data presented and include forces on the end plates and jet forces. The forces due to the end plate BLC nozzles have been subtracted from the lift and drag.

The jet coefficients were computed using reaction forces from the nozzles alone, as measured by the wind tunnel scale system. The pressure ratio given is the pressure ratio in the model plenum. It is somewhat higher than the nozzle pressure ratio as evidenced by the low velocity coefficients shown in figure 5.

The overall sound pressure level (OASPL) noise data have been corrected to the thrust of nozzle 1 by adding 10 log $\sqrt{T_1/T}$ to the OASPL levels of the various nozzles. The noise data have not been corrected for the effect of reverberation, thus show trends only.

RESULTS

An index to the data is given in Table 2. The characteristics of the various nozzles are presented in figures 4 to 6. Figures 7 to 15 present static augmentation values for various augmentor configurations. Typical static augmentor exit velocity profiles are shown in figures 16 to 23.

The wind-on force characteristics are presented in figures 24 to 28. Typical wind-on augmentor exit velocity profiles are shown in figures 29 to 36. Typical surface pressure distributions are given in figures 37 to 40.

The acoustic directivity is shown in figures 41 to 44. Typical spectrums are shown in figure 45.

Figures 46 to 53 are summary plots of static augmentation, static and wind-on augmentor exit velocity profiles, and lift and drag characteristics.

DISCUSSION

The basic objectives of the investigation reported herein were to:

1. Assess the static and wind-on aerodynamic and static noise characteristics of lobe-type augmentors relative to normal slot-type augmentors.

2. Eliminate the need for the tertiary gap.

The first objective resulted from the suggested use of multi-element nozzles for noise suppression and improved static augmentation in short augmentors (low ℓ/t). The second objective resulted from the desire to block any noise emanating from the tertiary gap. Closure of the tertiary gap was also desired to enable the use of the lower surface as one wall of a folding flap duct.

Static Results

Figures 46 and 47 indicate that the maximum static augmentation is increased with multi-element nozzles. The curves also show the strong dependence of augmentation on the mixing length, ℓ/t. The augmentation ratio is higher than that of an optimum slot nozzle by up to 14% at 0° of turning (δ_f = 30° for this test) and 5% at 30° of turning (δ_f = 60° for this test). The data from this and other tests are compared at equal turning angles since at static conditions, the angle of interest is the difference between the nozzle cant angle (30° in this test) and the augmentor flap angle.

Figures 48 and 49 show the effect of flap angle (or turning angle) on the static augmentation. All of the nozzles were canted so that their thrust was approximately 30° from the chord plane. These figures indicate this resulted in maximum augmentation for the lobe nozzles results (except for 2b, which has the lowest lobes) when the turning angle was 0° and the tertiary gap was open. Figure 48 also indicates that the maximum augmentation for the slot nozzle occurs at a turning angle of 30°. Figure 49 indicates that the turning angle for maximum augmentation occurs at approximately 15° with the tertiary gap closed. The maximum augmentation is less when the tertiary gap is closed, but the augmentation is higher at turning angles greater than 15° (flap angles greater than 45° for this test).

Figure 50 shows the difference in exit velocity profiles for various nozzles.

Wind-On Results

Figure 51 and 52 indicate that closure of the tertiary gap at δ_f = 30° (for the two lobe-type nozzles, 3b and 5c) improves the lift and thrust performance even though the static augmentation is less with the gap closed. Figure 53 also indicates that closure of the tertiary gap improves the lift performance at other flap deflections. Only at the 75° flap deflection does the blown flap (shroud off) lift exceed the best lobe nozzle configuration. Figure 54 shows that the high lifts at high flap angles were obtained by moving the shroud rearward parallel to the flap, thereby delaying upper shroud flow separation. Figure 14 indicates that the augmentation was decreased with this change.

The increase in lift with the gap closure is perhaps due to the effect reported by Chan in reference 9. He indicates that suction applied at the augmentor knee increases the lift. With the tertiary gap closed, the effective upper surface suction is increased.

Figure 55 shows the effect of forward speed on the exit velocity profiles of the three nozzles. The data indicates that the freestream dynamic pressure is partially recovered.

Noise

Figure 41 indicates a substantial reduction in overall sound pressure level from nozzle 1 (slot) to nozzles 3b and 4b. Figure 42 shows further reductions below the wing with use of a blown flap (shroud off). Comparison of figure 43 and 44 indicate that there is little or no suppression below the wing for an augmentor with or without the tertiary gap open. The data indicates, as reference 10 does, that a blown flap suppresses the noise below the wing, but not behind it, while the augmentor suppresses the noise behind the wing, but not below it. However, reference 10 indicates that closure of the tertiary gap does substantially suppress the noise below the wing for an augmentor. It is not known why the same suppression was not obtained for this test. The results have not been corrected for reverberation due to the tunnel walls. Therefore, the data represent trends between different configurations, not absolute noise levels.

CONCLUDING REMARKS

An investigation was made at the static and wind-on aerodynamic and static noise characteristics of an augmentor wing having lobe-type nozzles. The data were compared to data from similar tests on slot-type nozzle augmentors. The basic conclusions are:

1. Lobe-type nozzles improve maximum static augmentation ratios from slot-type nozzles,

2. Closing the tertiary gap improves wind-on aerodynamic characteristics, even though static augmentation is usually lowered, therefore, augmentors should be optimized at forward speeds as well as statically,

3. Noise trends obtained are similar to those obtained in other investigations.

REFERENCES

1. Koenig, David G.; Corsiglia, Victor R.; Morelli, Joseph P.: Aerodynamic Characteristics of a Large-Scale Model with an Unswept Wing and Augmented Jet Flap. NASA TN D-4610, June, 1968.

2. Cook, Anthony M.; Aiken, Thomas N.: Low-Speed Aerodynamic Characteristics of a Large-Scale STOL Transport Model with an Augmented Jet Flap. NASA TM X-62,017, March, 1971.

3. Falarski, Michael D.; Koenig, David G.: Aerodynamic Characteristics of a Large-Scale Model with a Swept Wing and Augmented Jet Flap. NASA TM X-62,029, July, 1971.

4. Dorsch, Robert G.; Krejsa, Eugene A.; Olsen, William A.: Blown Flap Noise Research. AIAA Paper No. 71-745, June, 1971.

5. Ribner, H.S.; ed: Aerodynamics Noise. University of Toronto Press, Canada, 1969.

6. Design Integration and Noise Study for a Large STOL Augmentor Wing Transport, Task 1 Report D6-60139, The Boeing Company, Seattle, Washington. (Prepared under NASA Contract NAS2-6344)

7. Lilley, B. F.; Carland, D. B.: Preliminary Experimental Investigation of Jet Ejectors for Thrust Augmentation with Multiple (Piccolo) Nozzle Arrays. DHC-DIR 71-4, April, 1971. The deHavilland Aircraft of Canada, Ltd., Downsview, Ontario. (Work performed Grant No. DRB 0301-27)

8. Lawrence, R. L.: DHC Multi-element Nozzle/Augmentor Performance Compared to DNS. Coordination Sheet DNS-CS-262, The Boeing Company, Seattle, Washington. (Prepared under NASA Contract NAS2-6344)

9. Chan, Y. Y.: The Lift on a Two-Dimensional Augmentor Wing. NRC No. 10819, Report LR-523, 1969.

10. Gibson, Frederick W.: Noise Measurements of Model Jet-Augmented Lift Systems. NASA TN D-6710, April, 1972.

TABLE 1.- NOZZLE GEOMETRIC DETAILS

Dimensions in cm(in) or sq cm(sq in)

Nozzle	a	b	c	d	A_n	ℓ/t	NAR
1	.465 (.183)	—	—	—	35.5 (5.50)	56	1.00
2a	0	.465 (.183)	2.54 (1.0)	2.54 (1.0)	35.5 (5.50)	56	5.45
2b	.117 (.046)	.465 (.183)	2.54 (1.0)	2.54 (1.0)	44.4 (6.88)	45	4.60
2c	.234 (.092)	.465 (.183)	2.54 (1.0)	2.54 (1.0)	53.3 (8.25)	37	3.97
3b	.086 (.034)	.236 (.093)	2.54 (1.0)	3.81 (1.5)	33.3 (5.16)	60	8.93
4a	0	.465 (.183)	3.81 (1.5)	3.81 (1.5)	26.7 (4.13)	75	10.90
4b	.086 (.034)	.465 (.183)	3.81 (1.5)	3.81 (1.5)	33.3 (5.16)	60	8.93
4c	.175 (.069)	.465 (.183)	3.81 (1.5)	3.81 (1.5)	40.0 (6.19)	50	7.60
5a	0	.348 (.137)	3.81 (1.5)	5.08 (2.0)	26.7 (4.13)	75	14.52
5b	.086 (.034)	.348 (.137)	3.81 (1.5)	5.08 (2.0)	33.3 (5.16)	60	11.83
5c	.175 (.069)	.348 (.137)	3.81 (1.5)	5.08 (2.0)	40.0 (6.19)	50	10.03
6c	.175 (.069)	.279 (.110)	3.81 (1.5)	6.35 (2.5)	40.0 (6.19)	50	12.45

TABLE 2.- INDEX TO DATA FIGURES

Figure	Type	Nozzles
5	Nozzle performance vs PR	all
6	Nozzle -elocity profiles	2a,2b,2c,4a,4c
7	Static augmentation vs δ_f	1
8	"	2b
9	"	3b
10	"	4b
11	"	5c
12	"	5a,5b,5c
13	"	6c
14	Statis augmentation vs shroud position	3b
15	Static augmentation vs PR	5c
16	Static exit velocity profiles	1
17	"	2b
18	"	3b
19	"	4b
20	"	5c
21	"	5c
22	"	5a,5b
23	"	6c
24	Lift and drag for several C_{J_n}'s	1
25	Lift and drag for several C_{J_n}'s tertiary gap closed	3b
26	Lift and drag for several C_{J_n}'s tertiary gap open	3b
27	Lift and drag for several C_{J_n}'s tertiary gap closed	5c
28	Lift and drag for several C_{J_n}'s tertiary gap open	5c
29	Wind-on exit velocity profiles	1
30	"	1 (shroud off)
31	Wind -on exit velocity profiles A_e/A_n = 15, tertiary closed	3b

TABLE 2.- Concluded

Figure	Type	Nozzles
32	Wind-on exit velocity profiles A_e/A_n = 20, tertiary closed	3b
33	Wind-on exit velocity profiles A_e/A_n = 20, tertiary open	3b
34	Wind-on exit velocity profiles A_e/A_n = 25, tertiary open	3b
35	Wind-on exit velocity profiles A_e/A_n = 15, tertiary closed	5c
36	Wind-on exit velocity profiles A_e/A_n = 20, tertiary closed	5c
37	Surface pressure distributions C_{J_n} = 1.5, $\delta_f = 30^o$.	1c,3b,5c
38	Surface pressure distributions C_{J_n} = 1.5, $\delta_f = 45^o$.	1,3b.5c
39	Surface pressure distributions C_{J_n} = 1.5, $\delta_f = 60^o$.	1,3b,5c
40	Surface pressure distributions C_{J_n} = 1.5, $\delta_f = 75^o$.	1,3b,5c
41	OASPL directivity	1,2b,3b,4b
42	Blown flap OASPL directivity	1,2b,3b
43	Augmentor OASPL directivity, tertiary open	1,2b,3b,4b
44	Augmentor OASPL directivity, tertiary closed	1,2b,3b
45	Spectrums	1,2b,3b,4b

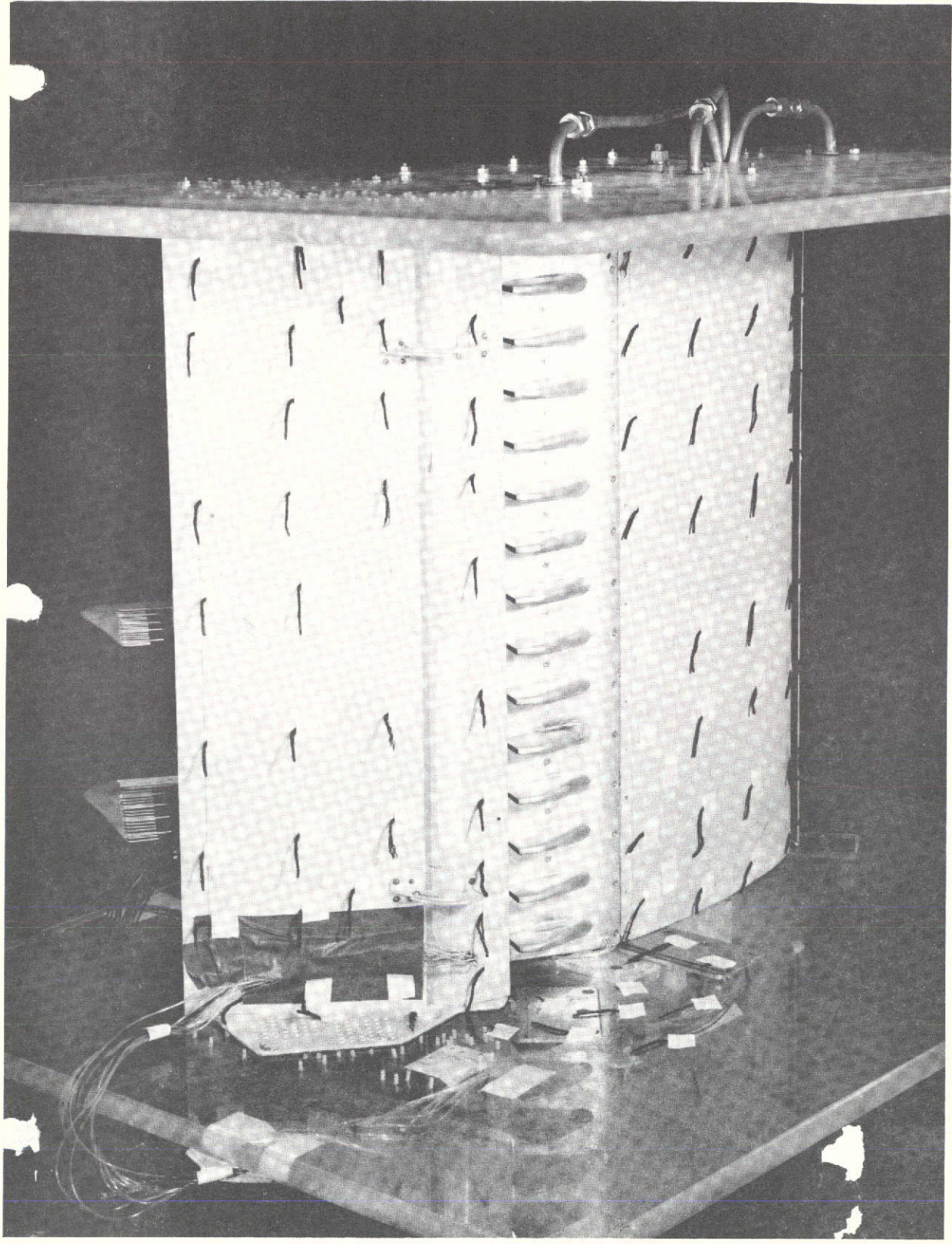

(a) Top rear view.

Figure 1.- Views of the model installed in the wind tunnel and nozzle details.

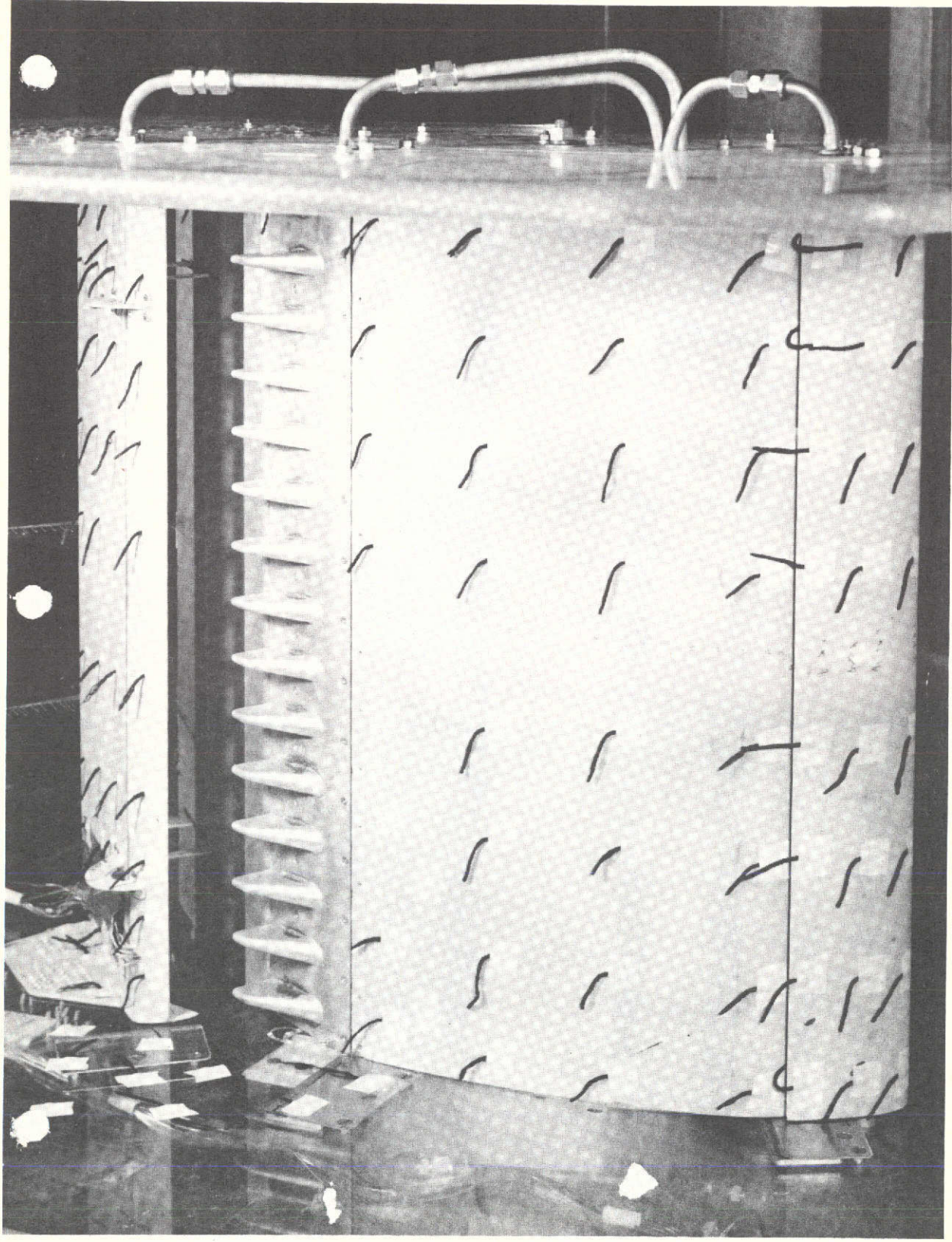

(b) Top view.

Figure 1.- Continued.

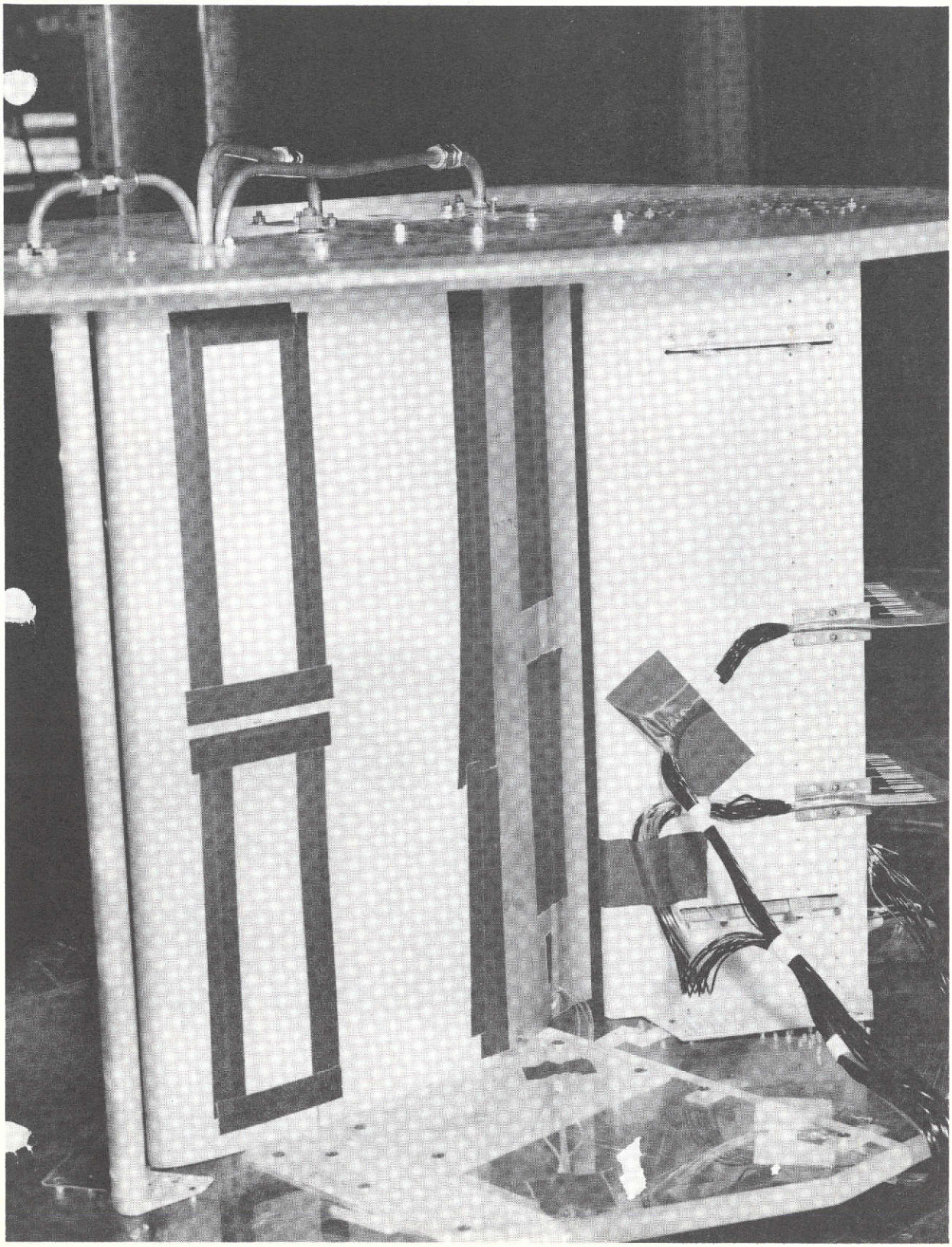

(c) Bottom view.

Figure 1.- Continued.

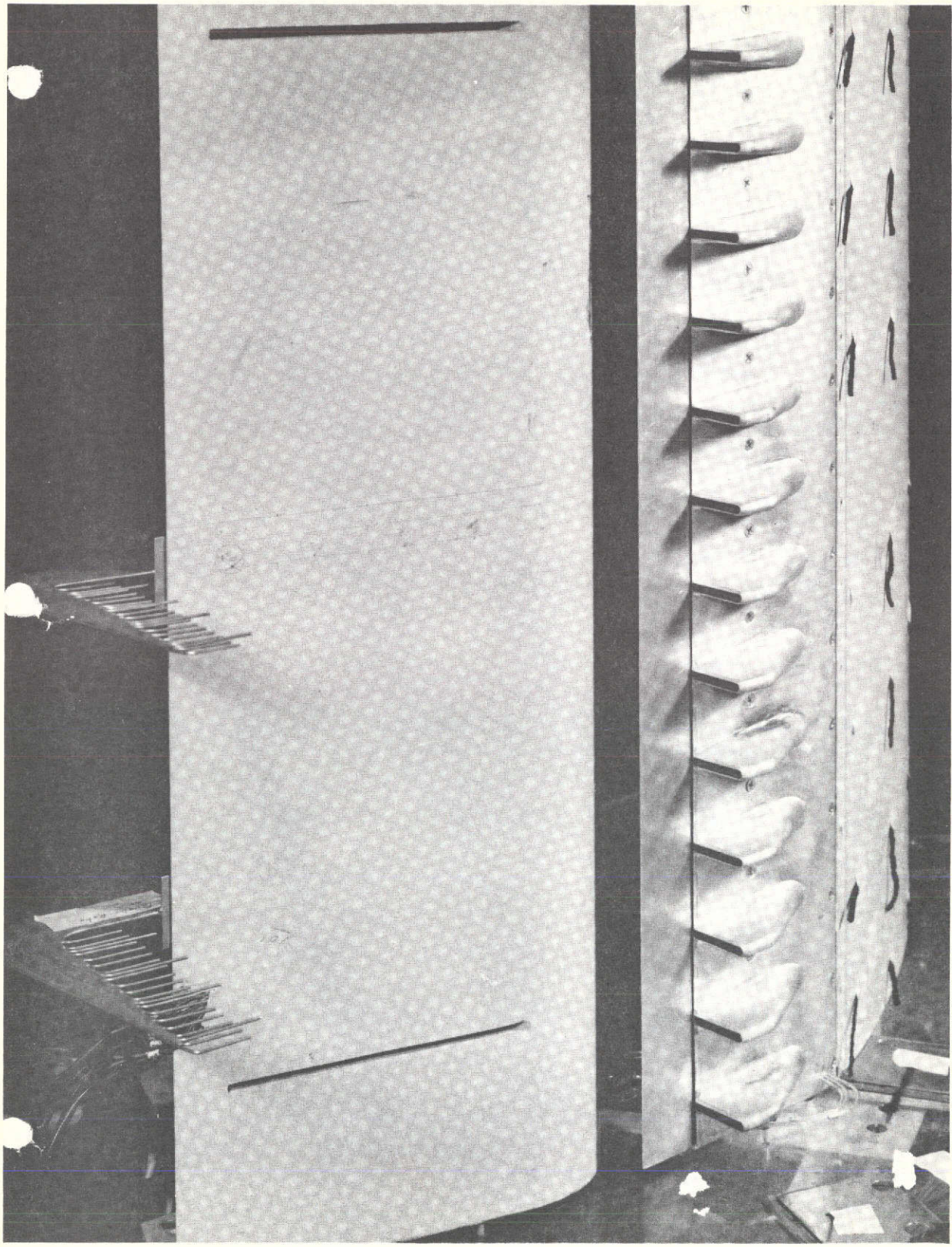

(d) Top view of flap (intake door and shroud removed).

Figure 1.- Continued.

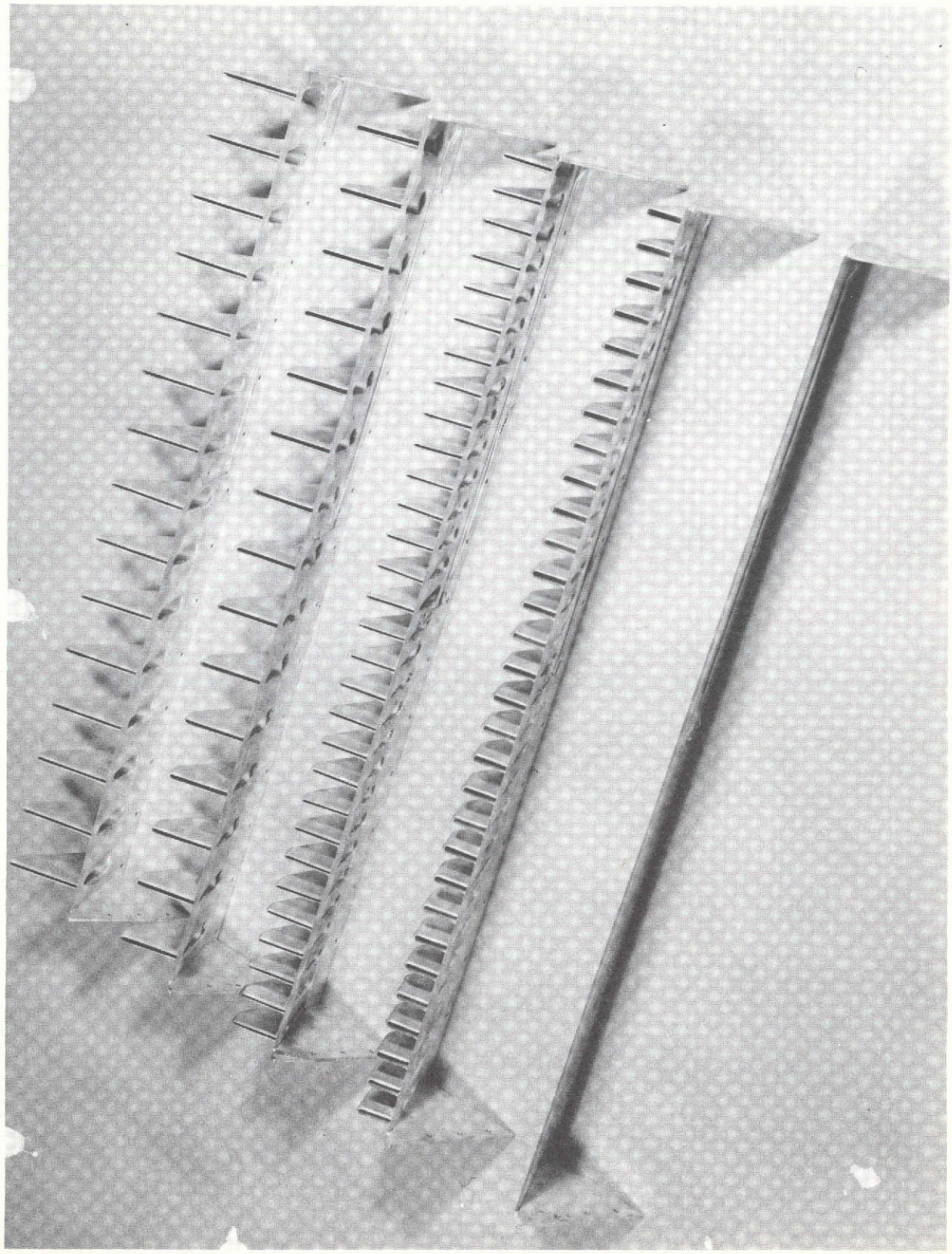

(e) Views of nozzles 6, 5, 3, 2, and 1.

Figure 1.- Continued.

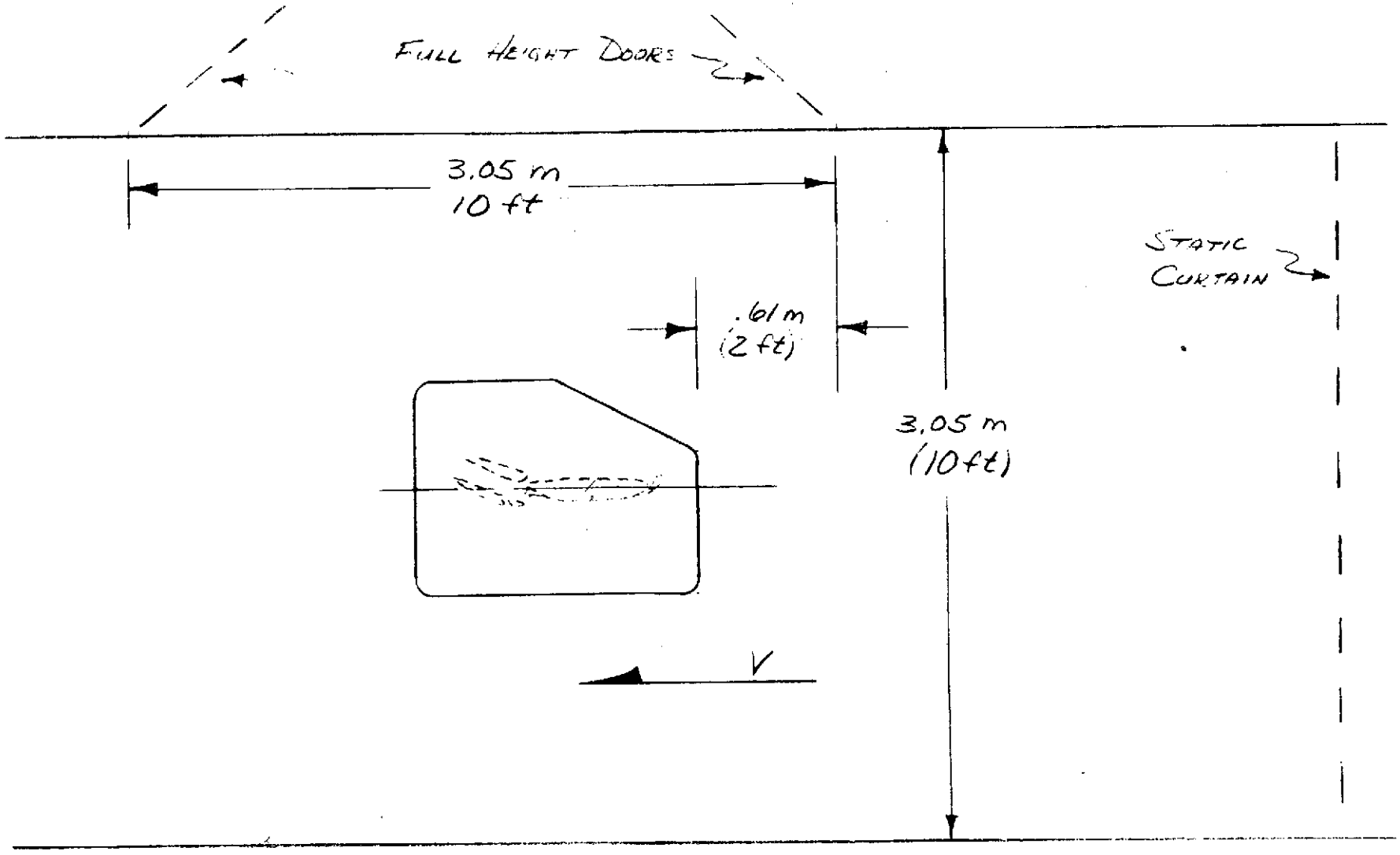

(f) Schematic planview of model in the Ames 7 X 10 No. 1 Wind Tunnel.

Figure 1.- Concluded.

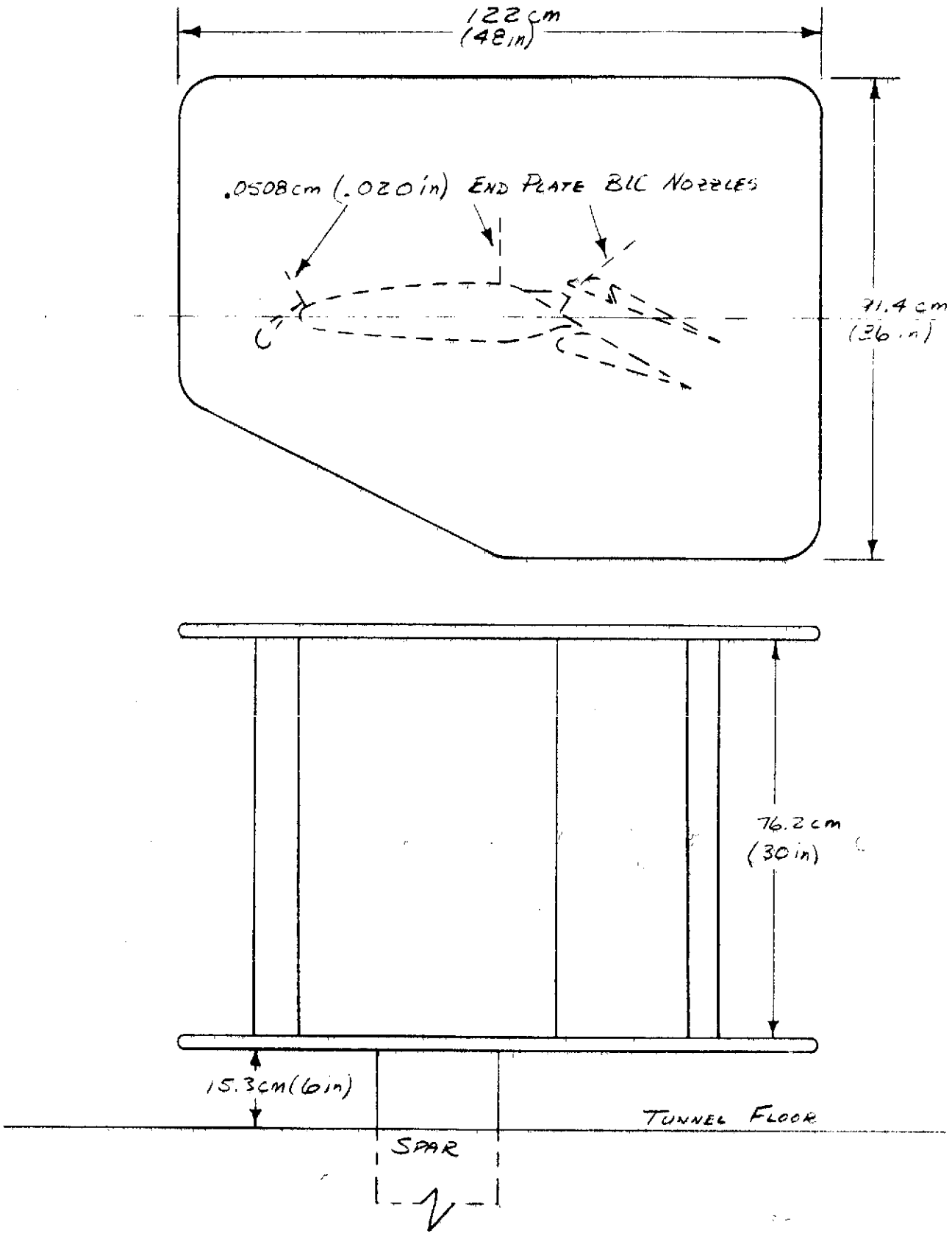

(a) Two-view of model.

Figure 2.- Geometric details of the model; dimensions in cm (in).

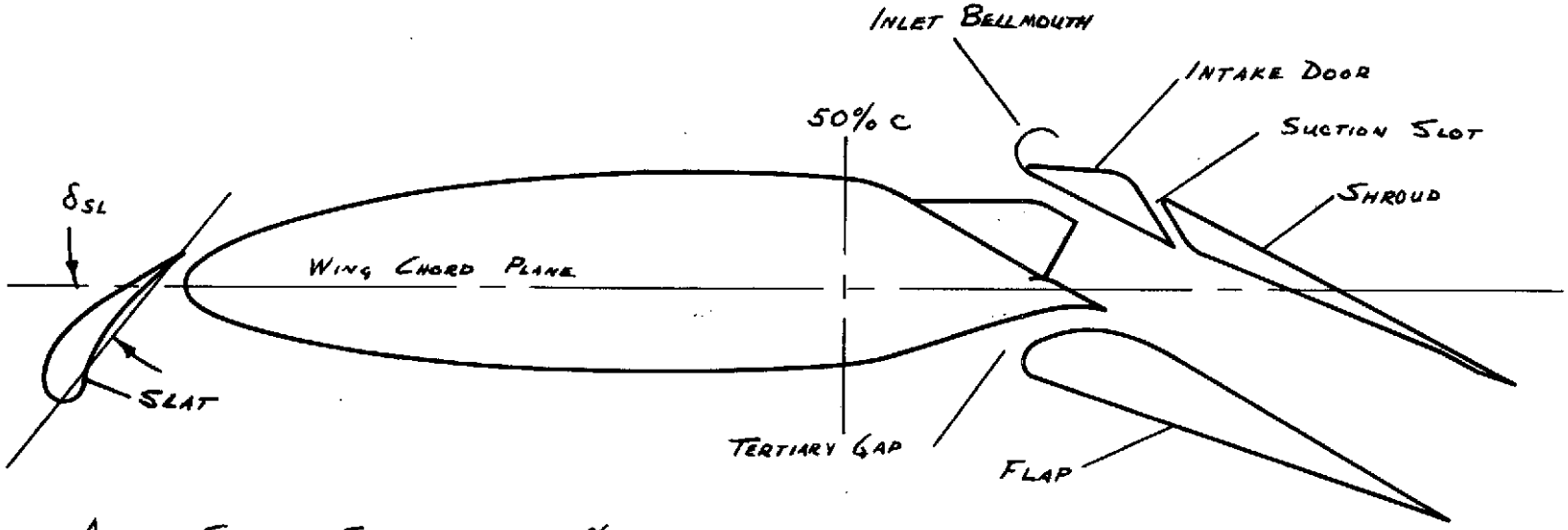

(b) Wing section.

Figure 2.- Continued.

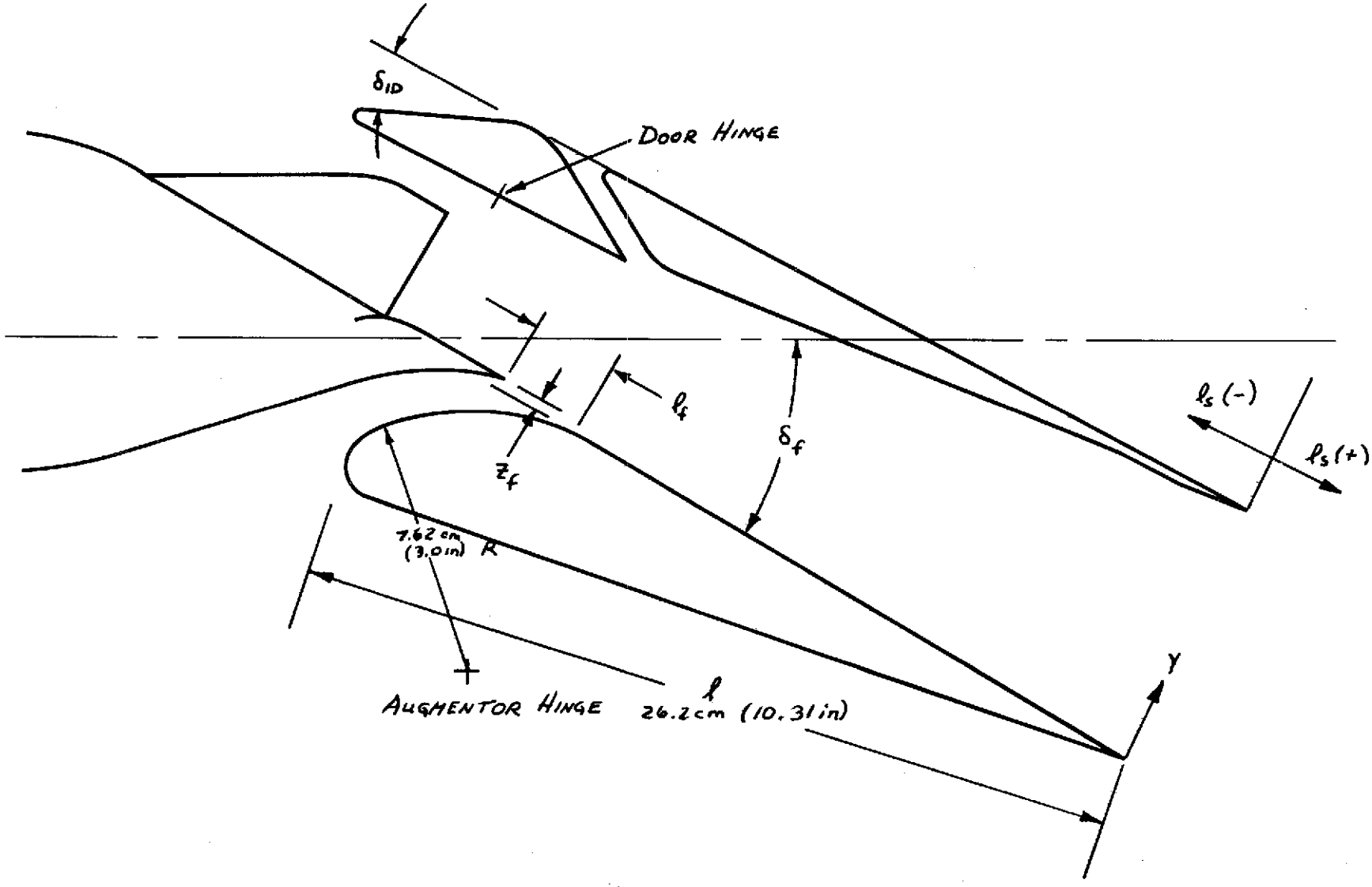

(c) Augmentor section.

Figure 2.- Continued.

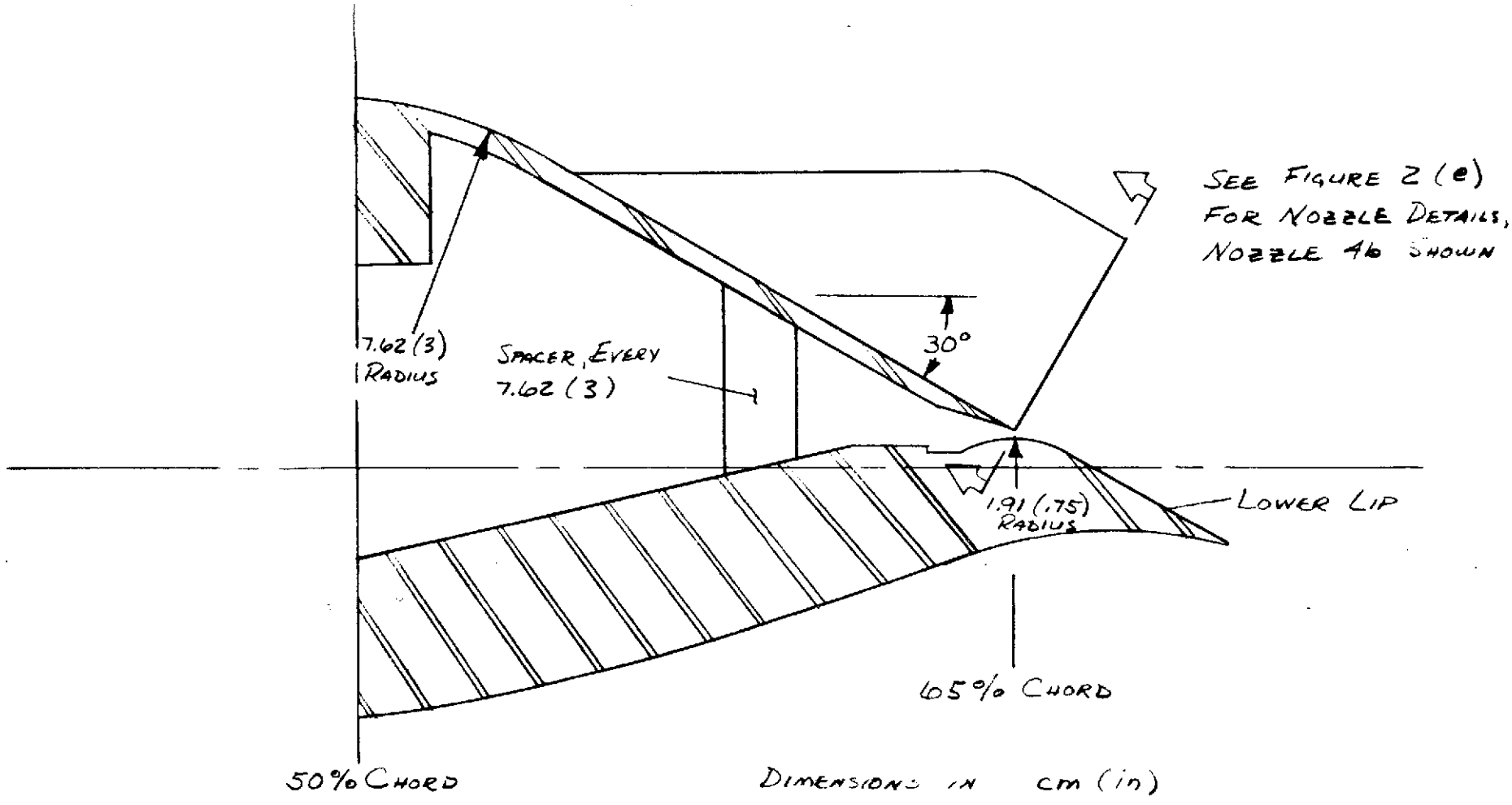

(d) Nozzle section.

Figure 2.- Continued.

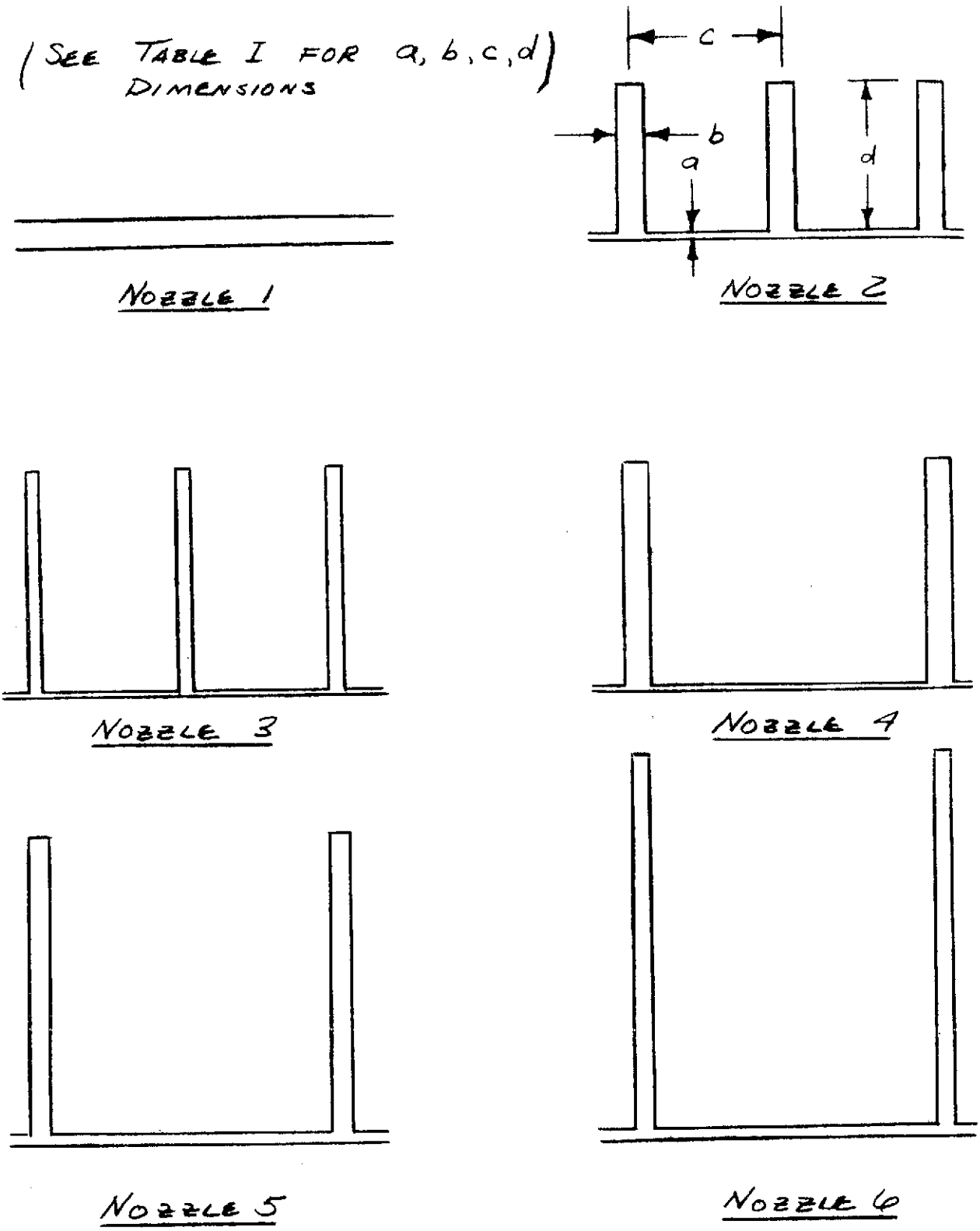

(e) Nozzle schematics.

Figure 2.- Concluded.

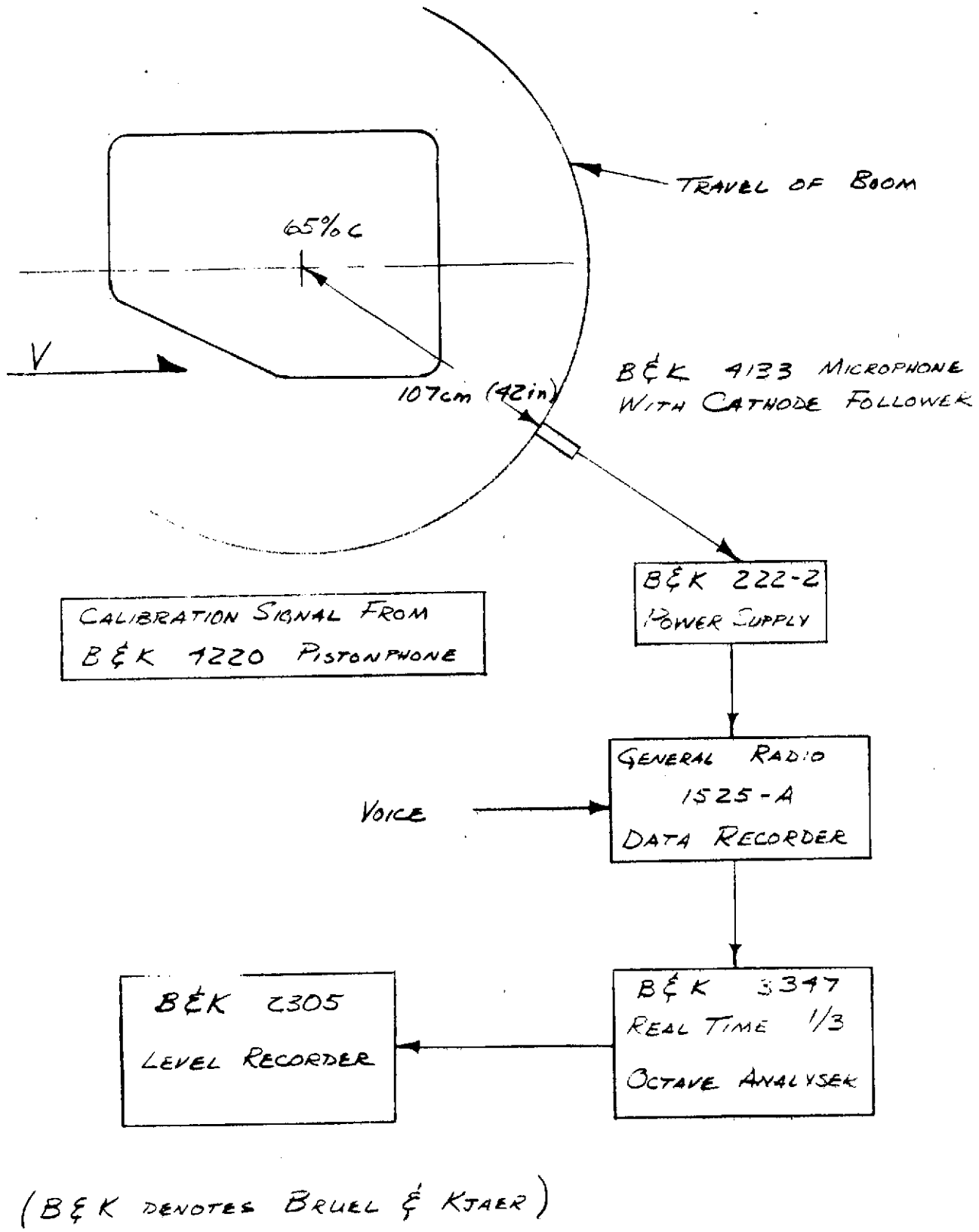

Figure 3.- Schematic of the noise acquisition and reduction system.

Figure 4.- Variation of nozzle pressure over span of model.

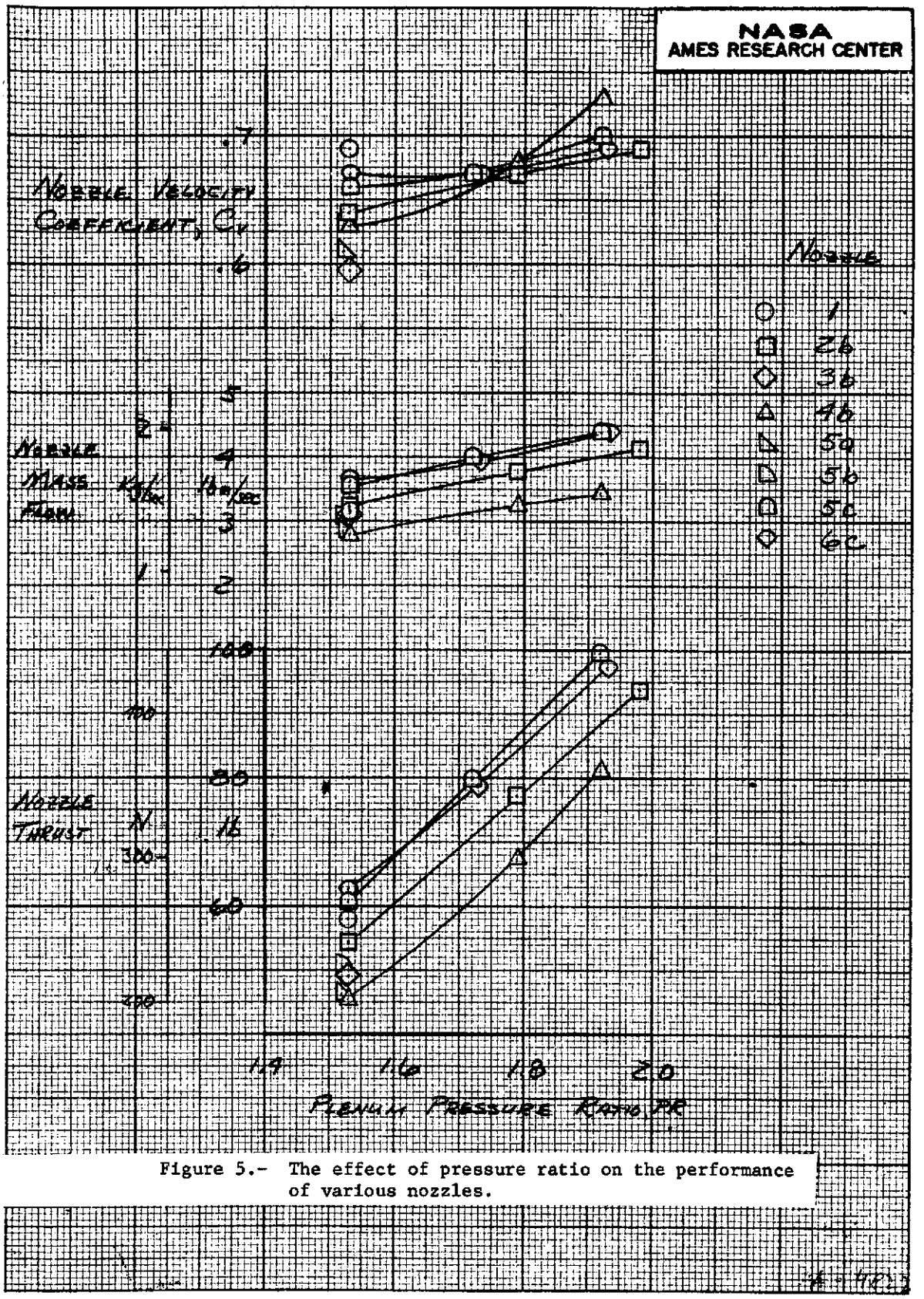

Figure 5.- The effect of pressure ratio on the performance of various nozzles.

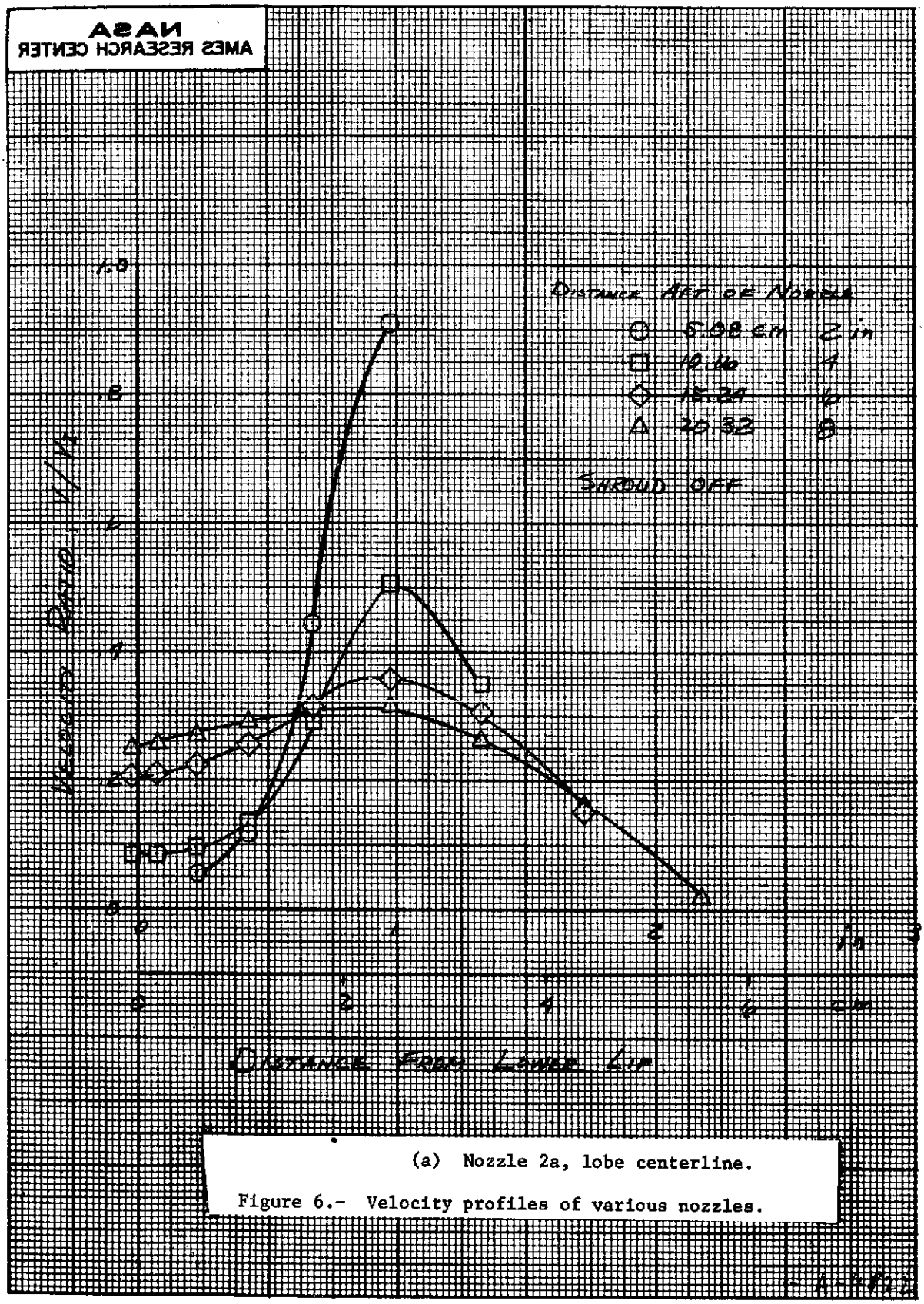

(a) Nozzle 2a, lobe centerline.

Figure 6.- Velocity profiles of various nozzles.

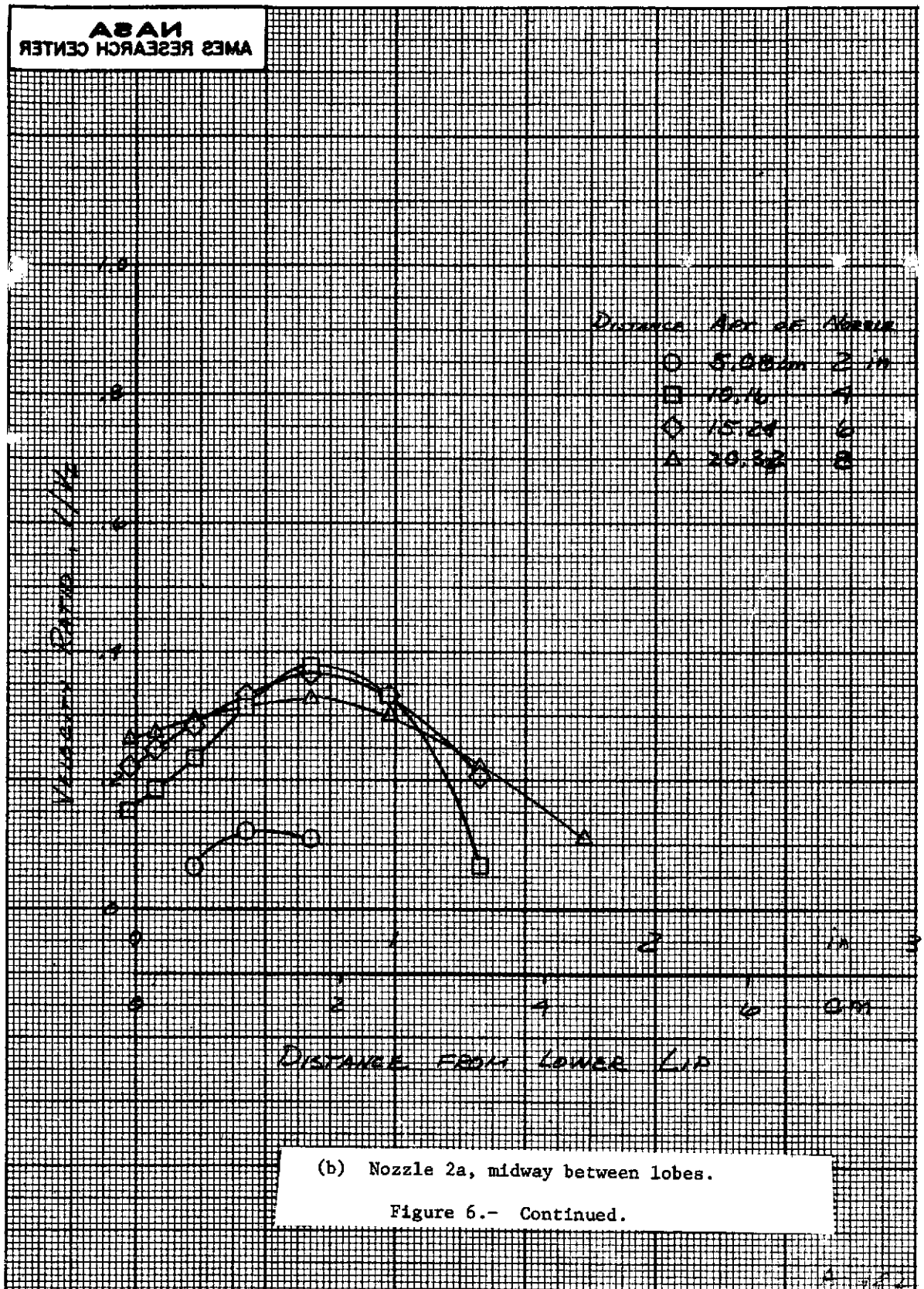

(b) Nozzle 2a, midway between lobes.

Figure 6.- Continued.

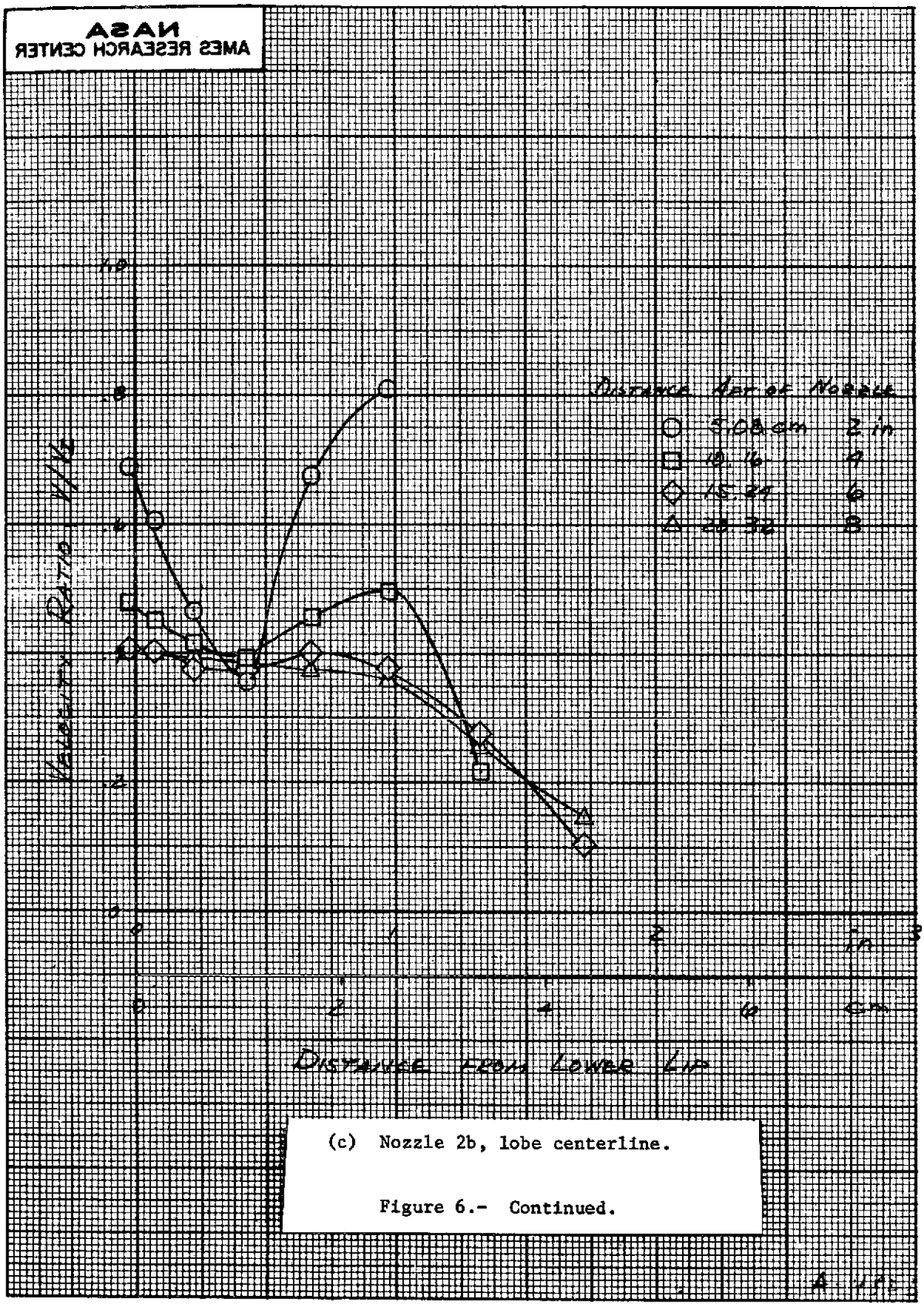

(c) Nozzle 2b, lobe centerline.

Figure 6.- Continued.

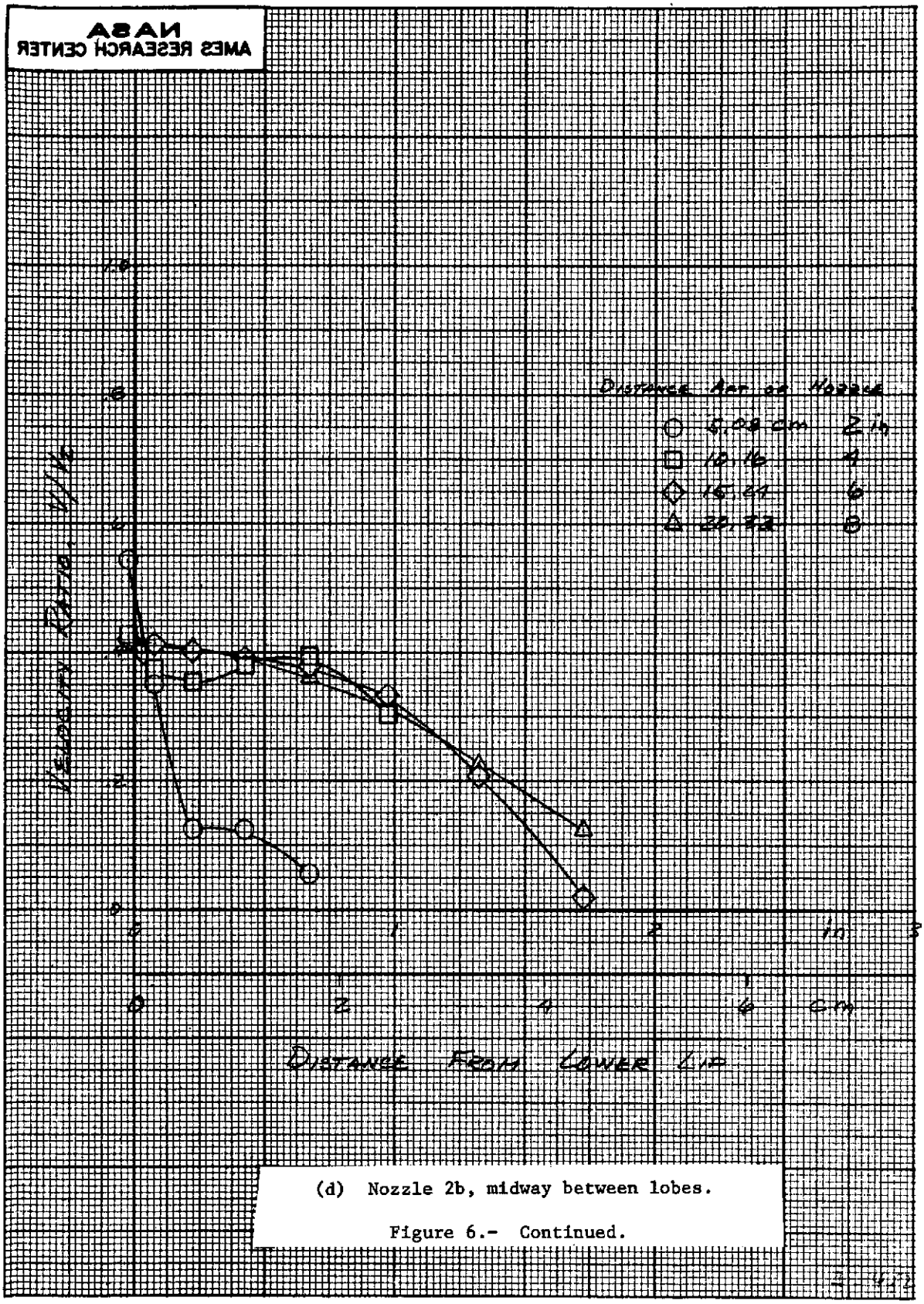

(d) Nozzle 2b, midway between lobes.

Figure 6.- Continued.

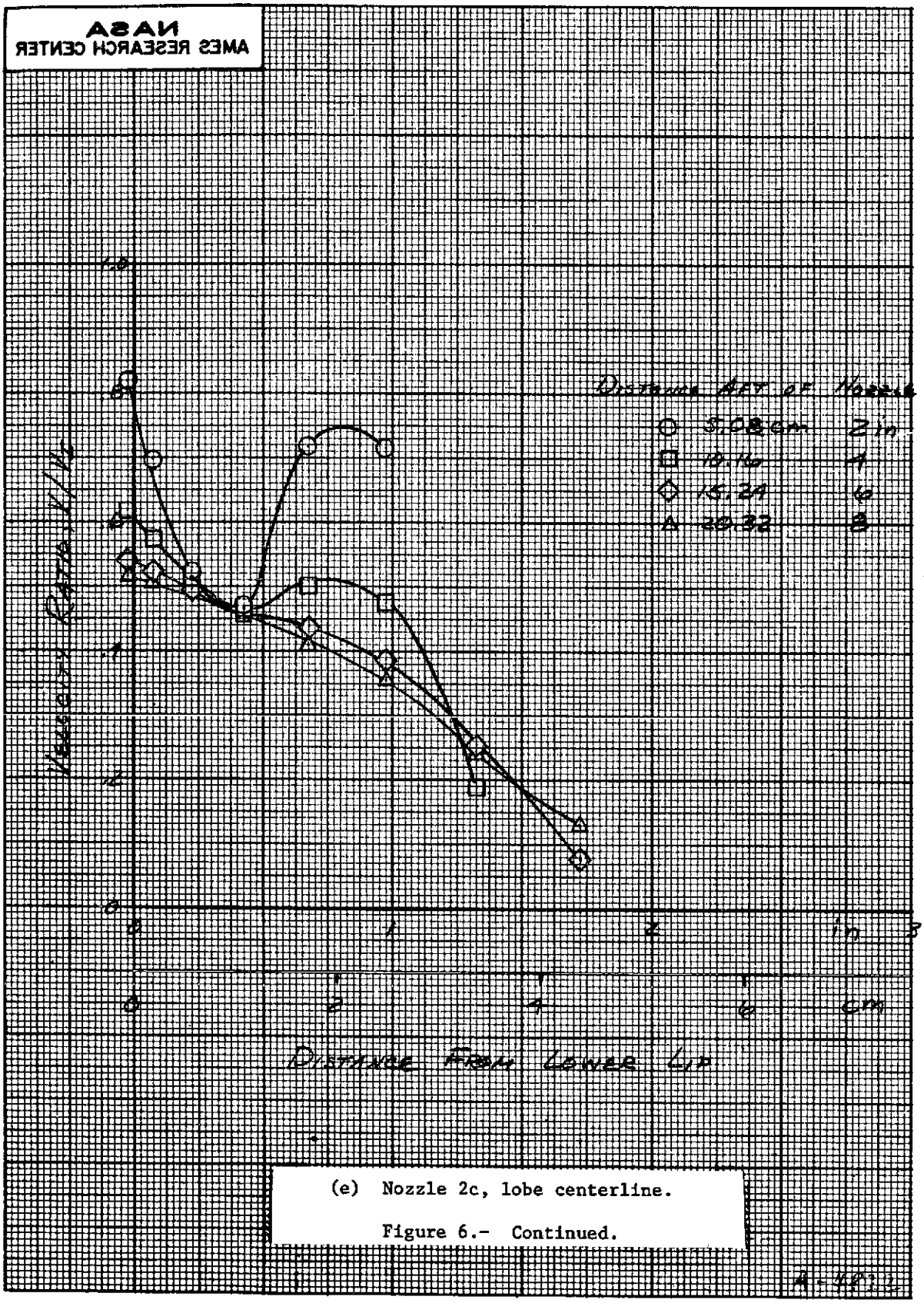

(e) Nozzle 2c, lobe centerline.

Figure 6.- Continued.

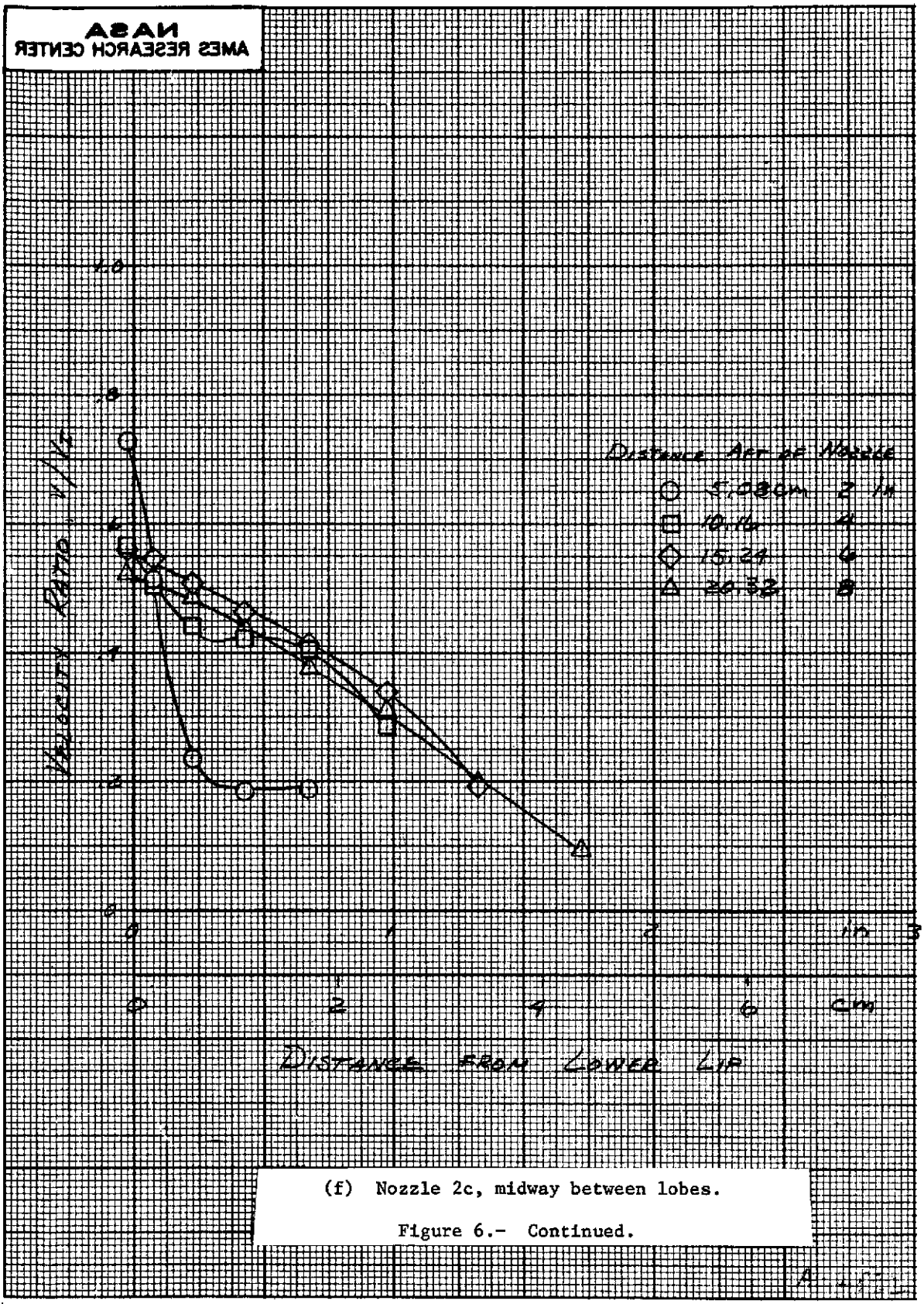

(f) Nozzle 2c, midway between lobes.

Figure 6.- Continued.

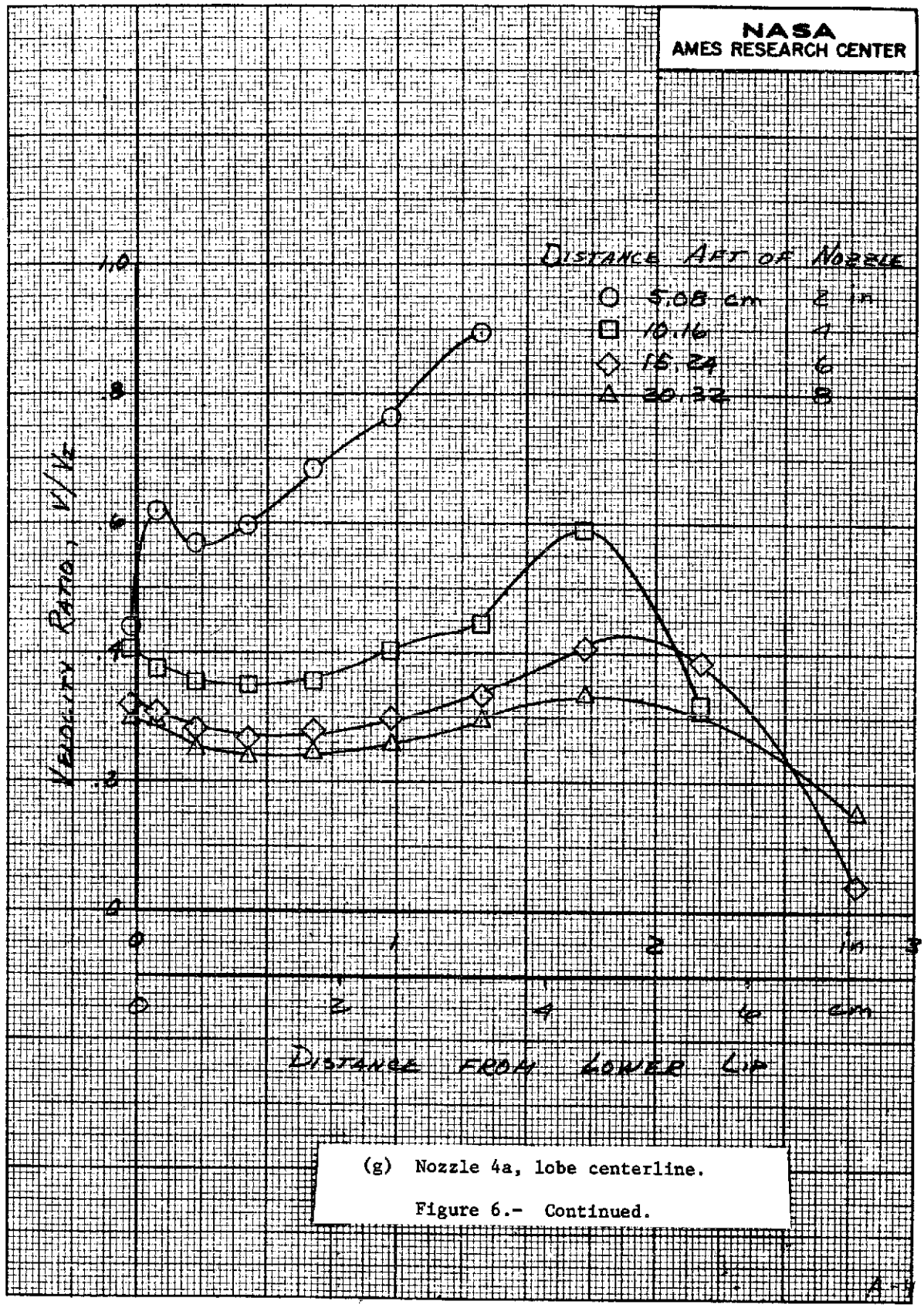

(g) Nozzle 4a, lobe centerline.

Figure 6.- Continued.

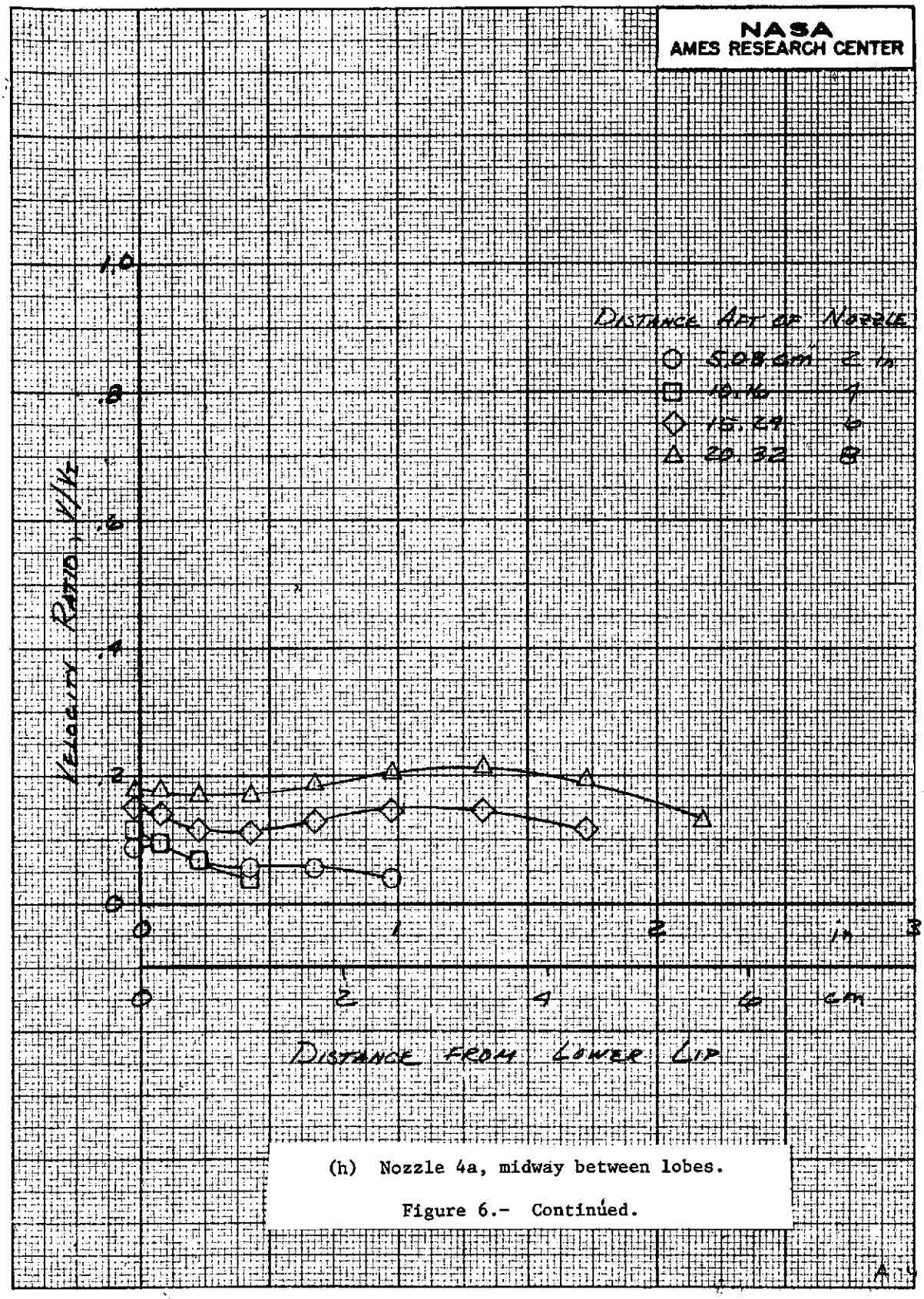

(h) Nozzle 4a, midway between lobes.

Figure 6.- Continued.

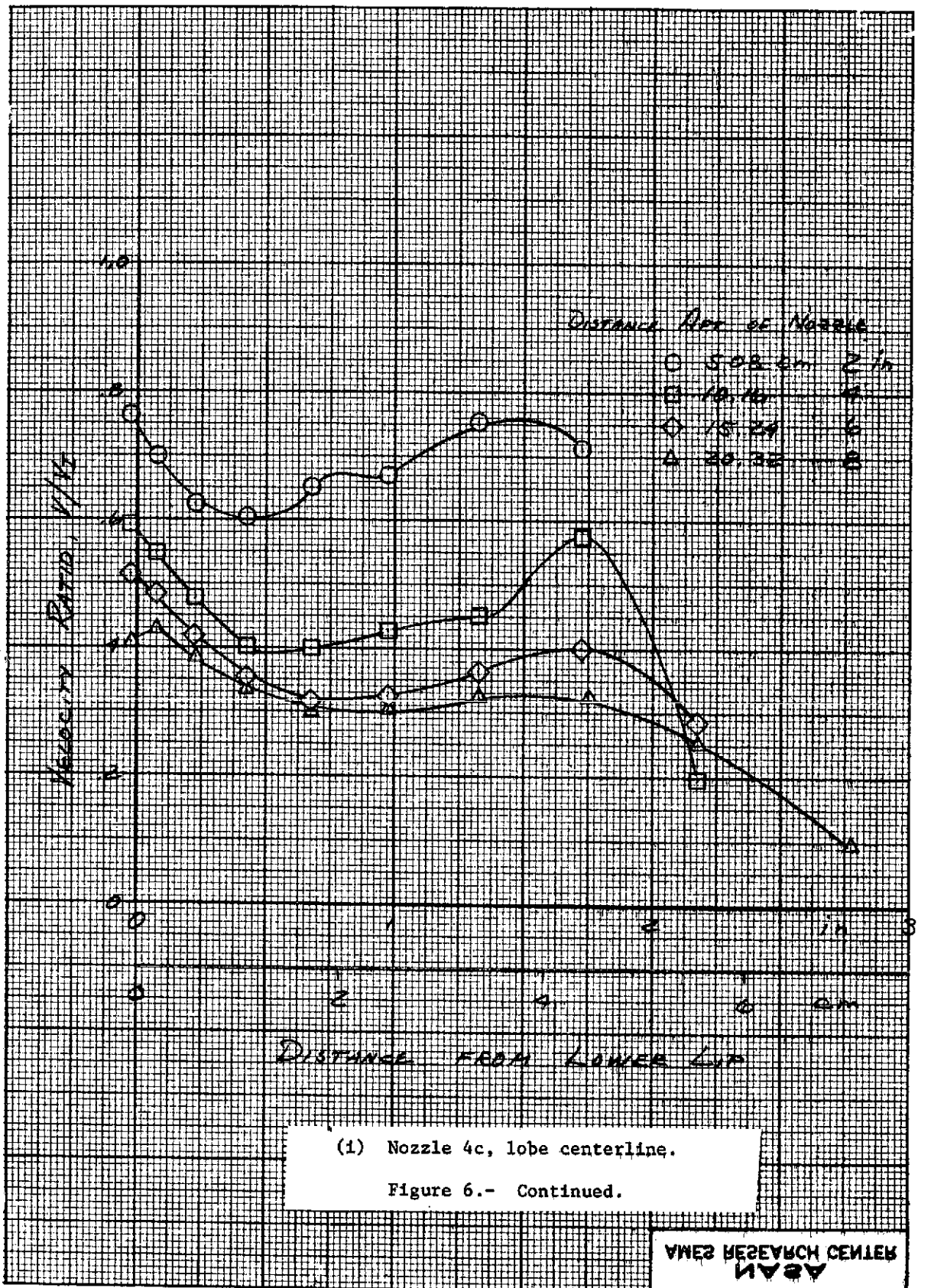

(i) Nozzle 4c, lobe centerline.

Figure 6.- Continued.

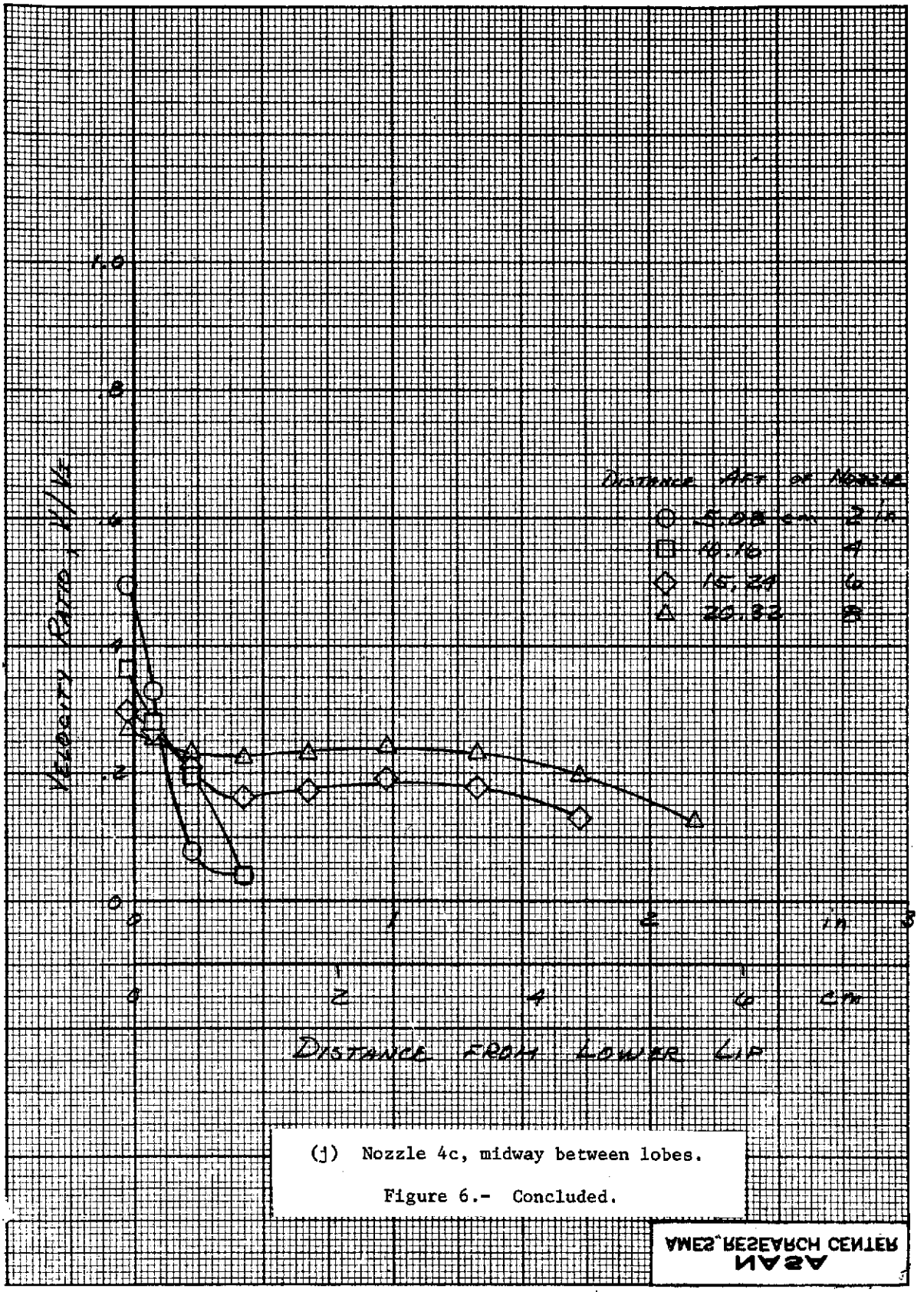

(j) Nozzle 4c, midway between lobes.

Figure 6.- Concluded.

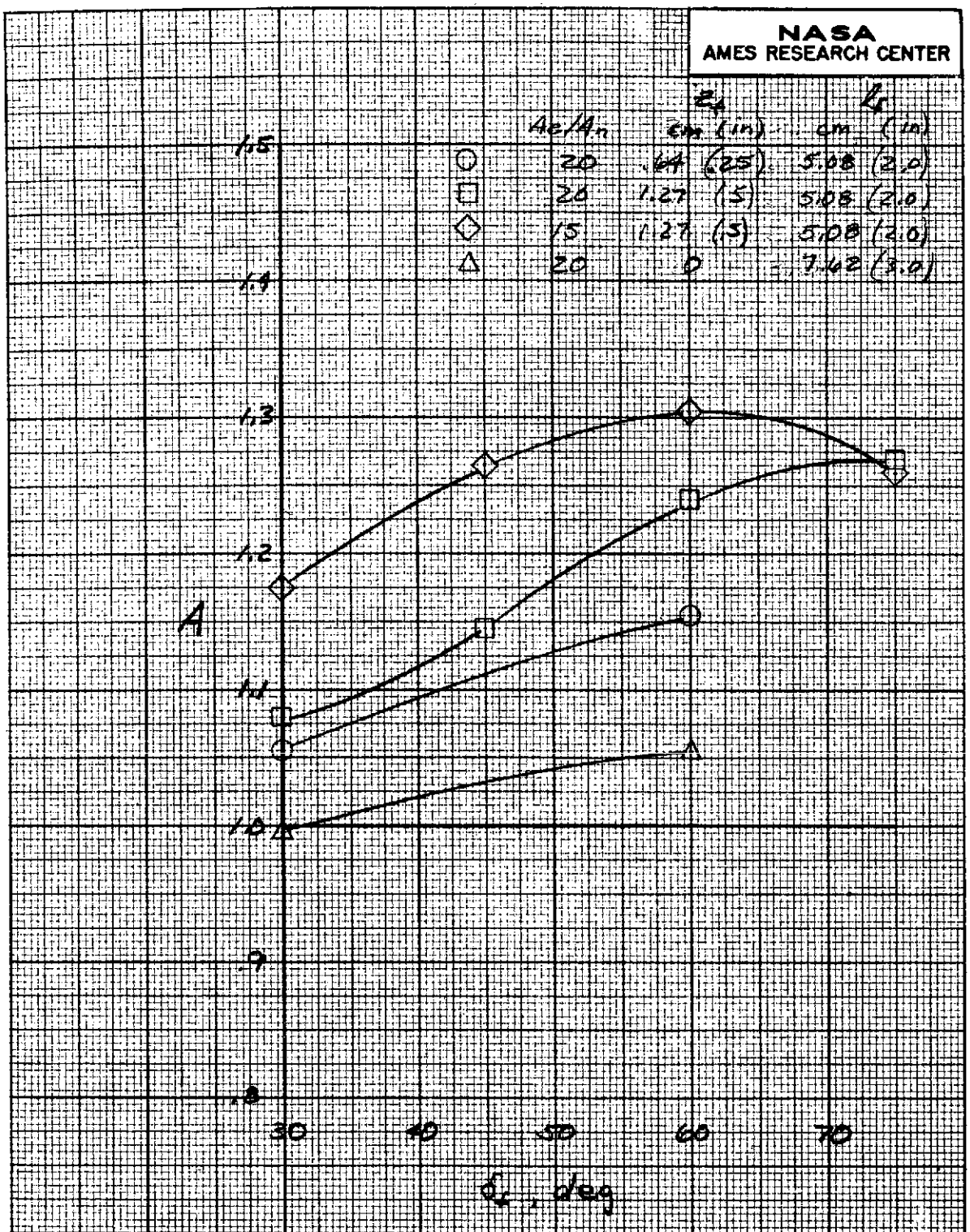

Figure 7.- The effect of flap angle on the static augmentation of nozzle 1; A_e/A_t = 1.25, ℓ_s = 0, PR = 1.53.

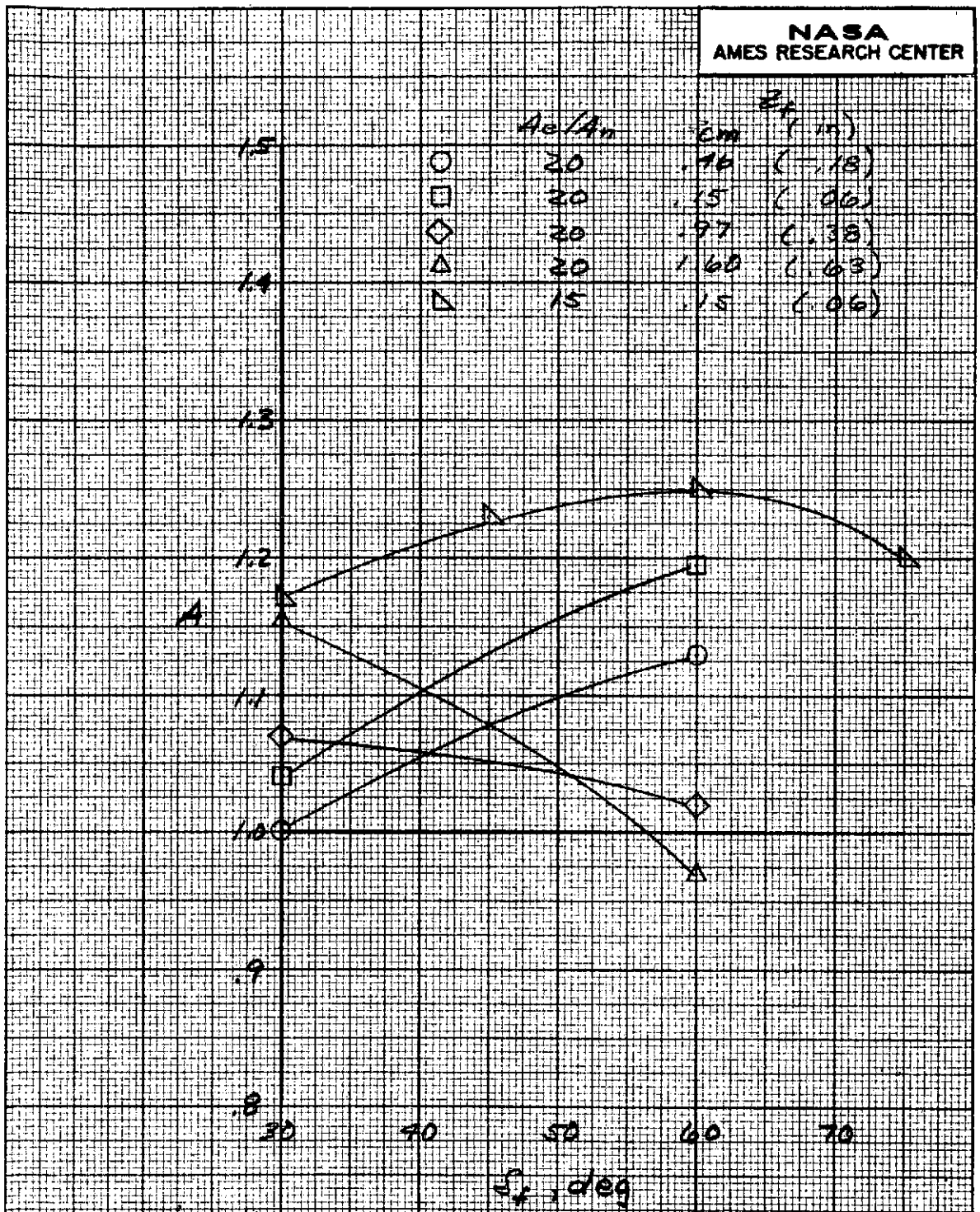

(a) ℓ_f = 5.08 cm (2.0 in).

Figure 8.- The effect of flap angle on the static augmentation of nozzle 2b; A_e/A_t = 1.25, ℓ_s = 0, PR = 1.53.

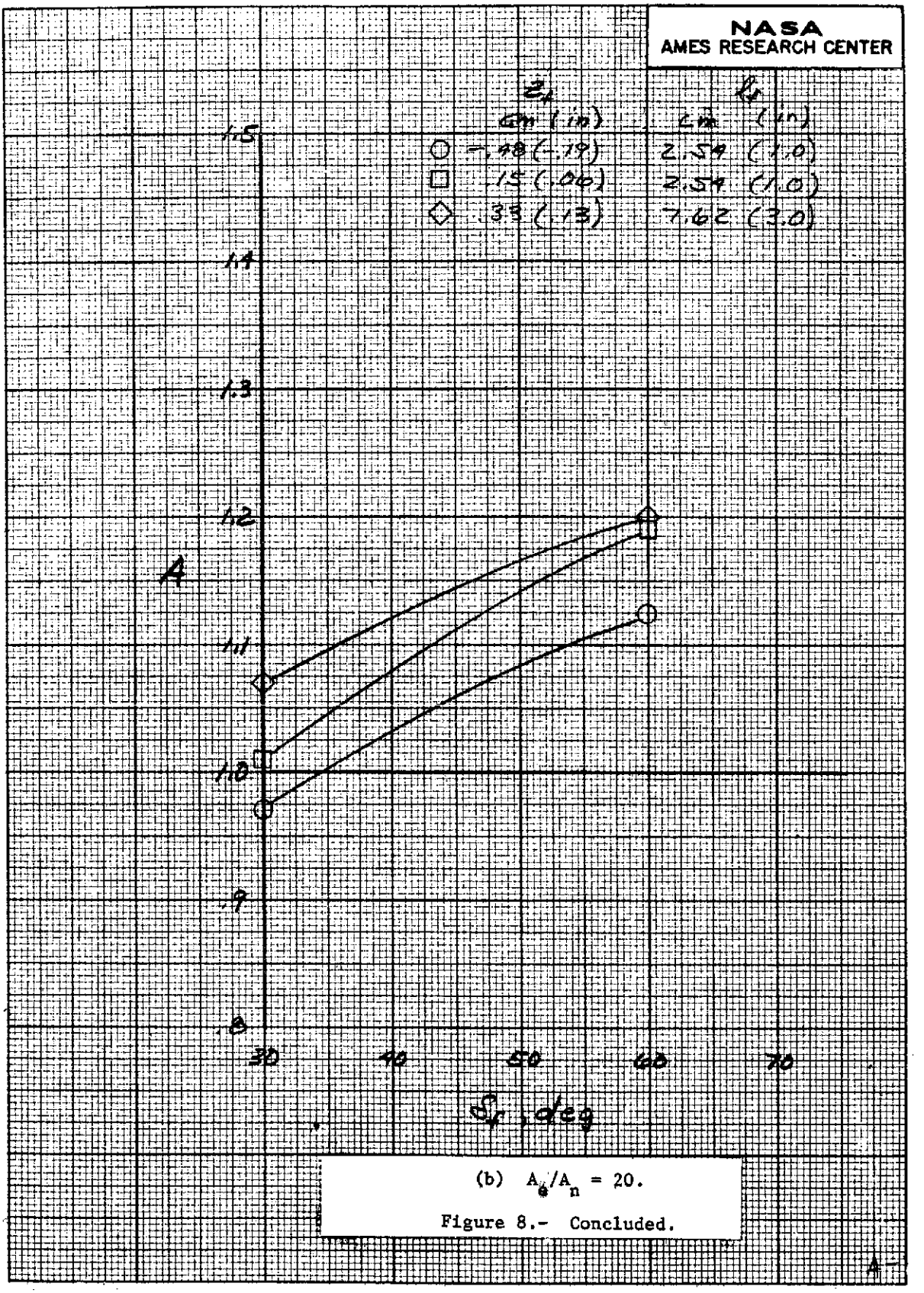

(b) $A_e/A_n = 20.$

Figure 8.- Concluded.

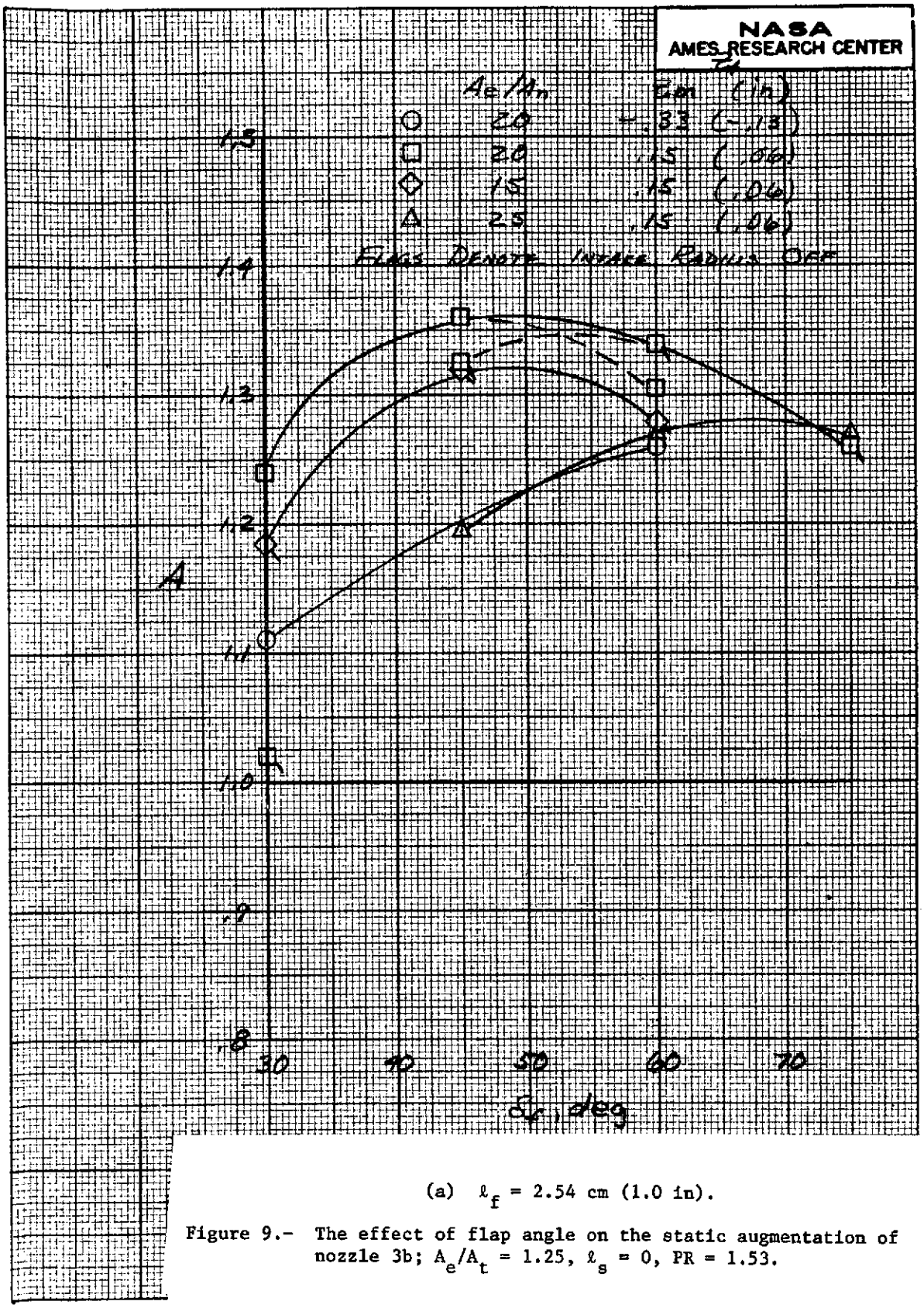

(a) ℓ_f = 2.54 cm (1.0 in).

Figure 9.- The effect of flap angle on the static augmentation of nozzle 3b; A_e/A_t = 1.25, ℓ_s = 0, PR = 1.53.

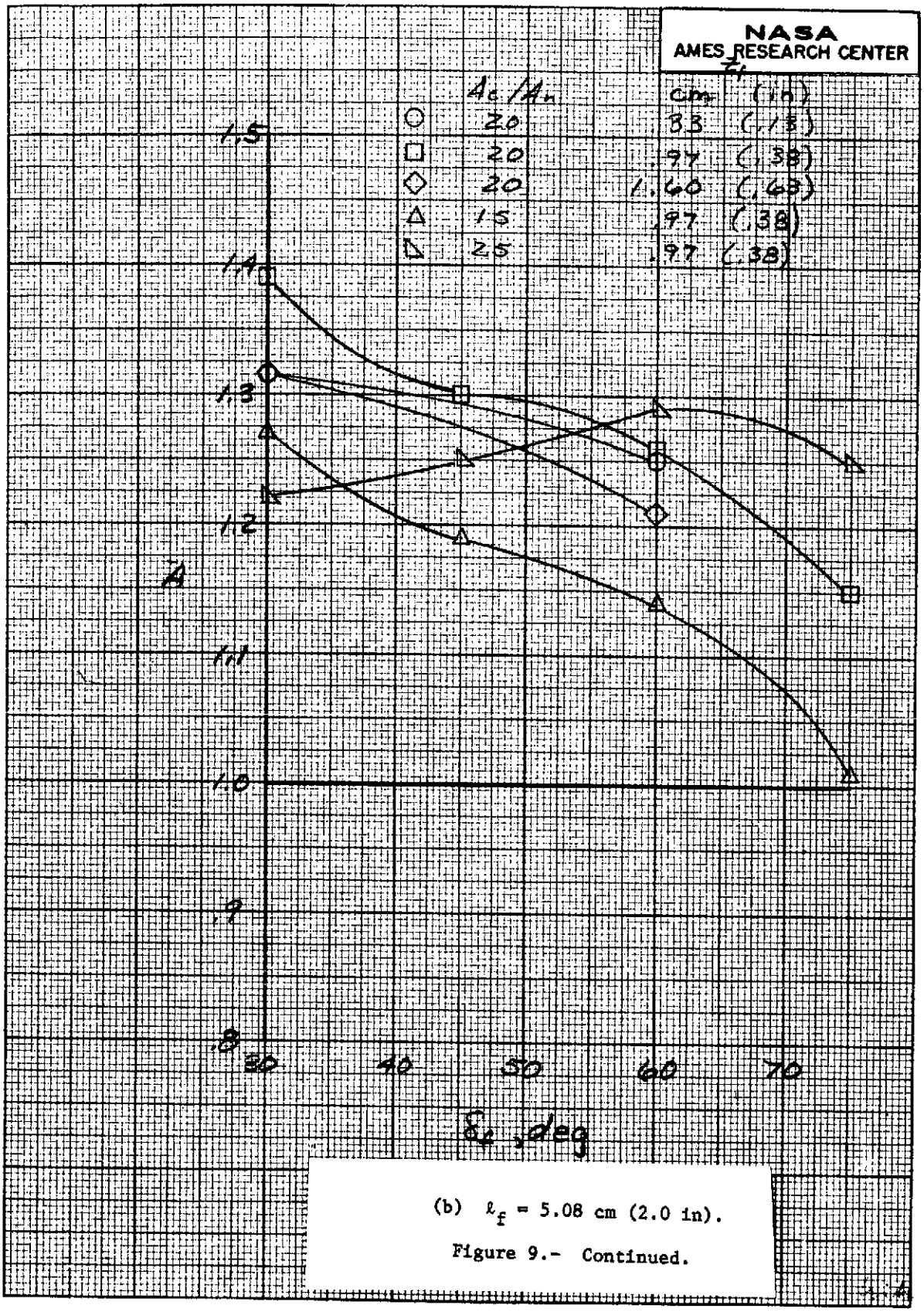

(b) ℓ_f = 5.08 cm (2.0 in).

Figure 9.- Continued.

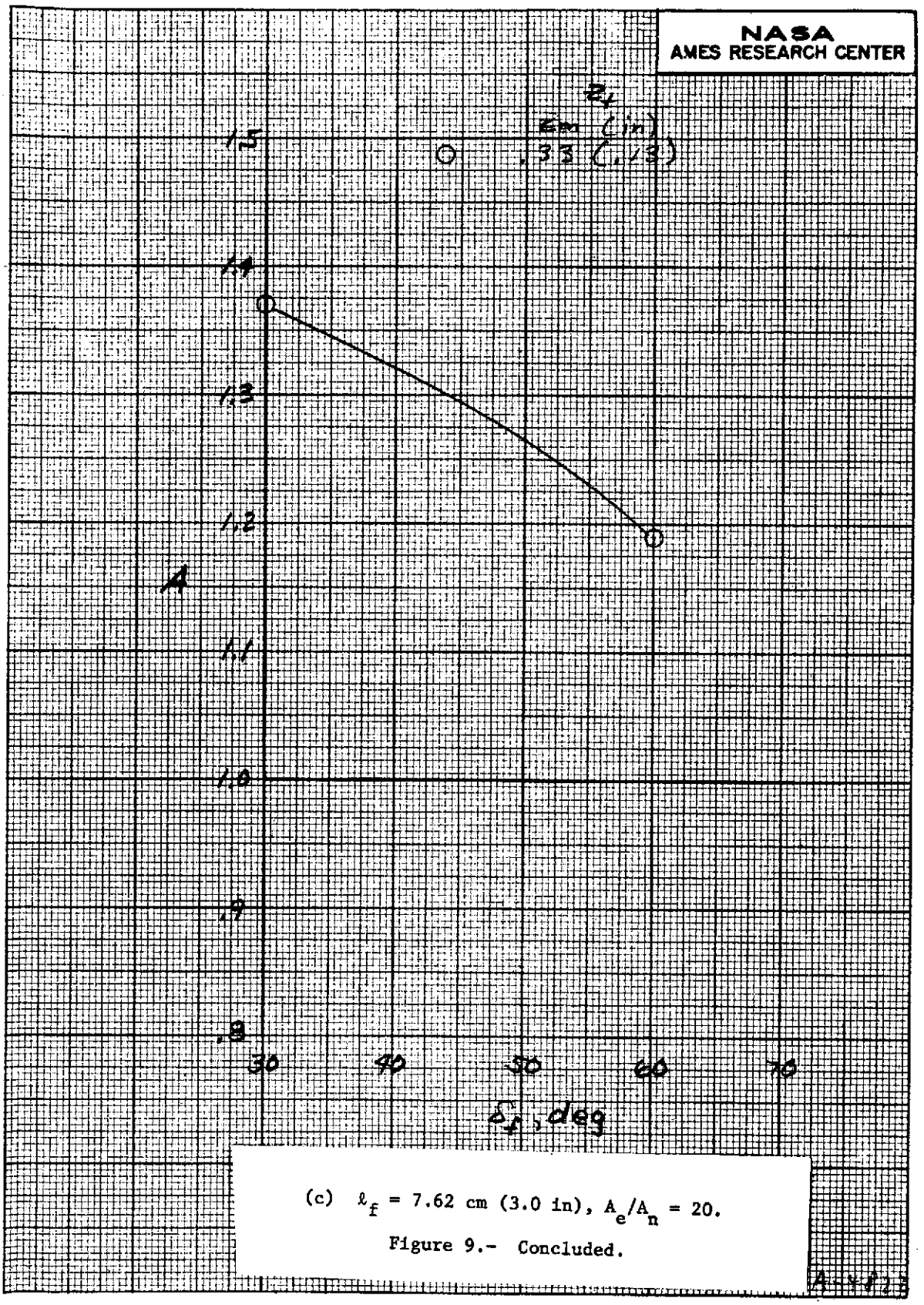

(c) ℓ_f = 7.62 cm (3.0 in), A_e/A_n = 20.

Figure 9.- Concluded.

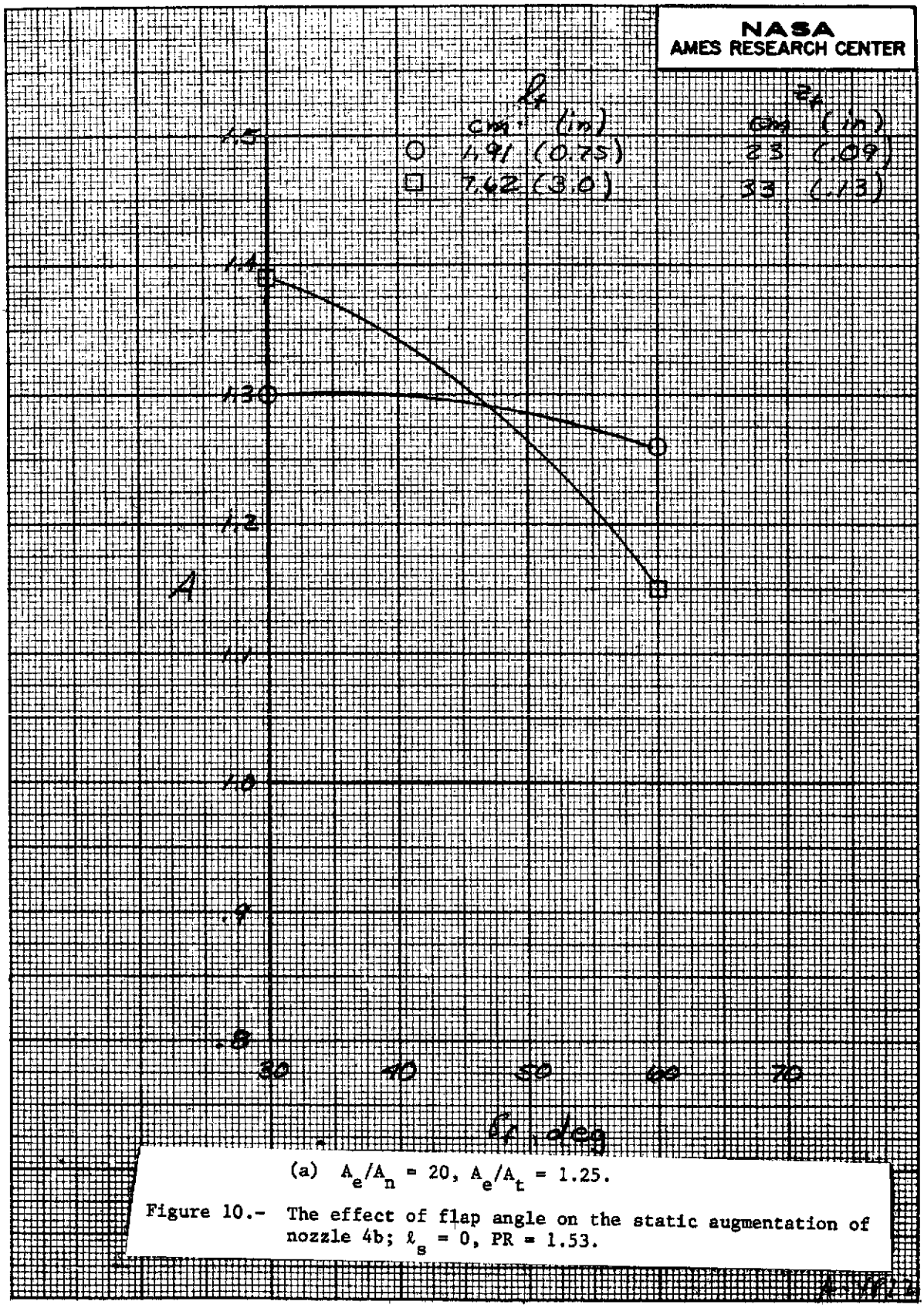

(a) $A_e/A_n = 20$, $A_e/A_t = 1.25$.

Figure 10.- The effect of flap angle on the static augmentation of nozzle 4b; $\ell_s = 0$, PR = 1.53.

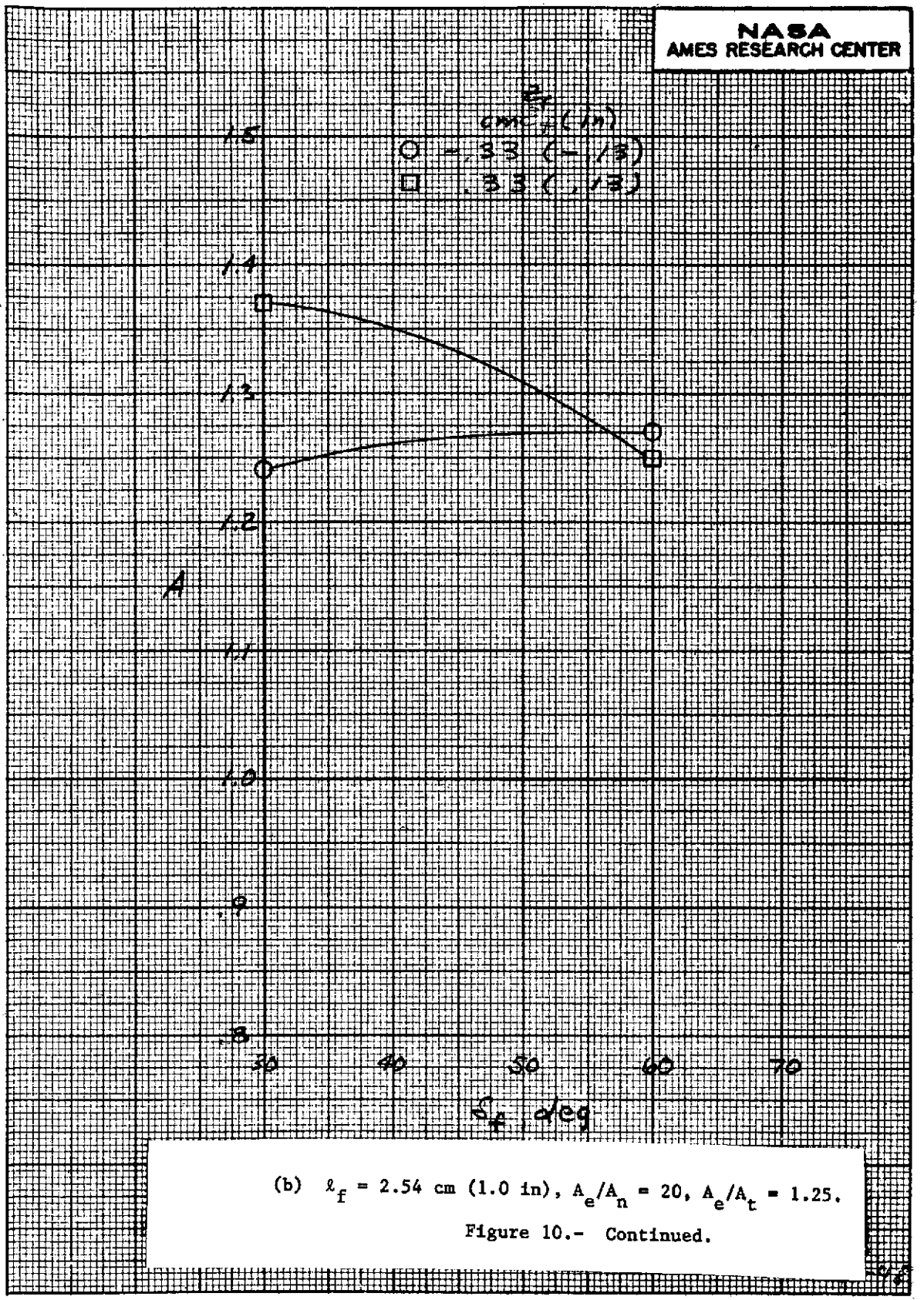

(b) ℓ_f = 2.54 cm (1.0 in), A_e/A_n = 20, A_e/A_t = 1.25.

Figure 10.- Continued.

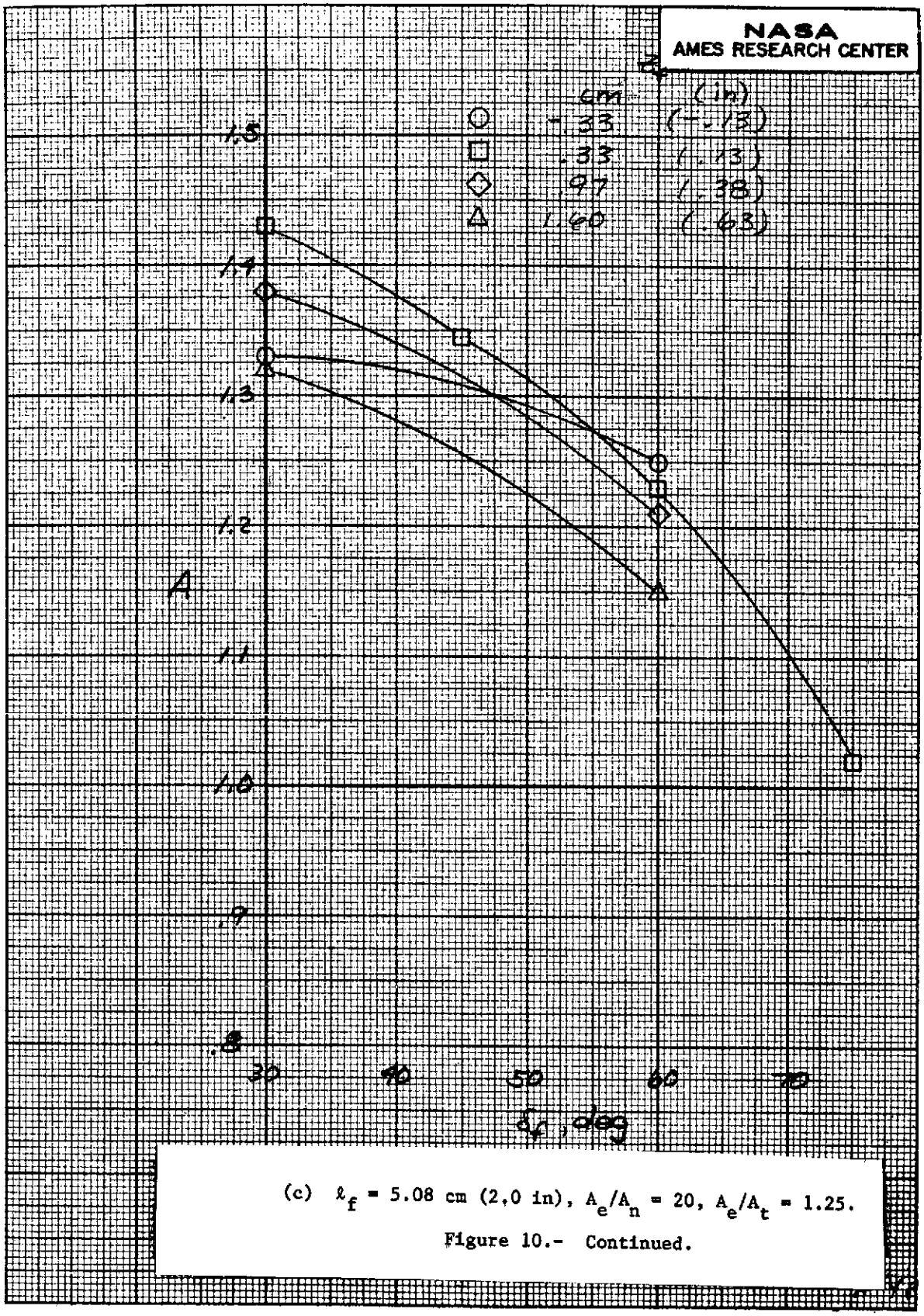

(c) ℓ_f = 5.08 cm (2.0 in), A_e/A_n = 20, A_e/A_t = 1.25.

Figure 10.- Continued.

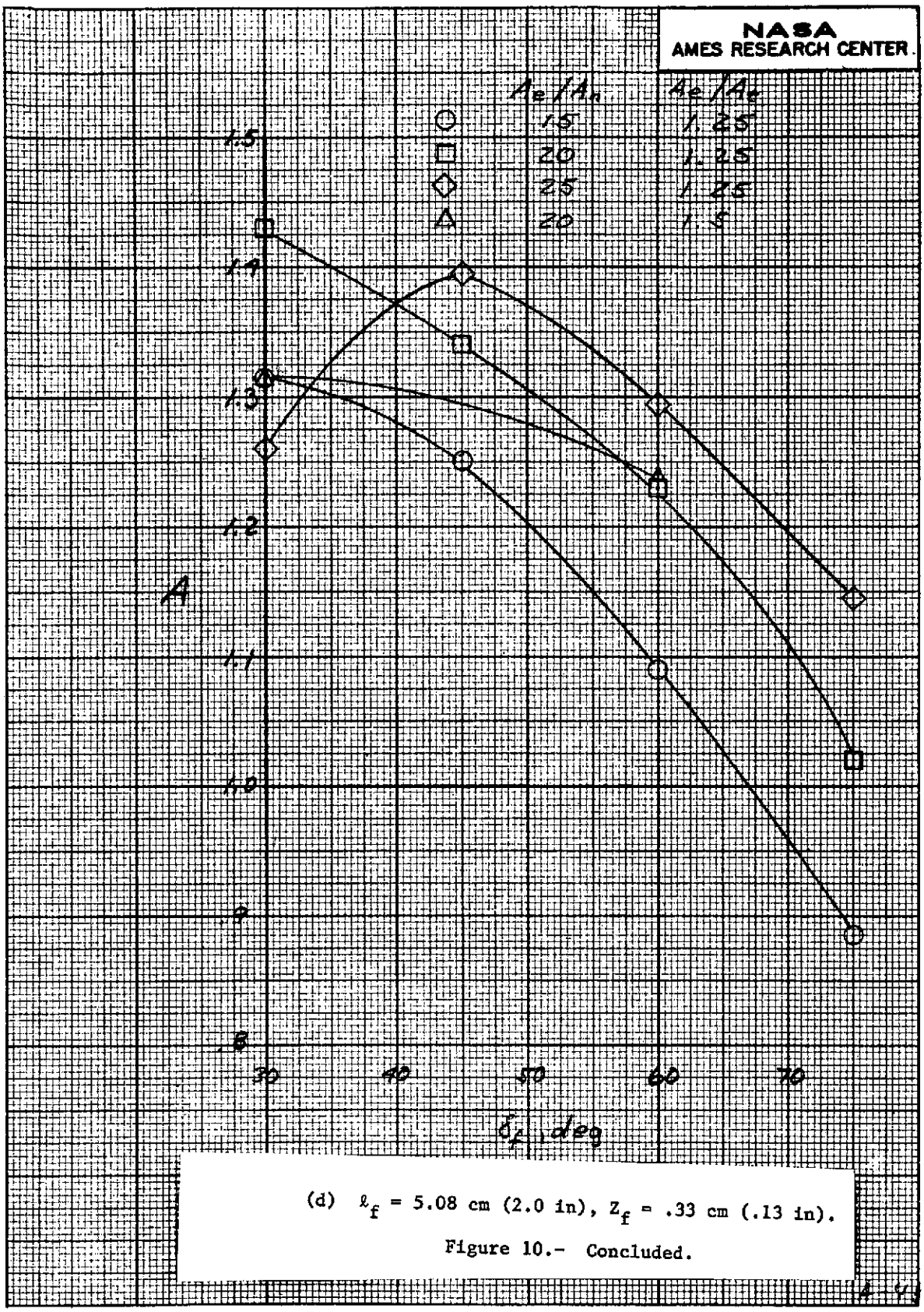

(d) ℓ_f = 5.08 cm (2.0 in), Z_f = .33 cm (.13 in).

Figure 10.- Concluded.

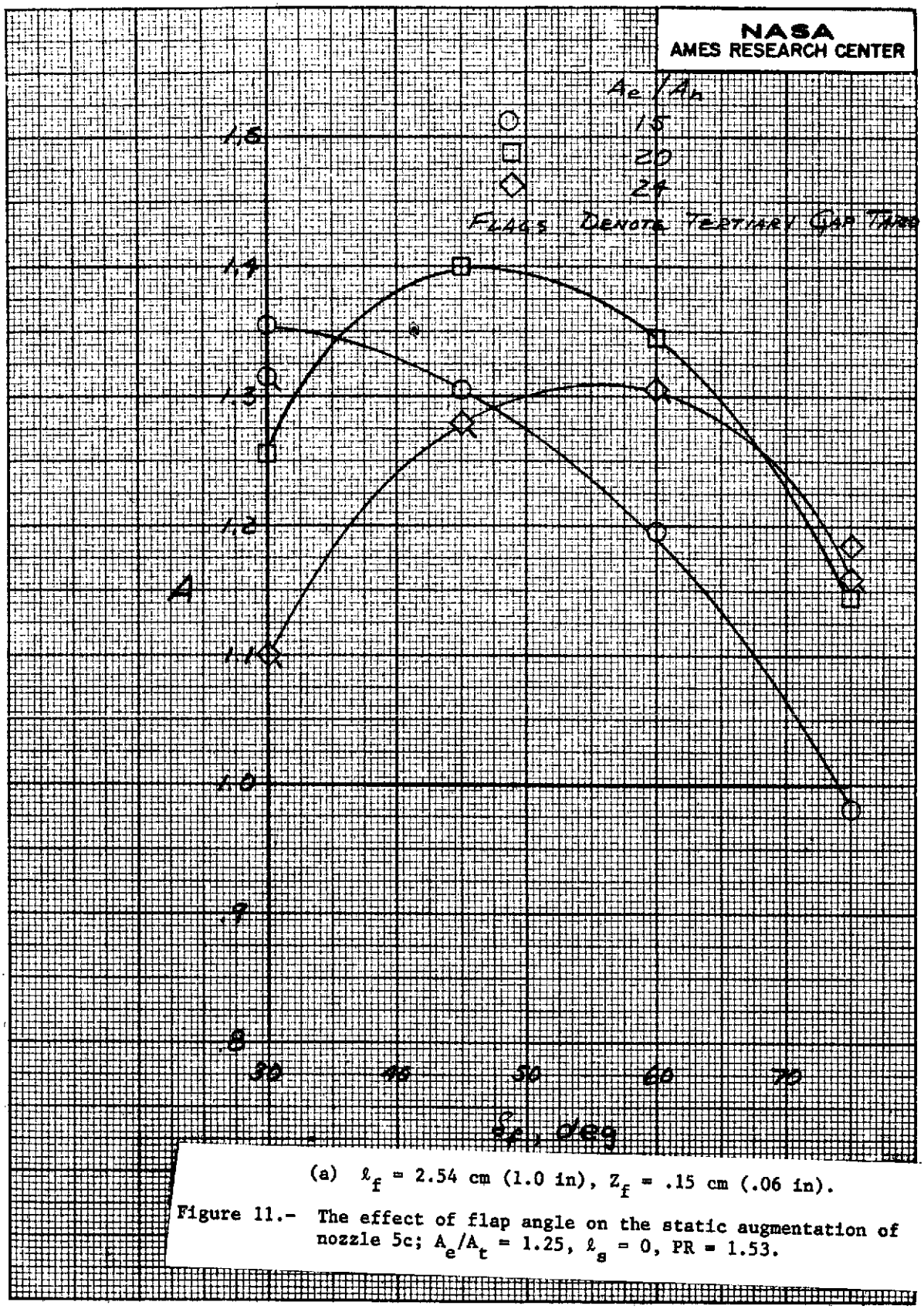

(a) ℓ_f = 2.54 cm (1.0 in), Z_f = .15 cm (.06 in).

Figure 11.- The effect of flap angle on the static augmentation of nozzle 5c; A_e/A_t = 1.25, ℓ_s = 0, PR = 1.53.

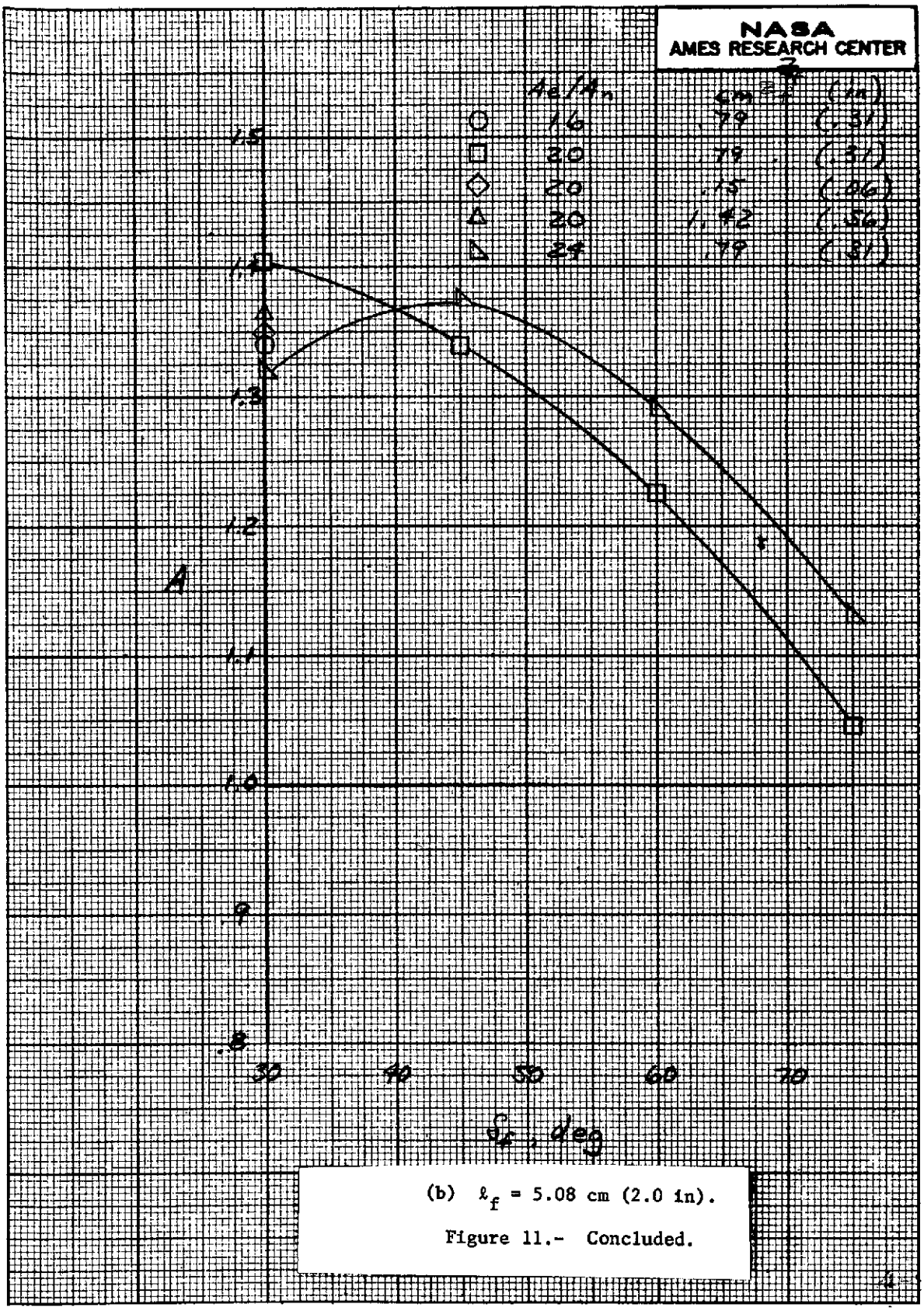

(b) ℓ_f = 5.08 cm (2.0 in).

Figure 11.- Concluded.

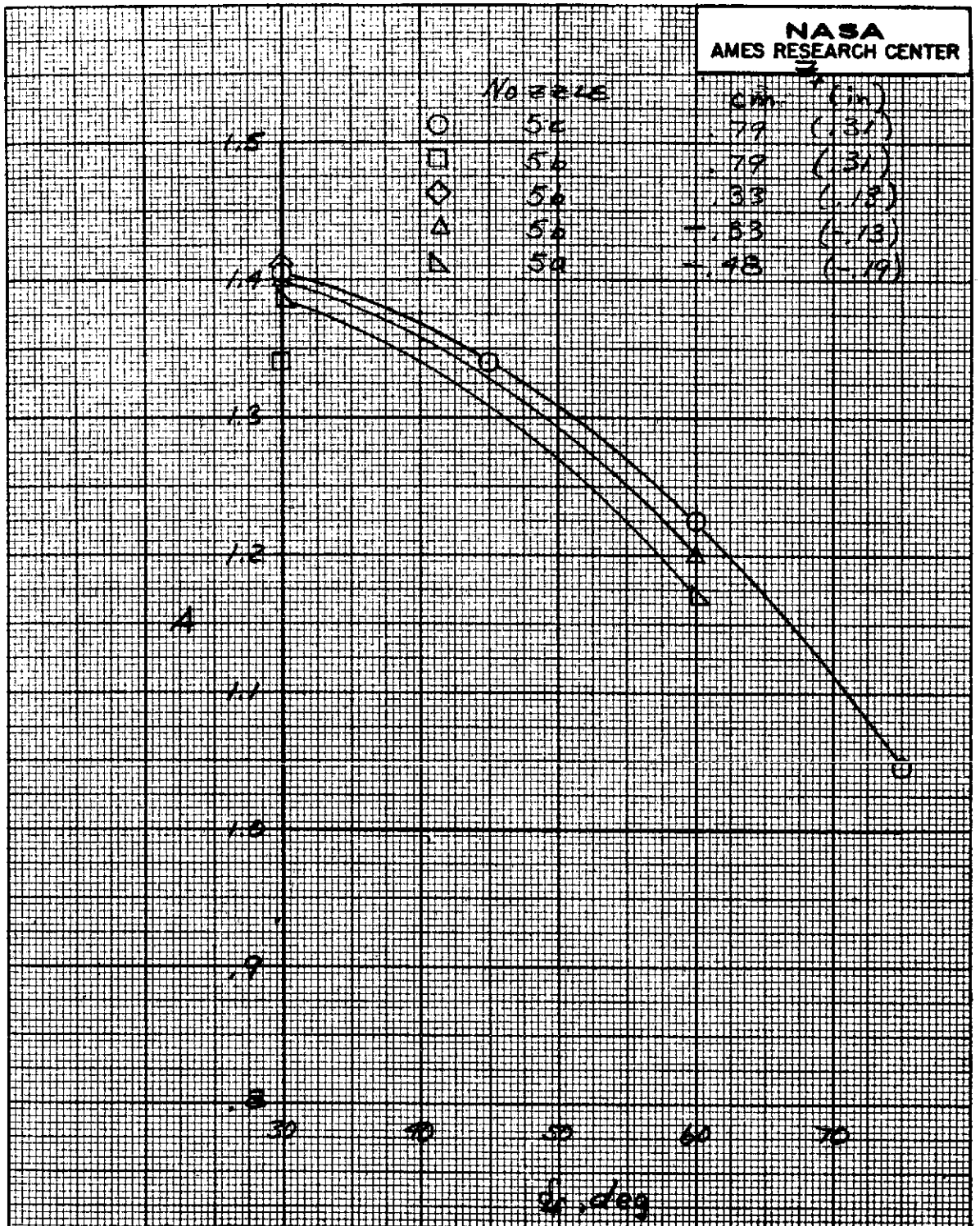

Figure 12.- The effect of flap angle on the static augmentation of several nozzles; A_e/A_n = 20, A_e/A_t = 1.25, ℓ_f = 5.08 cm (2.0 in), ℓ_s = 0, PR = 1.53.

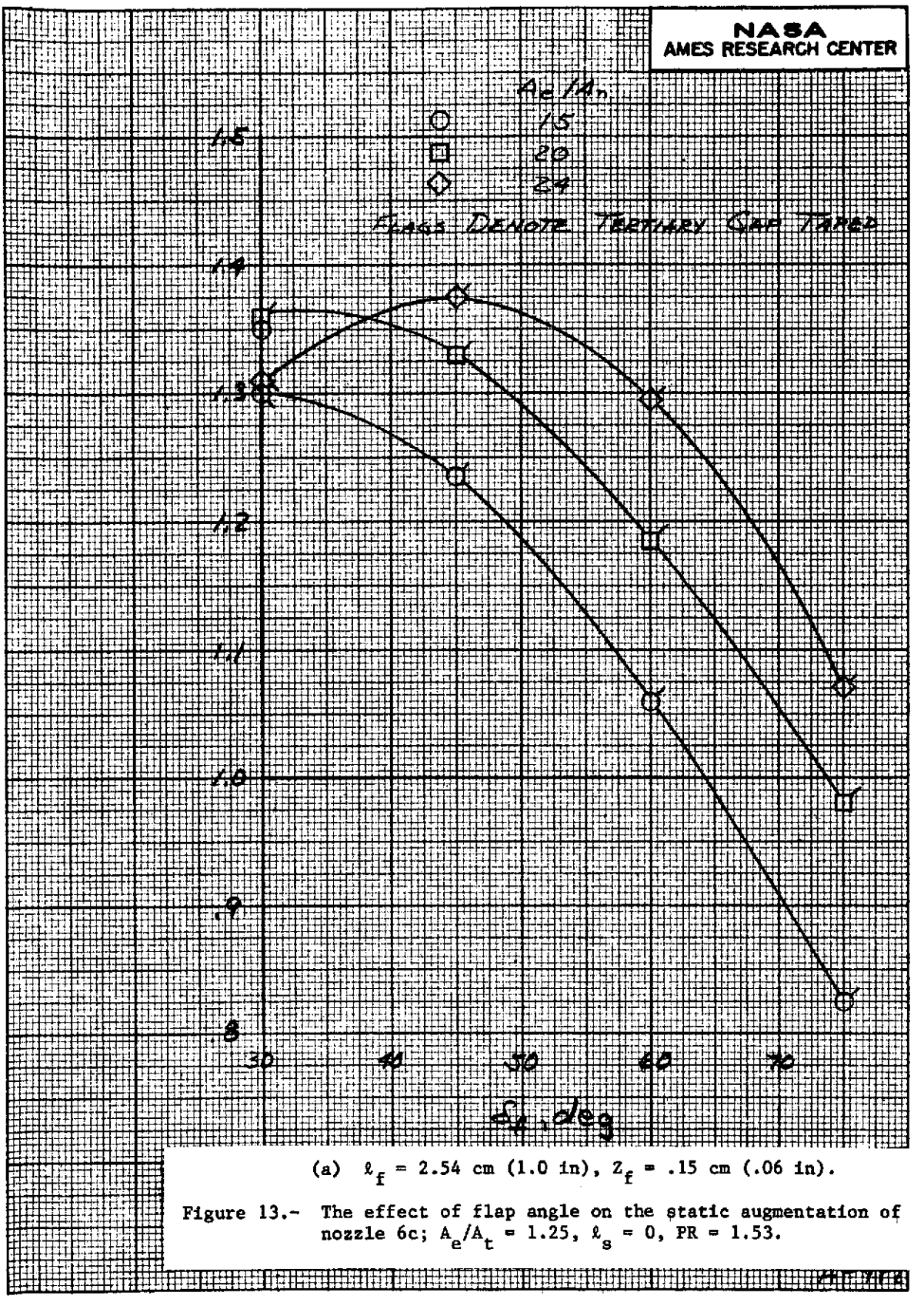

(a) ℓ_f = 2.54 cm (1.0 in), Z_f = .15 cm (.06 in).

Figure 13.- The effect of flap angle on the static augmentation of nozzle 6c; A_e/A_t = 1.25, ℓ_s = 0, PR = 1.53.

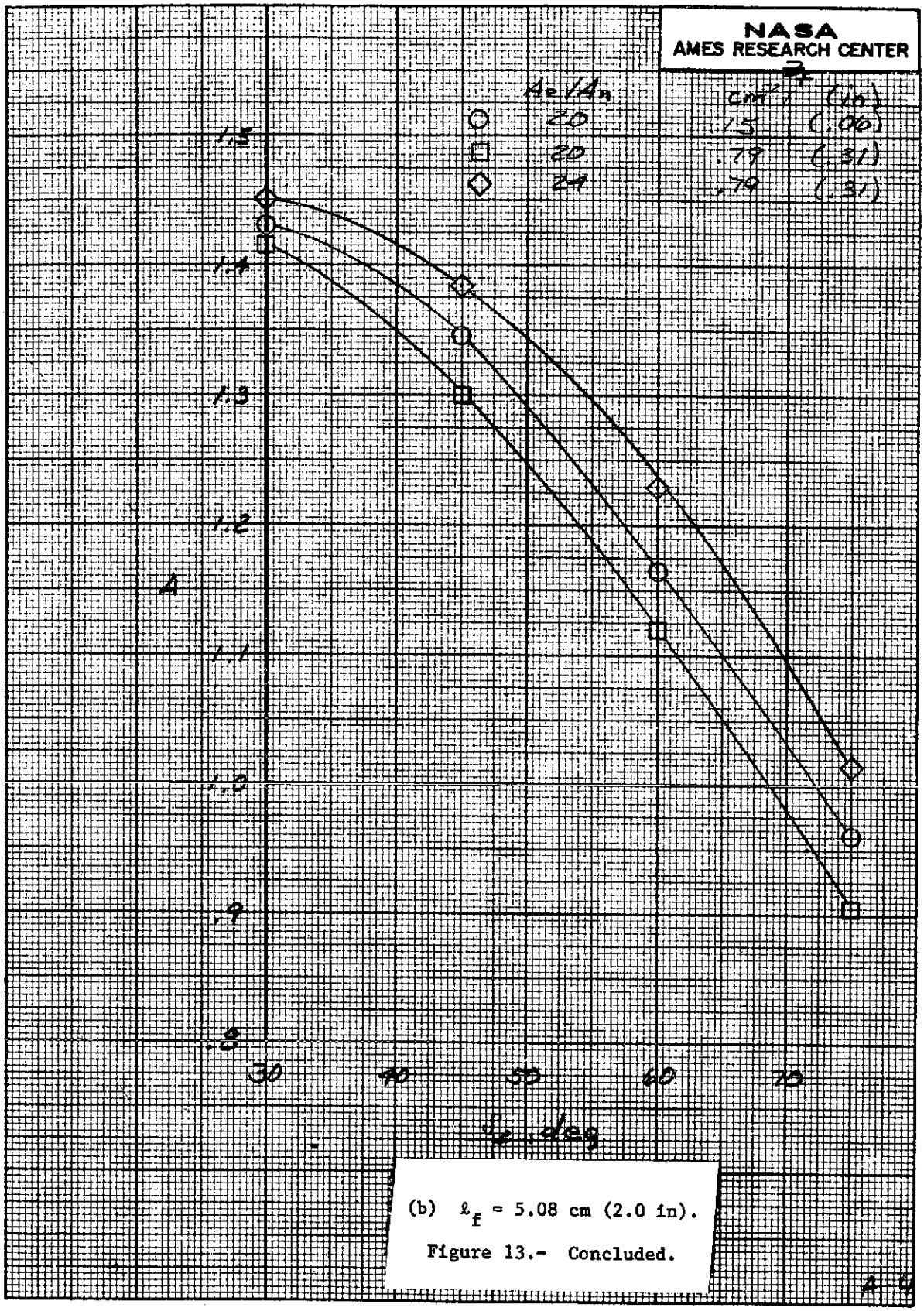

(b) ℓ_f = 5.08 cm (2.0 in).

Figure 13.- Concluded.

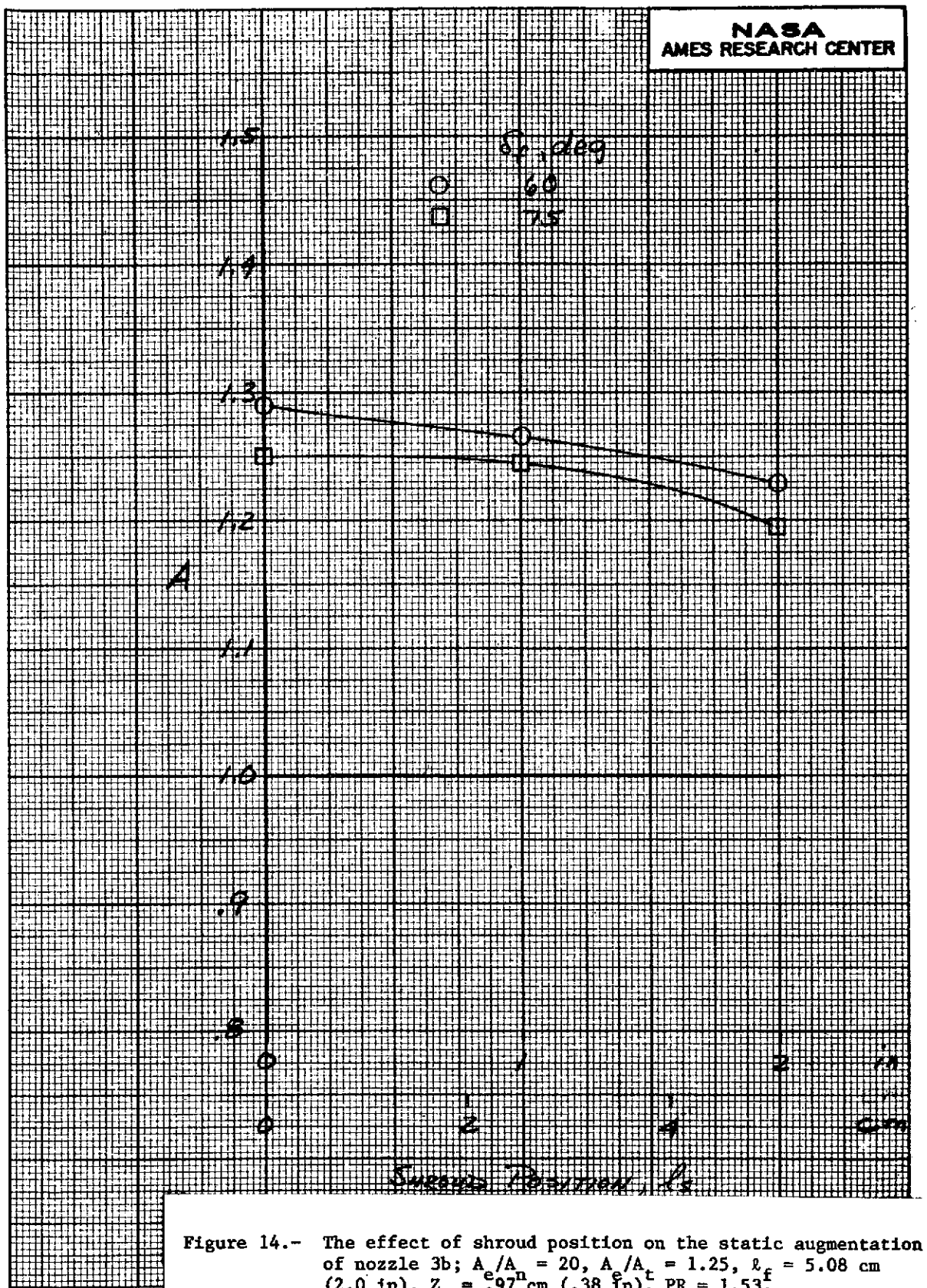

Figure 14.- The effect of shroud position on the static augmentation of nozzle 3b; A_e/A_n = 20, A_e/A_t = 1.25, ℓ_f = 5.08 cm (2.0 in), Z_f = .97 cm (.38 in), PR = 1.53.

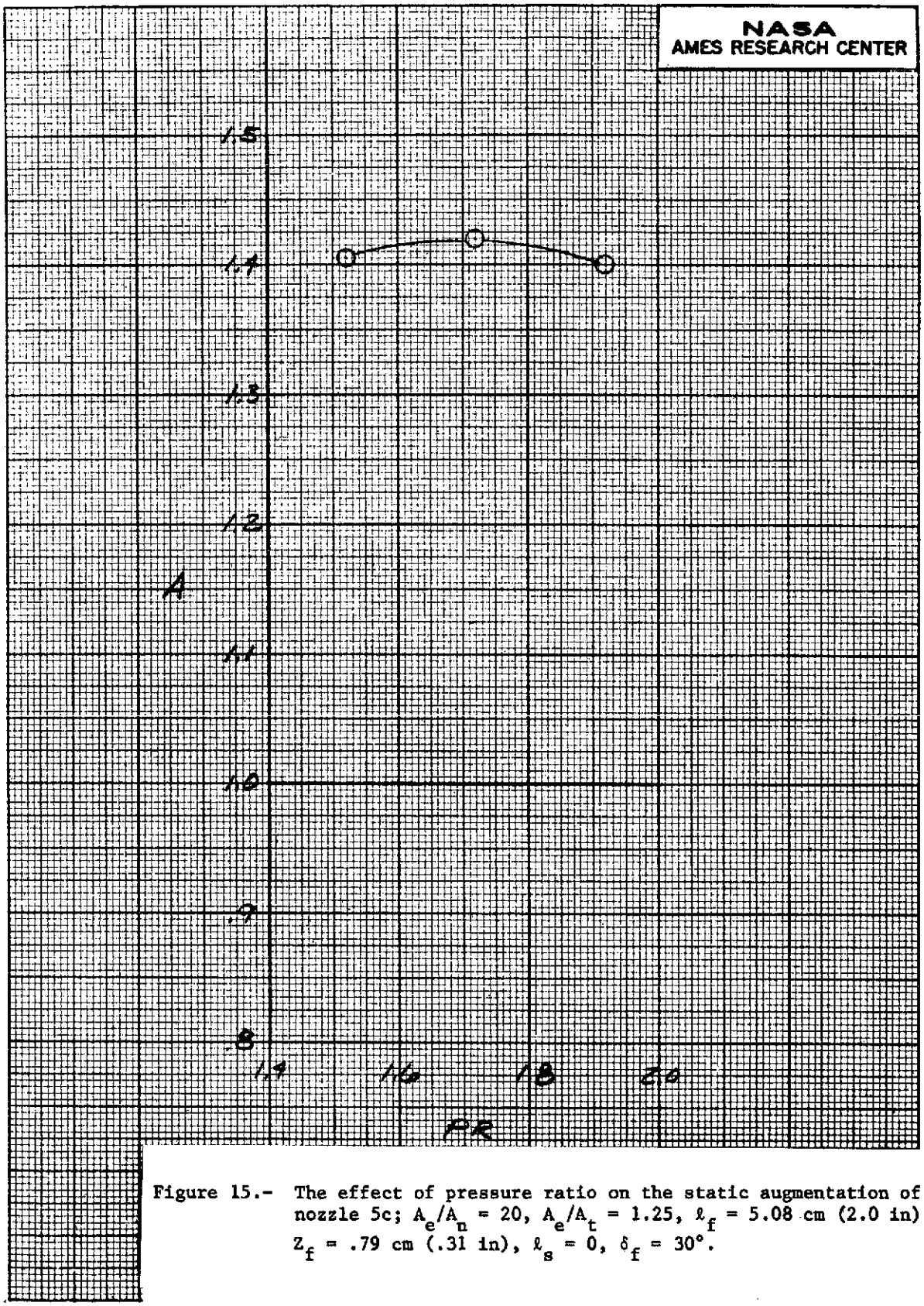

Figure 15.- The effect of pressure ratio on the static augmentation of nozzle 5c; A_e/A_n = 20, A_e/A_t = 1.25, ℓ_f = 5.08 cm (2.0 in), Z_f = .79 cm (.31 in), ℓ_s = 0, δ_f = 30°.

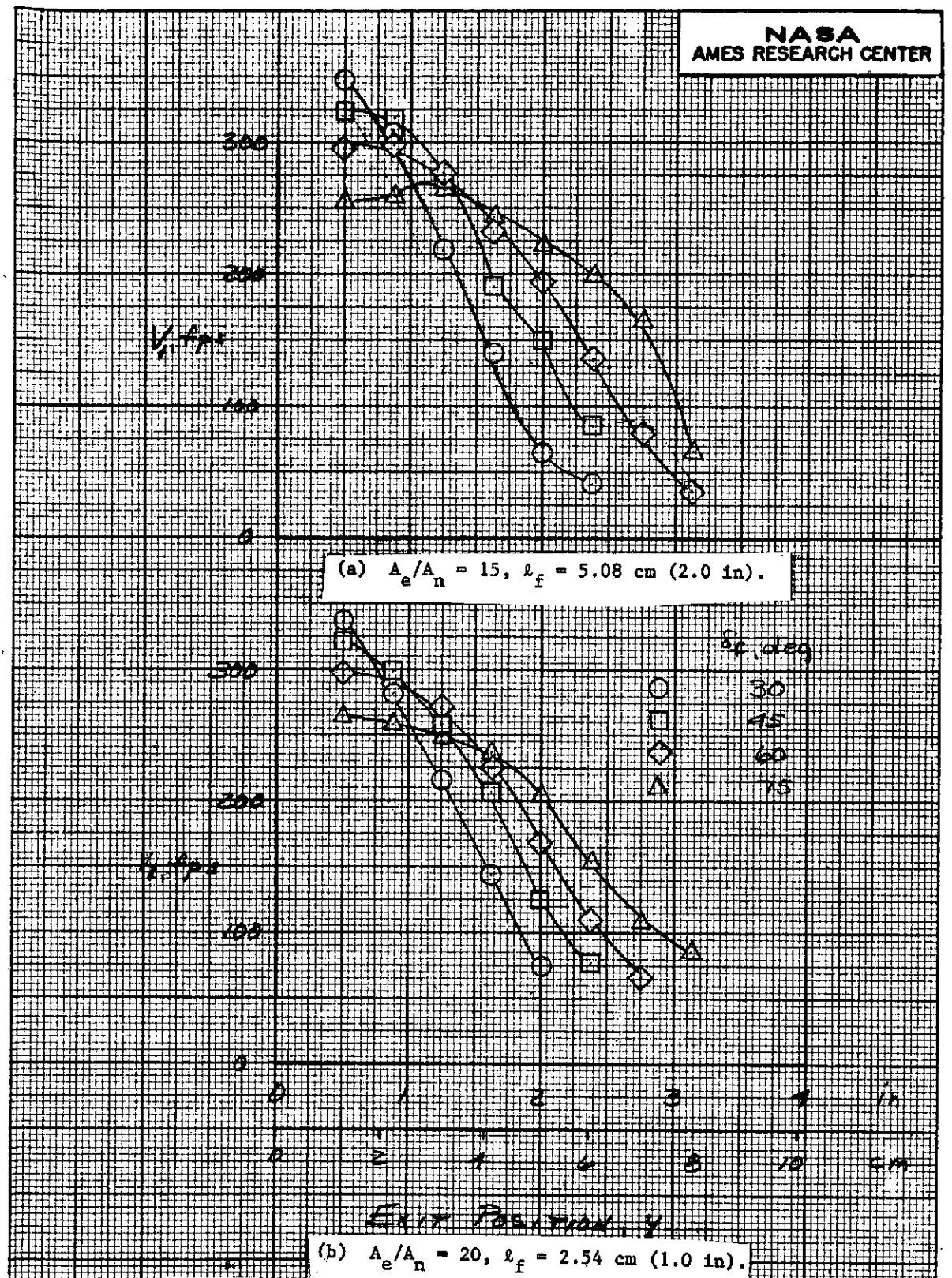

Figure 16.- Exit velocity profiles for nozzle 1; A_e/A_t = 1.25, ℓ_f = 5.08cm (2.0 in), Z_f = 1.27 cm (.5 in), ℓ_s = 0, PR = 1.53, q = 0.

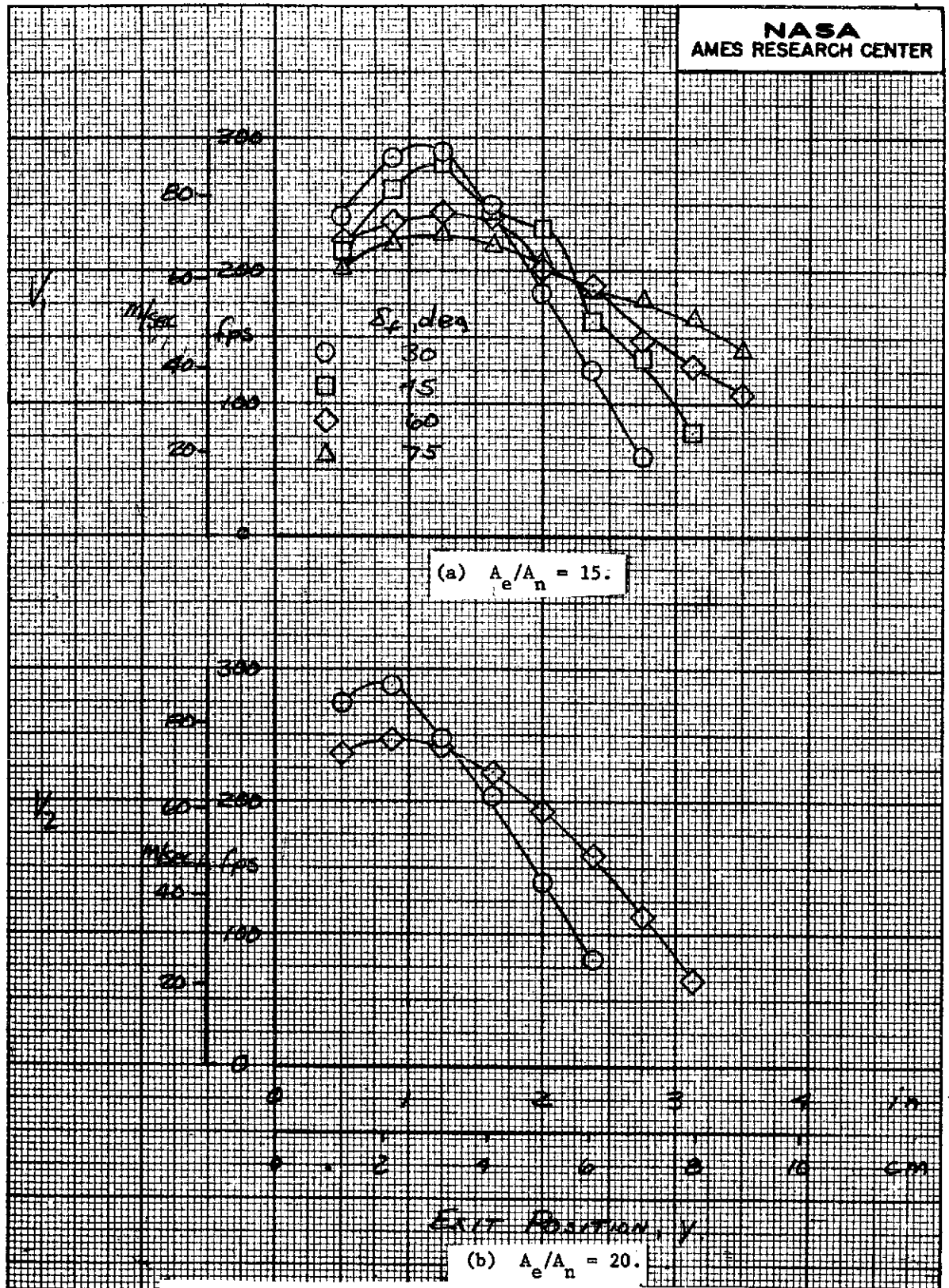

Figure 17.- Exit velocity profiles for nozzle 2b; A_e/A_t = 1.25, Z_f = .15 cm (.06 in), ℓ_s = 0, PR = 1.53, q = 0.

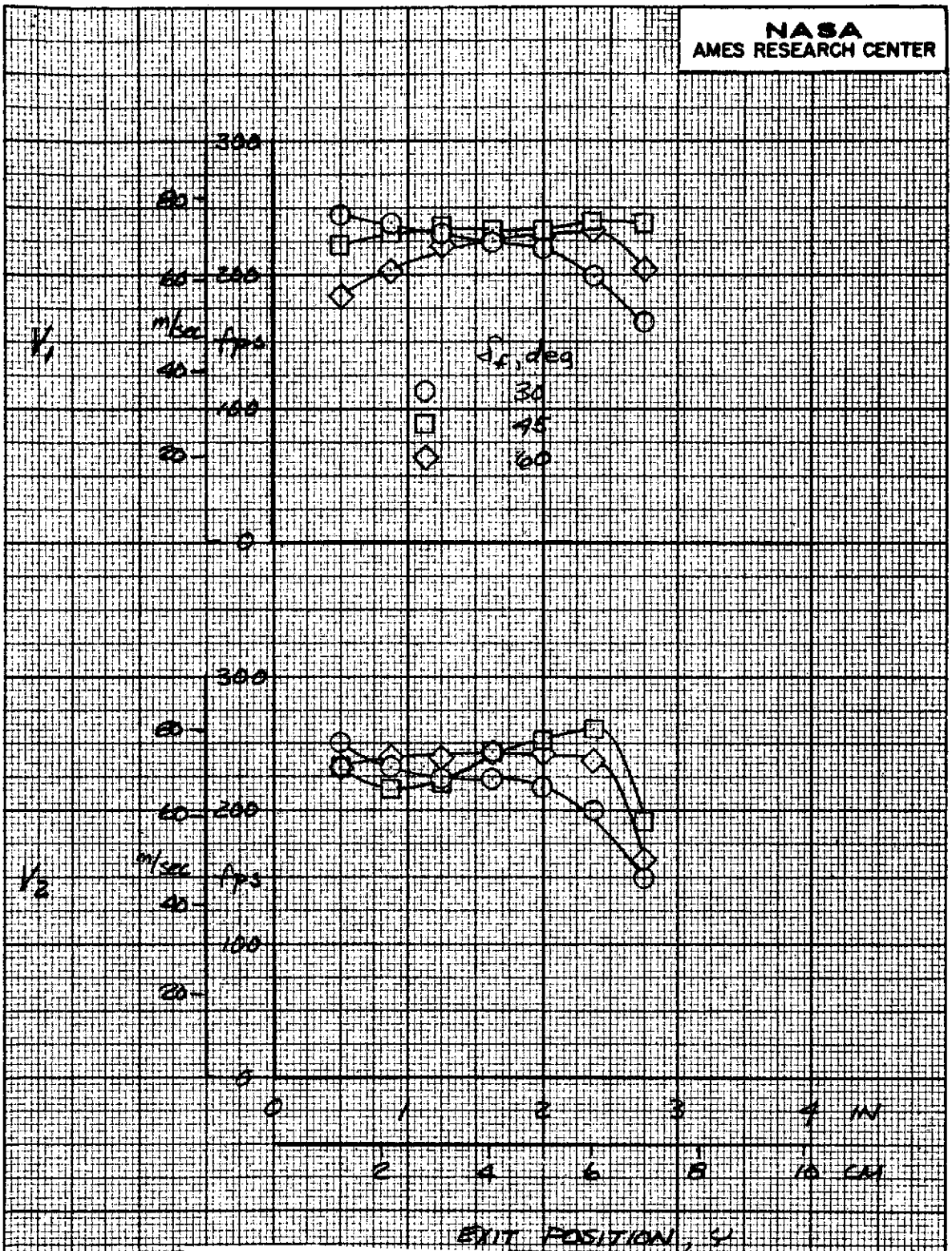

(a) A_e/A_n = 15, ℓ_f = 2.54 cm (1.0 in), Z_f = .15 cm (.06 in).

Figure 18.- Exit velocity profiles for nozzle 3b; A_e/A_t = 1.25, ℓ_s = 0, PR = 1.53, q = 0.

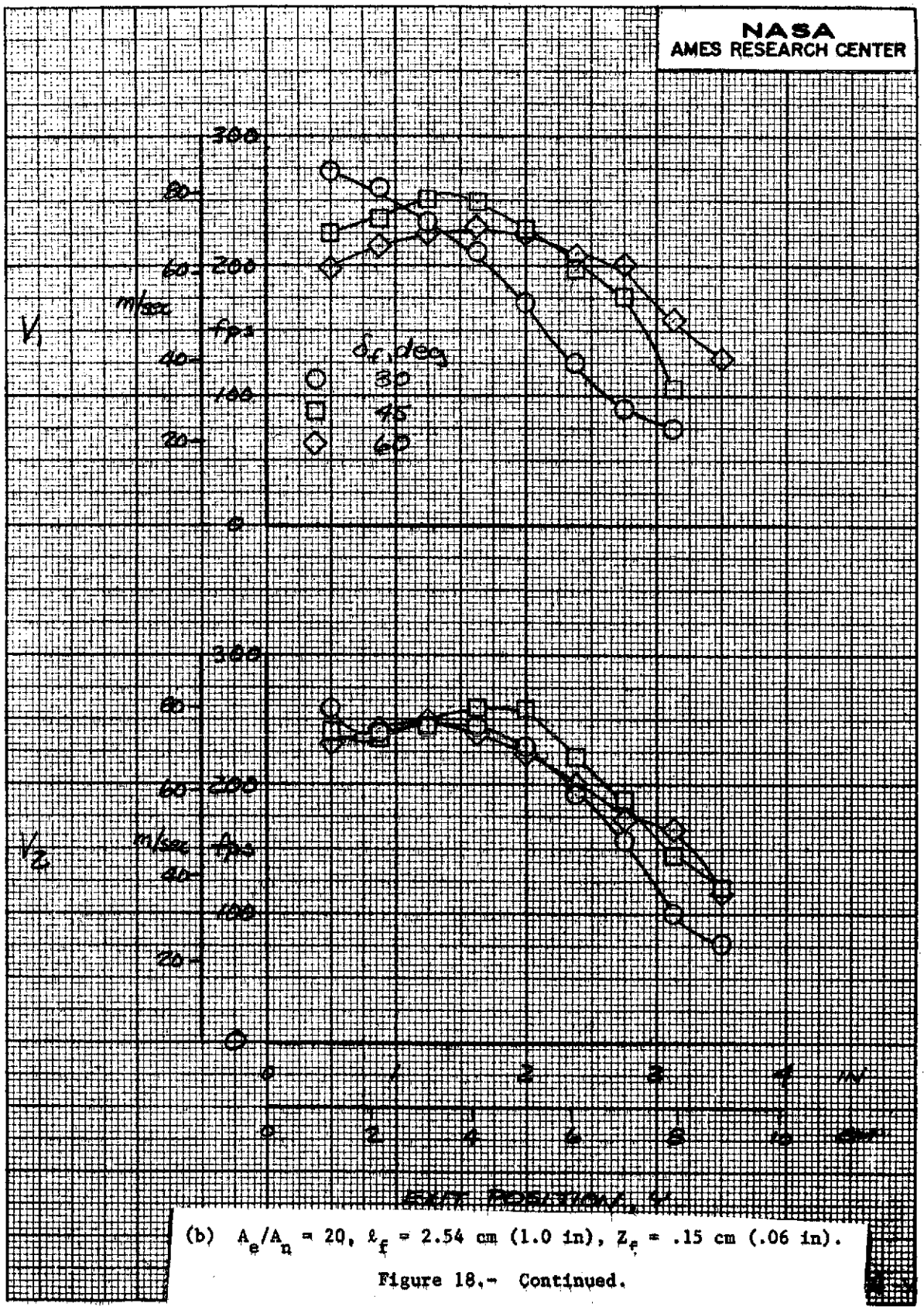

(b) A_e/A_n = 20, ℓ_f = 2.54 cm (1.0 in), Z_e = .15 cm (.06 in).

Figure 18.- Continued.

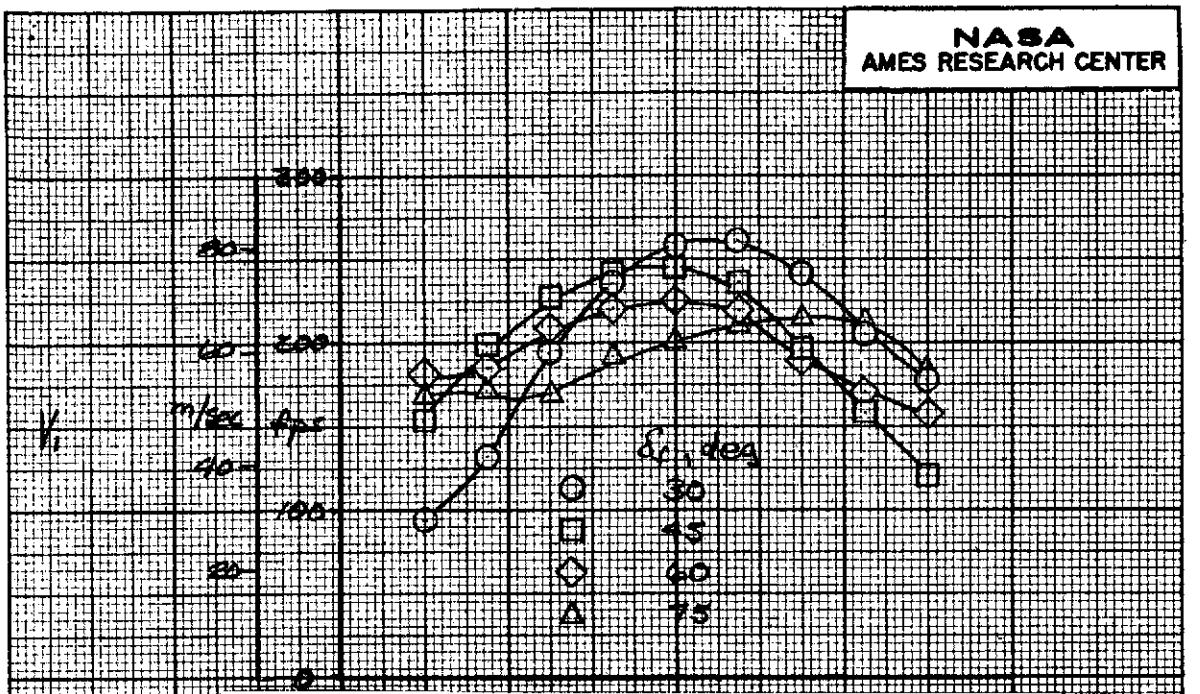

(c) A_e/A_n = 20, ℓ_f = 5.08 cm (2.0 in), Z_f = .97 cm (.38 in).

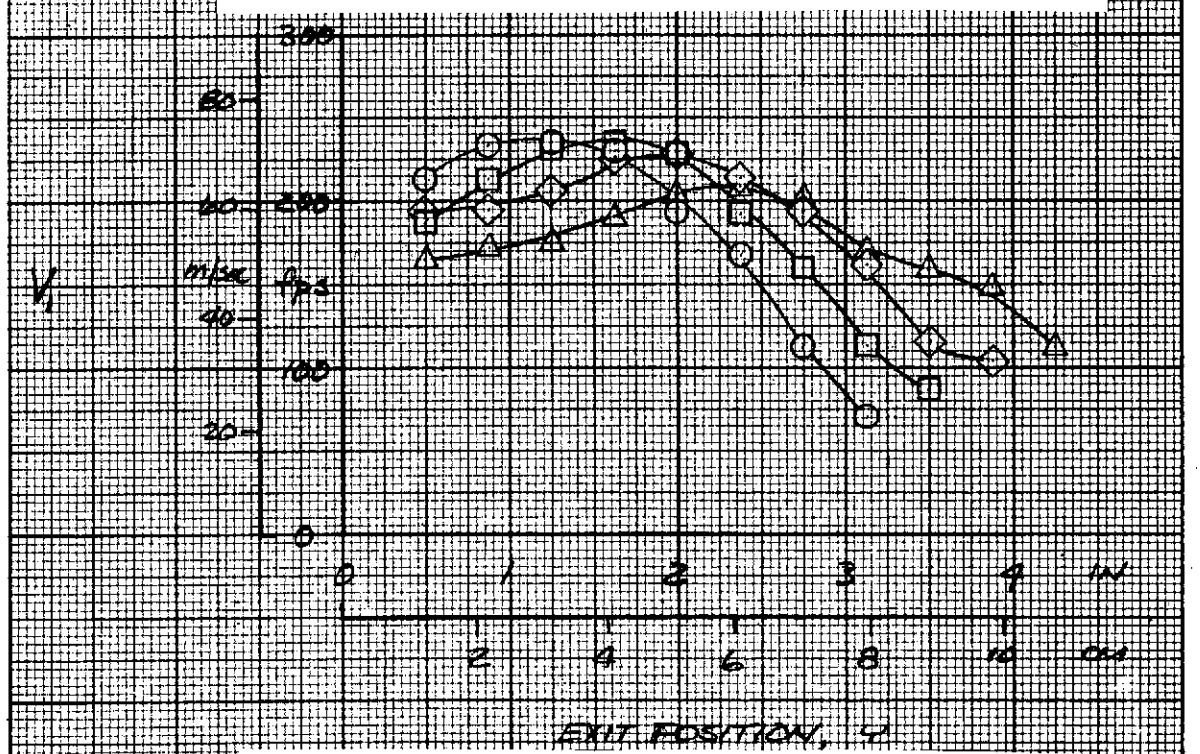

(d) A_e/A_n = 25, ℓ_f = 5.08 cm (2.0 in), Z_f = .97 cm (.38 in).

Figure 18.- Concluded.

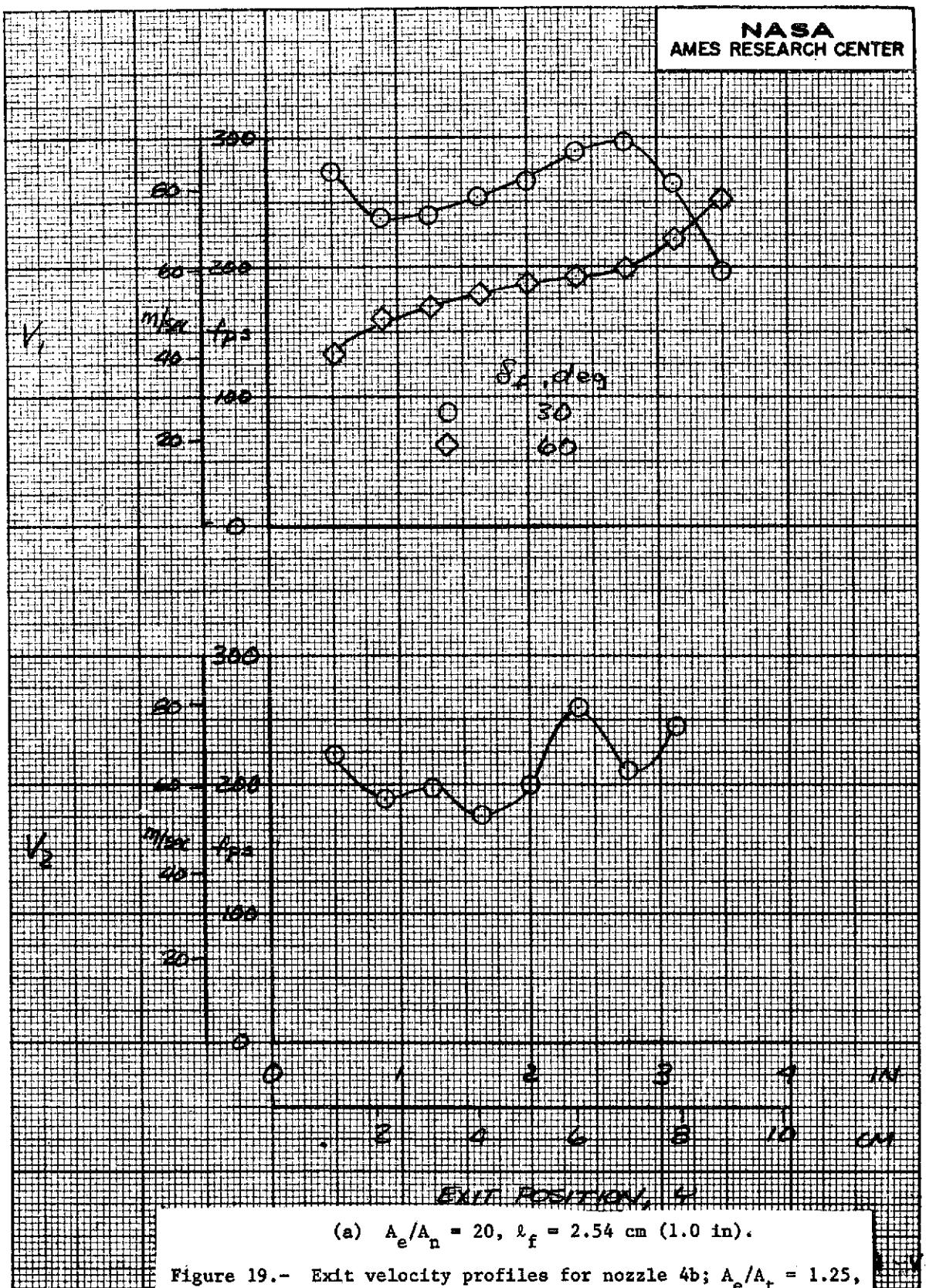

(a) A_e/A_n = 20, ℓ_f = 2.54 cm (1.0 in).

Figure 19.- Exit velocity profiles for nozzle 4b; A_e/A_t = 1.25, Z_f = .33 cm (.13 in), ℓ_s = 0, PR = 1.53, q = 0.

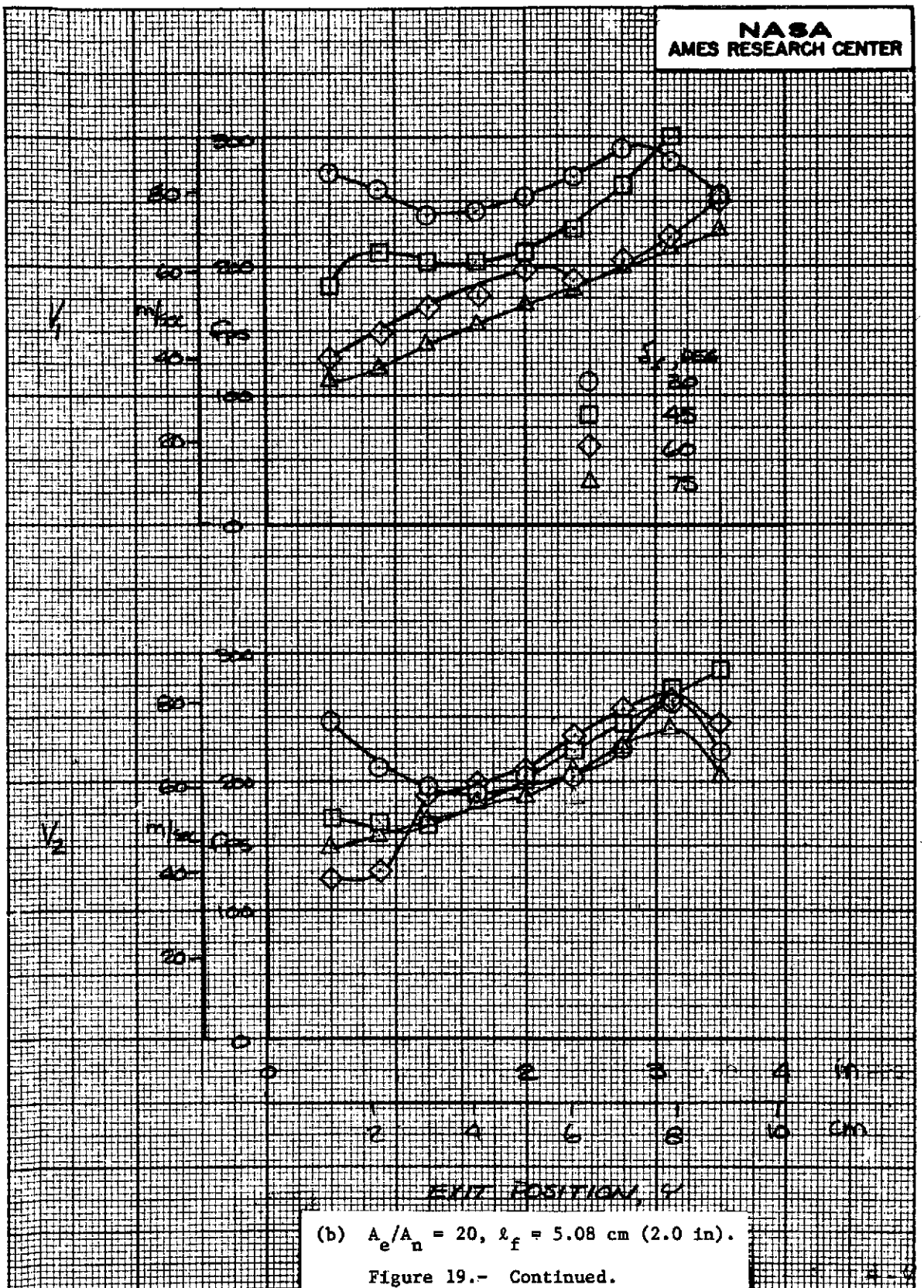

(b) A_e/A_n = 20, ℓ_f = 5.08 cm (2.0 in).

Figure 19.- Continued.

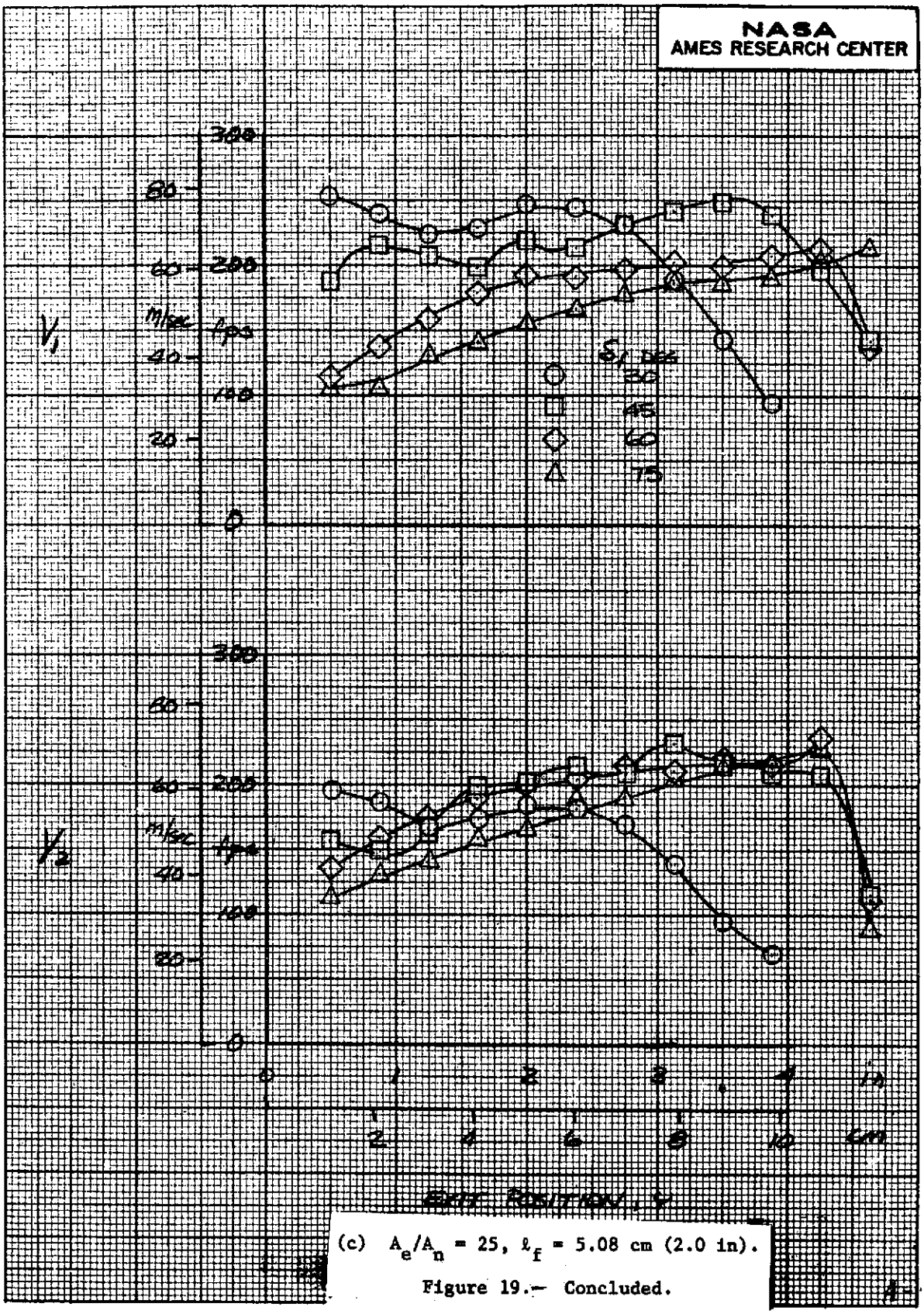

(c) $A_e/A_n = 25$, $\ell_f = 5.08$ cm (2.0 in).

Figure 19.— Concluded.

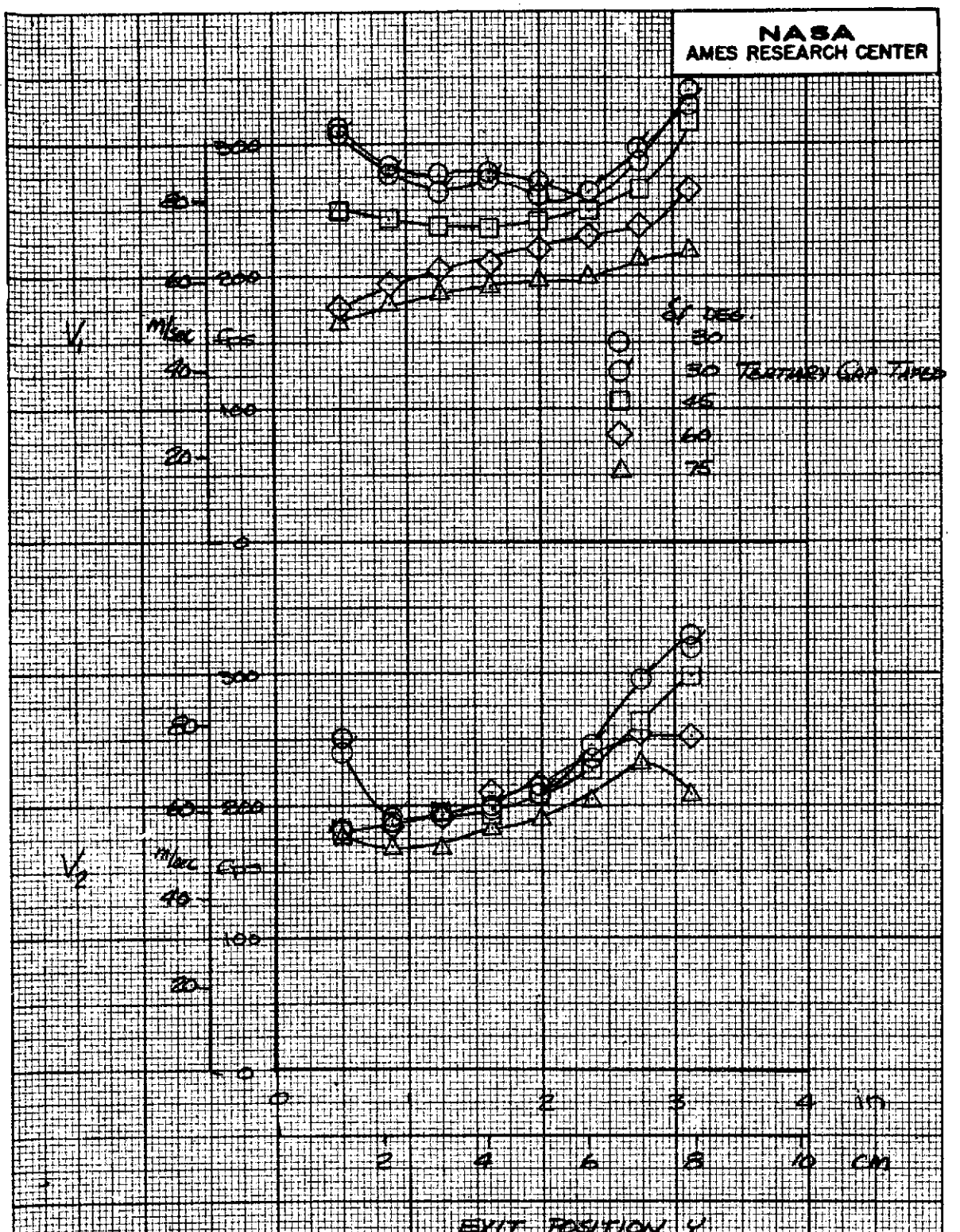

(a) A_e/A_n = 15, ℓ_f = 2.54 cm (1.0 in), Z_f = .15 cm (.06 in).

Figure 20.- Exit velocity profiles for nozzle 5c; A_e/A_t = 1.25, ℓ_s = 0, PR = 1.53, q = 0.

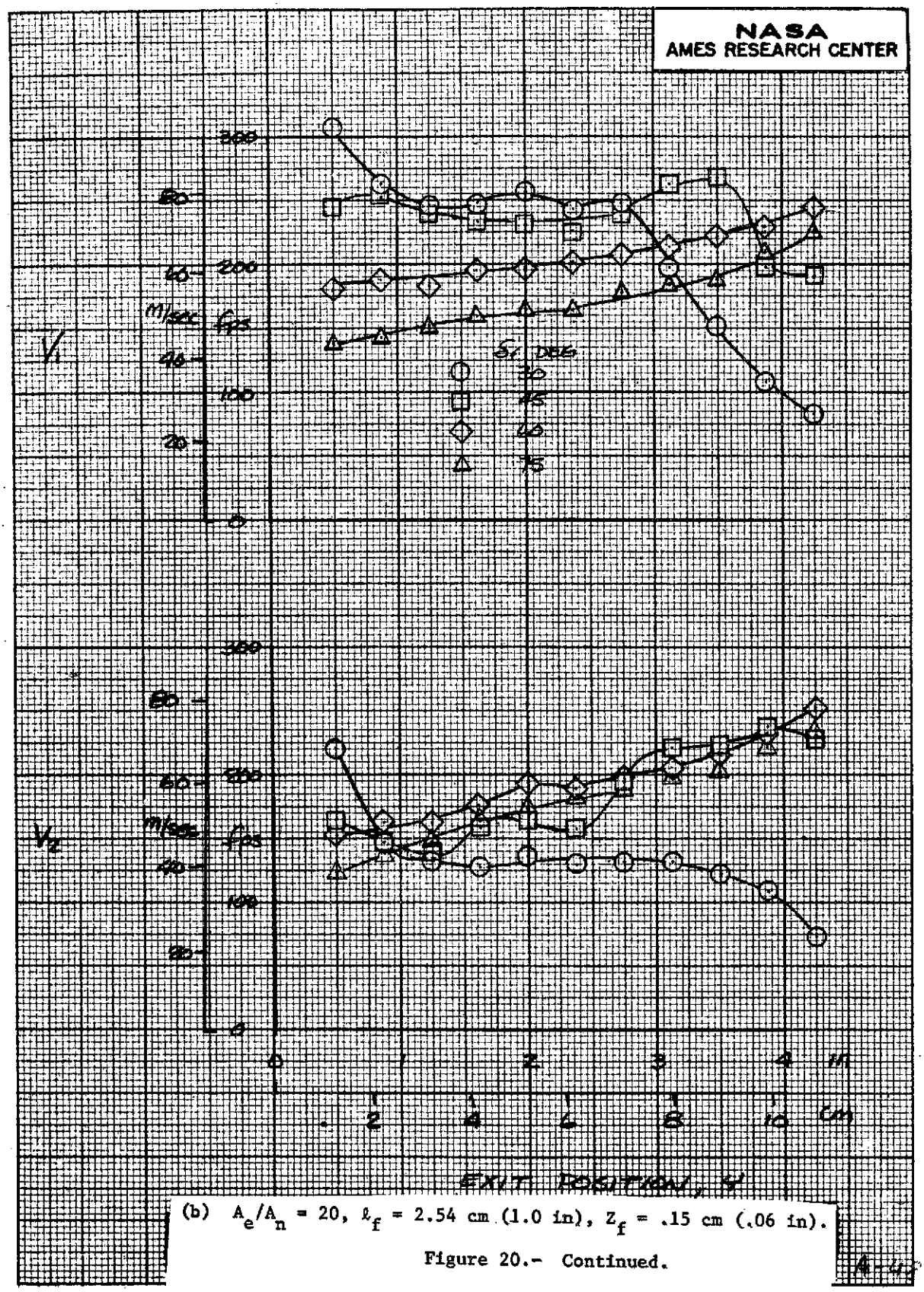

(b) $A_e/A_n = 20$, $\ell_f = 2.54$ cm (1.0 in), $Z_f = .15$ cm (.06 in).

Figure 20.- Continued.

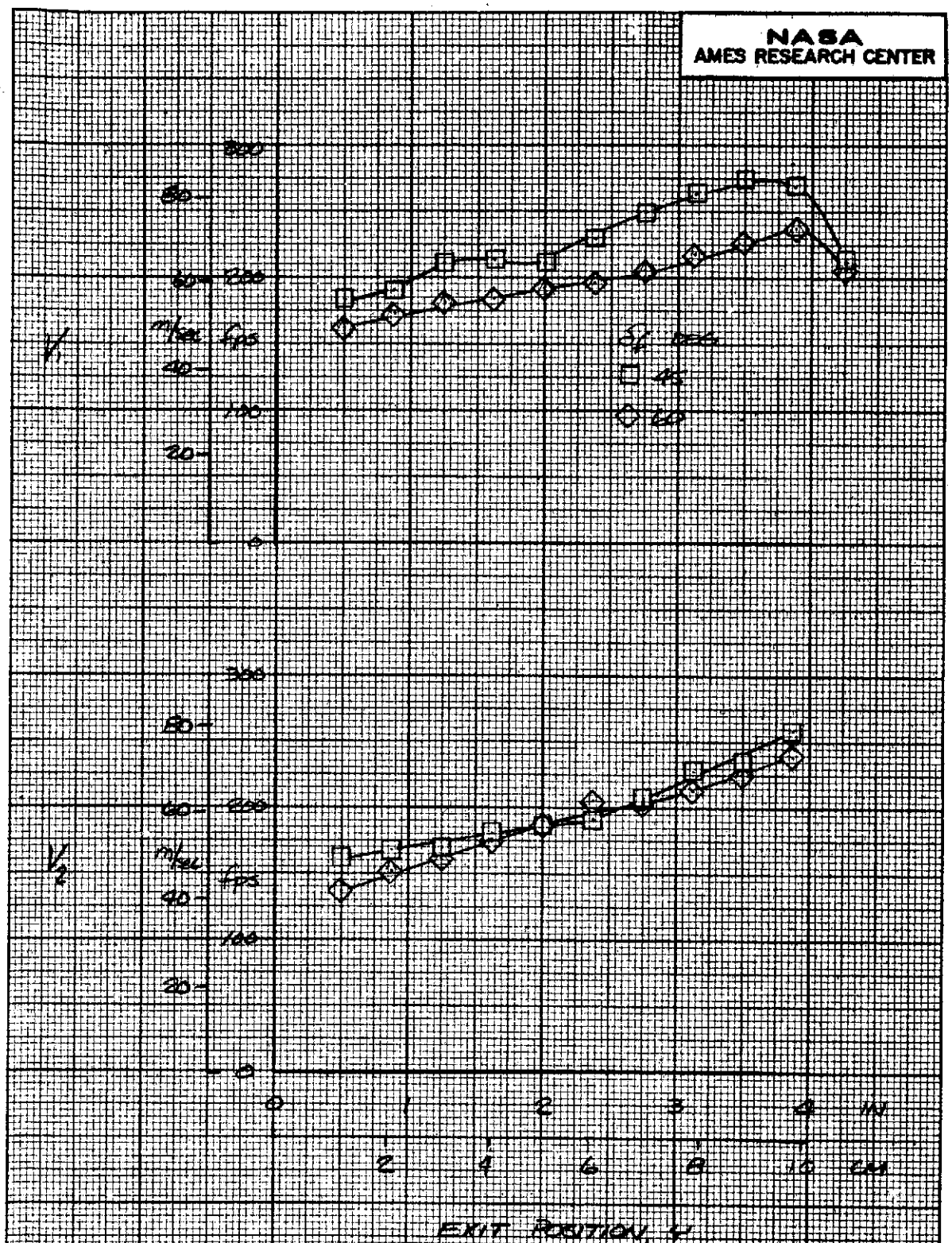

(c) $A_e/A_n = 20$, $\ell_f = 5.08$ cm (2.0 in), $Z_f = .79$ cm (.31 in).

Figure 20.- Continued.

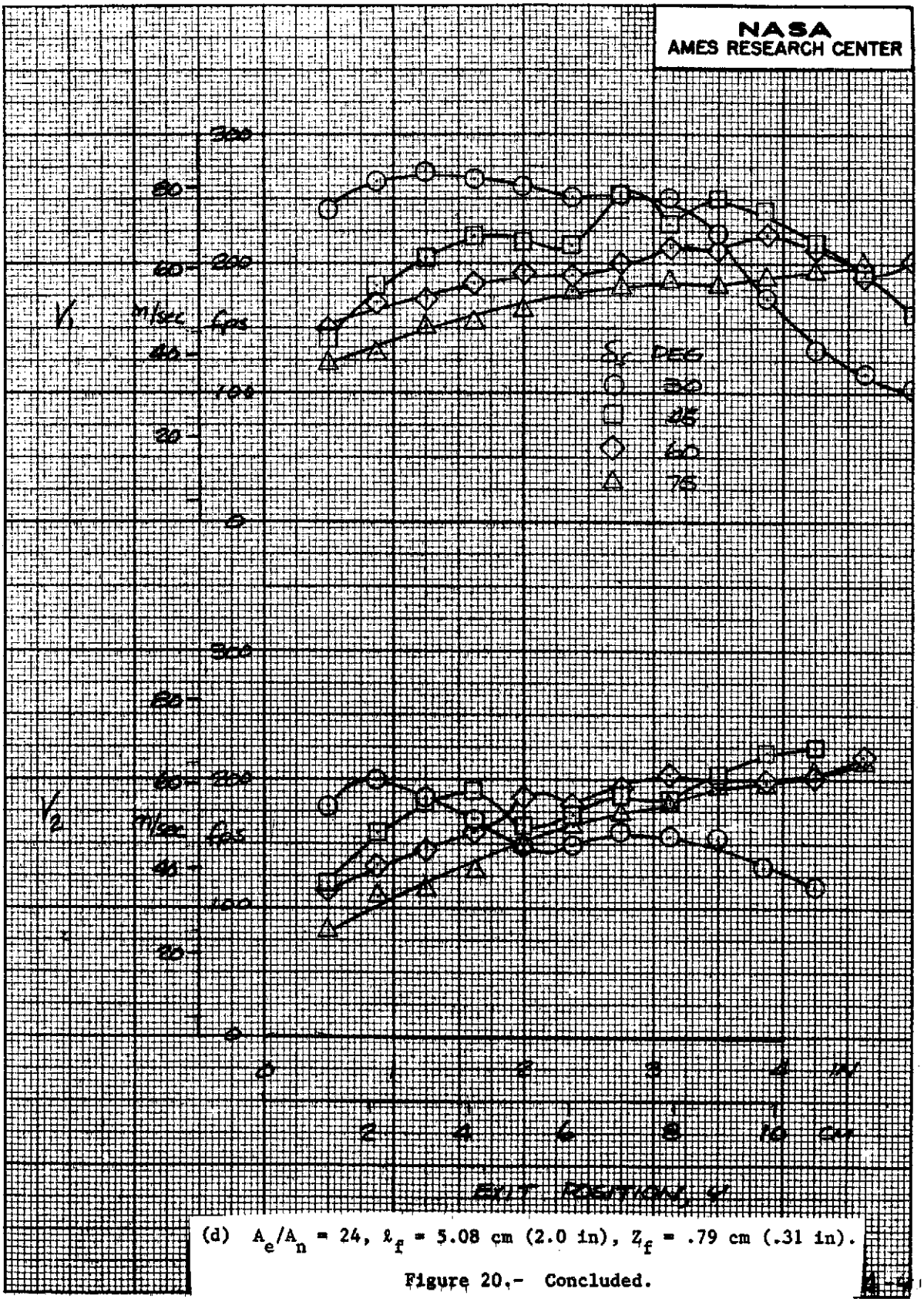

(d) $A_e/A_n = 24$, $\ell_f = 5.08$ cm (2.0 in), $Z_f = .79$ cm (.31 in).

Figure 20.- Concluded.

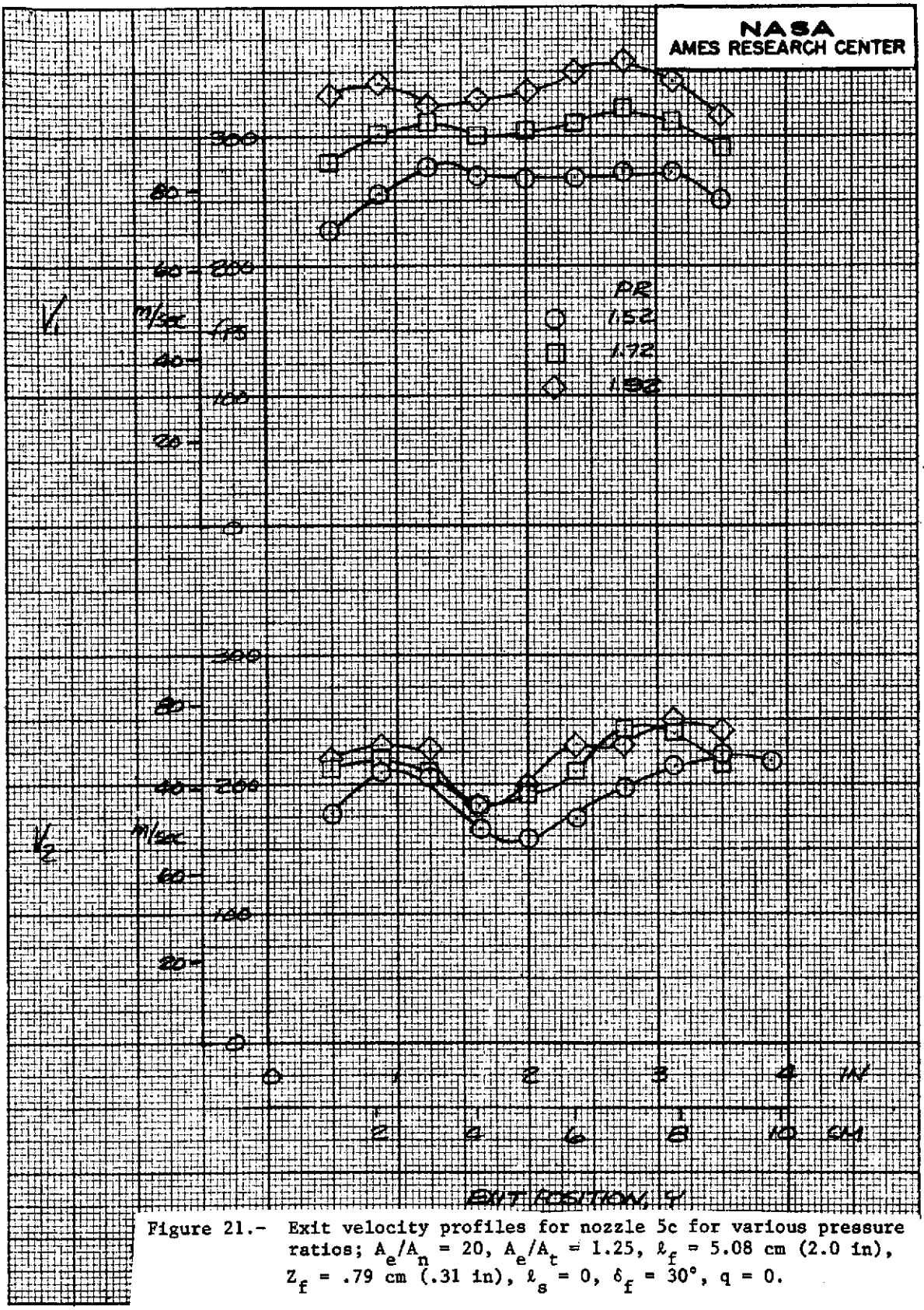

Figure 21.- Exit velocity profiles for nozzle 5c for various pressure ratios; A_e/A_n = 20, A_e/A_t = 1.25, ℓ_f = 5.08 cm (2.0 in), Z_f = .79 cm (.31 in), ℓ_s = 0, δ_f = 30°, q = 0.

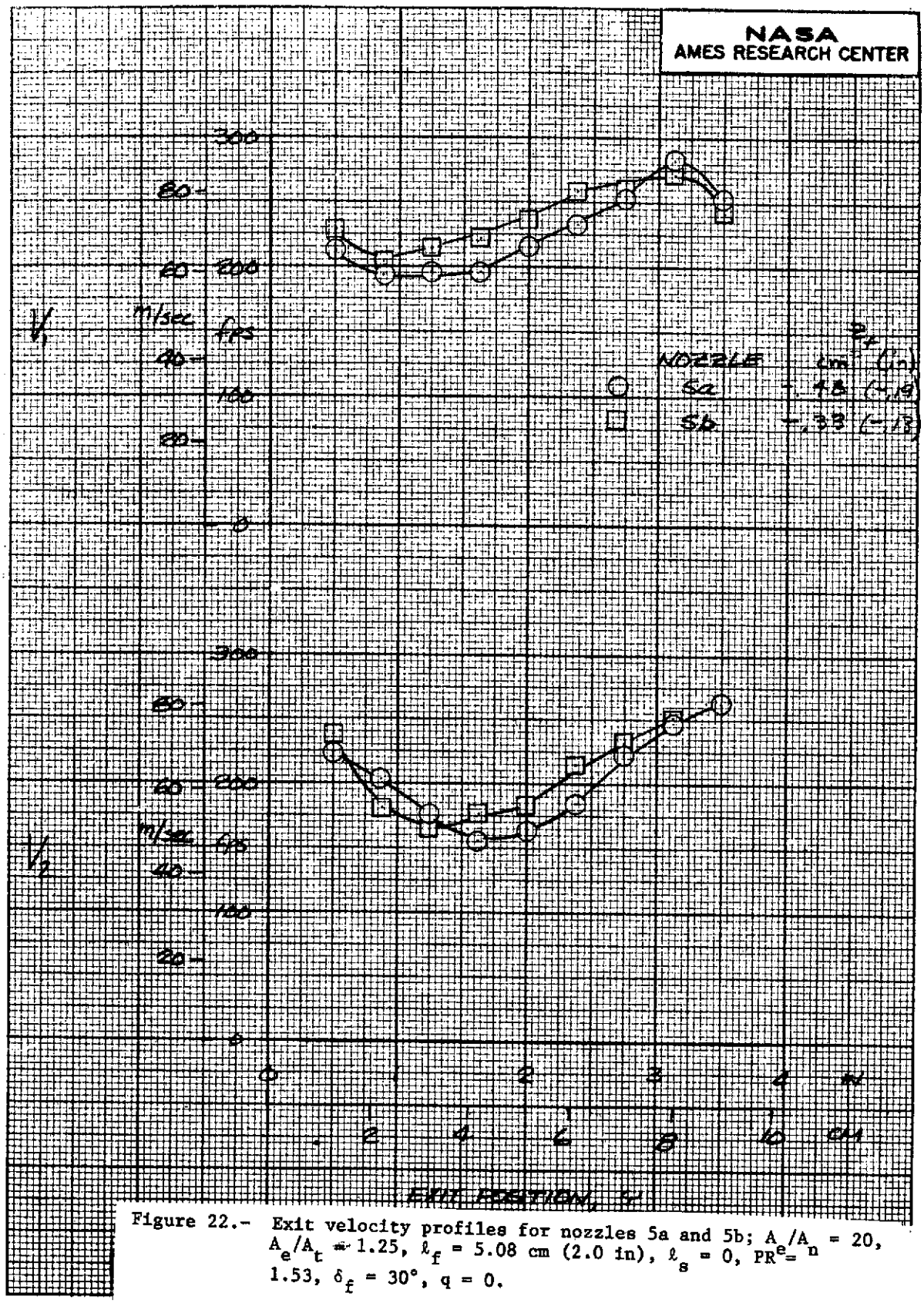

Figure 22.- Exit velocity profiles for nozzles 5a and 5b; $A_e/A_n = 20$, $A_e/A_t = 1.25$, $\ell_f = 5.08$ cm (2.0 in), $\ell_s = 0$, $PR = 1.53$, $\delta_f = 30°$, $q = 0$.

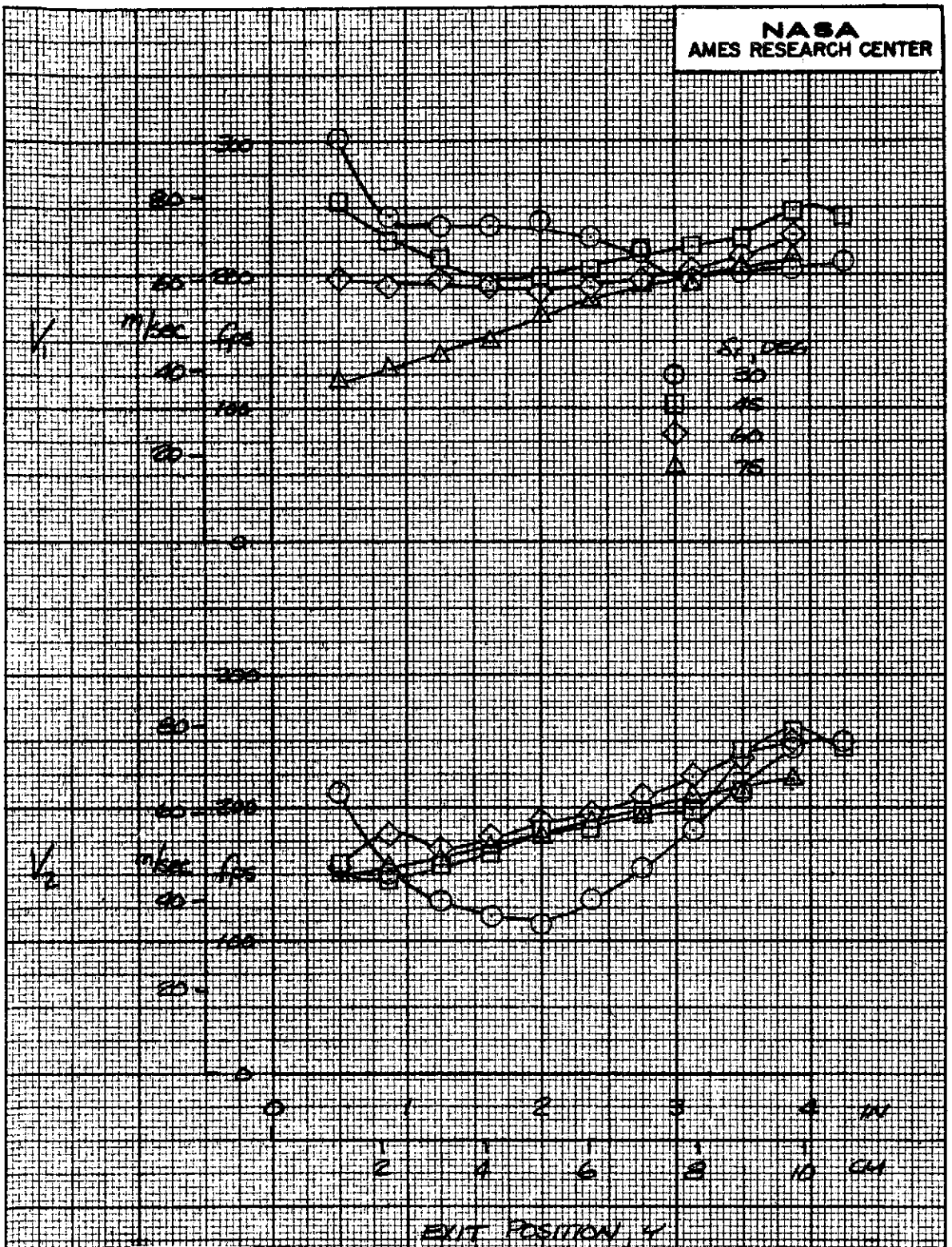

(a) A_e/A_n = 20, ℓ_f = 2.54 cm (1.0 in), Z_f = .15 cm (.06 in).

Figure 23.- Exit velocity profiles for nozzle 6c; A_e/A_t = 1.25, ℓ_s = 0, PR = 1.53, q = 0.

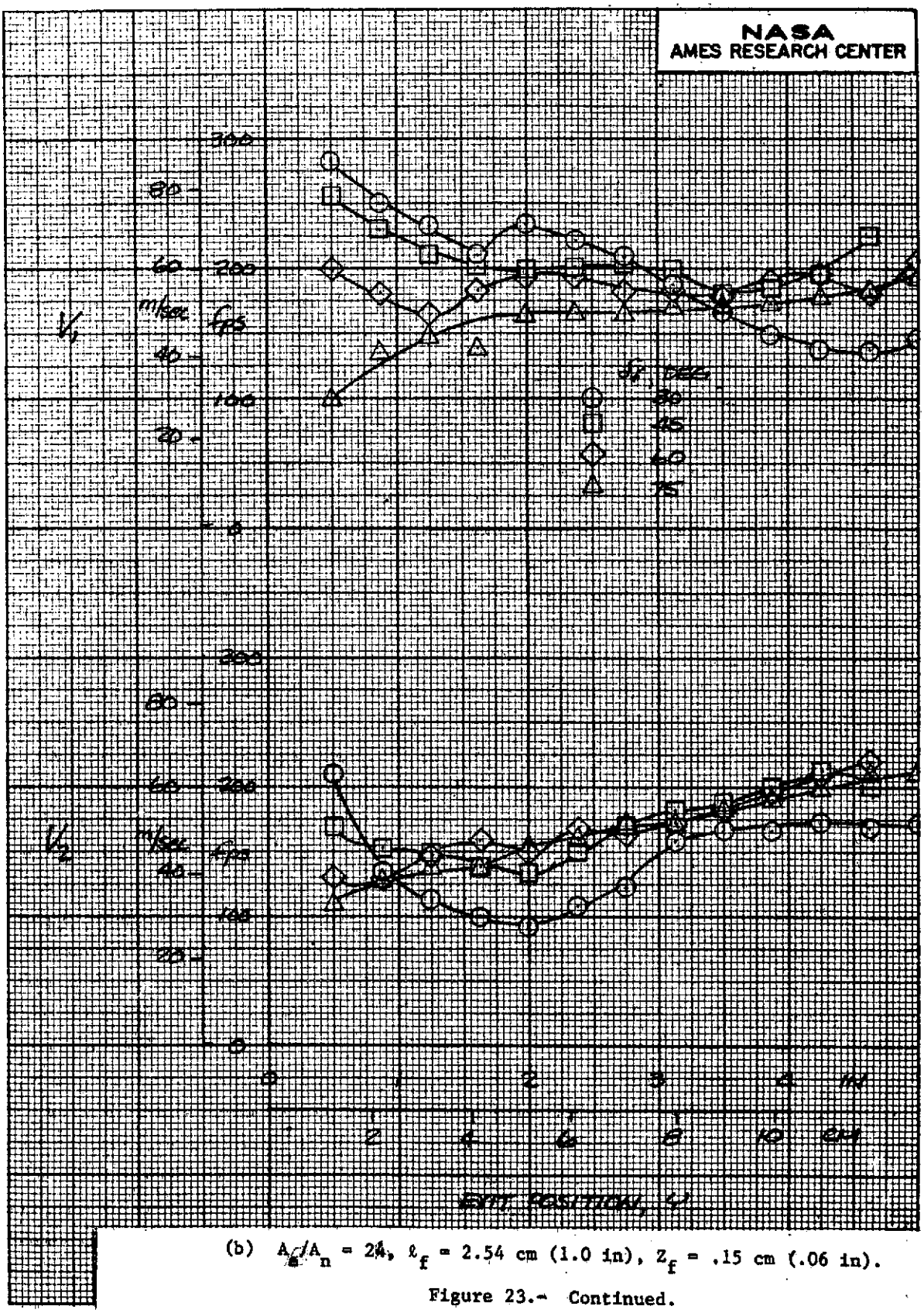

(b) $A_c/A_n = 24$, $\ell_f = 2.54$ cm (1.0 in), $Z_f = .15$ cm (.06 in).

Figure 23.- Continued.

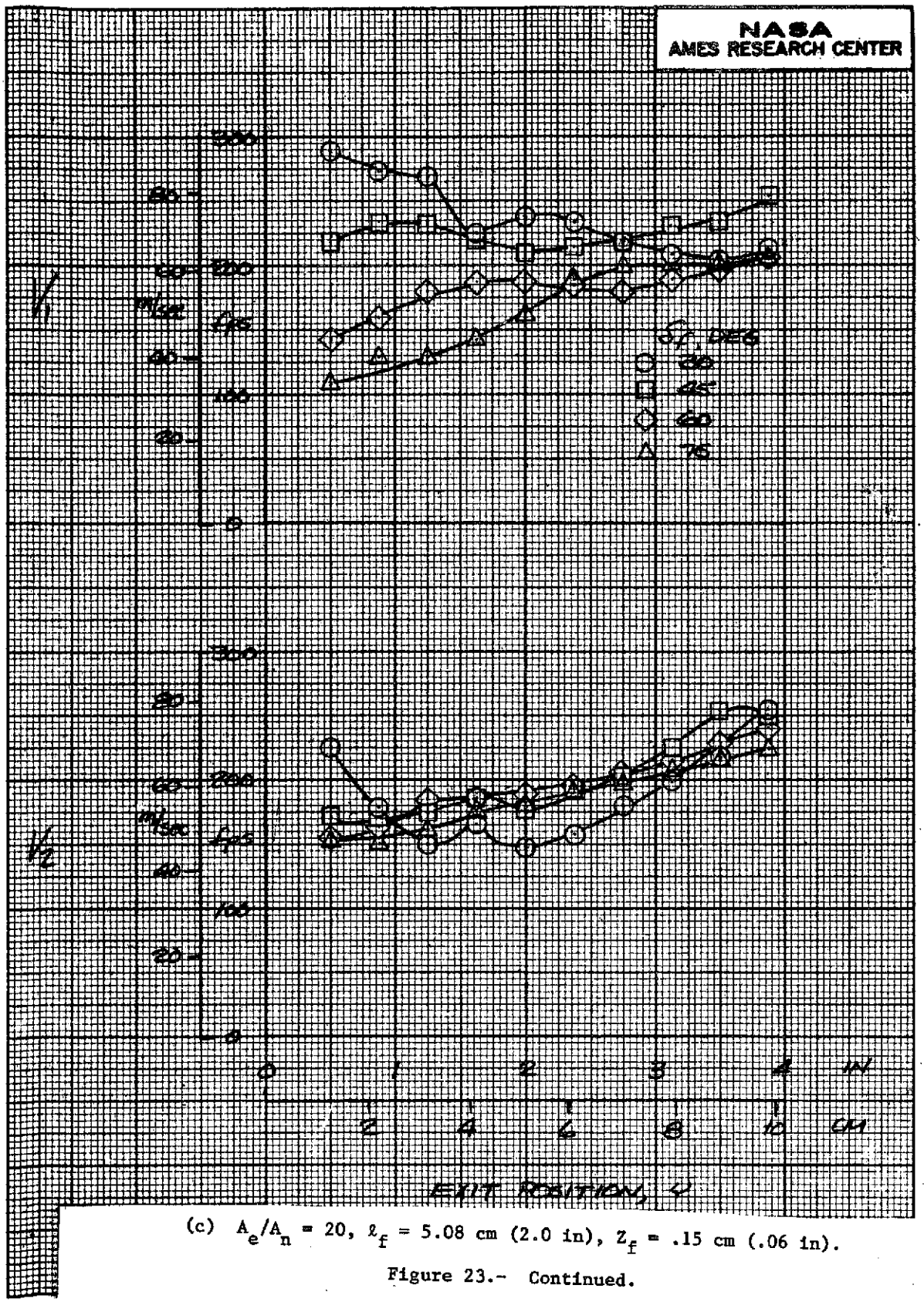

(c) $A_e/A_n = 20$, $\ell_f = 5.08$ cm (2.0 in), $Z_f = .15$ cm (.06 in).

Figure 23.- Continued.

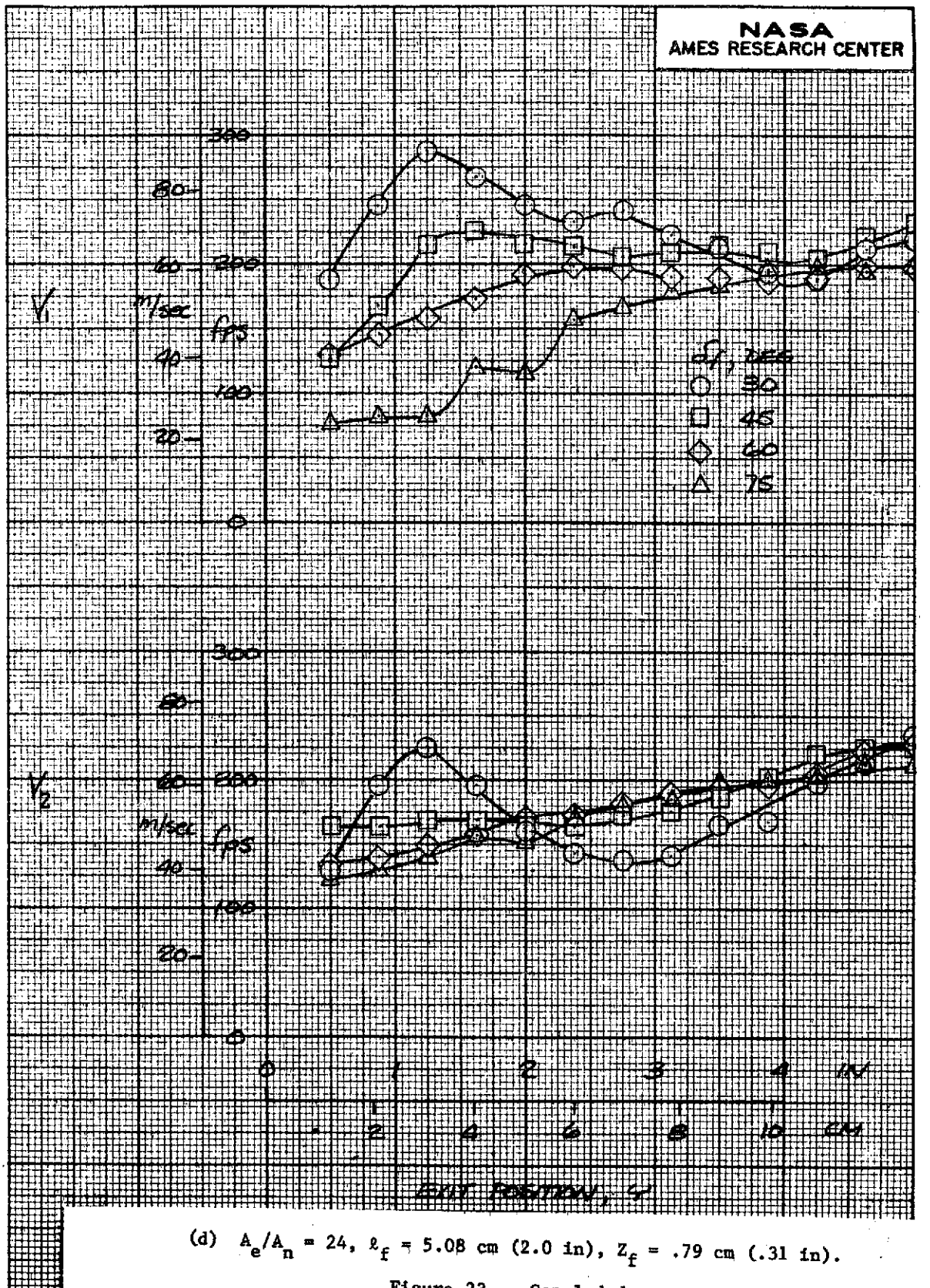

(d) A_e/A_n = 24, ℓ_f = 5.08 cm (2.0 in), Z_f = .79 cm (.31 in).

Figure 23.- Concluded.

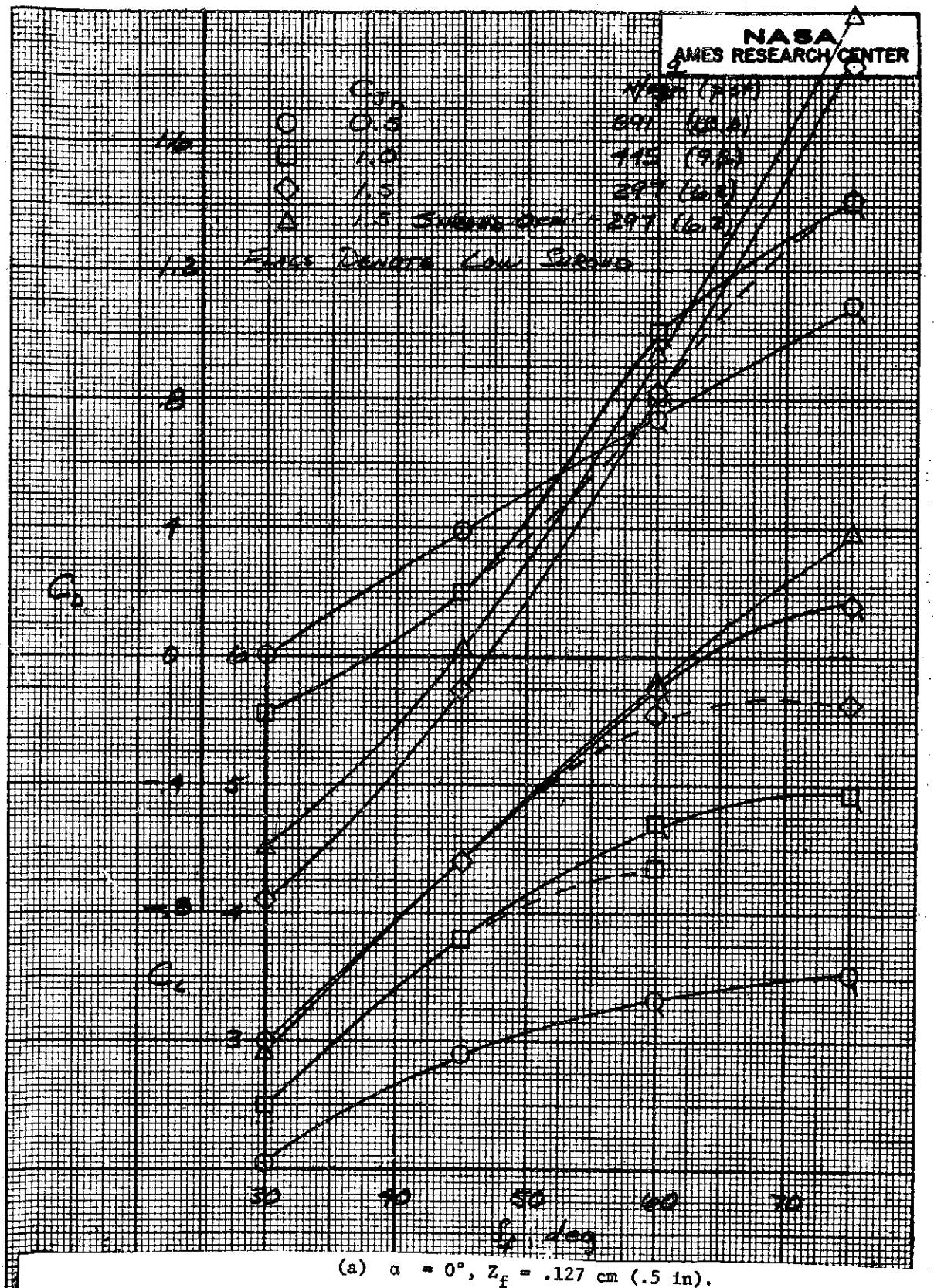

(a) $\alpha = 0°$, $Z_f = .127$ cm (.5 in).

Figure 24.- The effect of C_{J_n} on the lift and drag characteristics of the model with nozzle 1; $A_e/A_t = 1.25$, $\ell_f = 5.08$ cm (2.0 in), PR = 1.53, $A_\phi/A_n = 15$.

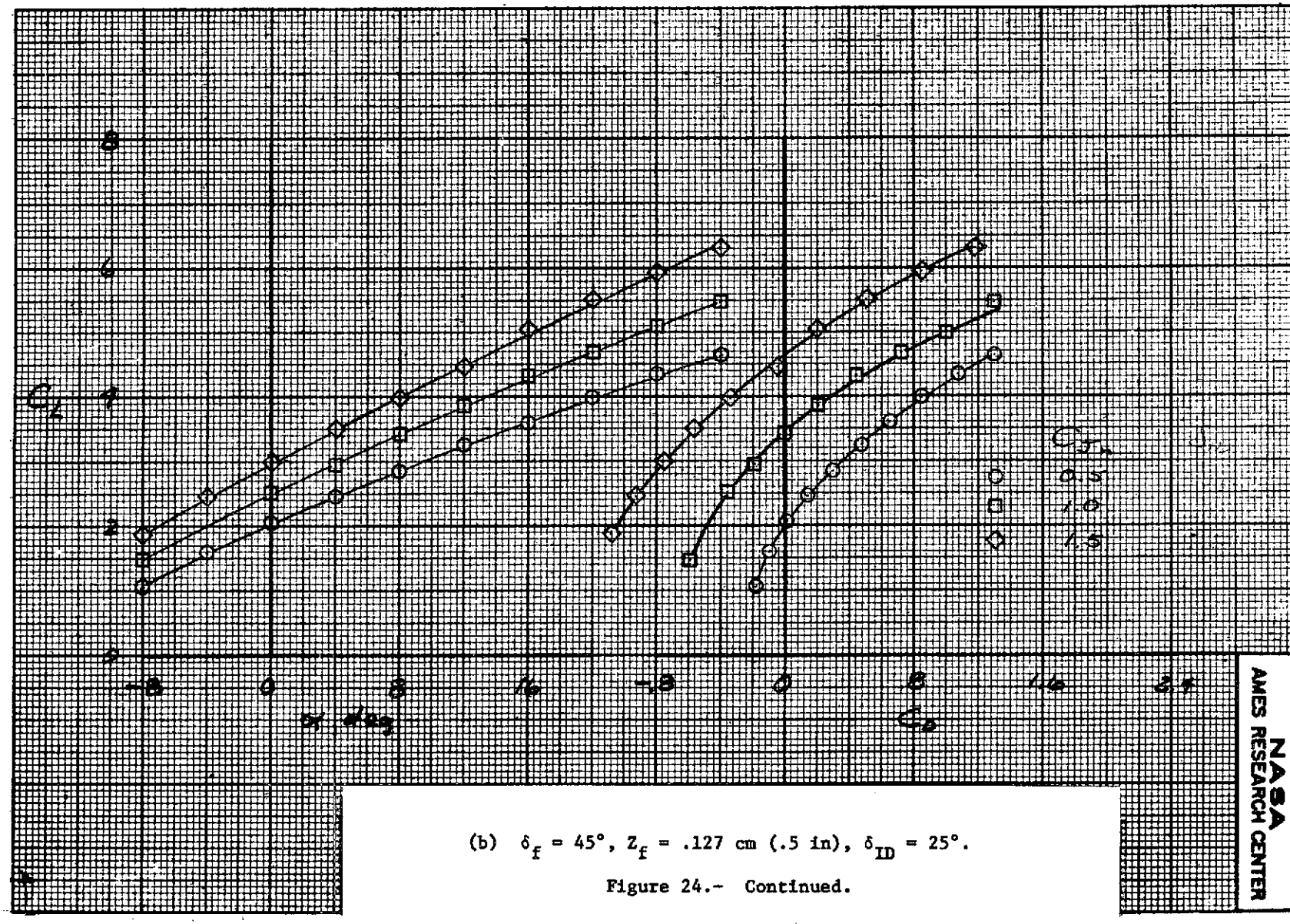

(b) $\delta_f = 45°$, $Z_f = .127$ cm (.5 in), $\delta_{ID} = 25°$.

Figure 24.- Continued.

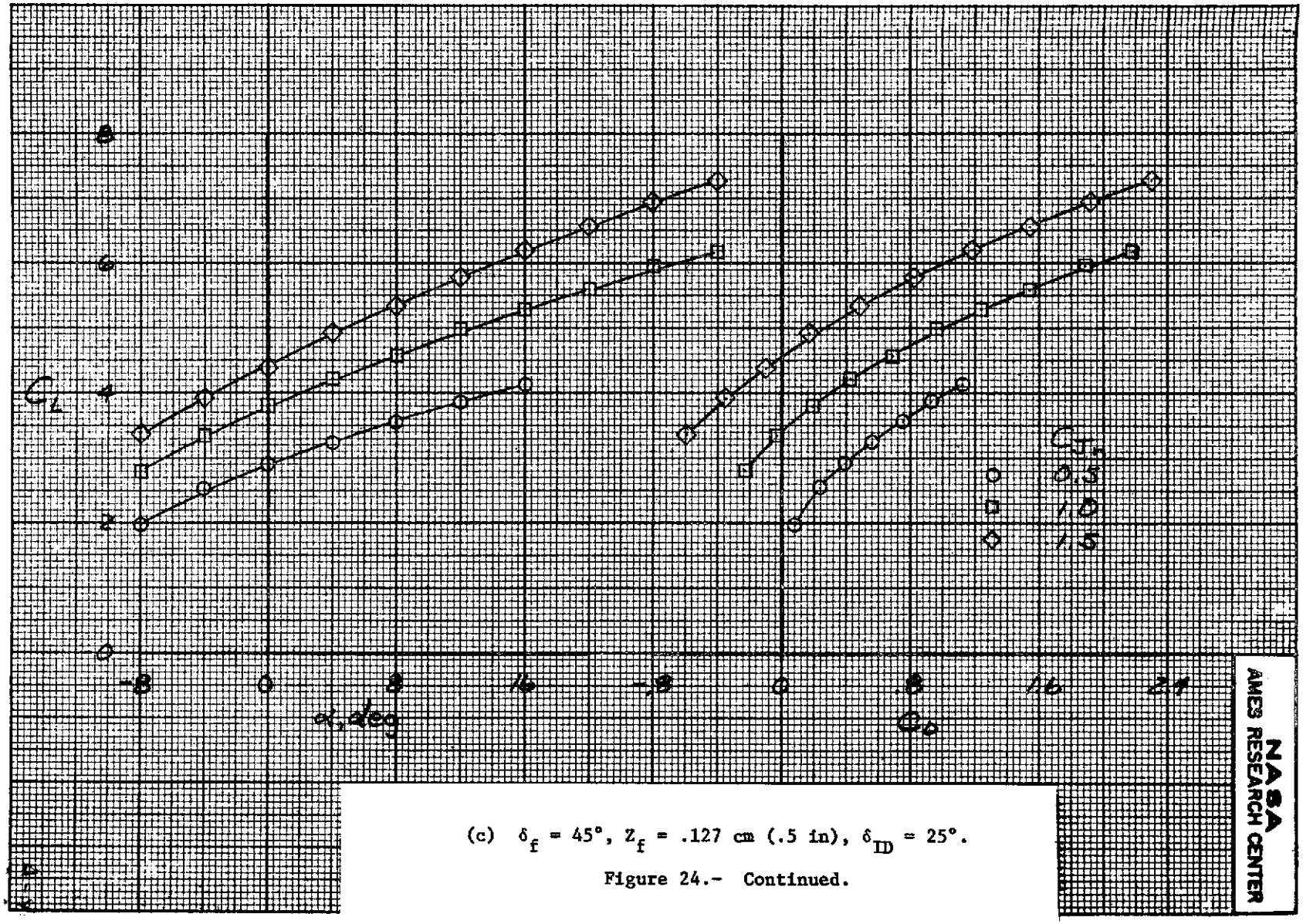

(c) $\delta_f = 45°$, $Z_f = .127$ cm (.5 in), $\delta_{ID} = 25°$.

Figure 24.- Continued.

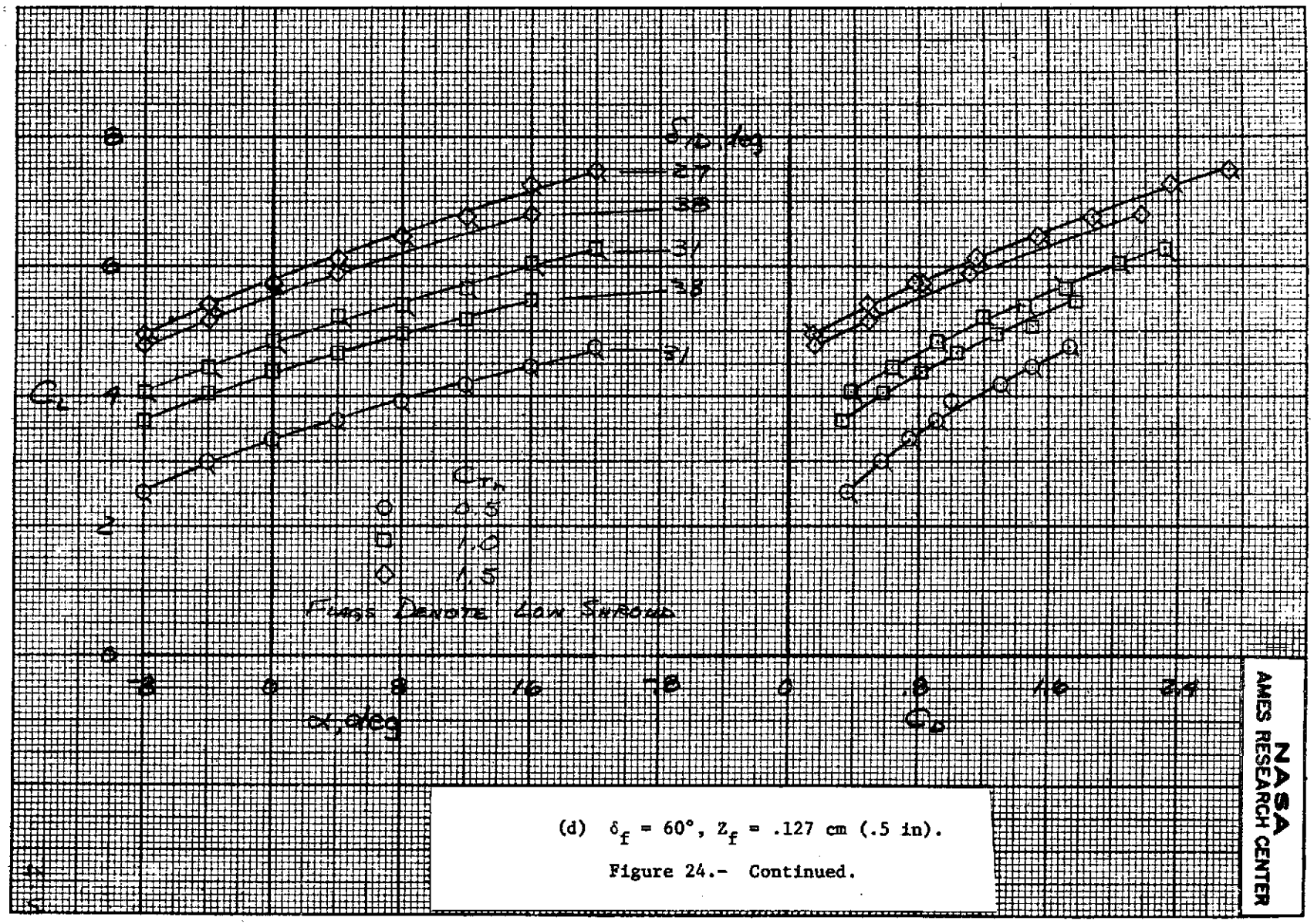

(d) $\delta_f = 60°$, $Z_f = .127$ cm (.5 in).

Figure 24.- Continued.

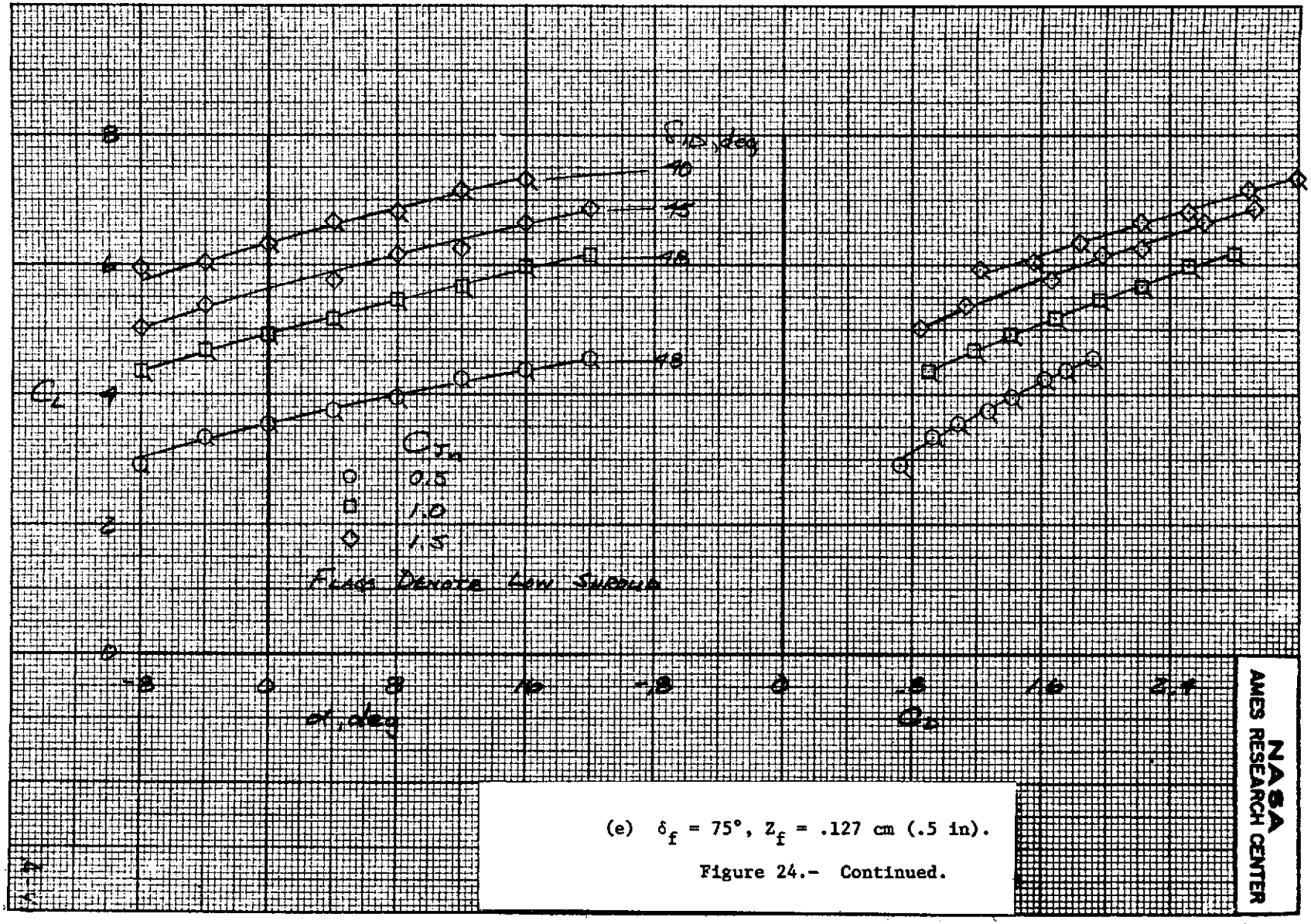

(e) $\delta_f = 75°$, $Z_f = .127$ cm (.5 in).

Figure 24.- Continued.

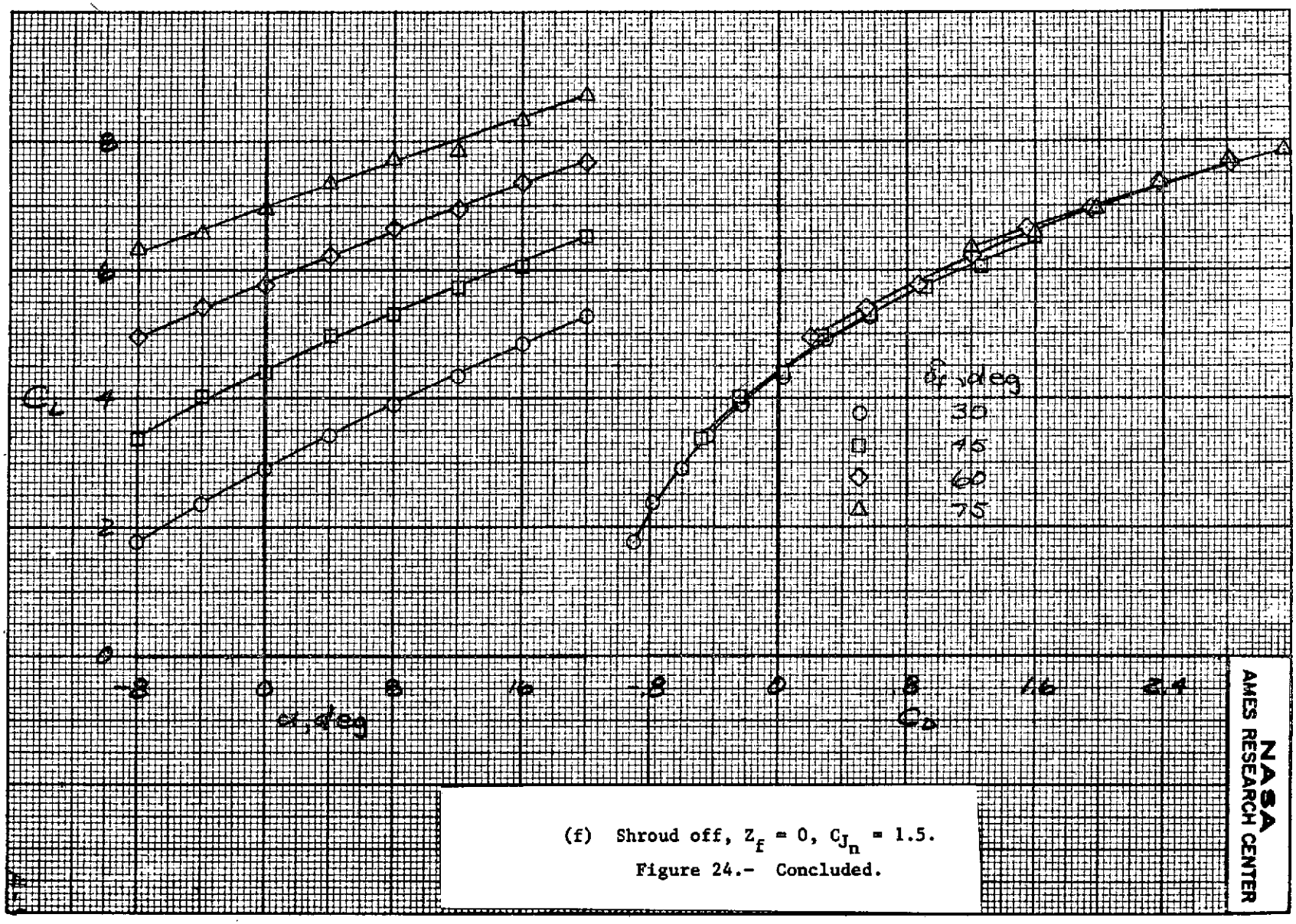

(f) Shroud off, $Z_f = 0$, $C_{J_n} = 1.5$.

Figure 24.- Concluded.

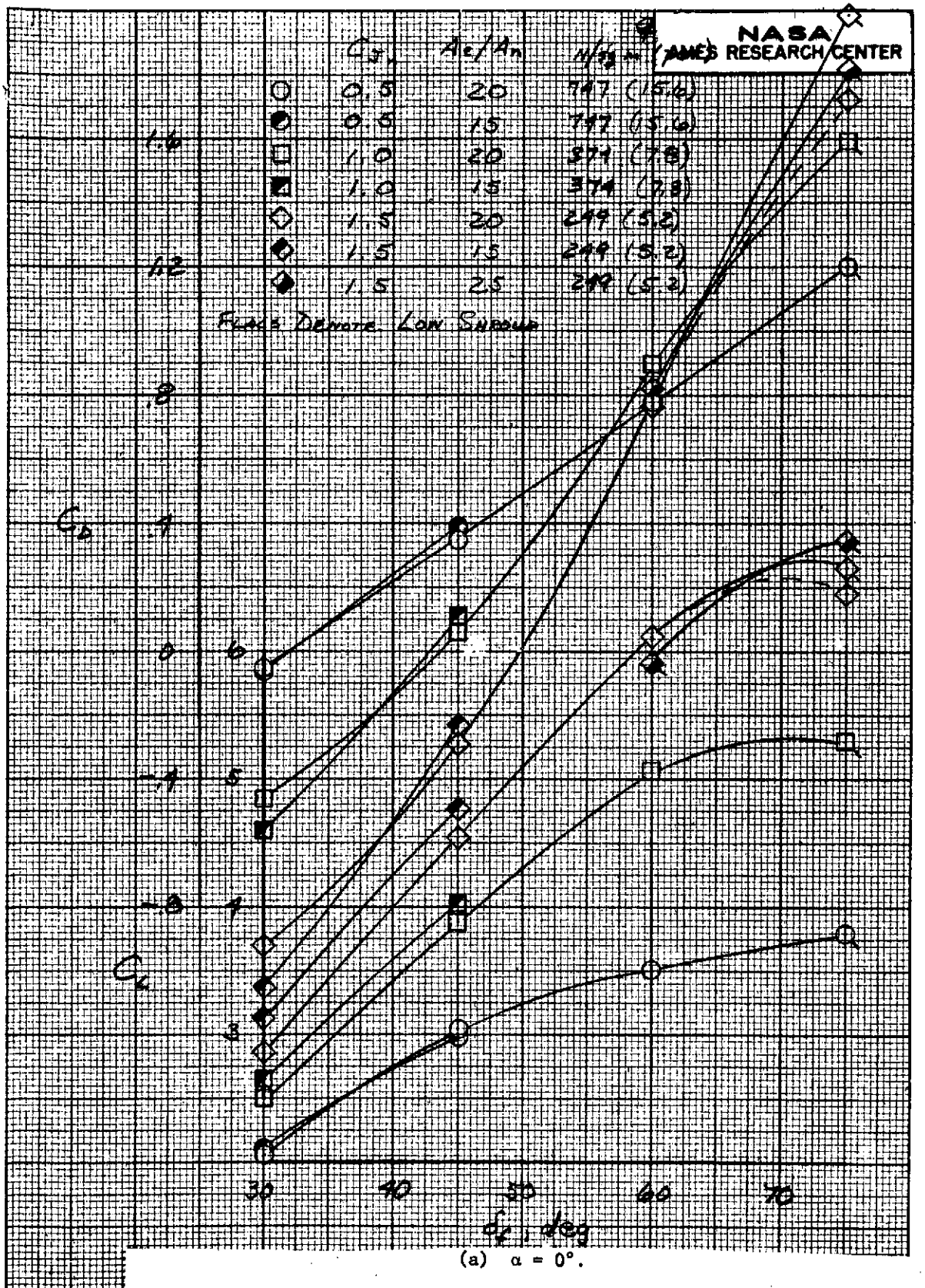

(a) $\alpha = 0°$.

Figure 25.- The effect of C_{J_n} on the lift and drag characteristics of the model with nozzle 3b; A_e/A_t = 1.25, ℓ_f = 2.54 cm (1.0 in) PR = 1.53, Z_f = .15 cm (.06 in).

(b) $\delta_f = 30^o$, $A_e/A_n = 20$, $\delta_{ID} = 20$.

Figure 25.- Continued.

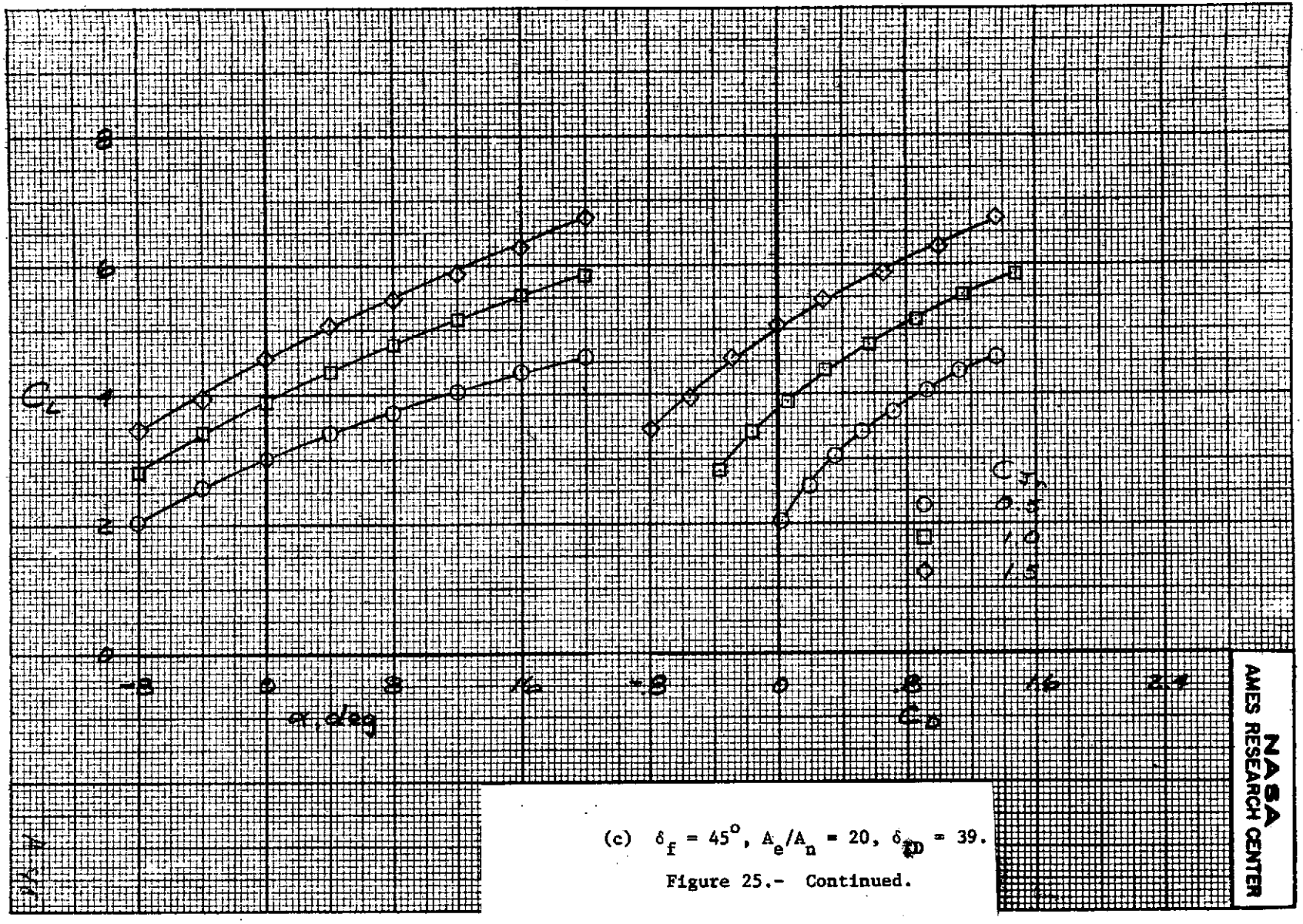

(c) $\delta_f = 45^o$, $A_e/A_n = 20$, $\delta_{TD} = 39$.

Figure 25.- Continued.

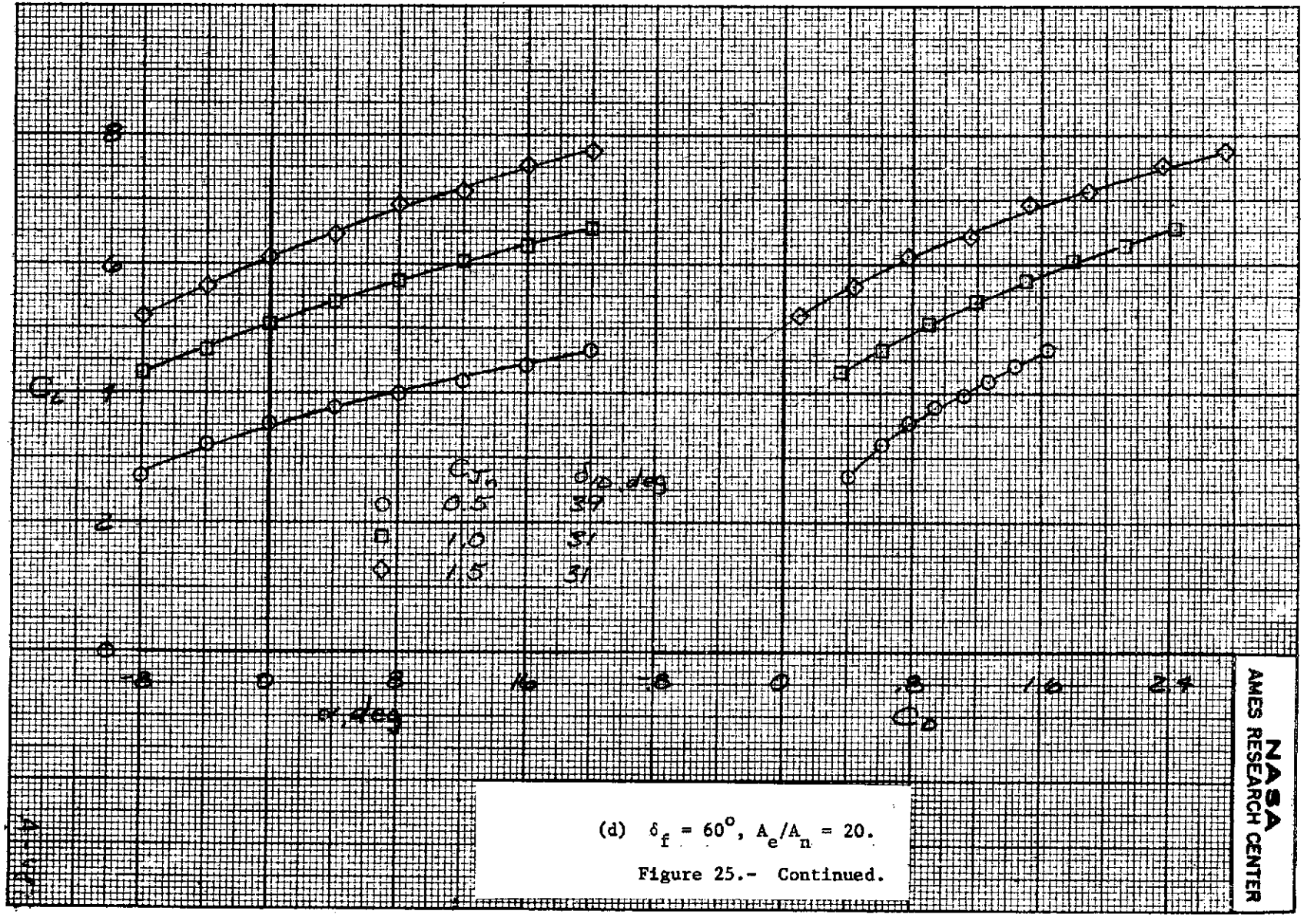

(d) $\delta_f = 60^o$, $A_e/A_n = 20.$

Figure 25.- Continued.

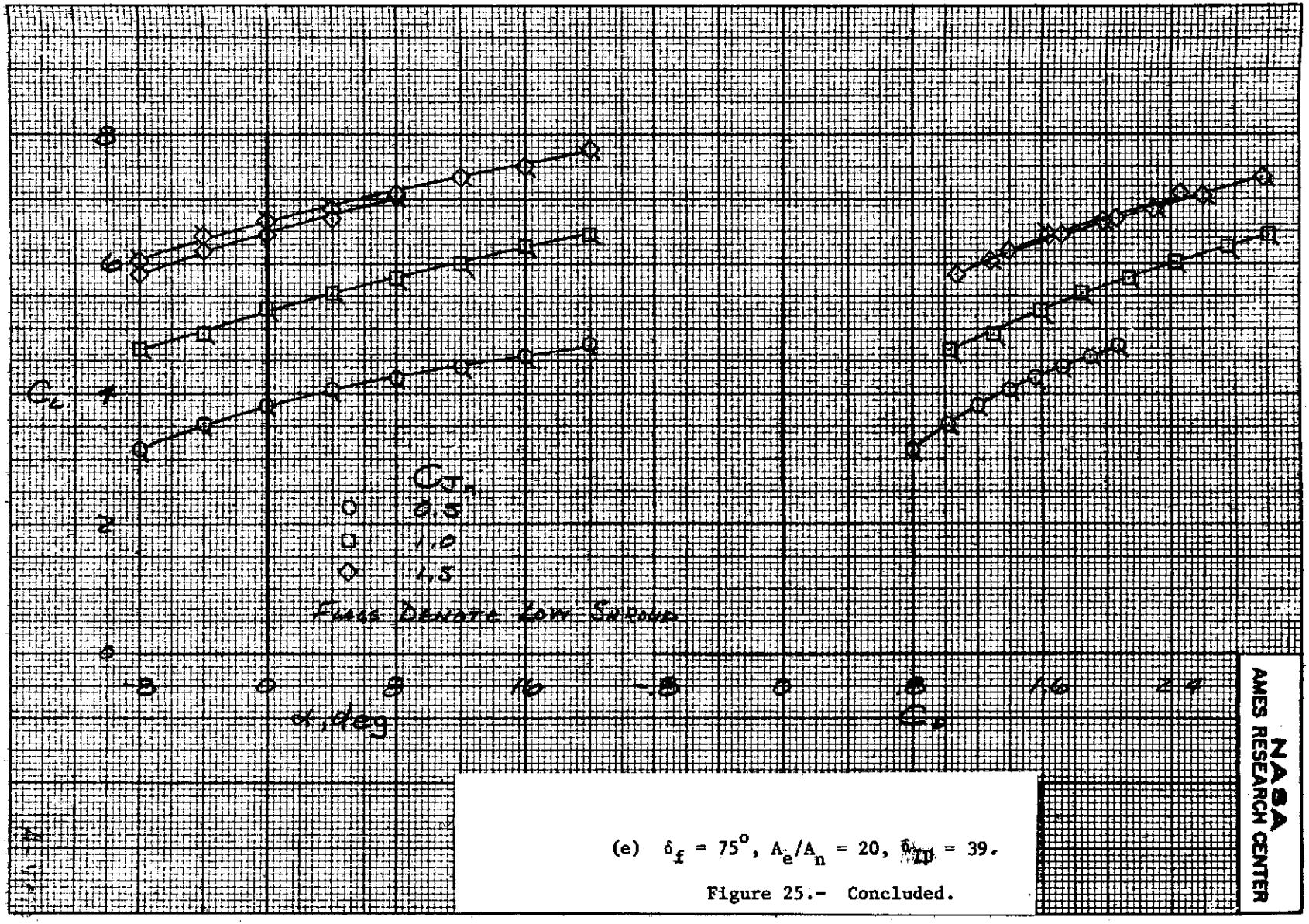

(e) $\delta_f = 75^o$, $A_e/A_n = 20$, $\delta_{TP} = 39$.

Figure 25.- Concluded.

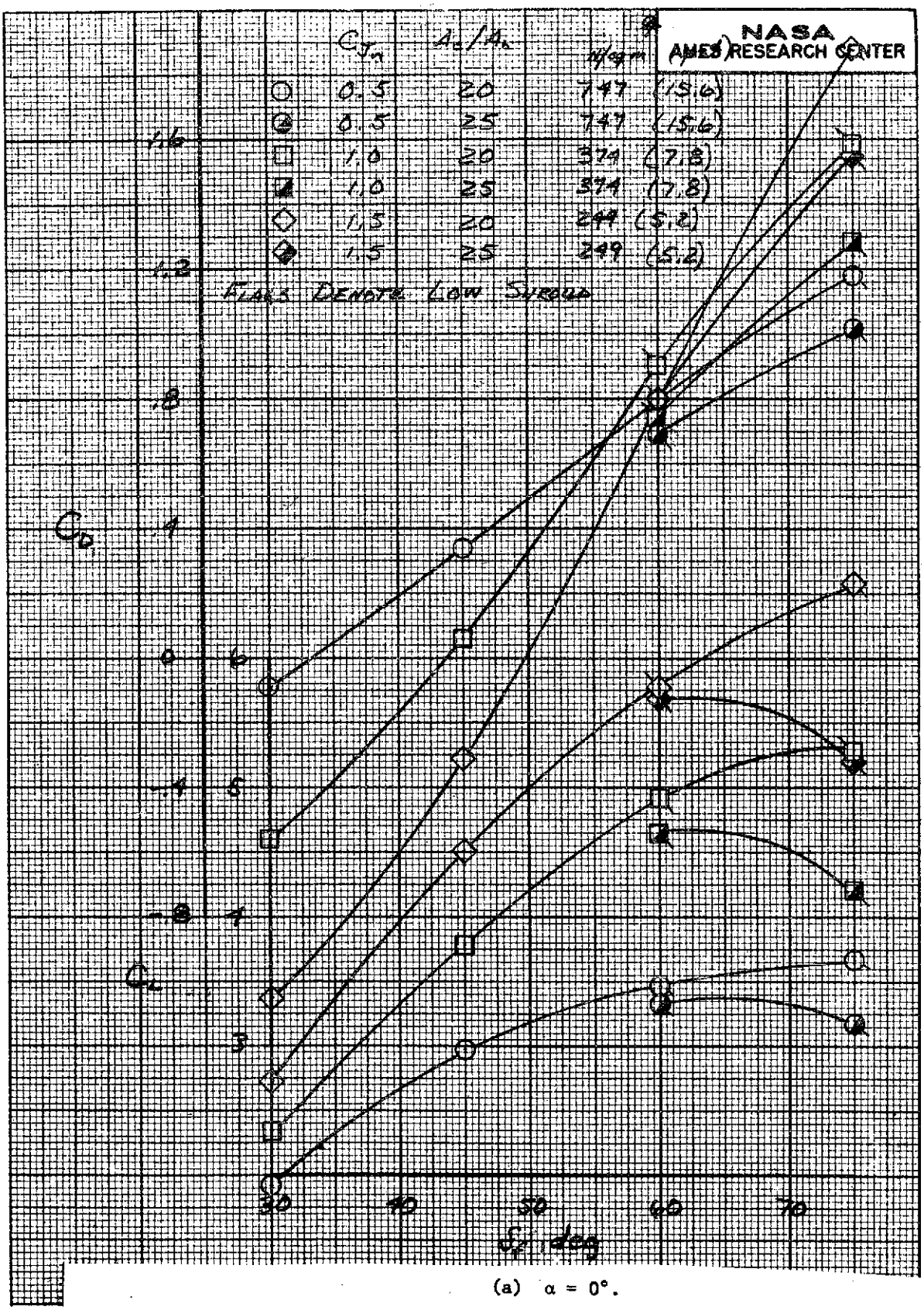

(a) $\alpha = 0°$.

Figure 26.- The effect of C_{J_n} on the lift and drag characteristics of the model with nozzle 3b; $A_e/A_t = 1.25$, $\ell_f = 5.08$ cm (2.0 in), $Z_f = .97$ cm (.38 in), PR = 1.53.

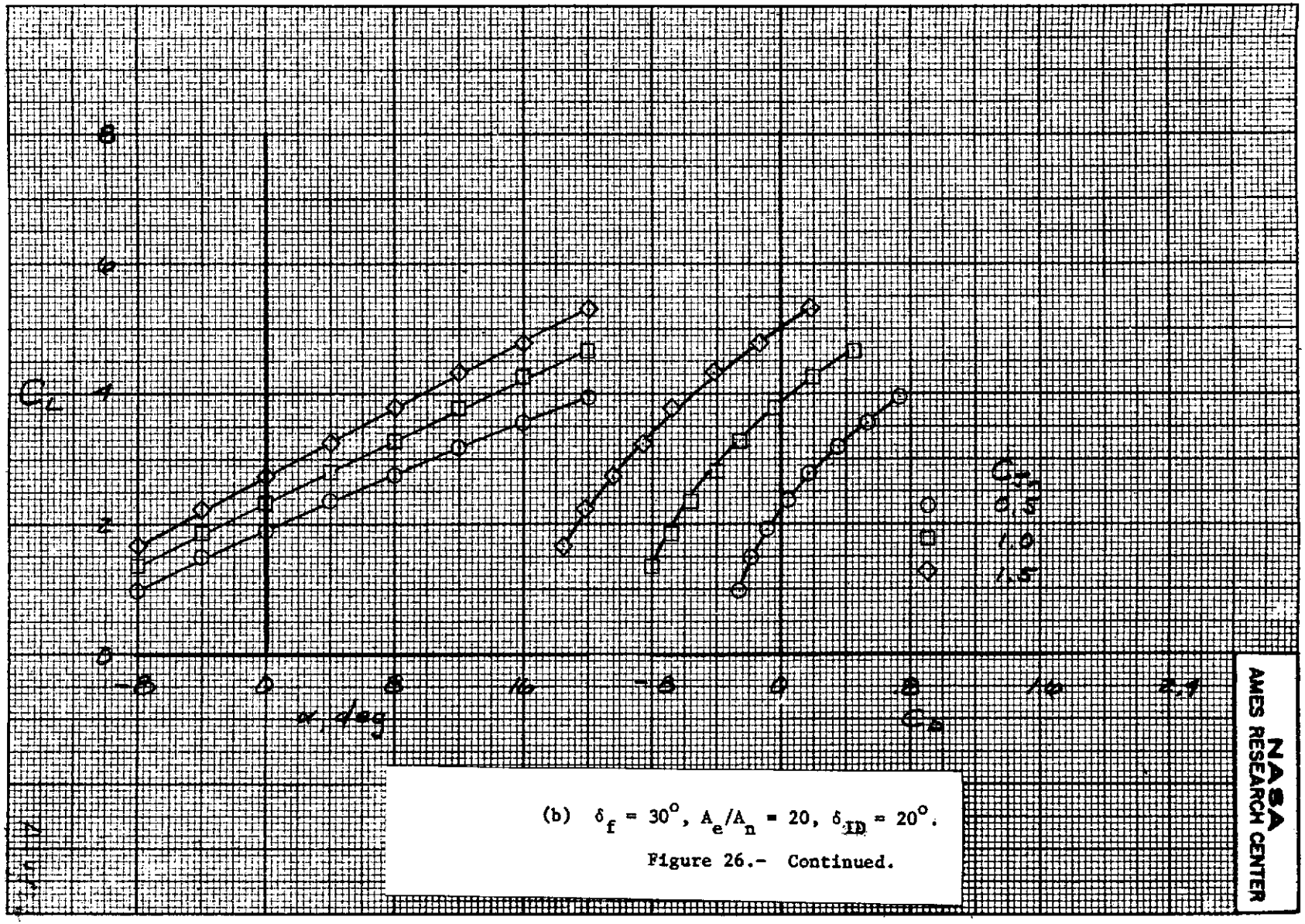

(b) $\delta_f = 30^\circ$, $A_e/A_n = 20$, $\delta_{ID} = 20^\circ$.

Figure 26.- Continued.

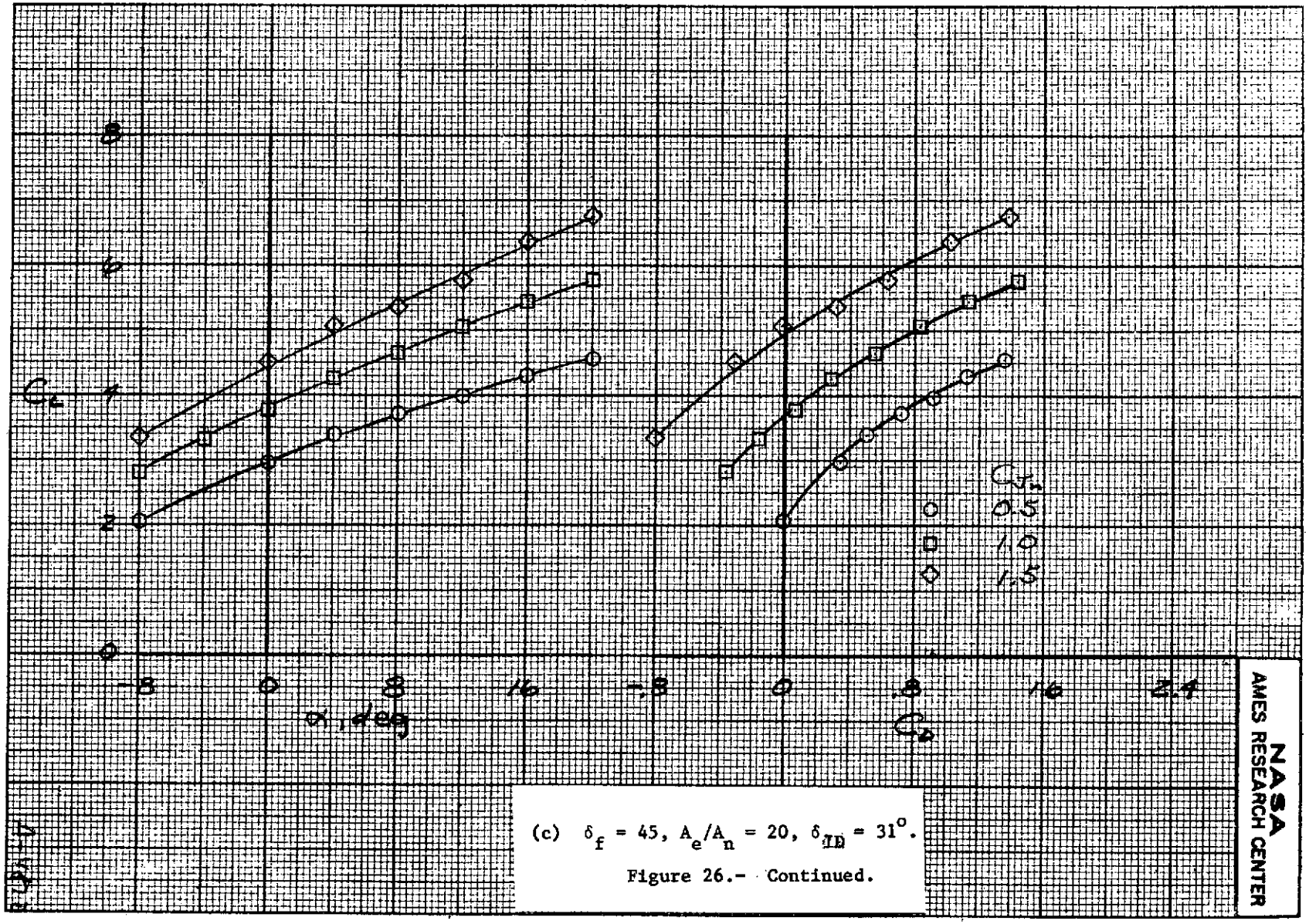

(c) $\delta_f = 45$, $A_e/A_n = 20$, $\delta_{TE} = 31^\circ$.

Figure 26.- Continued.

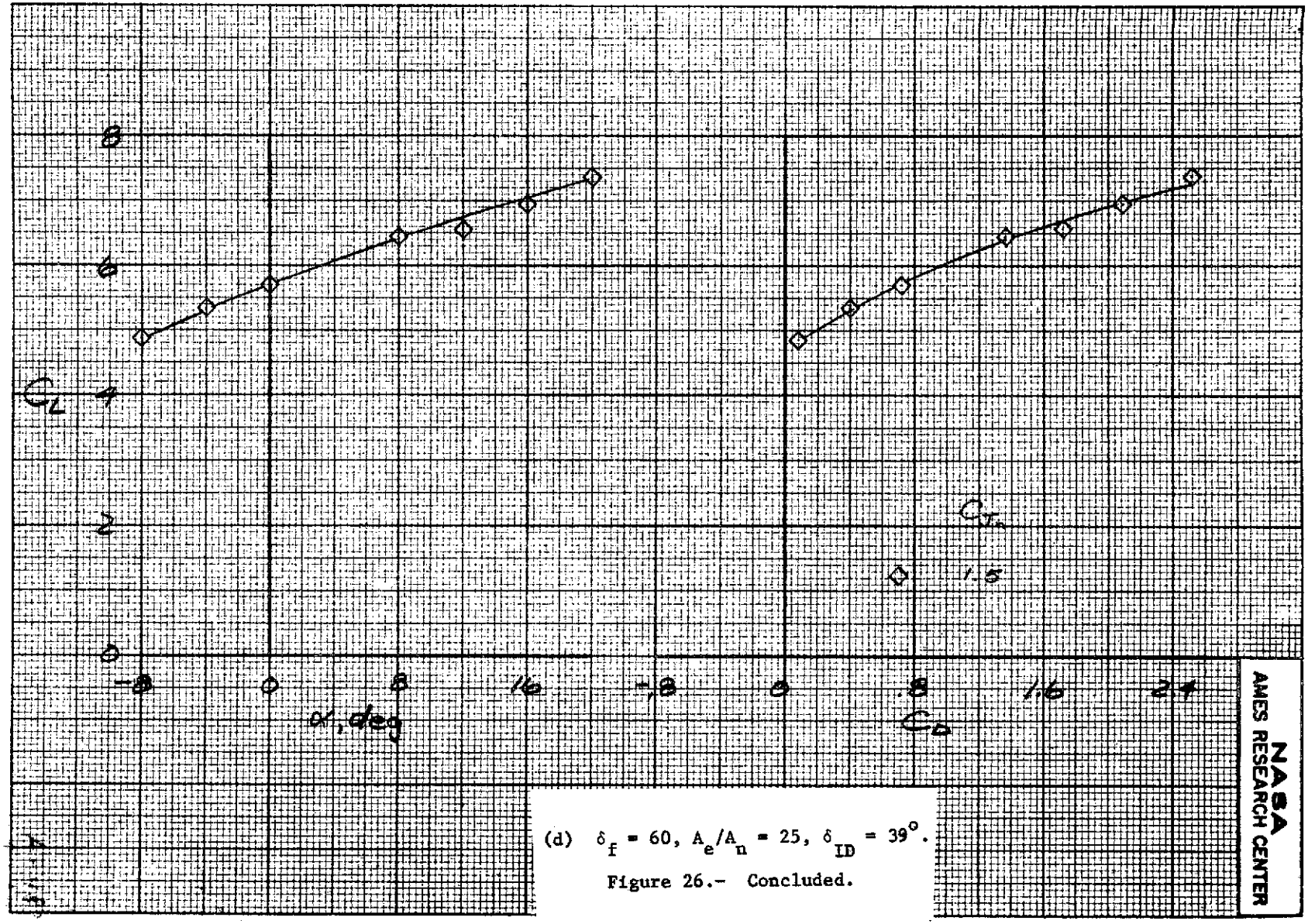

(d) $\delta_f = 60$, $A_e/A_n = 25$, $\delta_{ID} = 39^\circ$.

Figure 26.- Concluded.

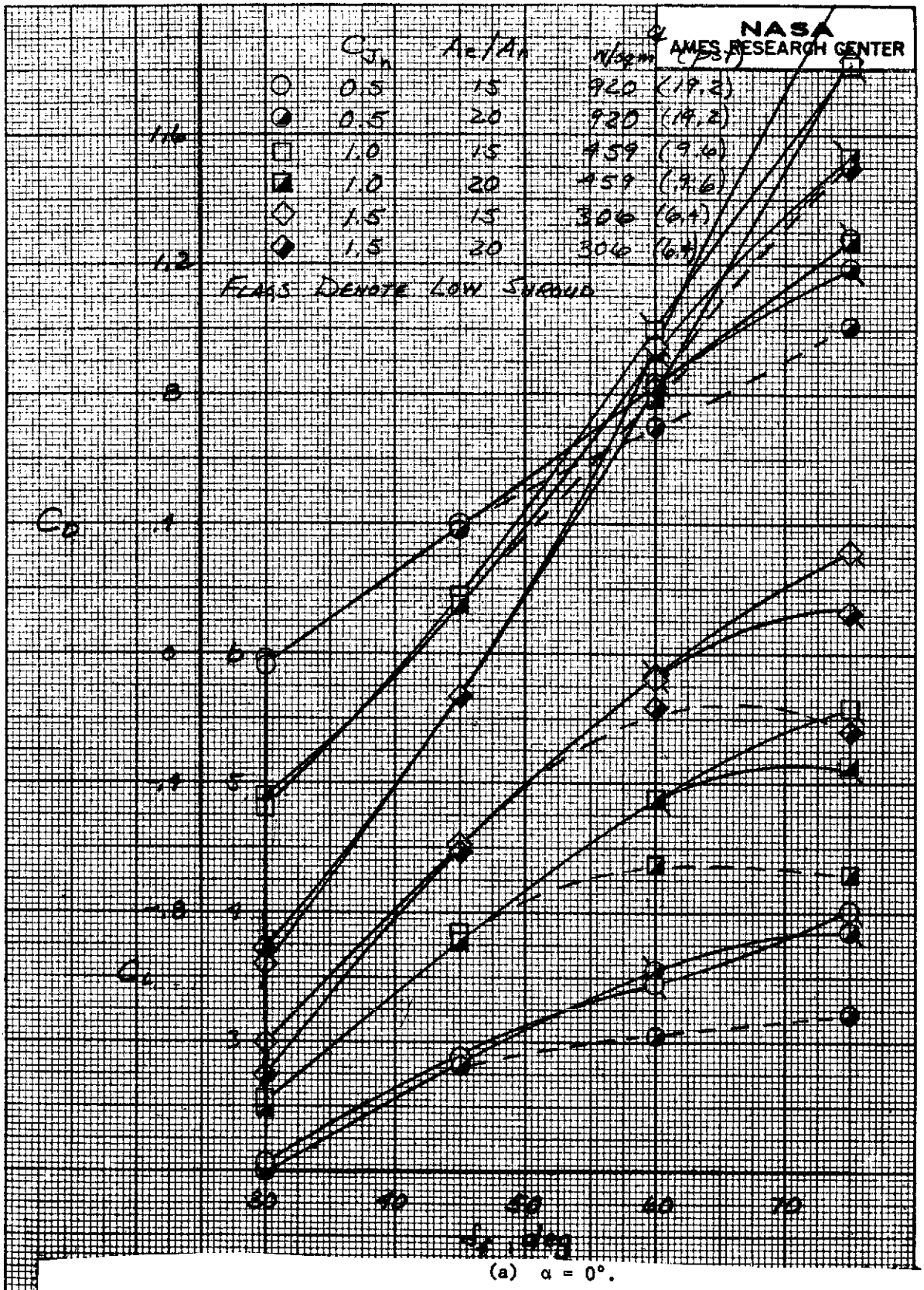

(a) $\alpha = 0°$.

Figure 27.- The effect of C_{J_n} on the lift and drag characteristics of the model with nozzle 5é; A_e/A_t = 1.25, ℓ_f = 2.54 cm (1.0 in), Z_f = .15 cm (.06 in), PR = 1.53.

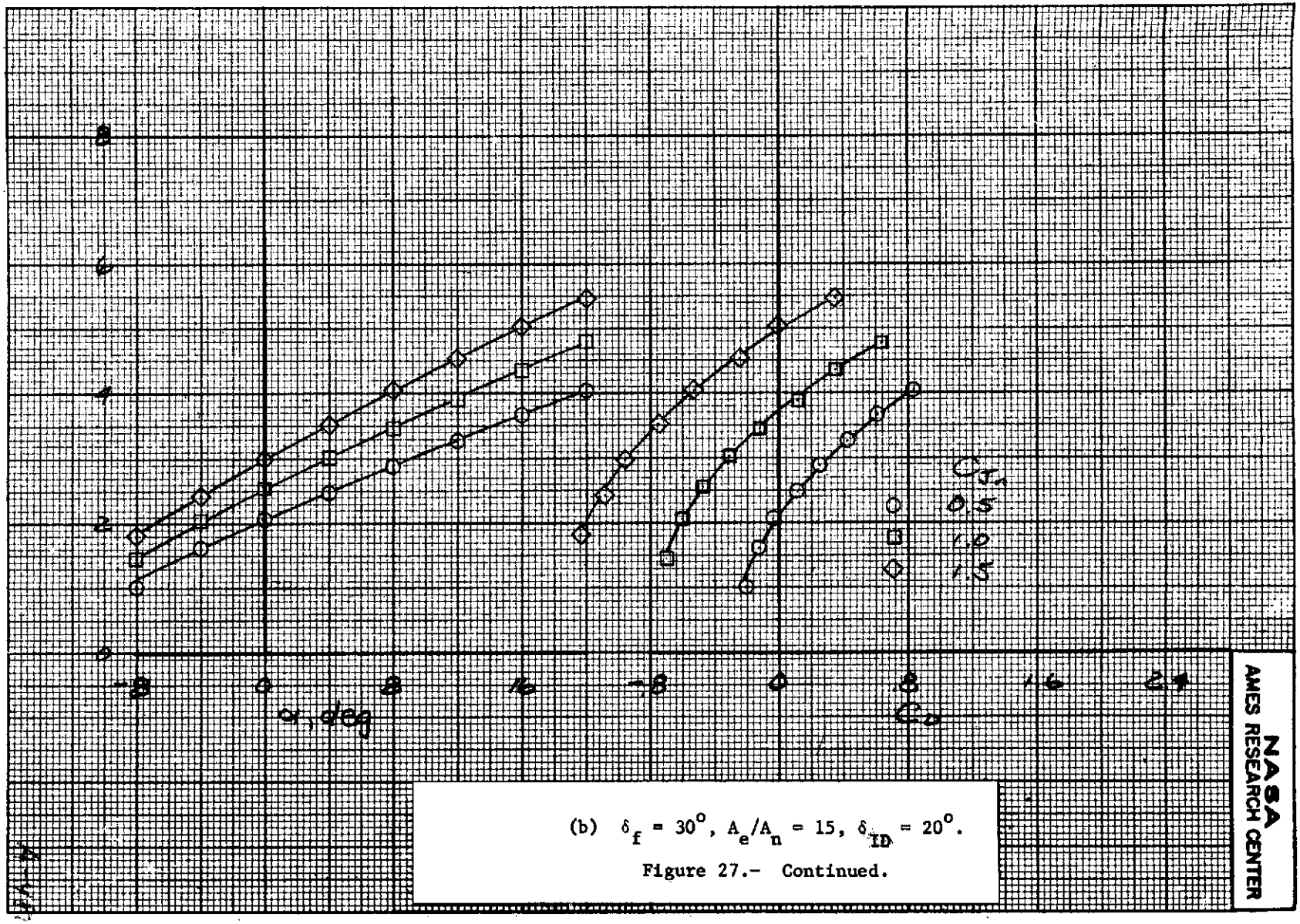

(b) $\delta_f = 30^\circ$, $A_e/A_n = 15$, $\delta_{ID} = 20^\circ$.

Figure 27.- Continued.

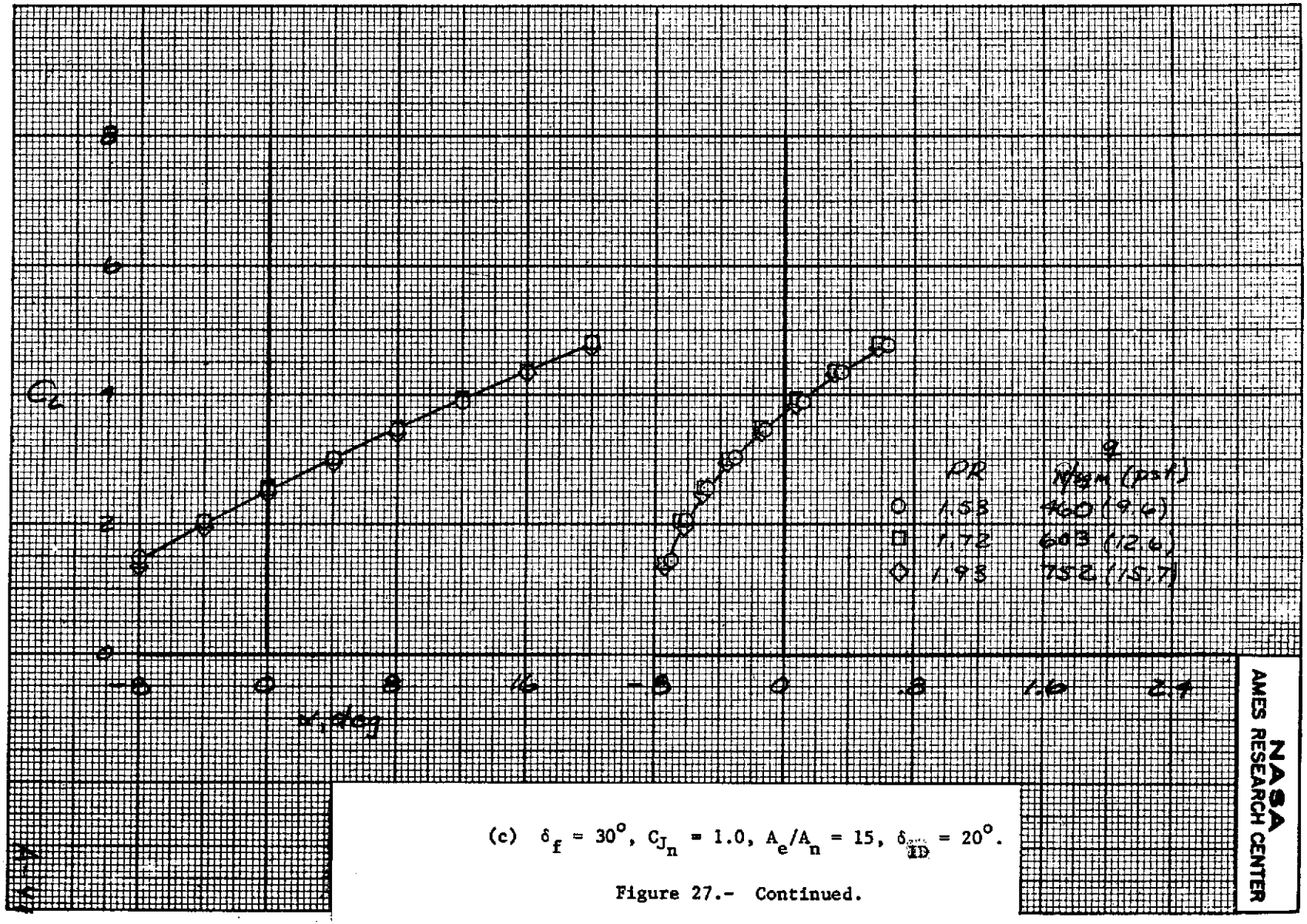

(c) $\delta_f = 30^\circ$, $C_{J_n} = 1.0$, $A_e/A_n = 15$, $\delta_{ID} = 20^\circ$.

Figure 27.- Continued.

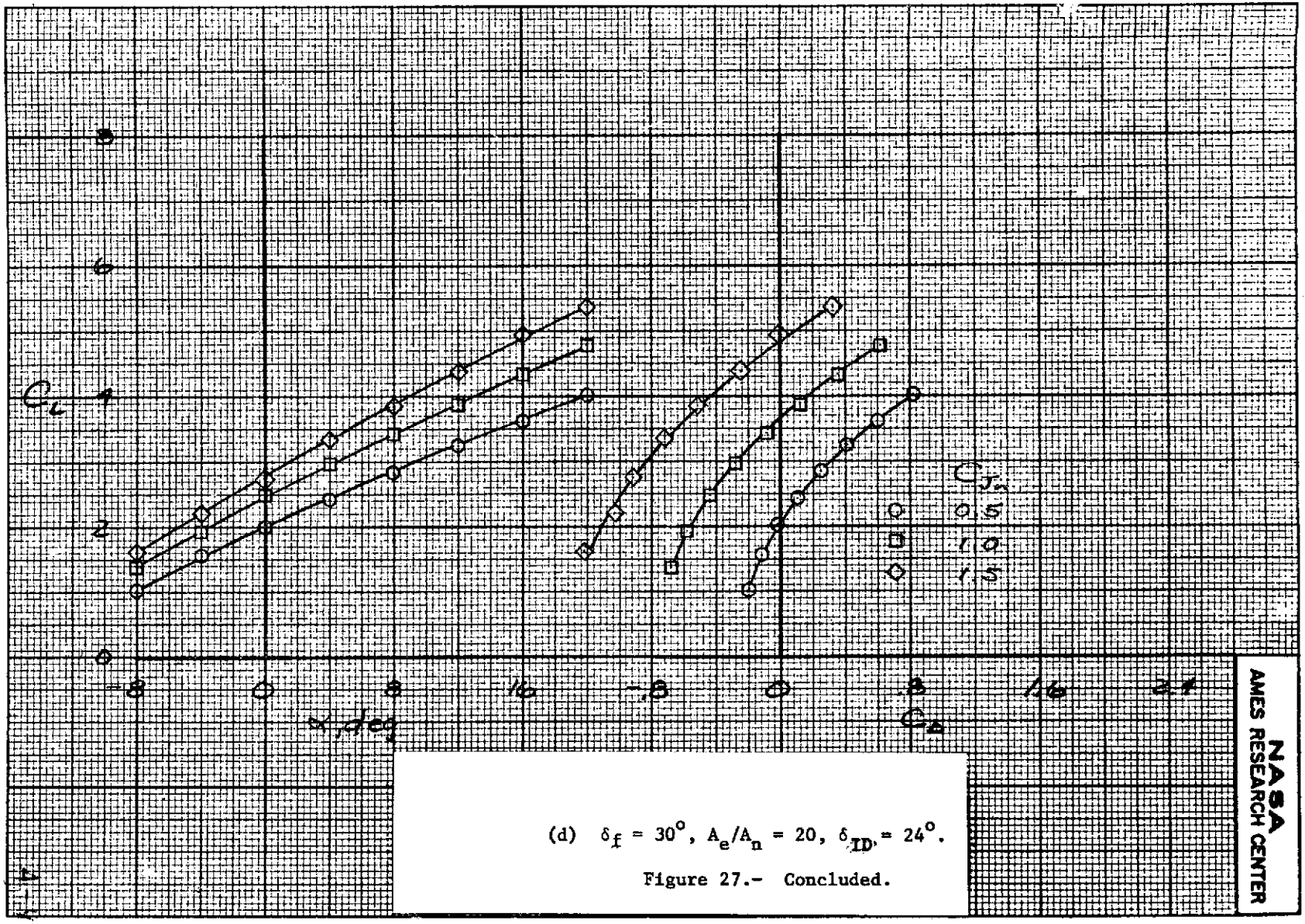

(d) $\delta_f = 30^\circ$, $A_e/A_n = 20$, $\delta_{ID} = 24^\circ$.

Figure 27.- Concluded.

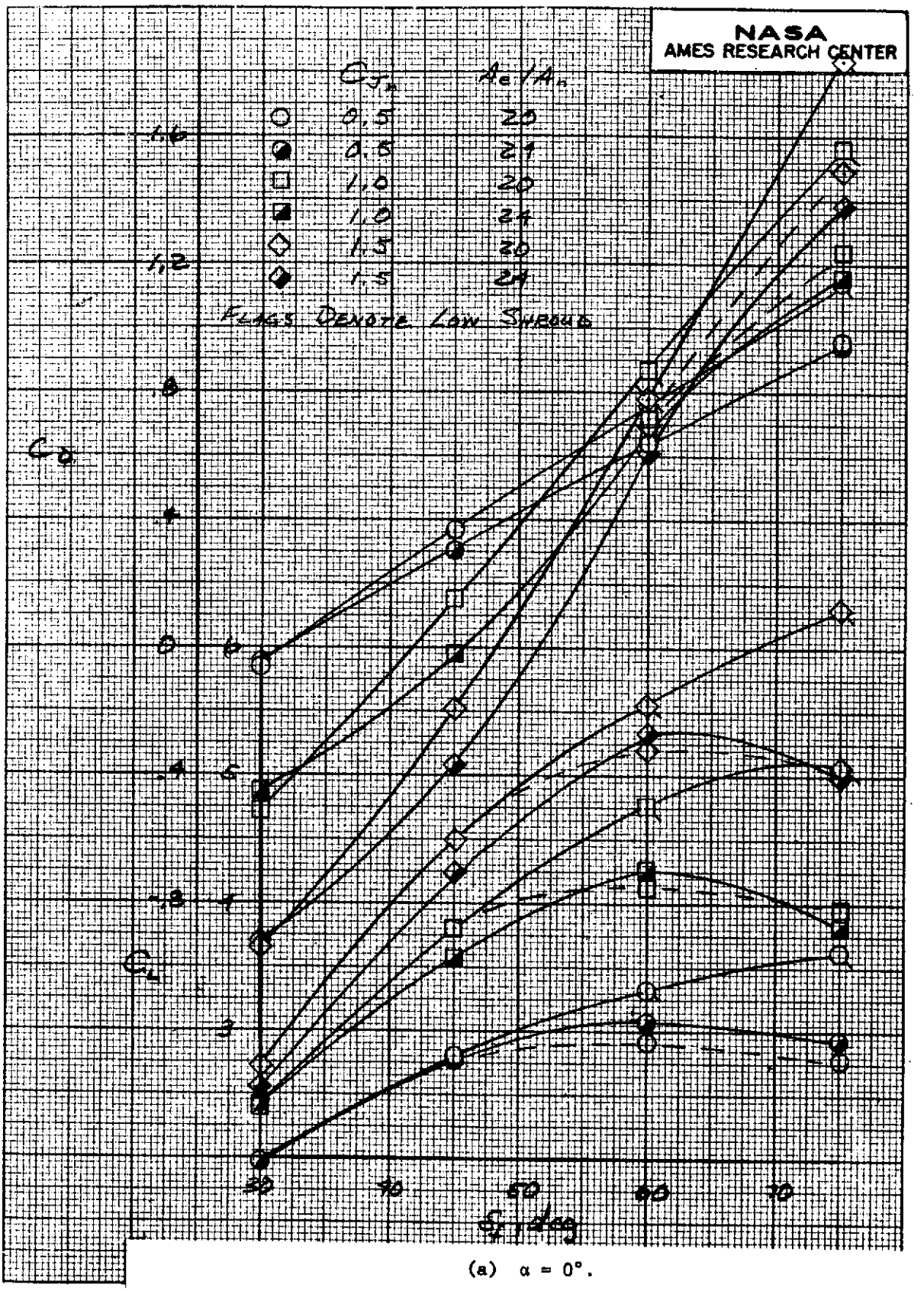

(a) $\alpha = 0°$.

Figure 28.- The effect of C_{J_n} on the lift and drag characteristics of the model with nozzle 5c; $A_e/A_t = 1.25$, $\ell_f = 5.08$ cm (2.0 in), $Z_f = .79$ cm (.31 in), PR = 1.53.

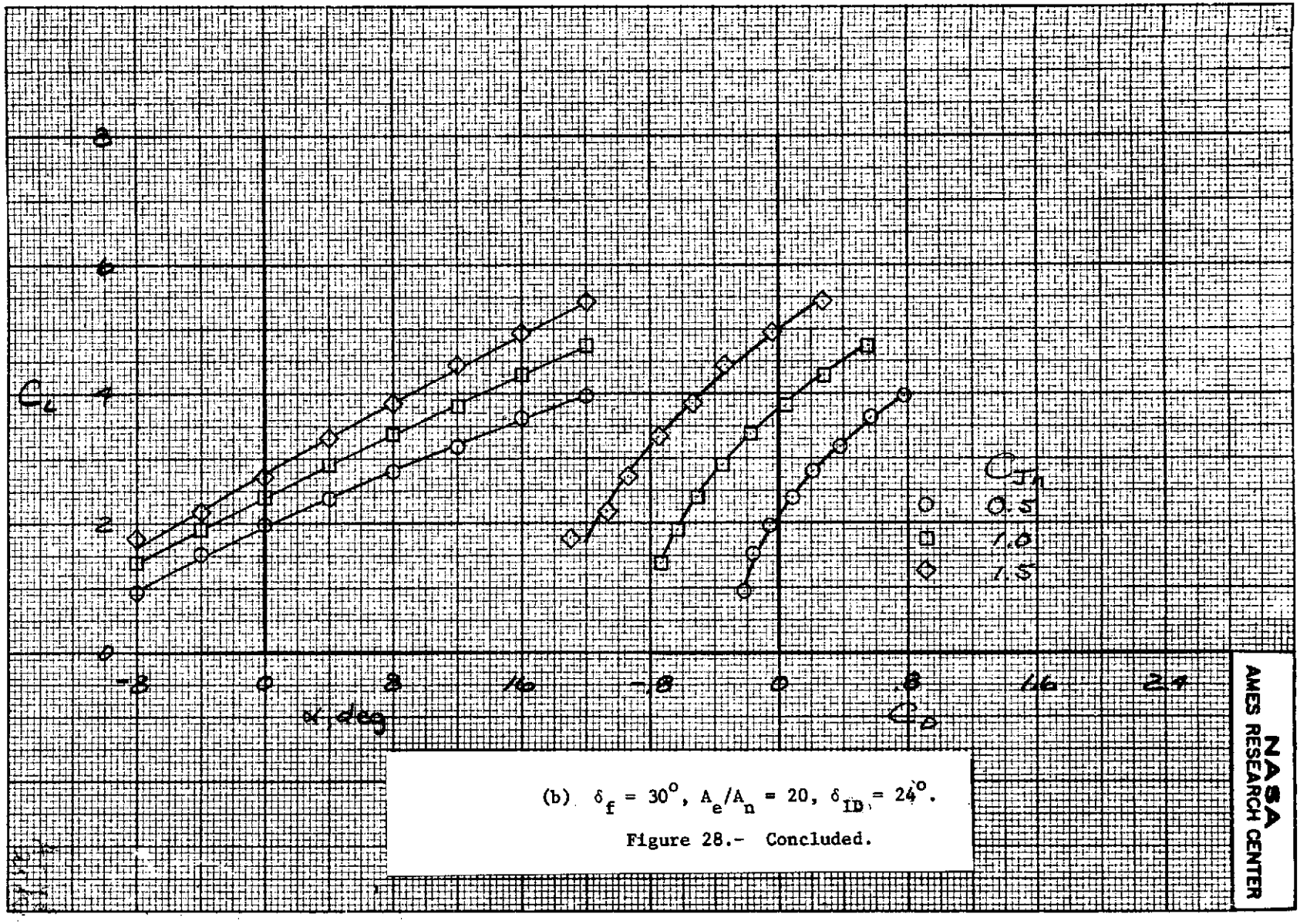

(b) $\delta_f = 30^o$, $A_e/A_n = 20$, $\delta_{ID} = 24^o$.

Figure 28.- Concluded.

NASA
AMES RESEARCH CENTER

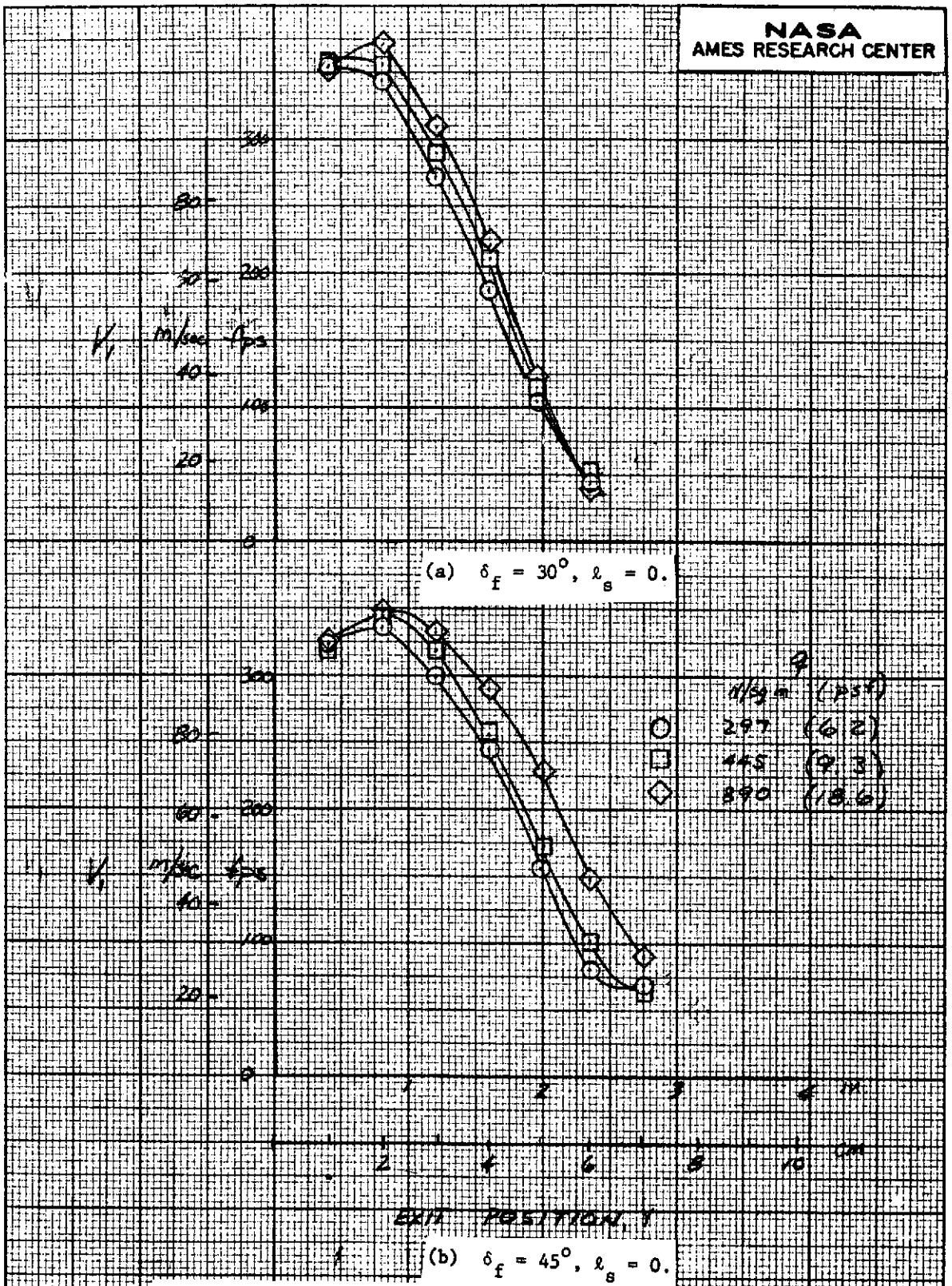

Figure 29.- The effect of q on the exit velocity profiles for nozzle 1; $\alpha = 0°$, $A_e/A_n = 15$, $A_e/A_t = 1.25$, $Z_f = 1.27$ cm (.50 in), $\ell_f = 5.08$ cm (2.0 in), PR = 1.53.

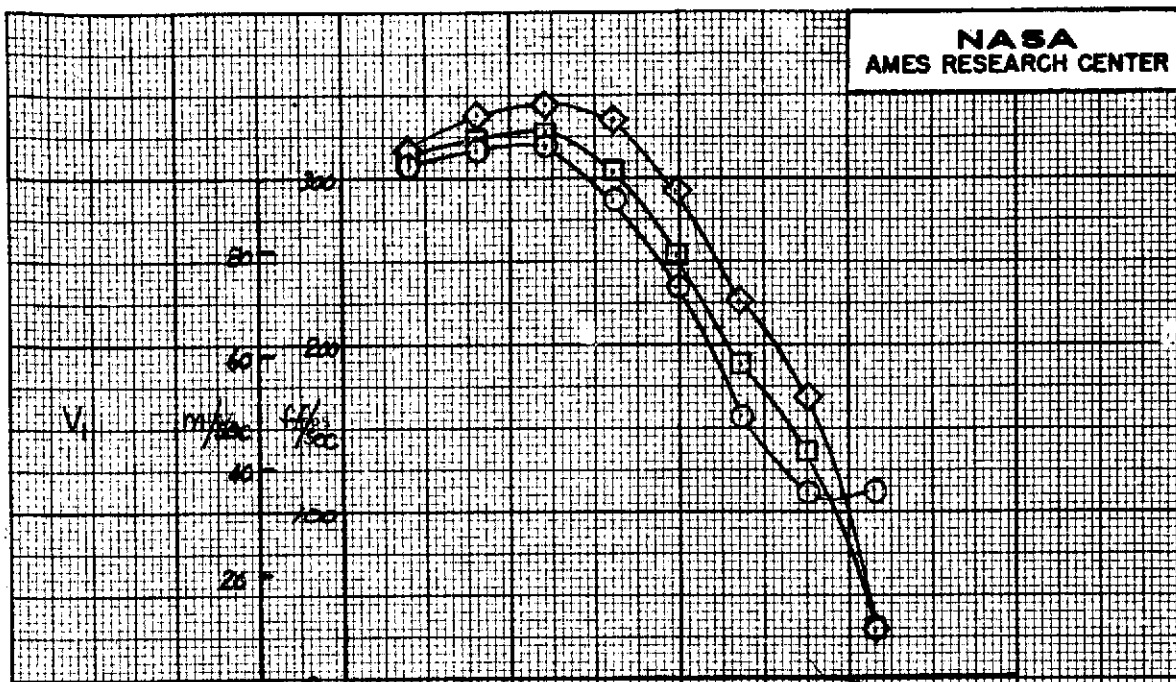

(c) δ_f = 60°, ℓ_s = 5.08 cm (2.0 in).

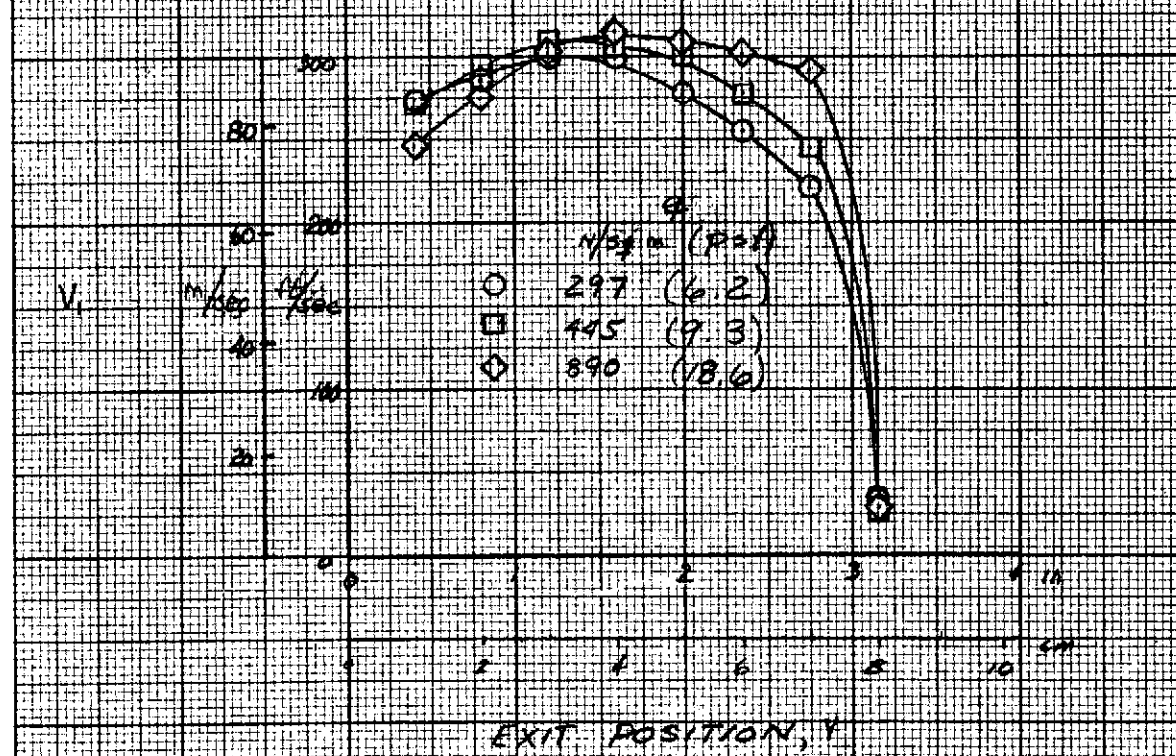

(d) δ_f = 75°, ℓ_s = 5.08 cm (2.0 in).

Figure 29.- Concluded.

C2

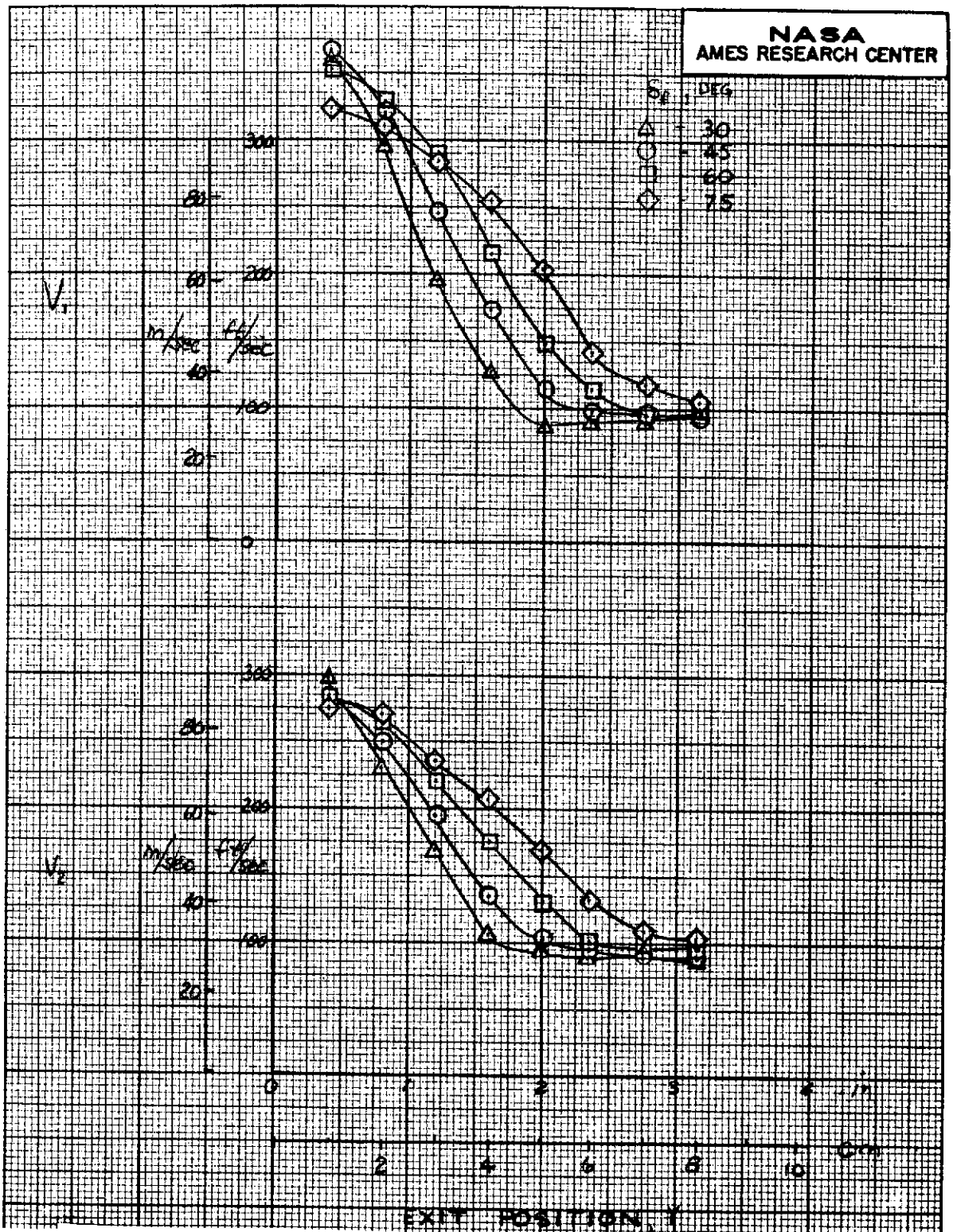

Figure 30.- The effect of flap angle on the exit velocity profiles for nozzle 1, shroud off; $\alpha = 0°$, $Z_f = 0$, $\ell_f = 5.08$ cm (2.0 in), PR = 1.53, q = 297 N/sq m (6.2 psf).

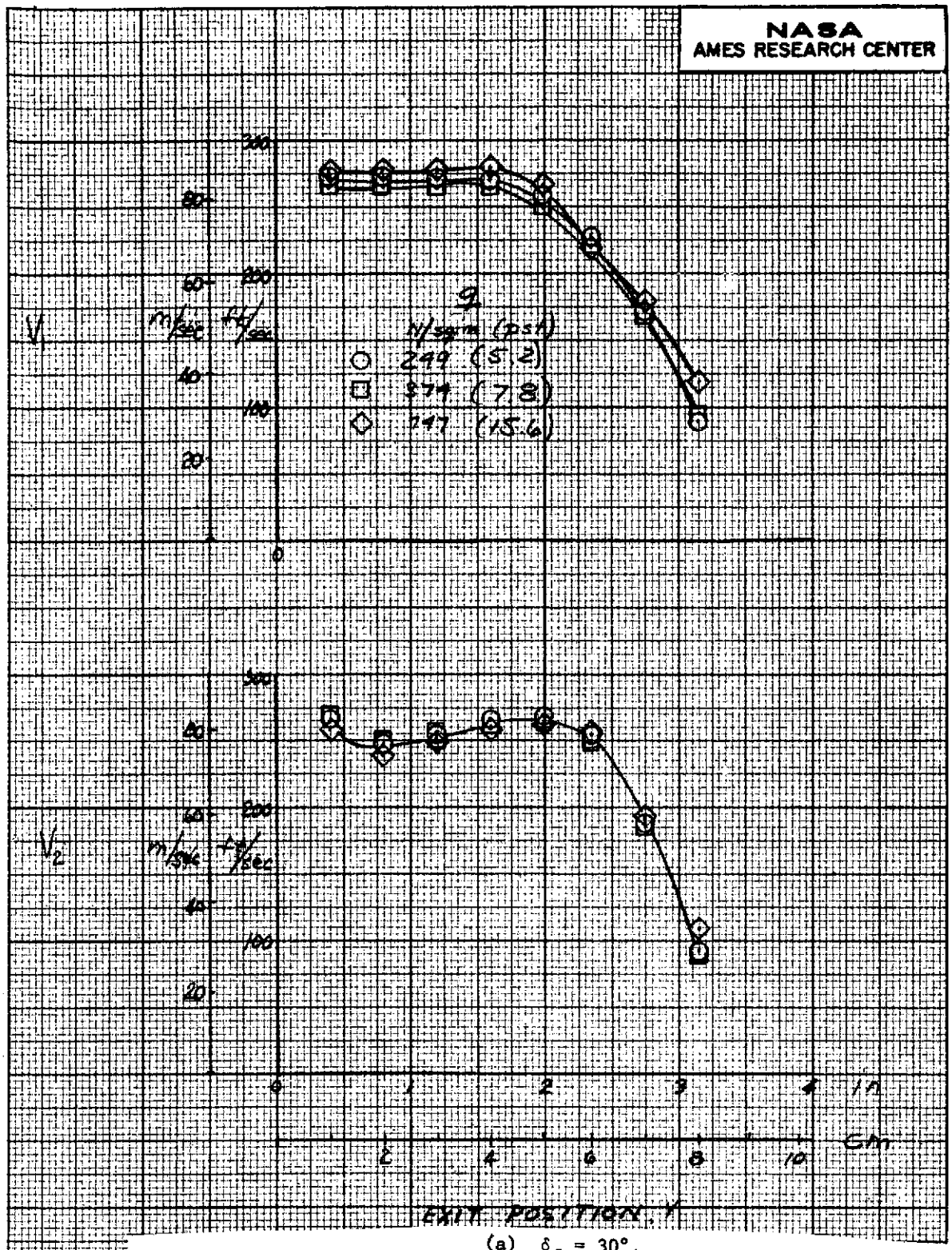

(a) $\delta_f = 30°$.

Figure 31.- The effect of q on the exit velocity rpofiles for nozzle 3b; $\alpha = 0°$, $A_e/A_n = 15$, $A_e/A_t = 1.25$, $Z_f = .15$ cm (.06 in), $\ell_f = 2.54$ cm (1.0 in), $\ell_s = 0$, PR = 1.53.

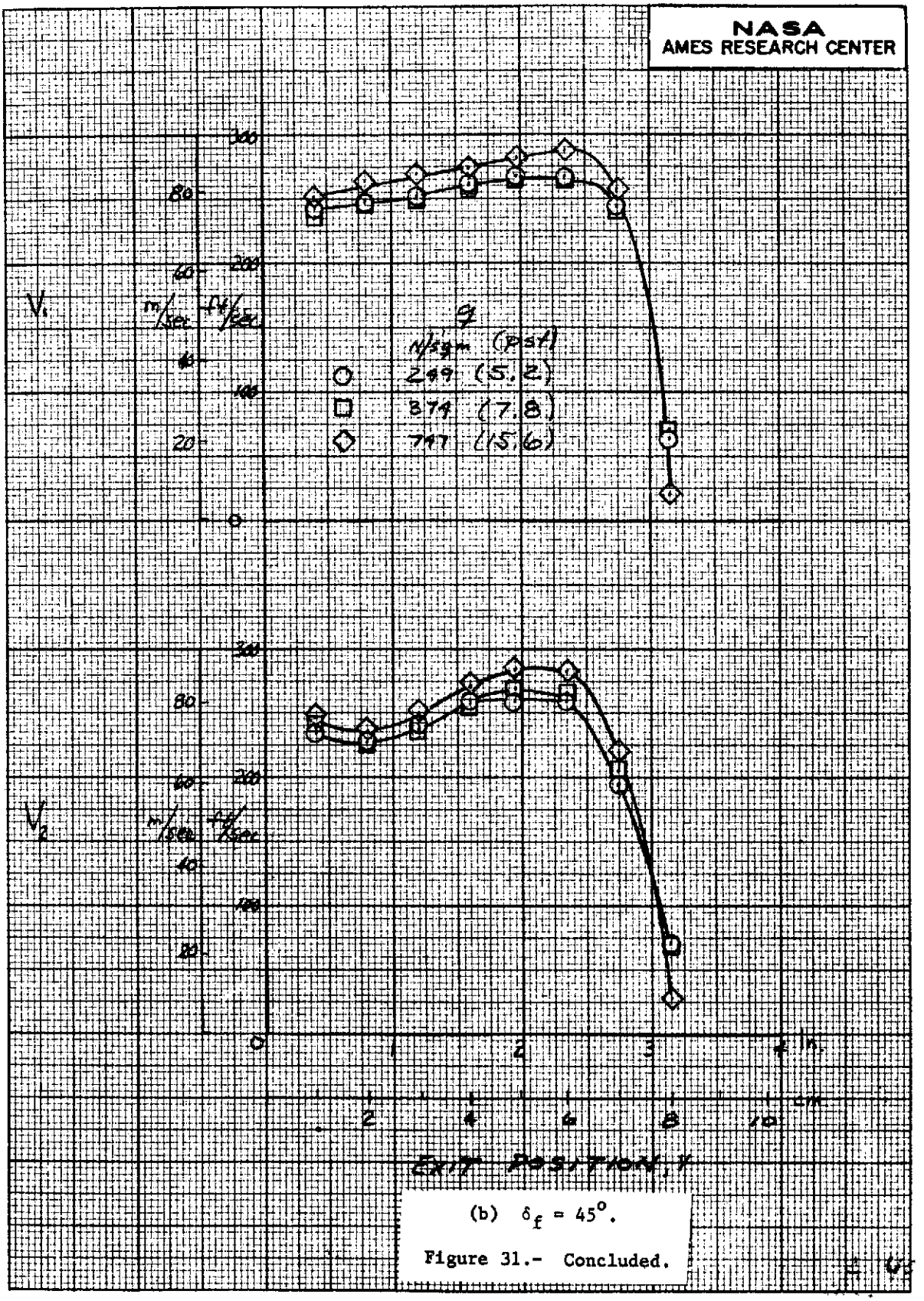

(b) $\delta_f = 45^\circ$.

Figure 31.- Concluded.

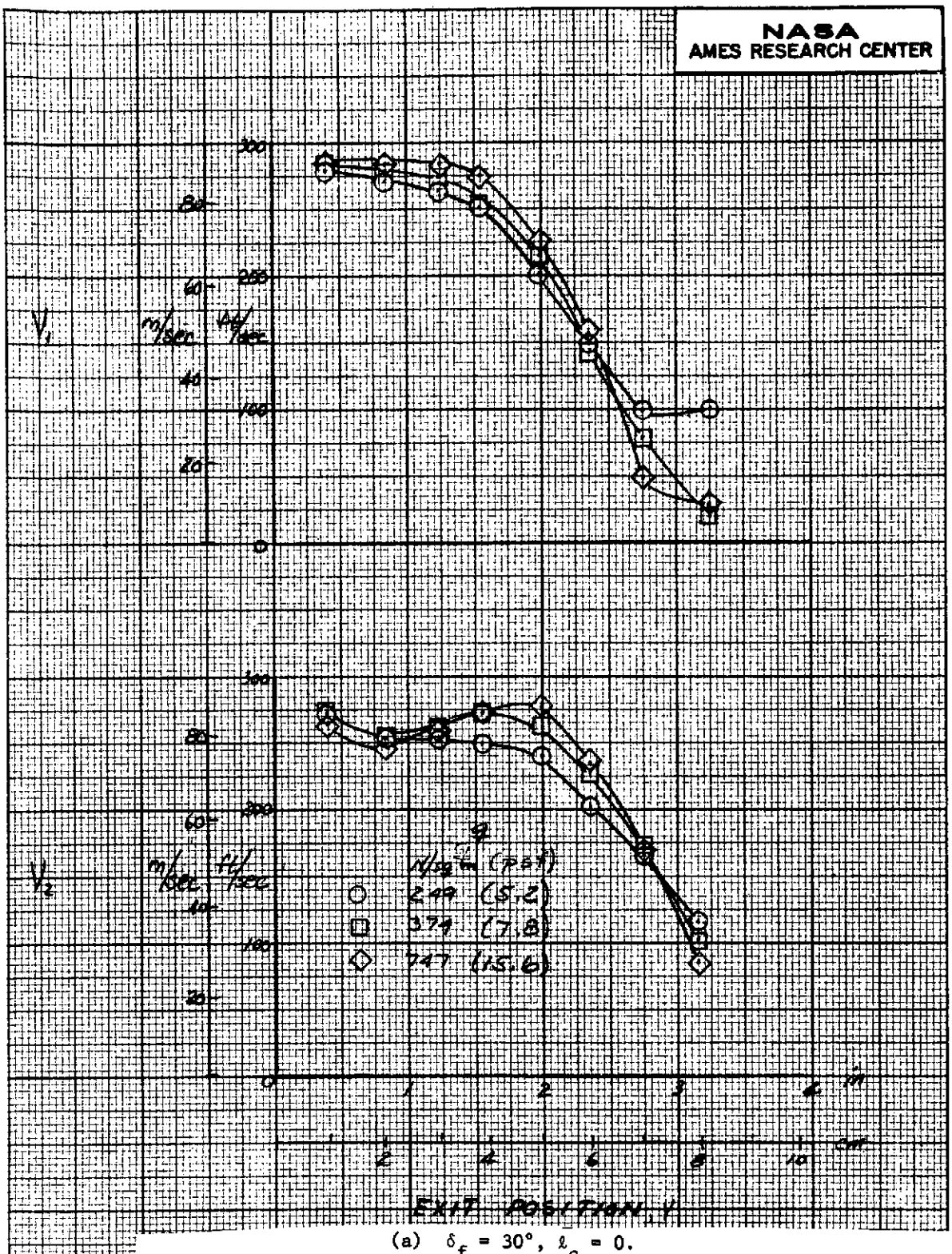

(a) $\delta_f = 30°$, $\ell_s = 0$.

Figure 32.- The effect of q on the exit velocity profiles for nozzle 3b; $\alpha = 0°$, $A_e/A_n = 20$, $A_e/A_t = 1.25$, $Z_f = .15$ cm (.06 in), $\ell_f = 2.54$ cm (1.0 in), PR = 1.53.

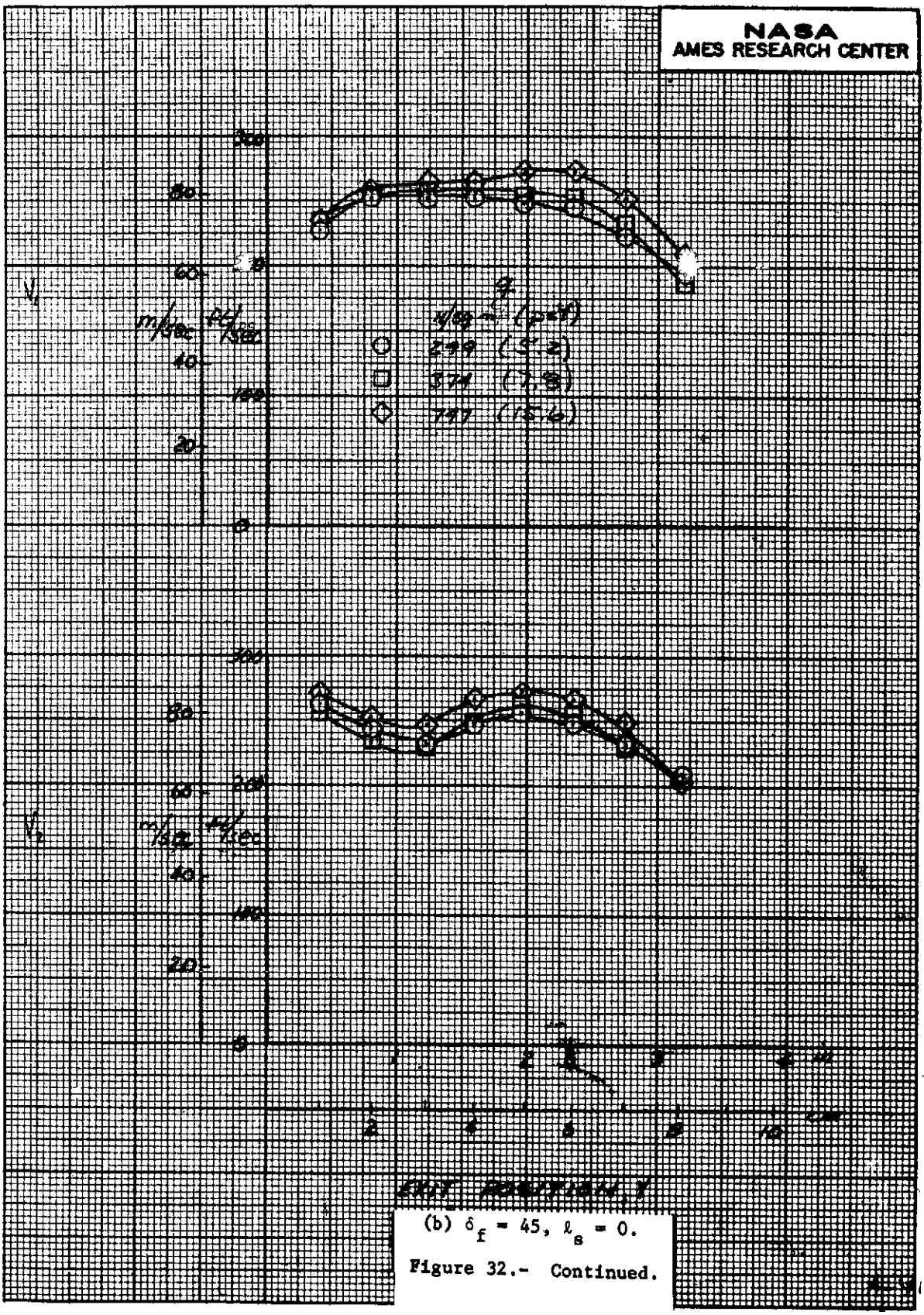

(b) $\delta_f = 45$, $\ell_s = 0$.

Figure 32.- Continued.

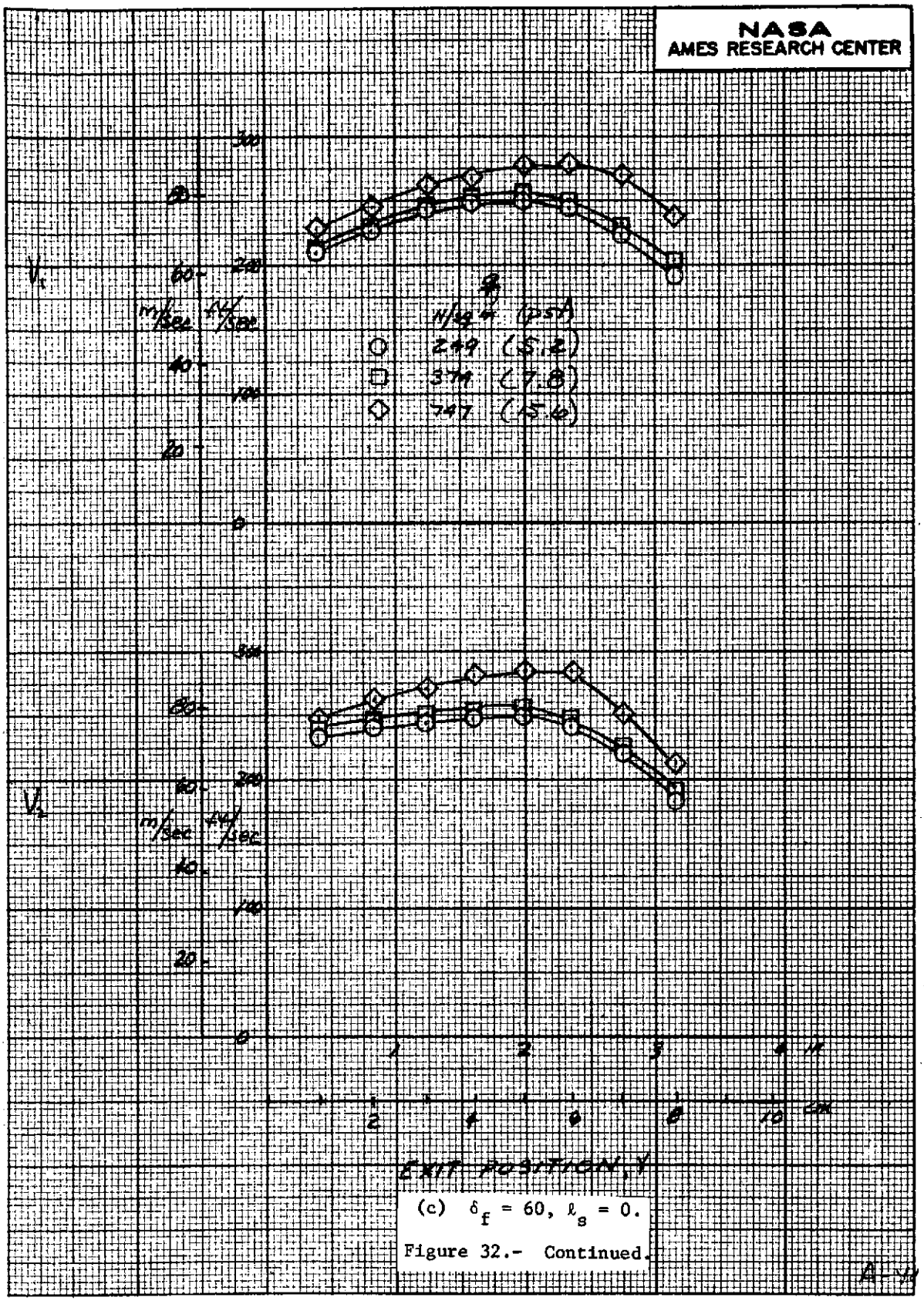

(c) $\delta_f = 60$, $\ell_s = 0.$

Figure 32.- Continued.

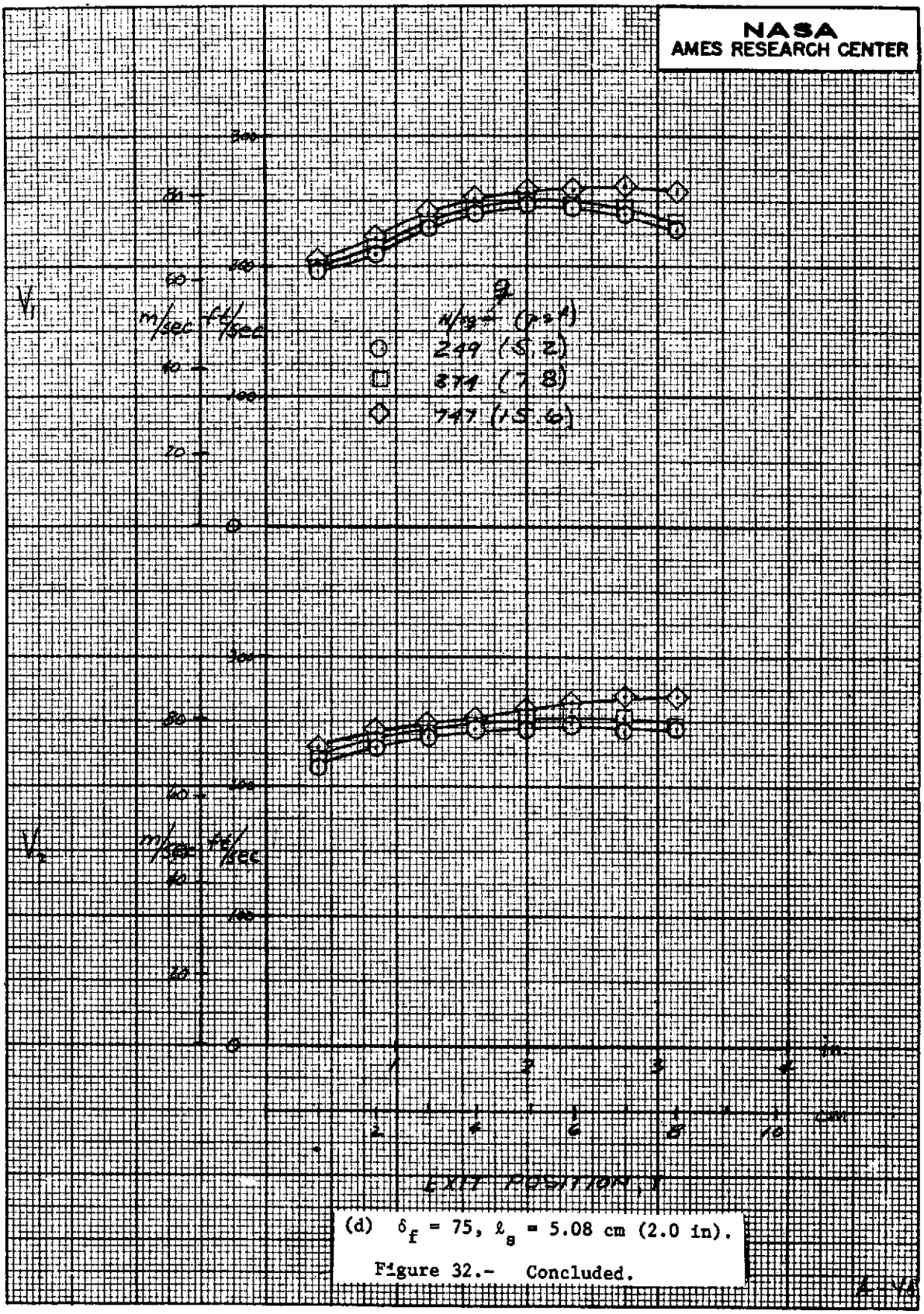

(d) δ_f = 75, ℓ_s = 5.08 cm (2.0 in).

Figure 32.- Concluded.

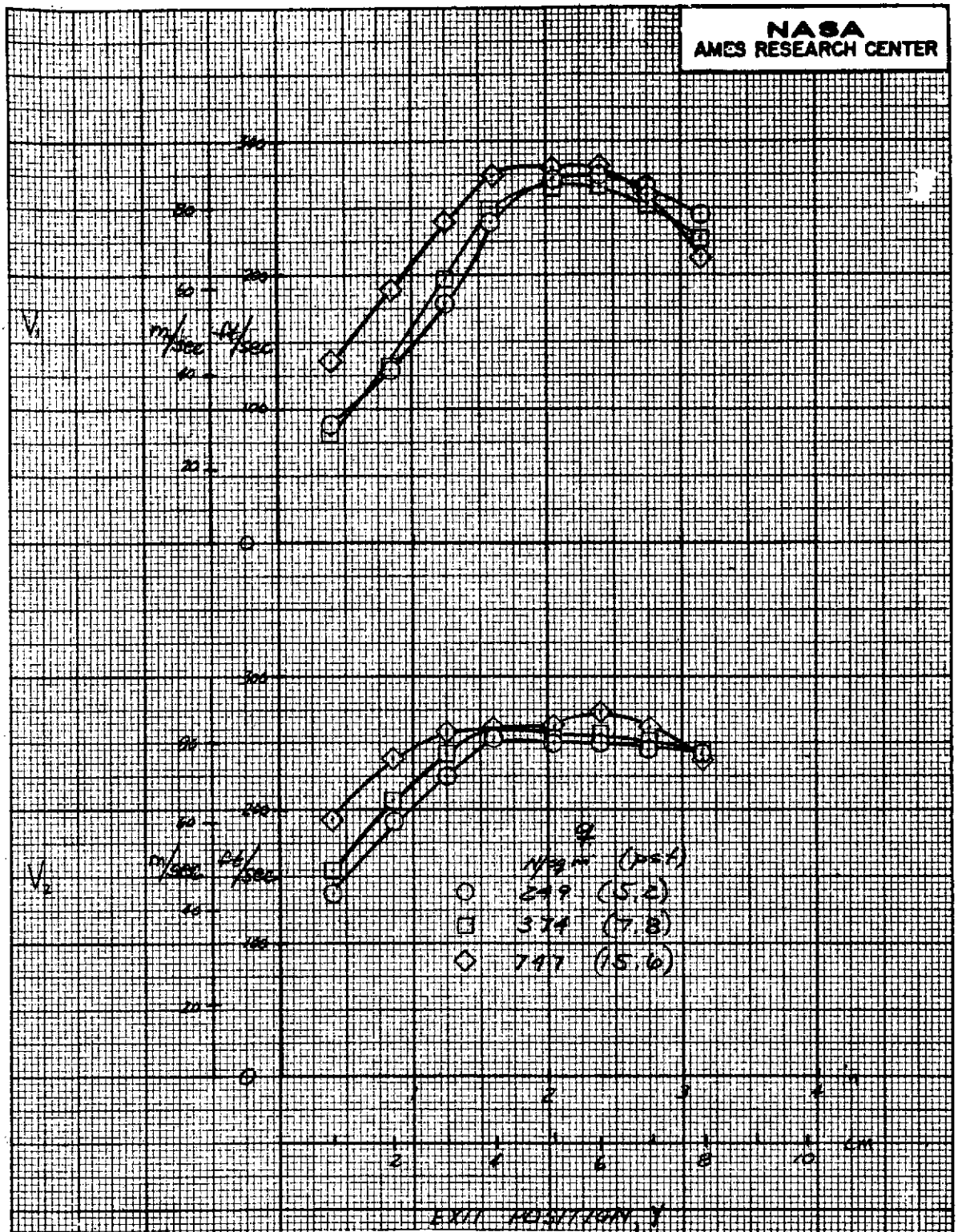

(a) $\delta_f = 30°$, $\ell_s = 0$.

Figure 33.- The effect of q on the exit velocity profiles for nozzle 3b; $\alpha = 0°$, $A_e/A_R = 20$, $A_e/A_t = 1.25$, $Z_f = .97$ cm (.38 in), $\ell_f = 5.08$ cm (2.0 in), PR = 1.53.

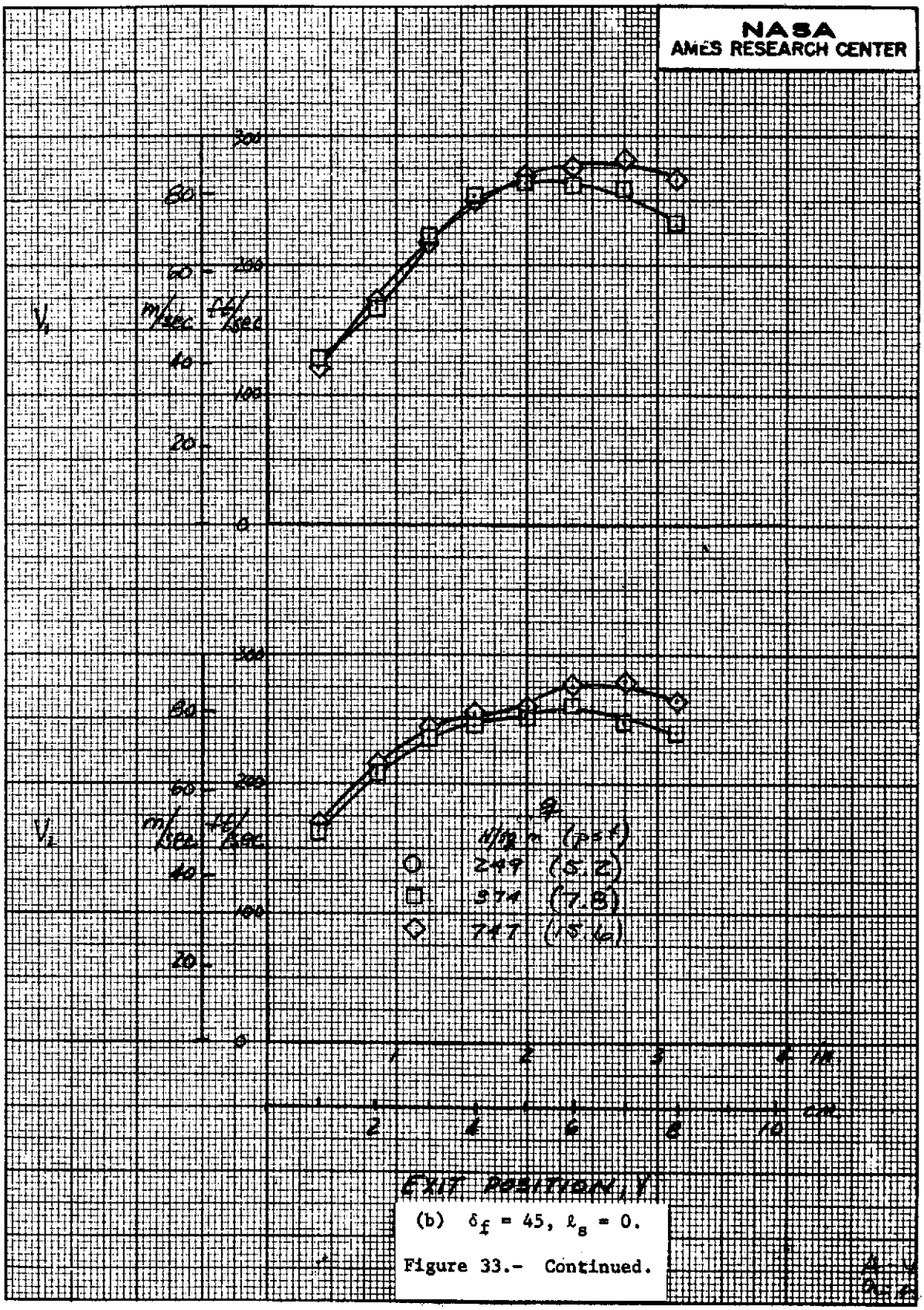

(b) $\delta_f = 45$, $\ell_s = 0$.

Figure 33.- Continued.

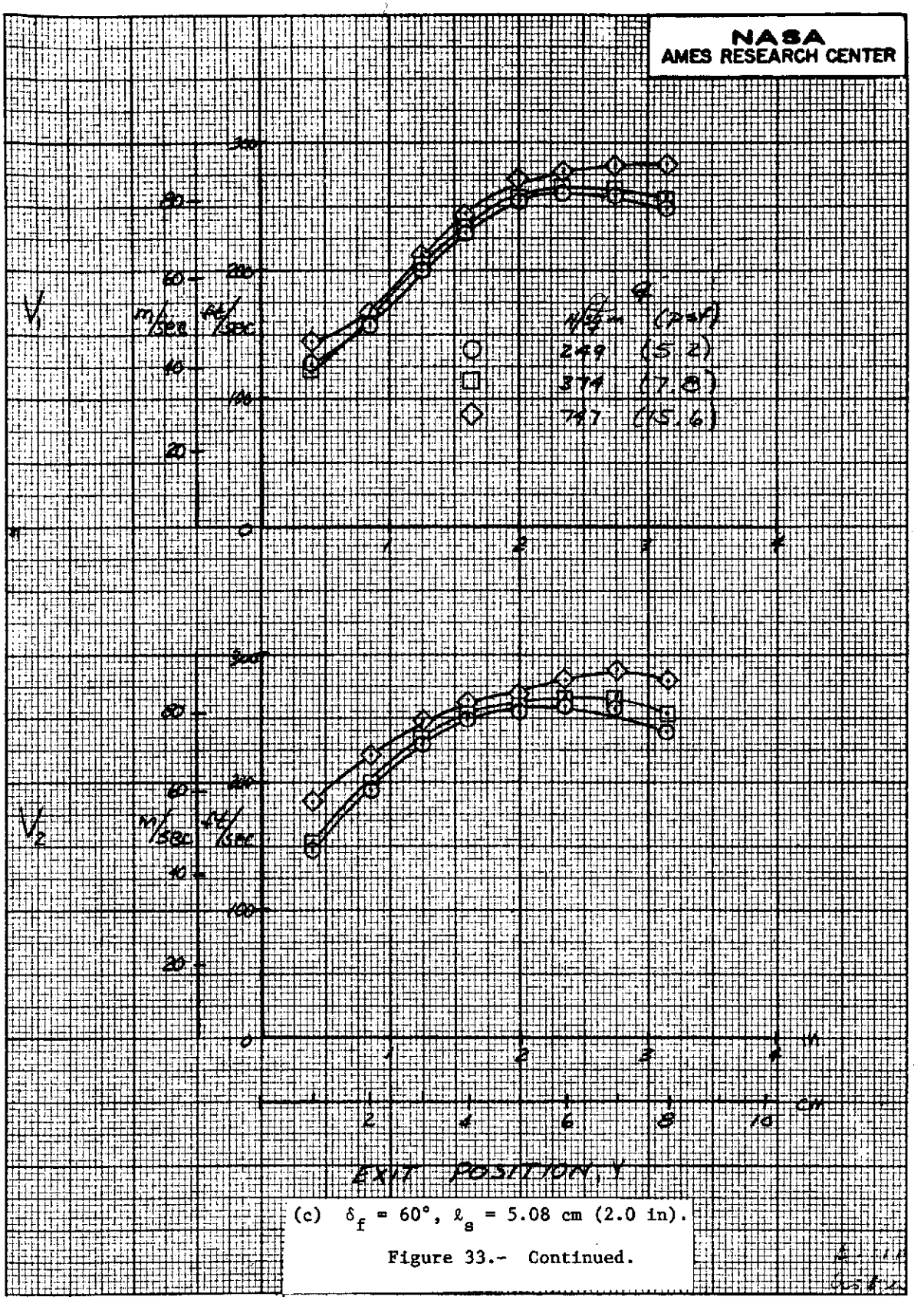

(c) $\delta_f = 60°$, $\ell_s = 5.08$ cm (2.0 in).

Figure 33.- Continued.

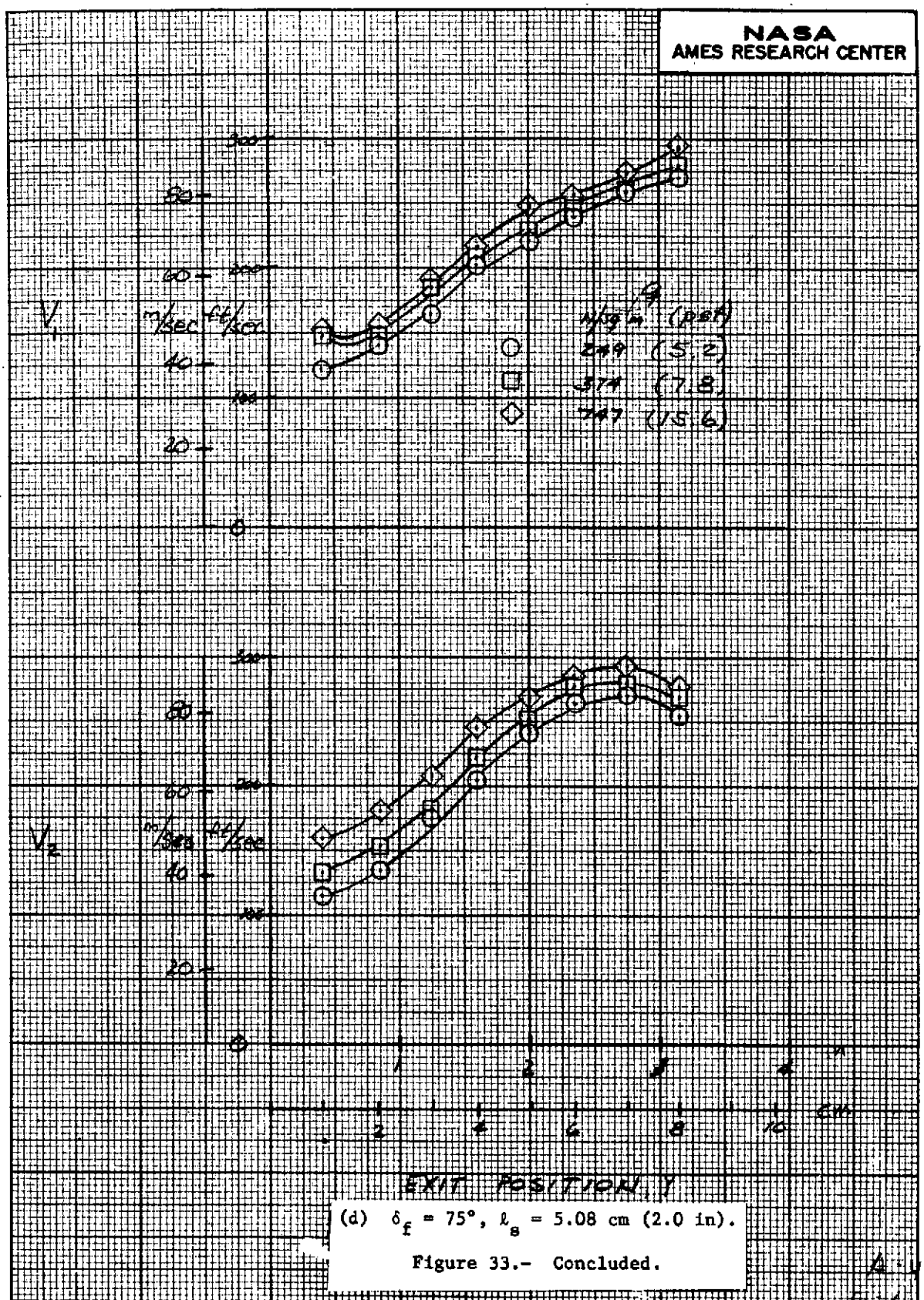

(d) $\delta_f = 75°$, $\ell_s = 5.08$ cm (2.0 in).

Figure 33.- Concluded.

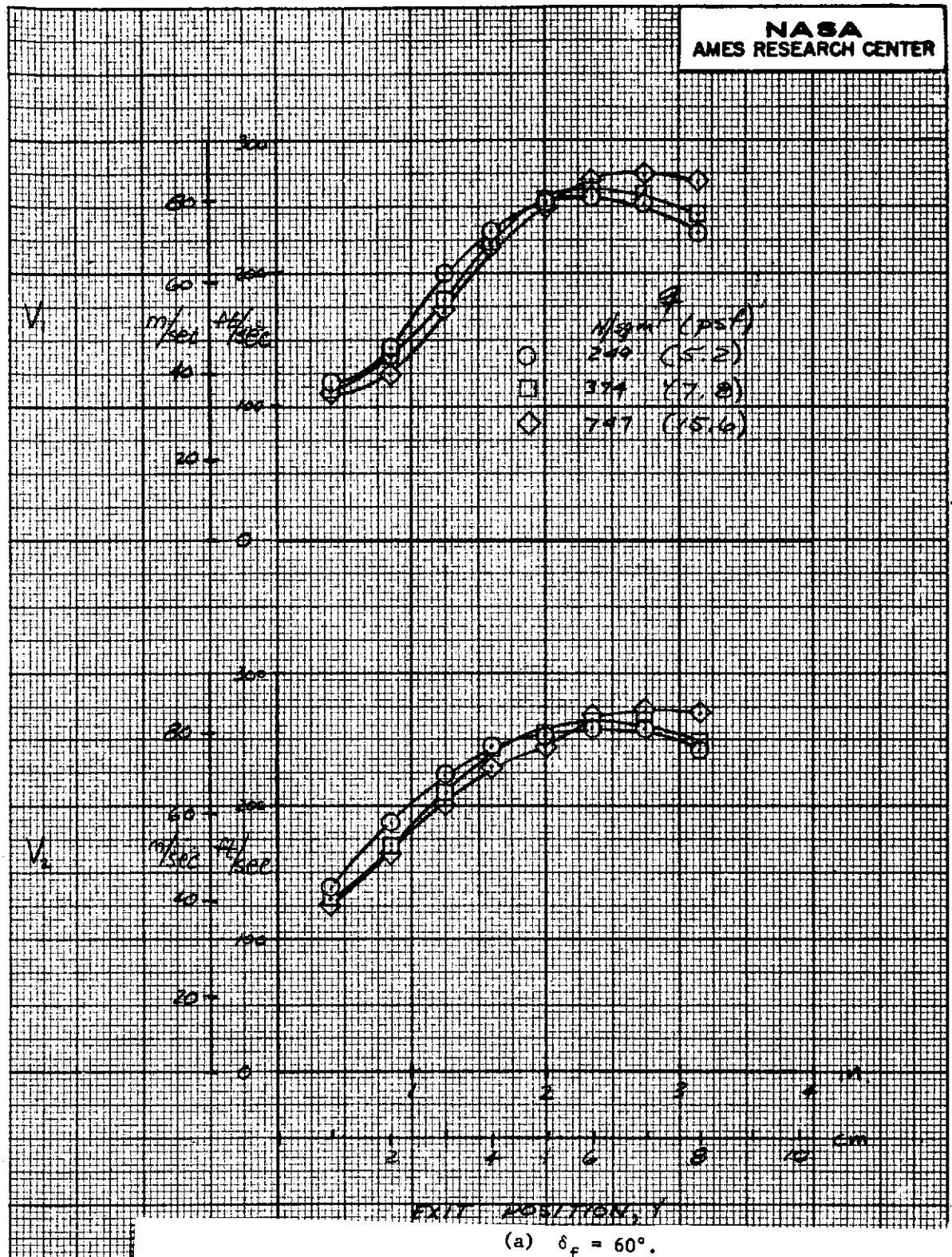

(a) $\delta_f = 60°$.

Figure 34.- The effect of q on the exit velocity profiles for nozzle 3b; $\alpha = 0°$, $A_e/A_n = 25$, $A_e/A_t = 1.25$, $Z_f = .97$ cm (.38 in), $\ell_f = 5.08$ cm (2.0 in), PR = 1.53, $\ell_s = 5.08$ cm (2.0 in).

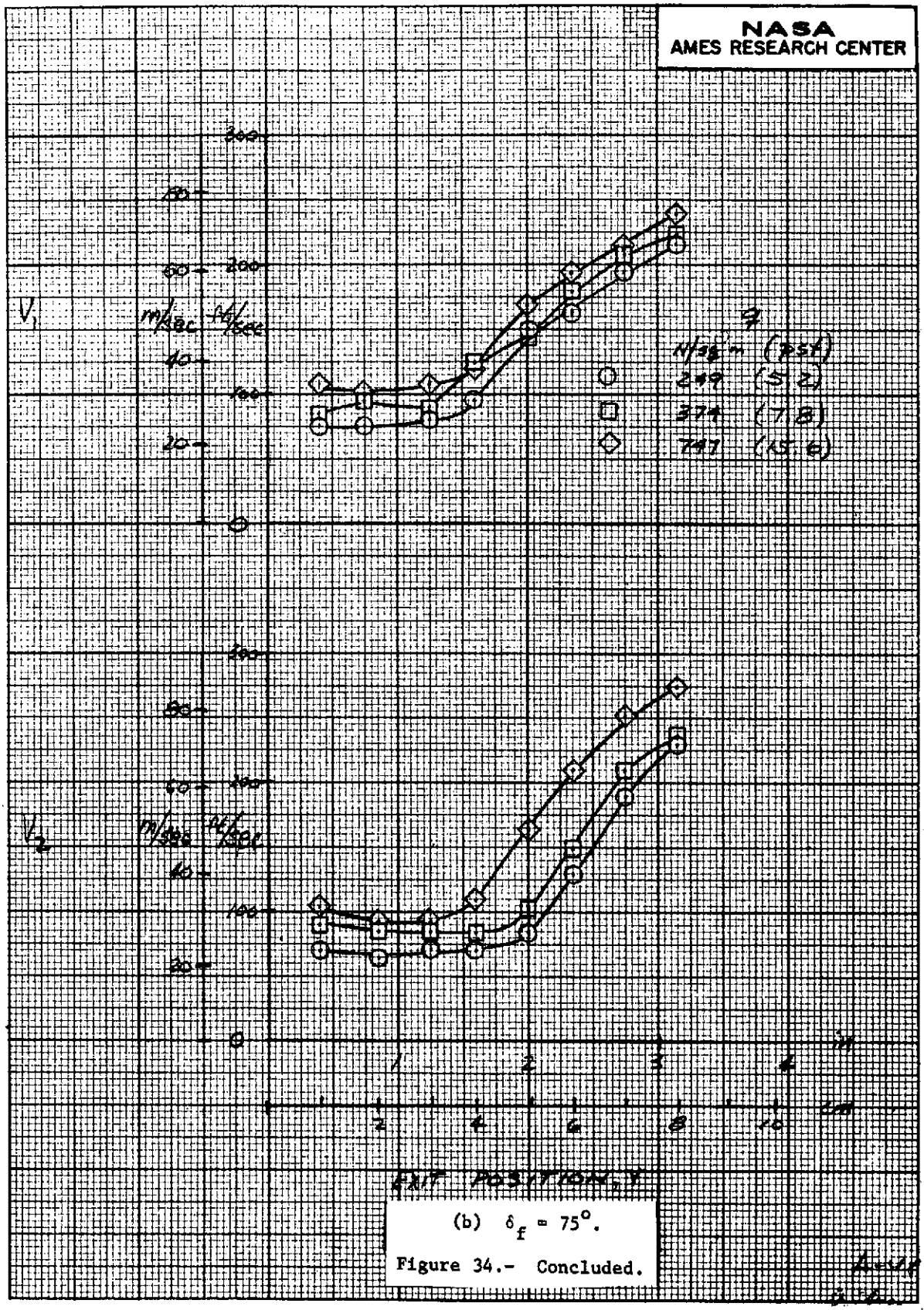

(b) $\delta_f = 75^\circ$.

Figure 34.- Concluded.

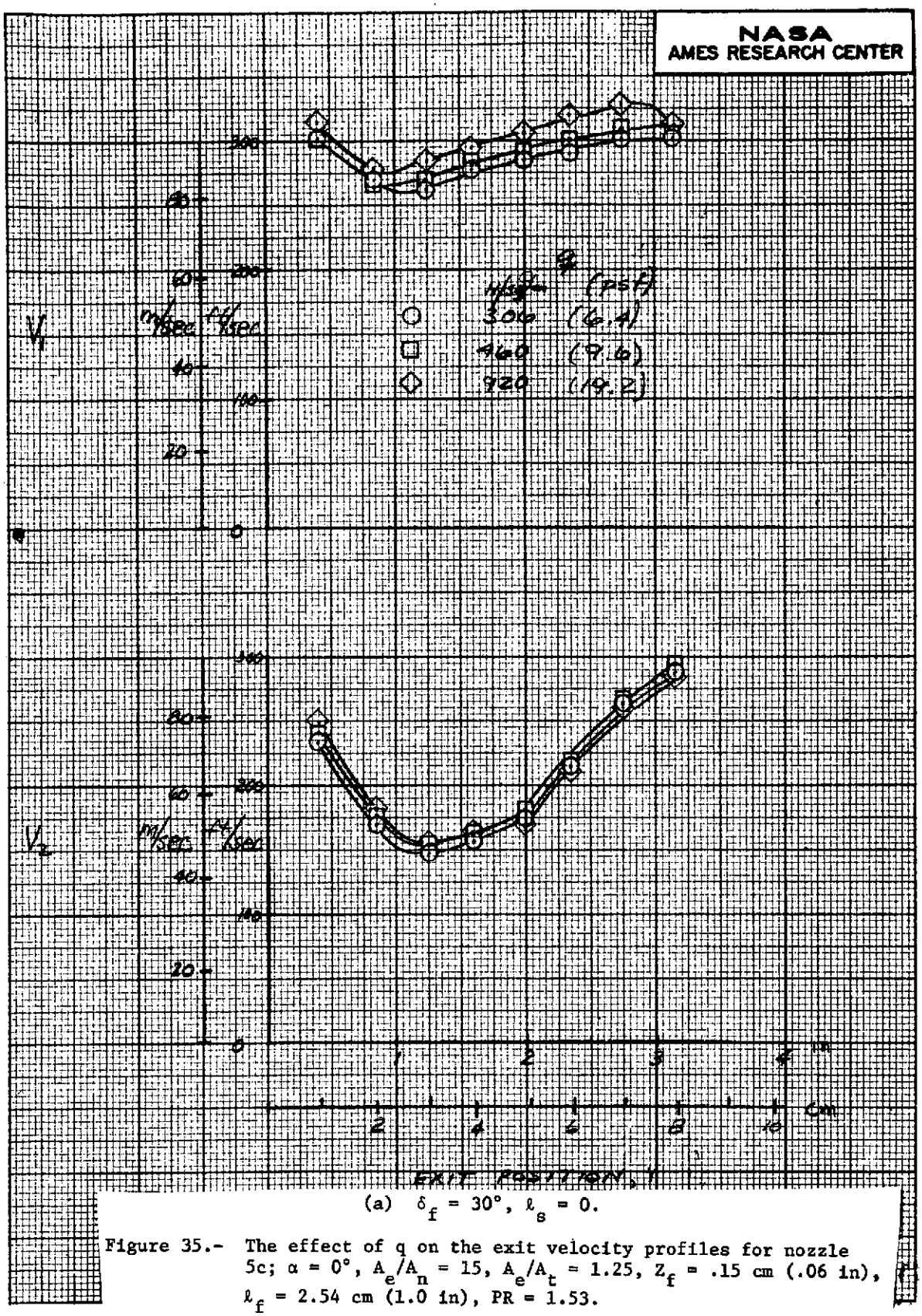

(a) $\delta_f = 30°$, $\ell_s = 0$.

Figure 35.- The effect of q on the exit velocity profiles for nozzle 5c; $\alpha = 0°$, $A_e/A_n = 15$, $A_e/A_t = 1.25$, $Z_f = .15$ cm (.06 in), $\ell_f = 2.54$ cm (1.0 in), PR = 1.53.

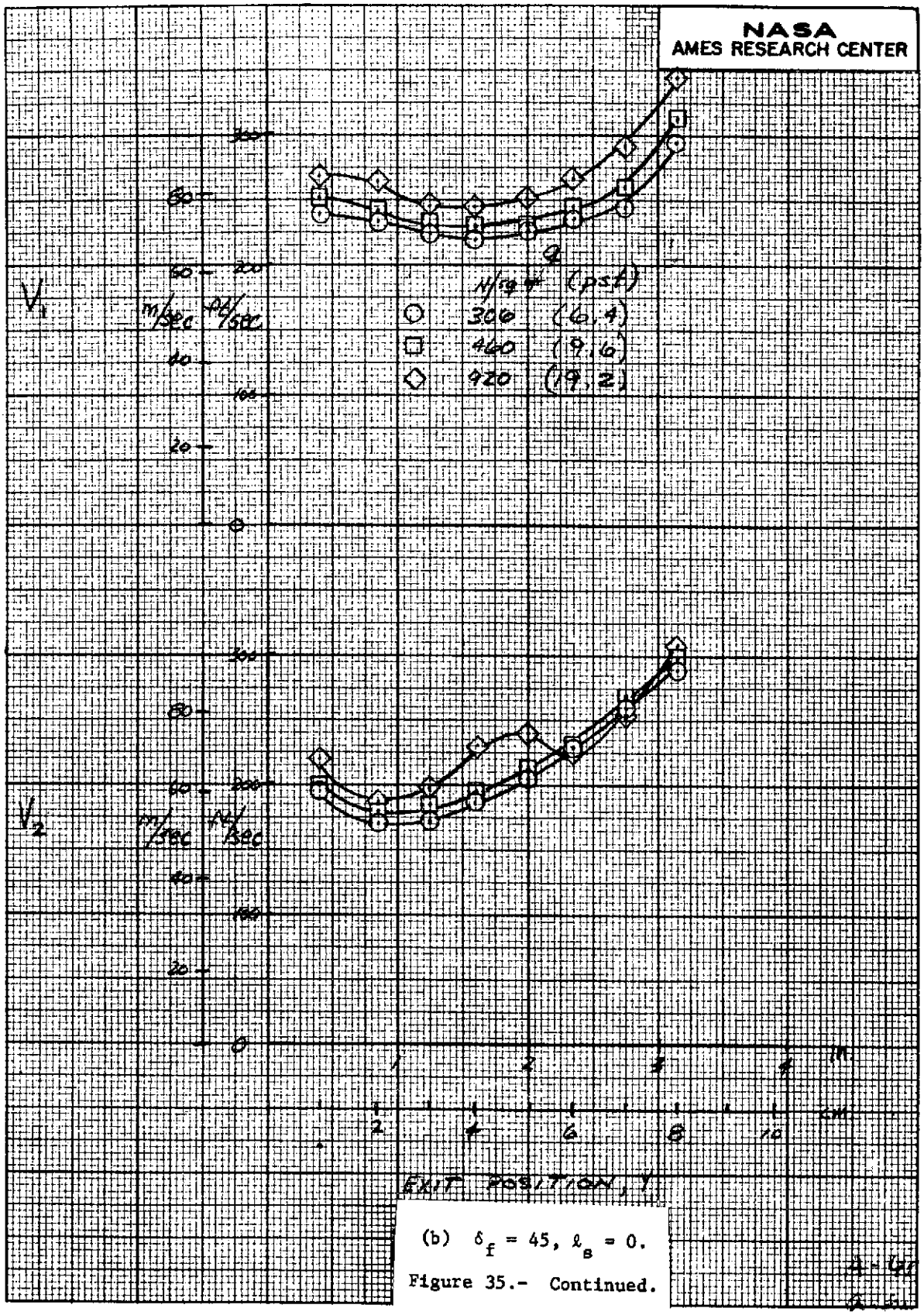

(b) $\delta_f = 45$, $\ell_s = 0$.

Figure 35.- Continued.

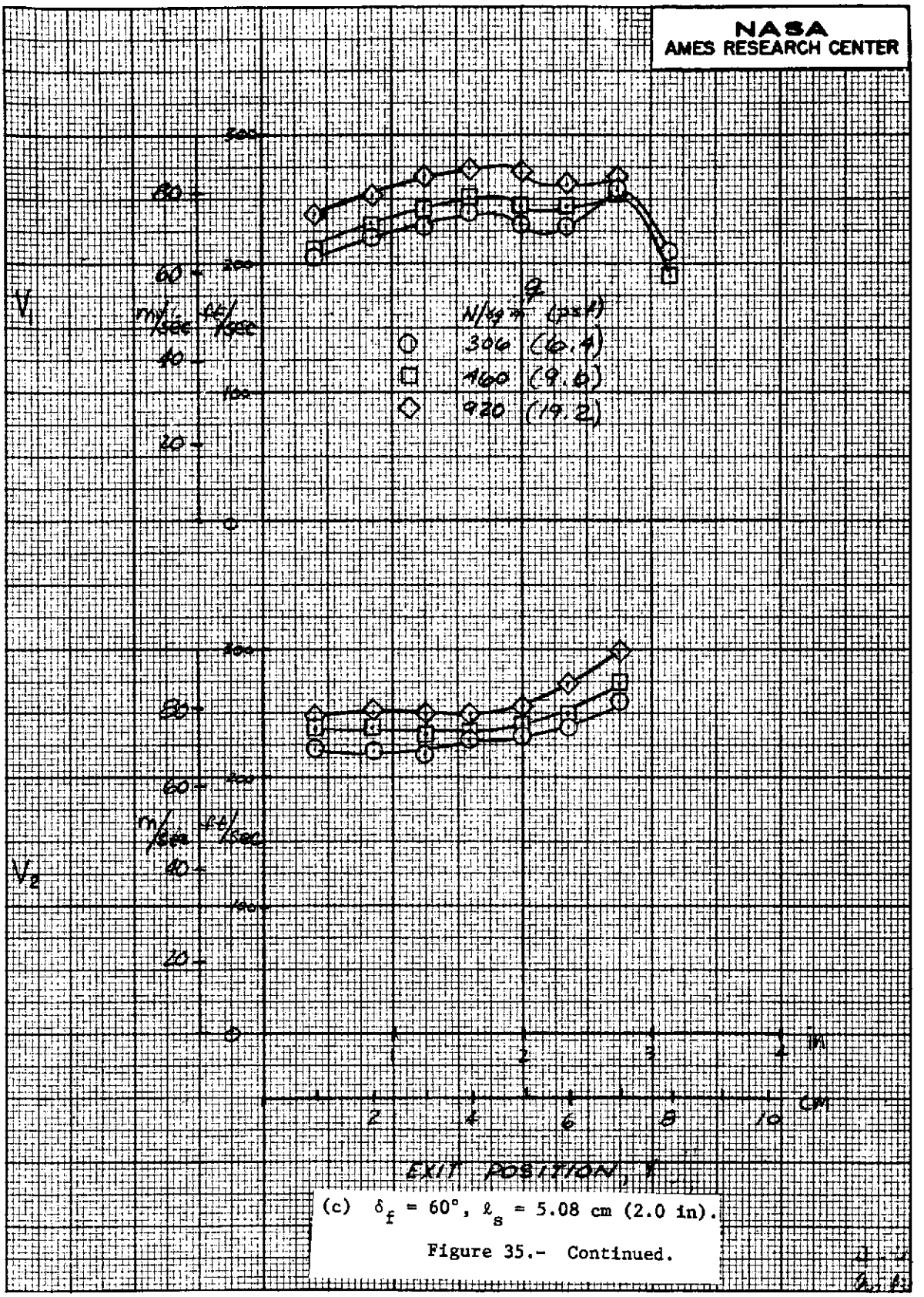

(c) $\delta_f = 60°$, $\ell_s = 5.08$ cm (2.0 in).

Figure 35.- Continued.

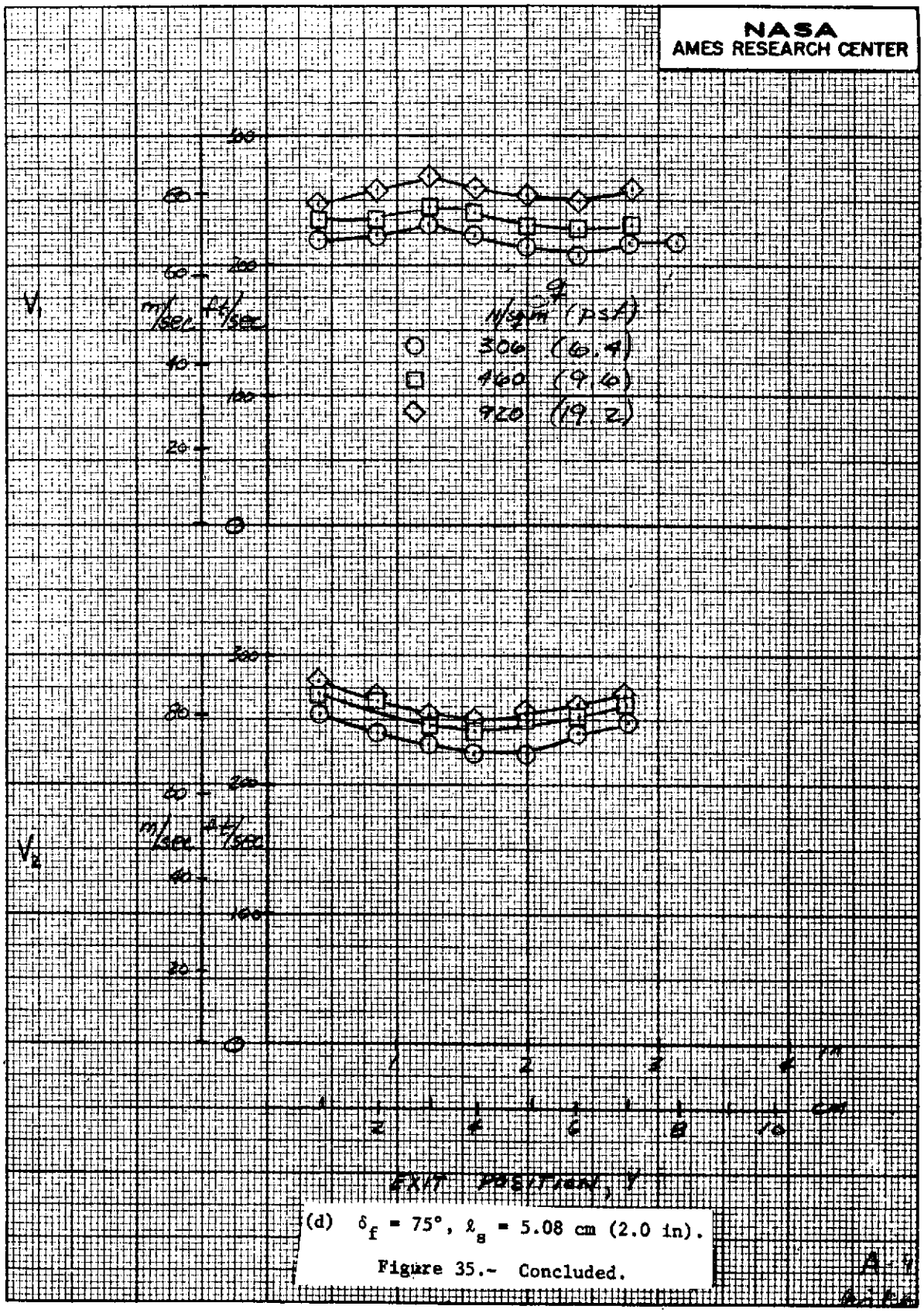

(d) $\delta_f = 75°$, $\ell_s = 5.08$ cm (2.0 in).

Figure 35.- Concluded.

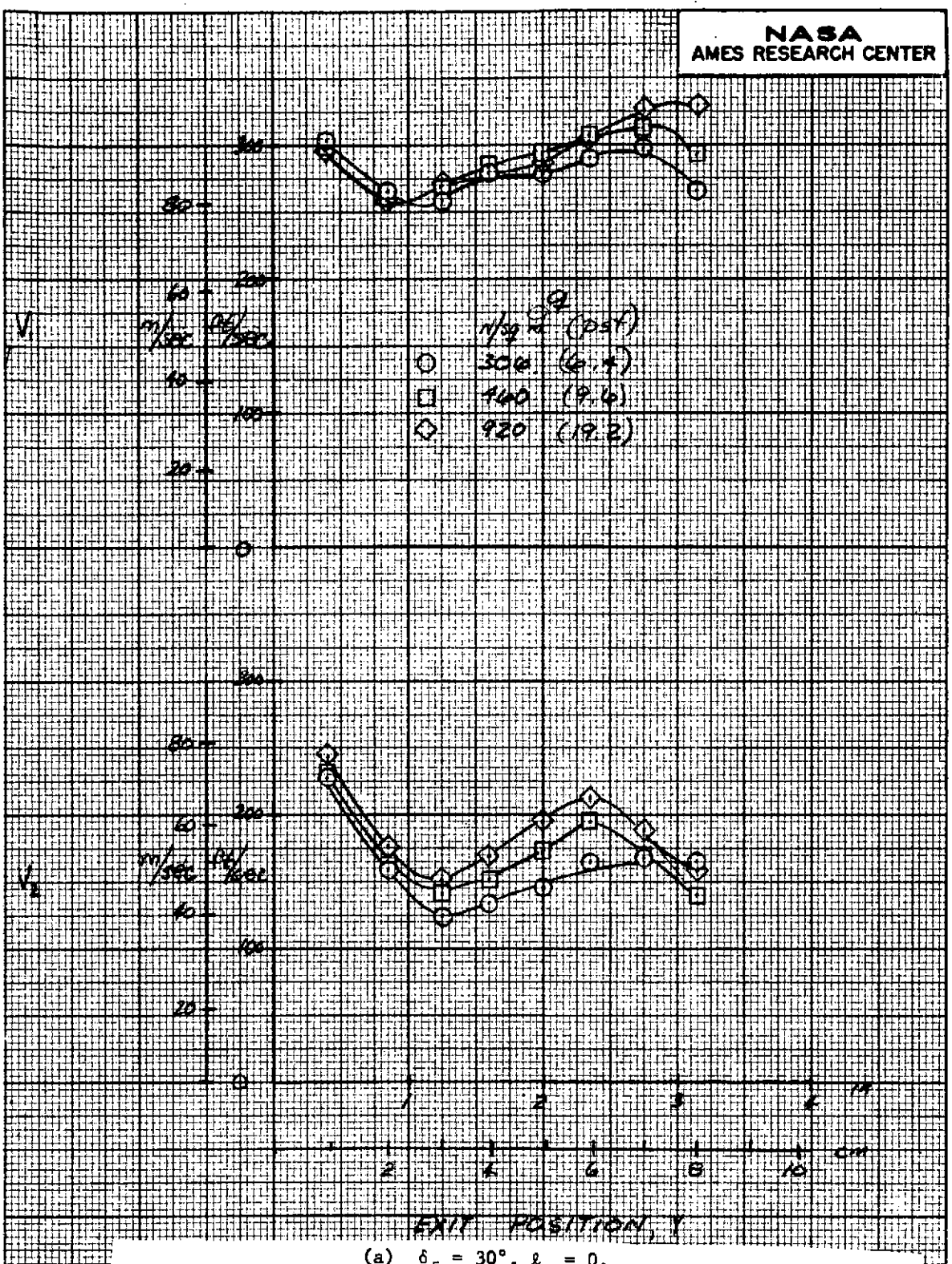

(a) $\delta_f = 30°$, $\ell_s = 0.$

Figure 36.- The effect of q on the exit velocity profiles for nozzle 5c; $\alpha = 0°$, $A_e/A_n = 20$, $A_e/A_t = 1.25$, $Z_f = .79$ cm (.31 in), $\ell_f = 5.08$ cm (2.0 in), PR = 1.53.

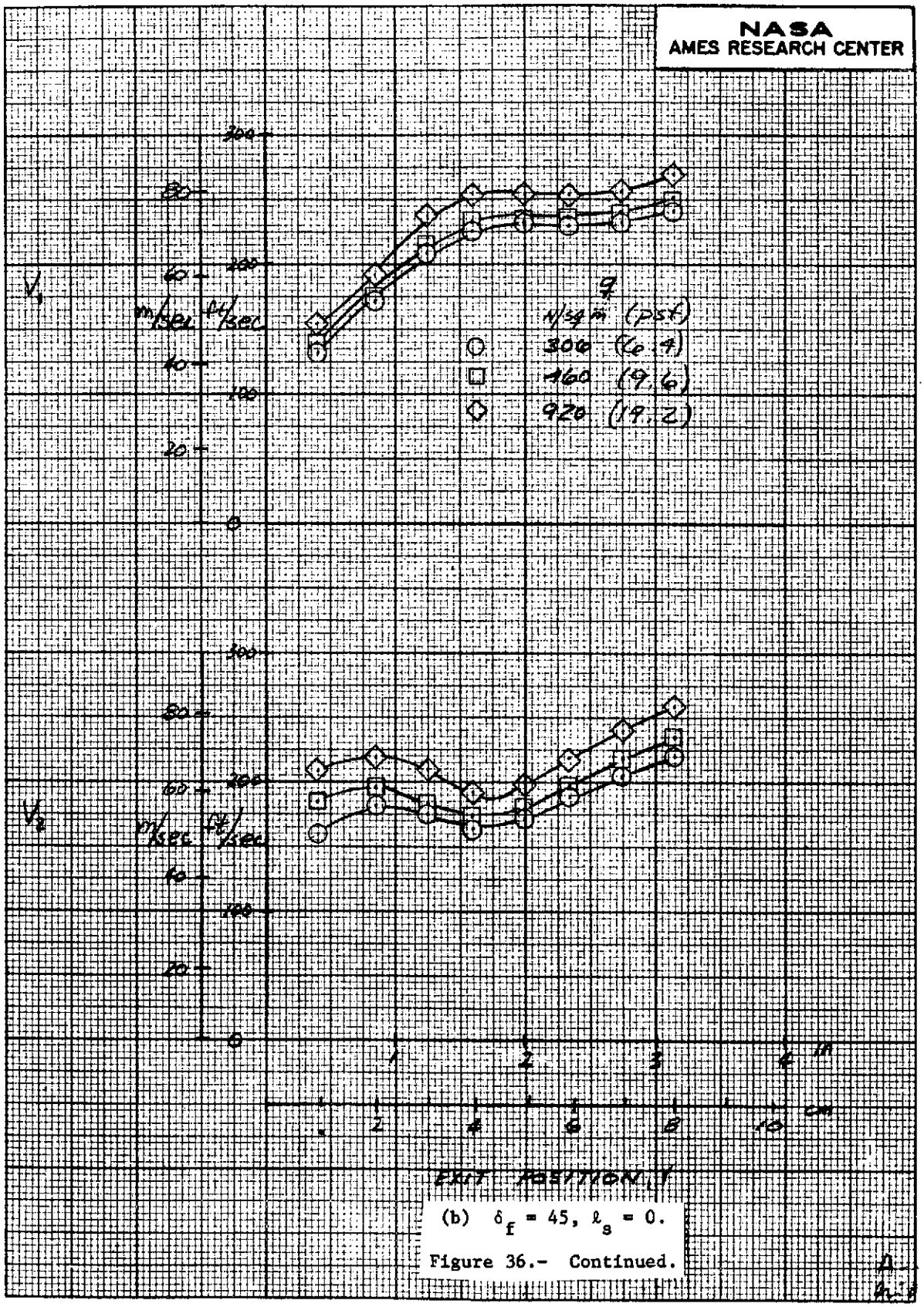

(b) $\delta_f = 45$, $\ell_s = 0$.

Figure 36.- Continued.

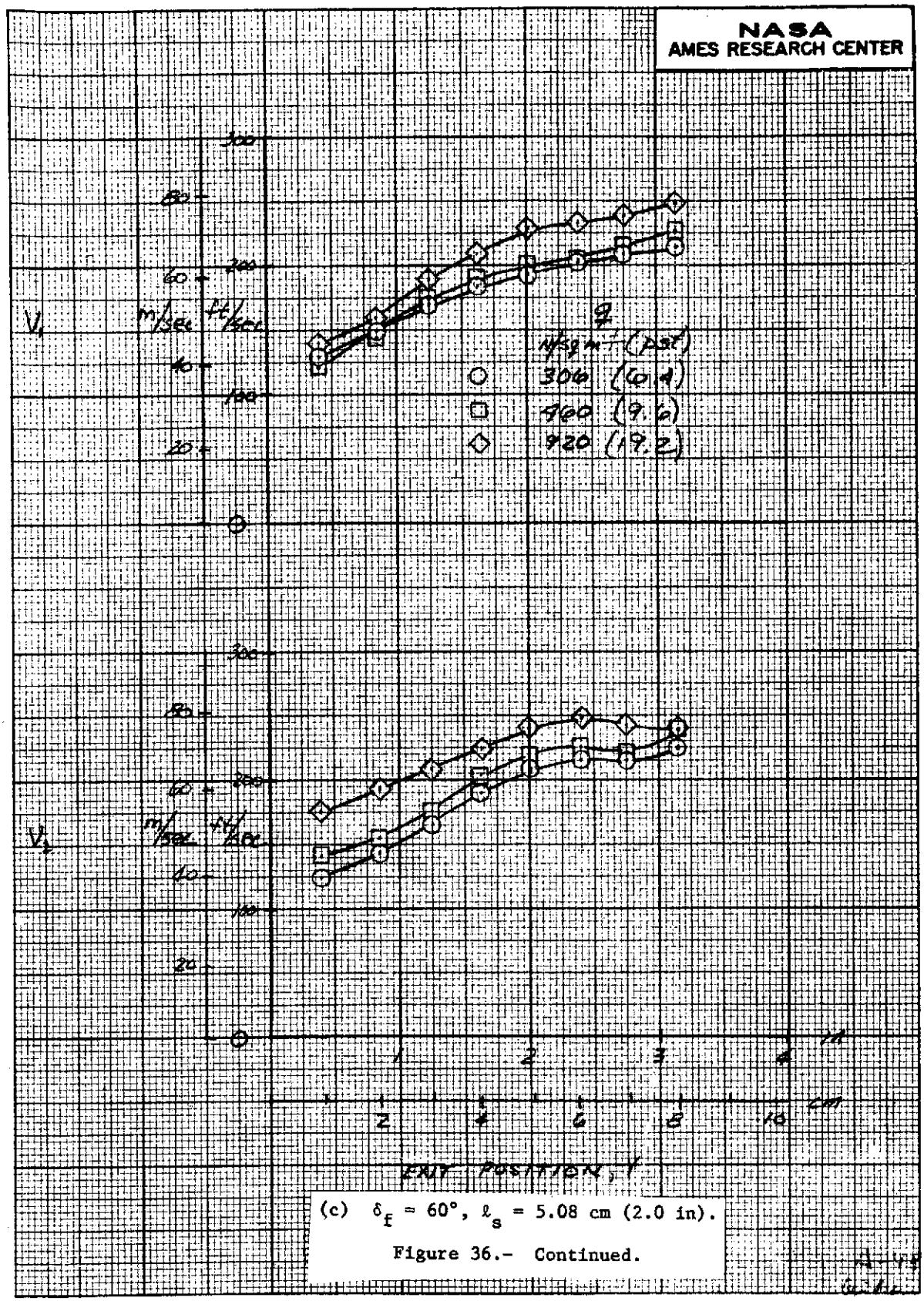

(c) $\delta_f = 60°$, $\ell_s = 5.08$ cm (2.0 in).

Figure 36.- Continued.

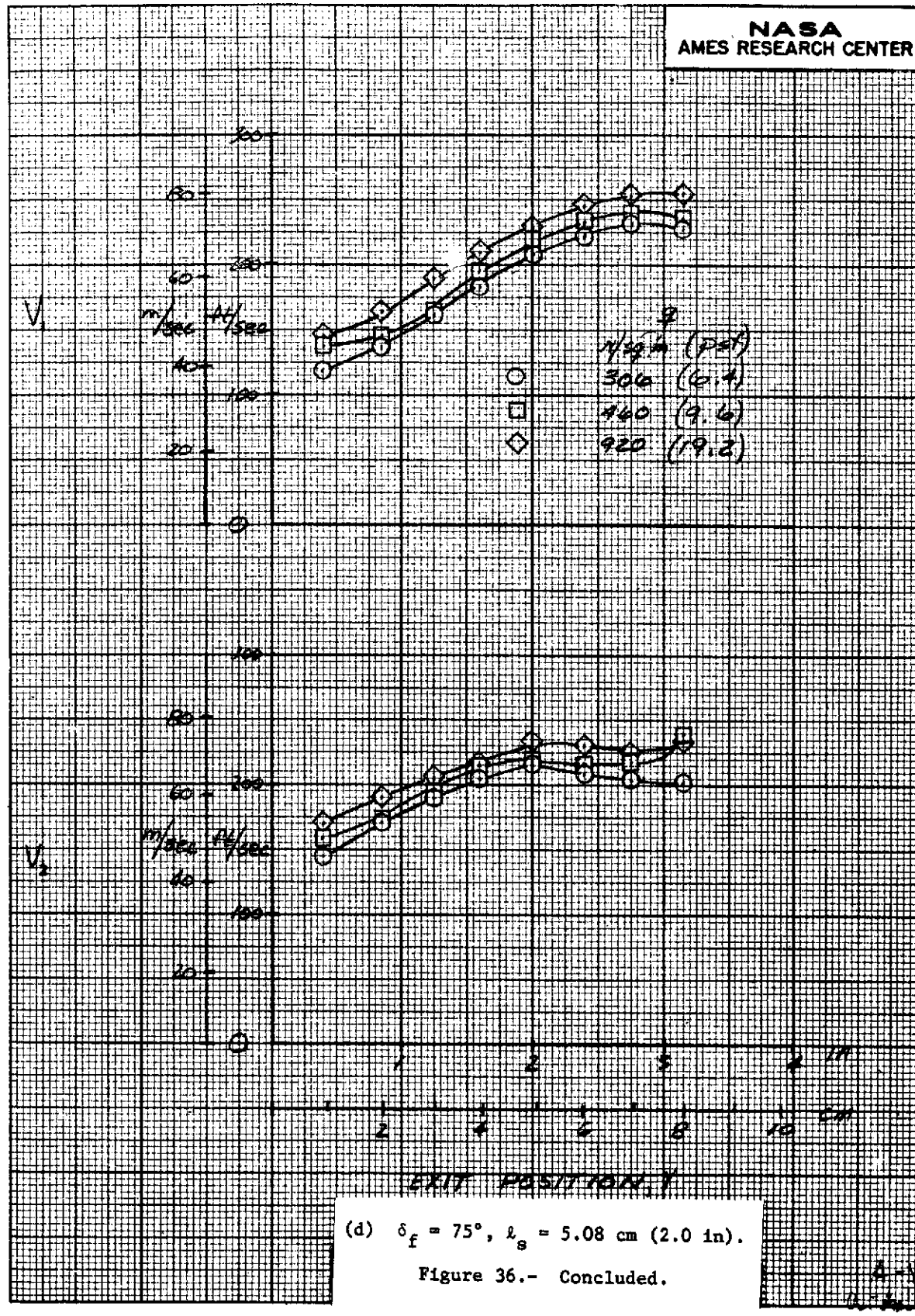

(d) $\delta_f = 75°$, $\ell_s = 5.08$ cm (2.0 in).

Figure 36.- Concluded.

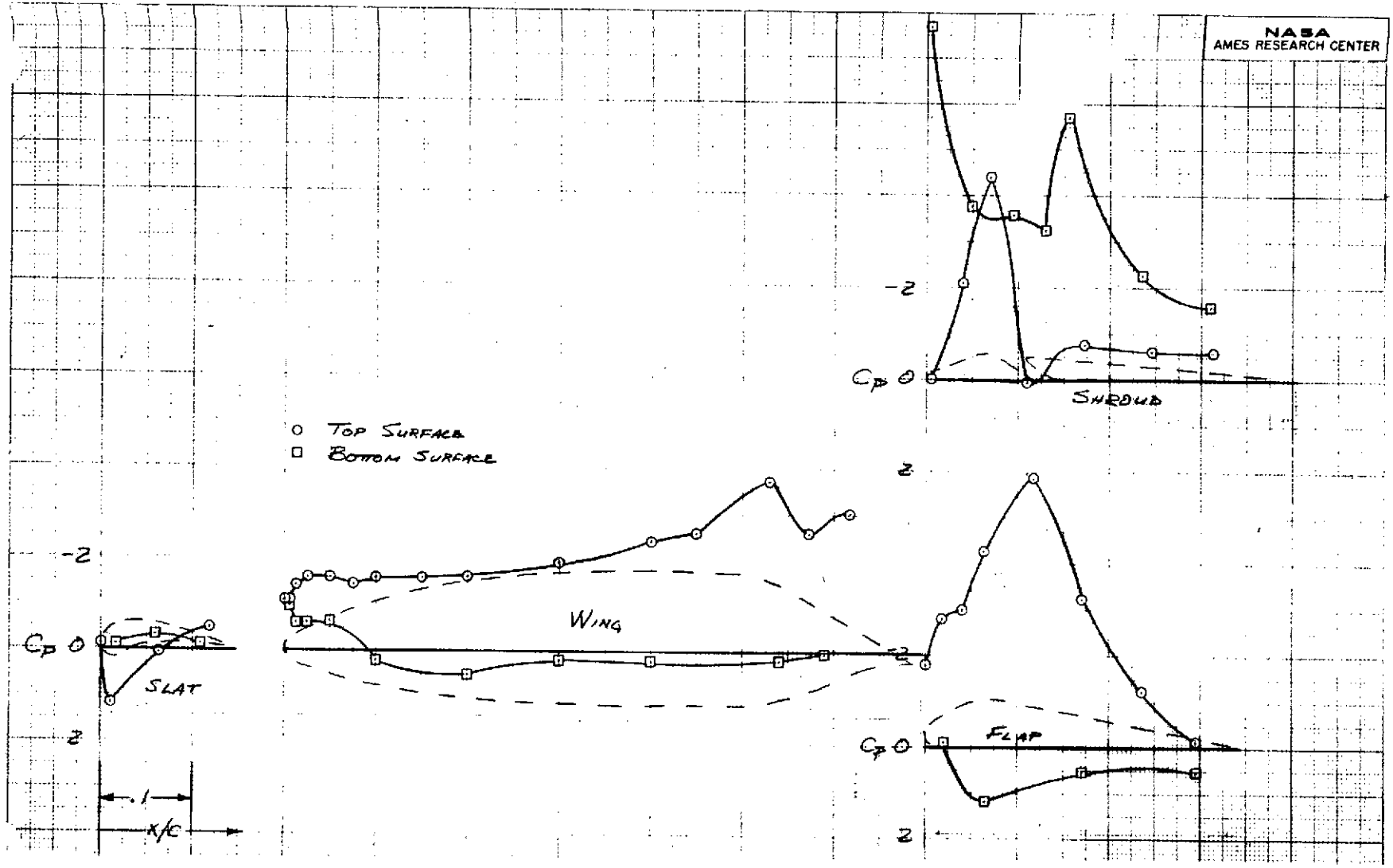

(a) Nozzle 1, $\alpha = 0°$, $A_e/A_n = 15$, $Z_f = 1.27$ cm (.5 in), $\ell_f = 5.08$ cm (2.0 in).

Figure 37.- Surface pressure distributions of various configurations at $\delta_f = 30°$, $C_{J_n} = 1.5$, $A_e/A_t = 1.25$, PR = 1.53, $\ell_s = 0$.

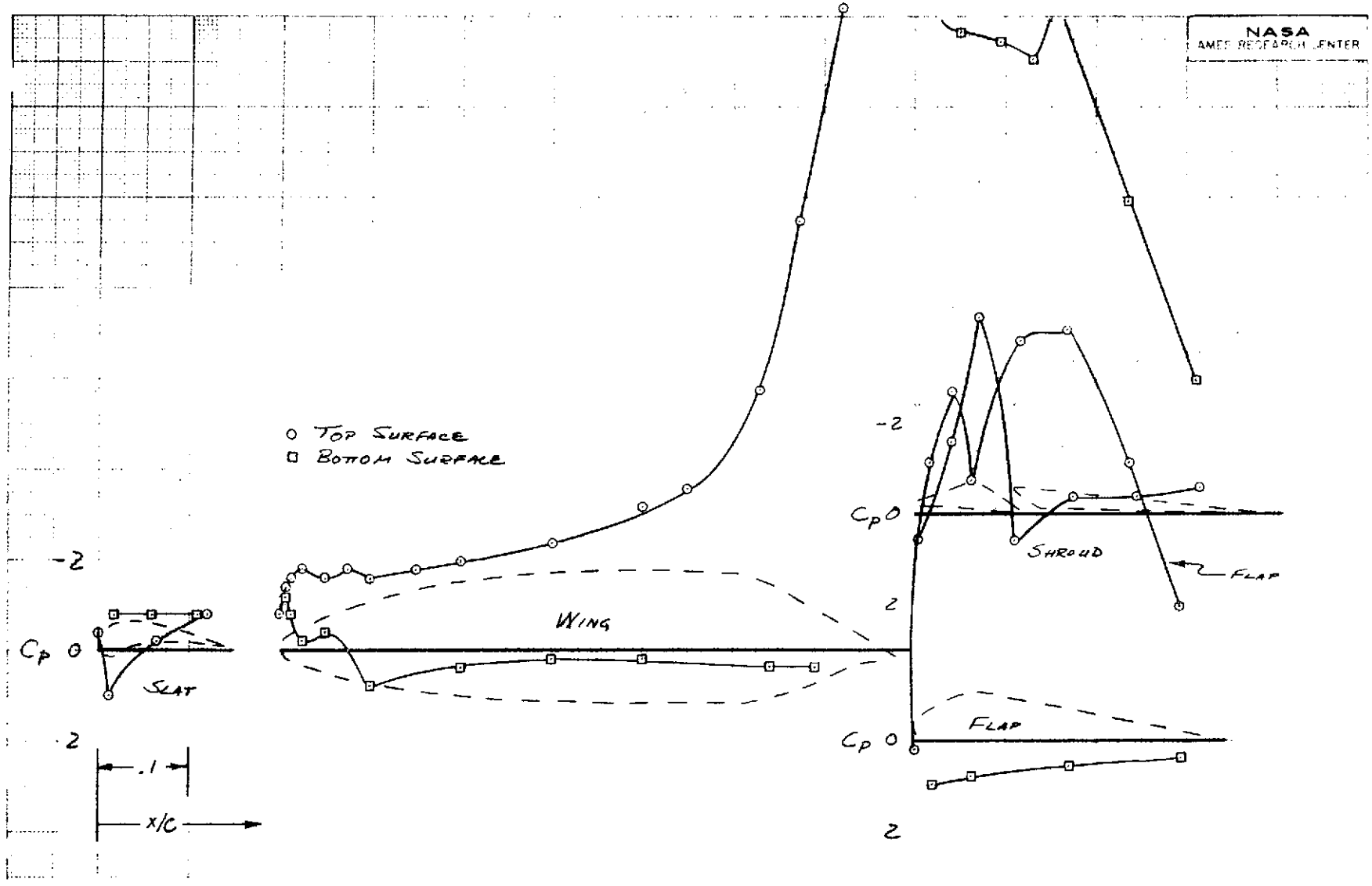

(b) Nozzle 3b, $\alpha = 0°$, $A_e/A_n = 15$, $Z_f = .15$ cm (.06 in), $\ell_f = 2.54$ cm (1.0 in).

Figure 37.- Continued.

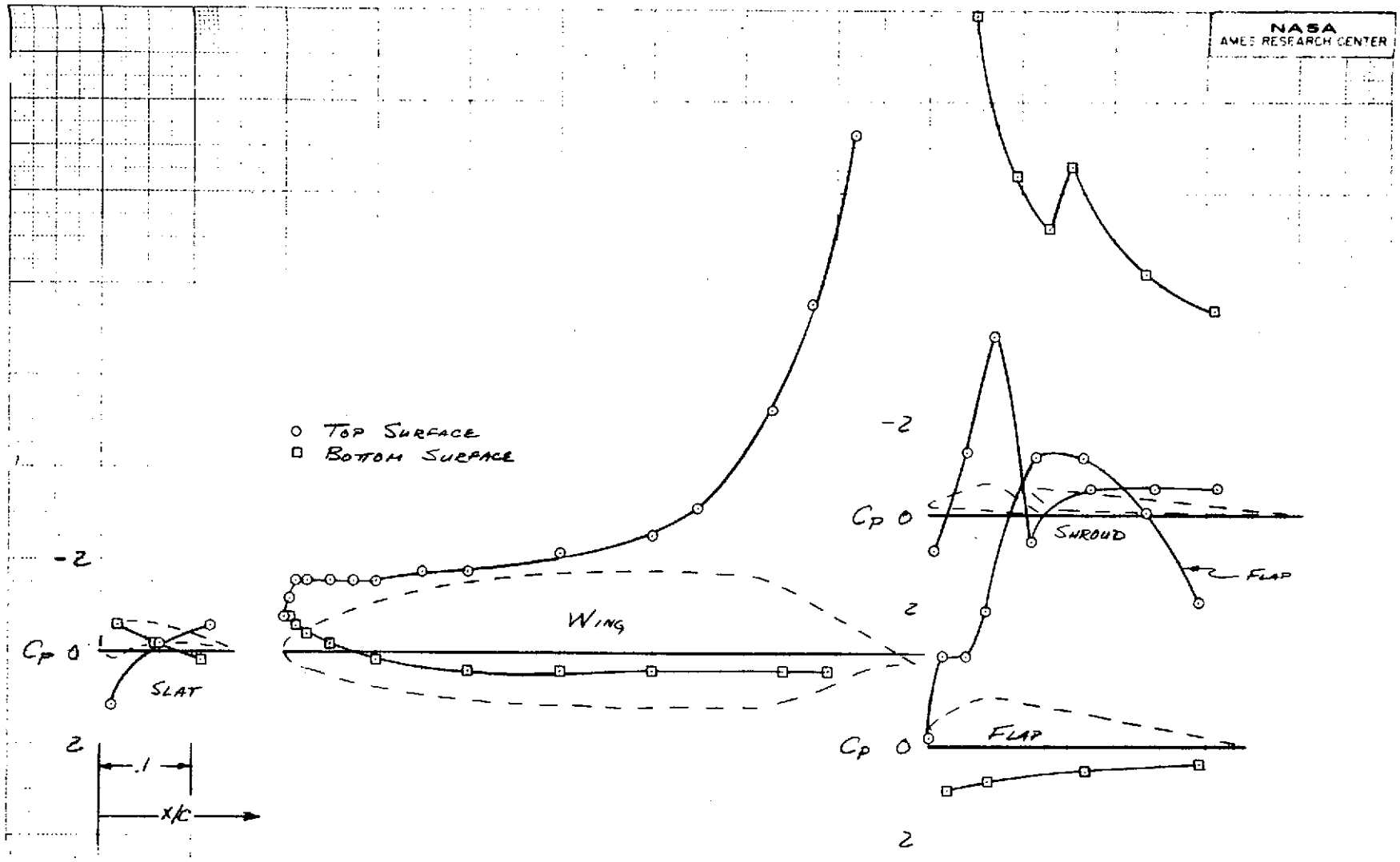

(c) Nozzle 3b, $\alpha = 0°$, $A_e/A_n = 20$, $Z_f = .15$ cm (.06 in), $\ell_f = 2.54$ cm (1.0 in).

Figure 37.- Continued.

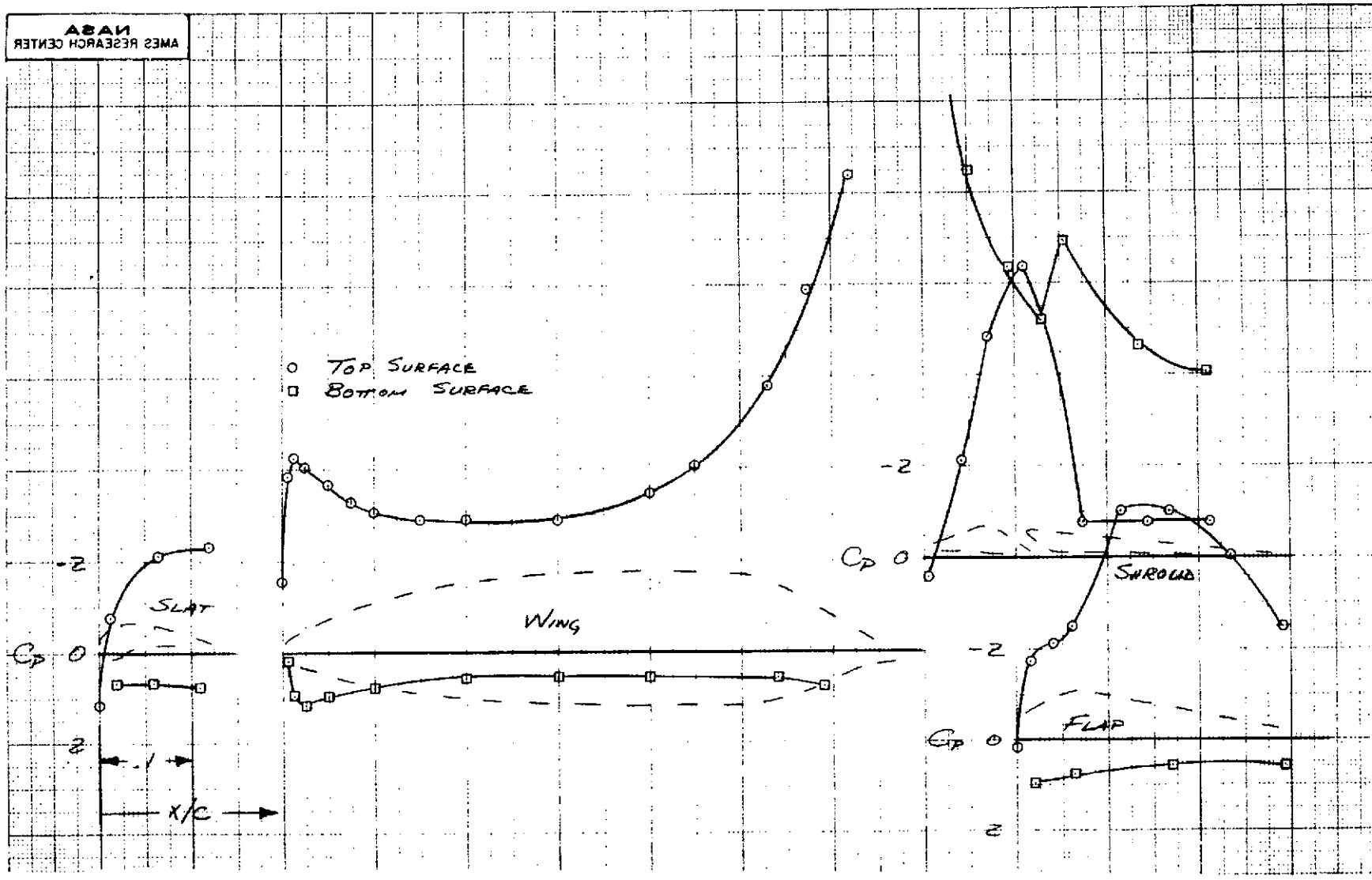

(d) Nozzle 3b, $\alpha = 12°$, $A_e/A_n = 20$, $Z_f = .15$ cm (.06 in), $\ell_f = 2.54$ cm (1.0 in).

Figure 37.- Continued.

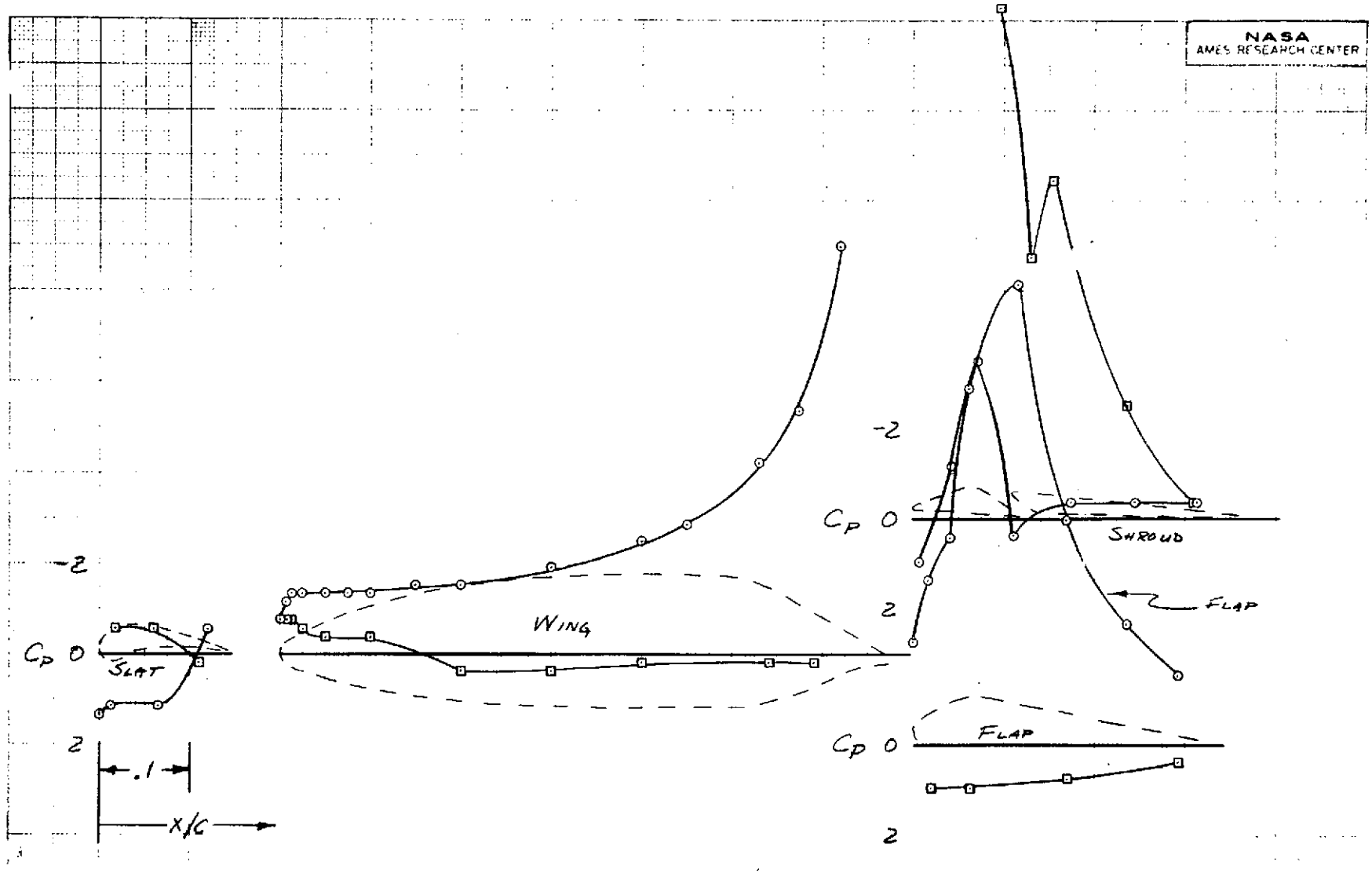

(e) Nozzle 3b, $\alpha = 0°$, $A_e/A_n = 20$, $Z_f = .97$ cm (.38 in), $\ell_f = 5.08$ cm (2.0 in).

Figure 37.- Continued.

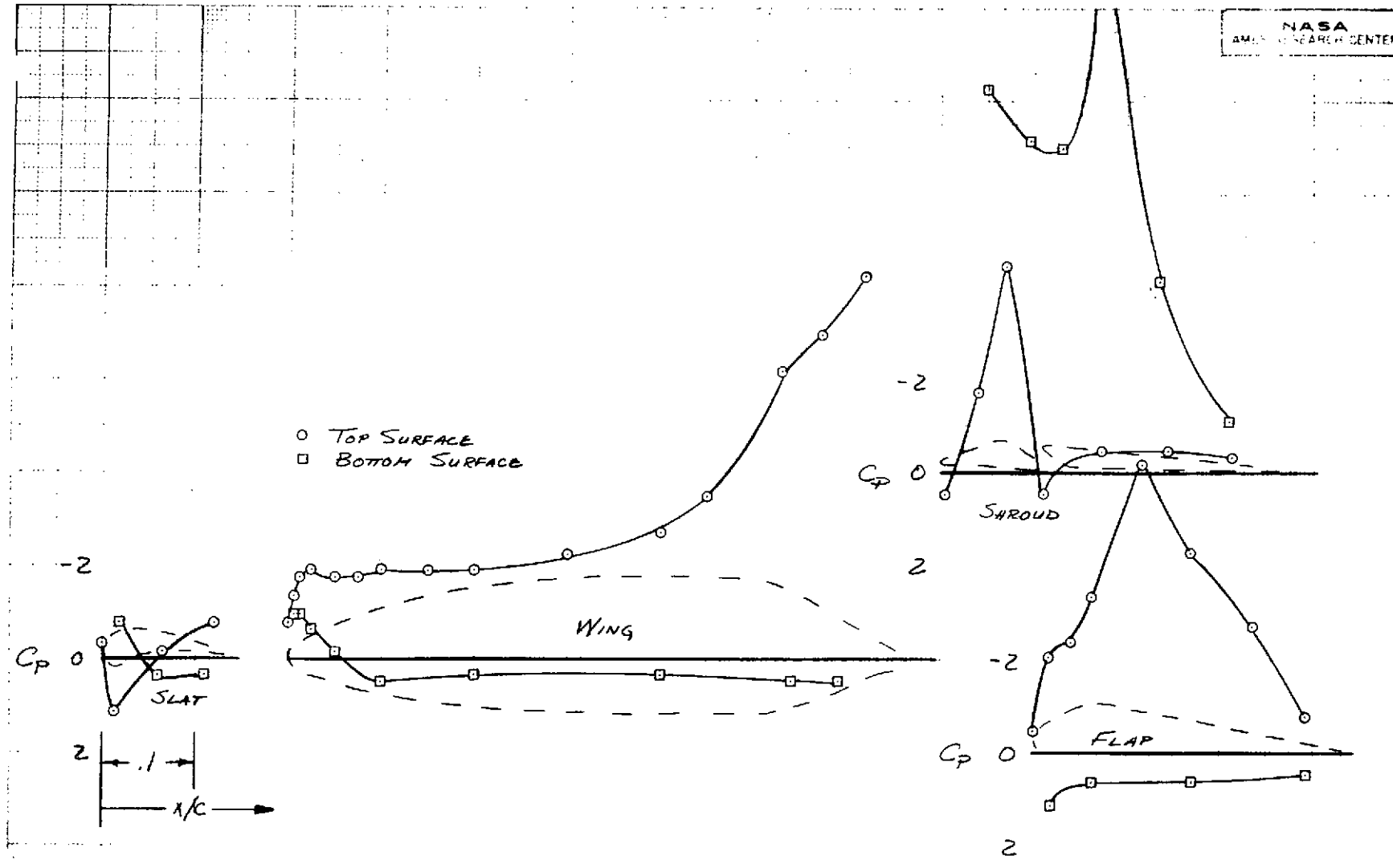

(f) Nozzle 5c, $\alpha = 0°$, $A_e/A_n = 15$, $Z_f = .15$ cm (.06 in), $\ell_f = 2.54$ cm (1.0 in).

Figure 37.- Continued.

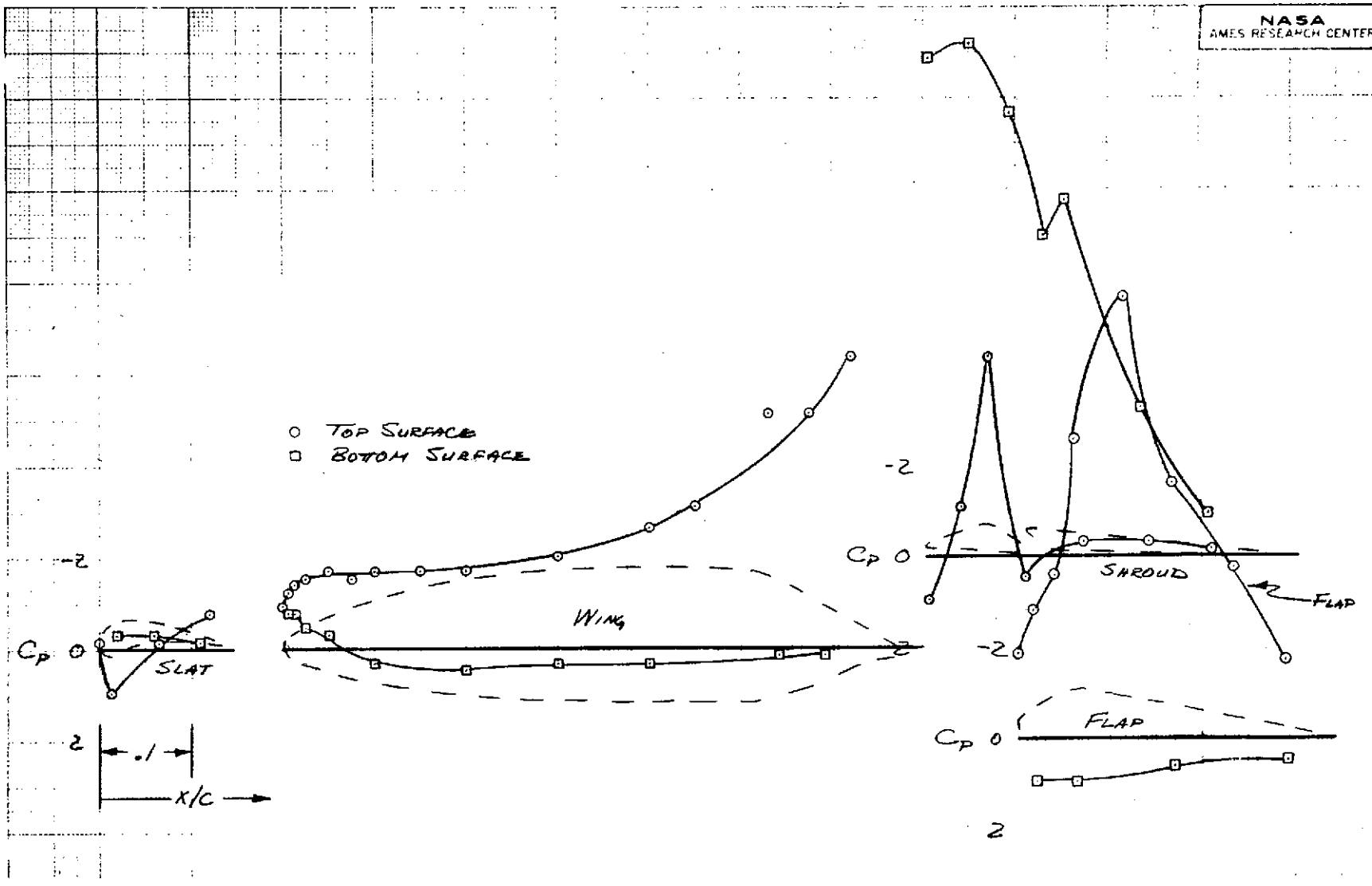

(g) Nozzle 5c, $\alpha = 0°$, $A_e/A_n = 20$, $Z_f = .79$ cm (.31 in), $\ell_f = 5.08$ cm (2.0 in).

Figure 37.- Concluded.

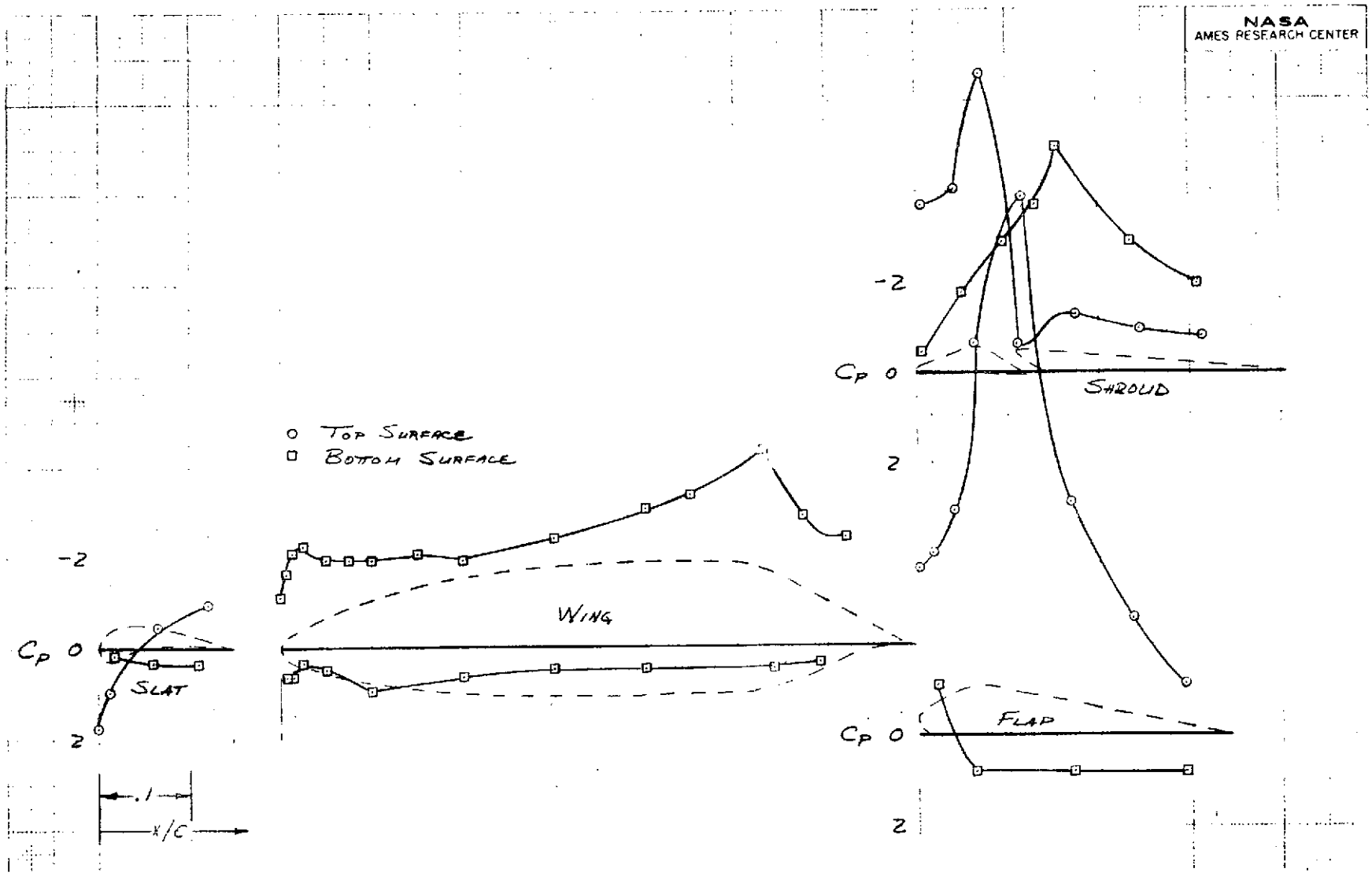

(a) Nozzle 1, A_e/A_n = 15, Z_f = 1.27 cm (.5 in), ℓ_f = 5.08 cm (2.0 in).

Figure 38.- Surface pressure distributions of various configurations at $\delta_f = 45°$; $\alpha = 0°$, $C_{J_n} = 1.5$, $A_e/A_t = 1.25$, $\ell_s = 0$, PR = 1.53.

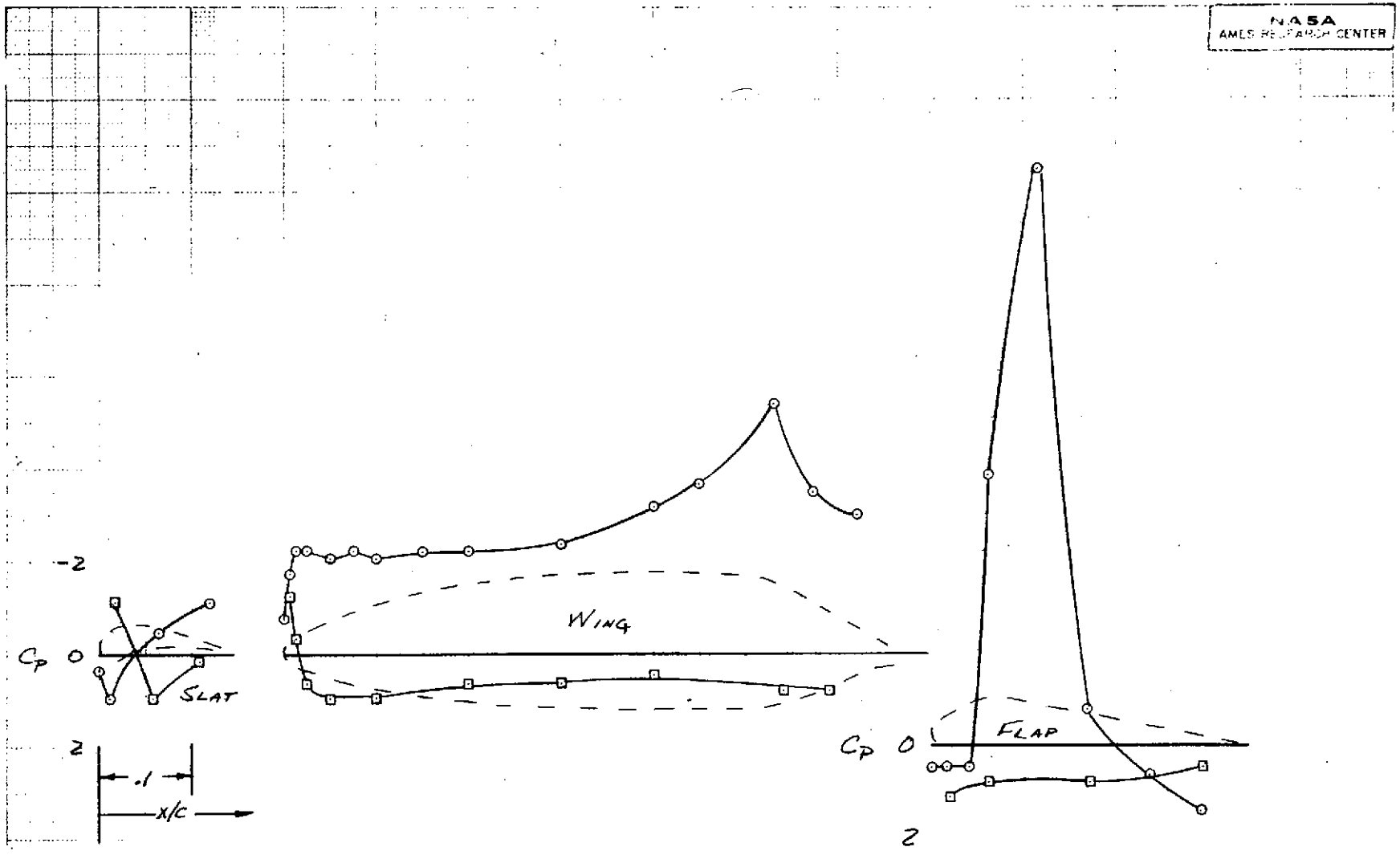

(b) Nozzle 1, shroud off, $Z_f = 0$, $\ell_f = 5.08$ cm (2.0 in).

Figure 38.- Continued.

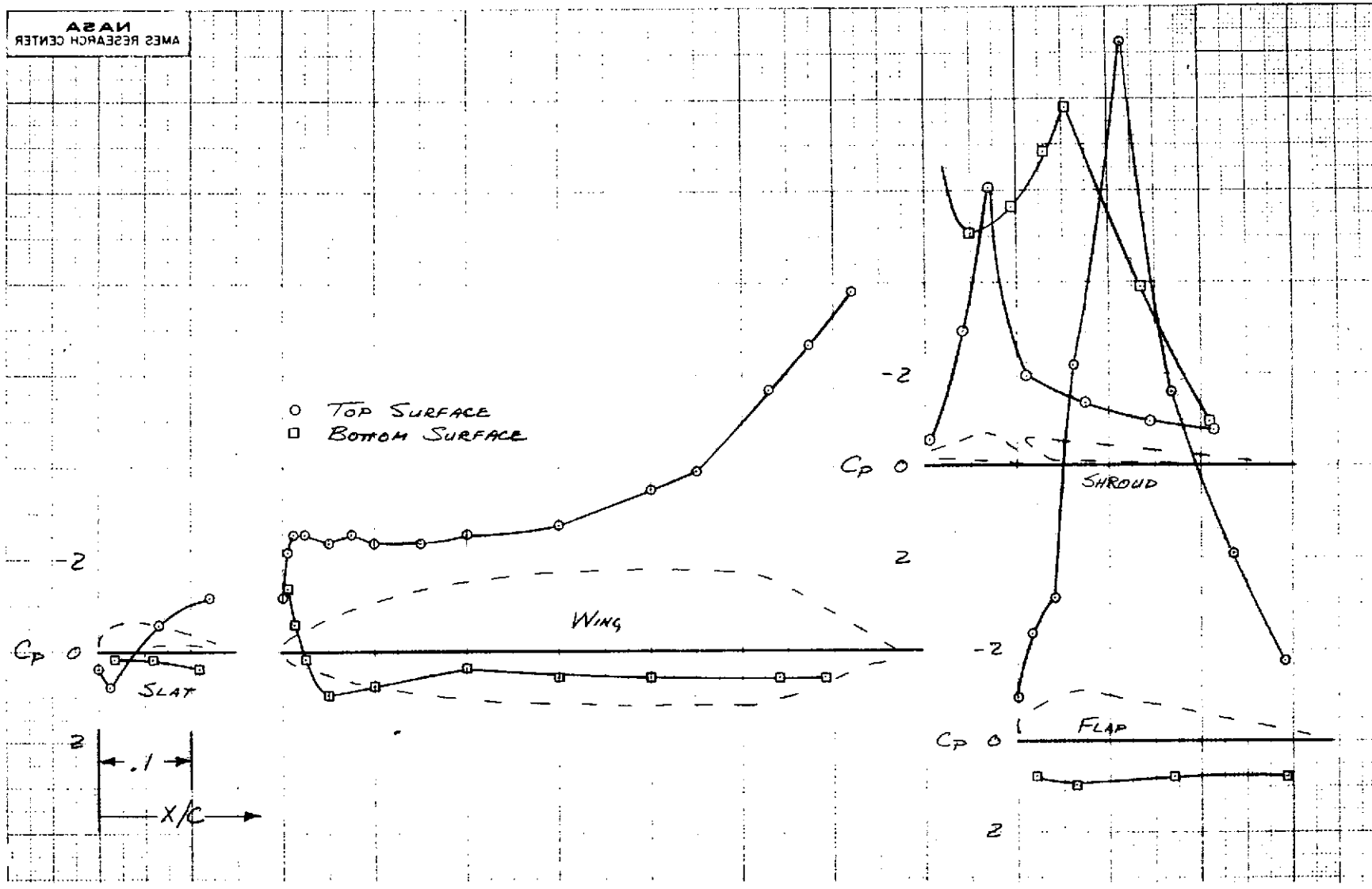

(c) Nozzle 3b, A_e/A_n = 15, Z_f = .15 cm (.06 in), ℓ_f = 2.54 cm (1.0 in).

Figure 38.- Continued.

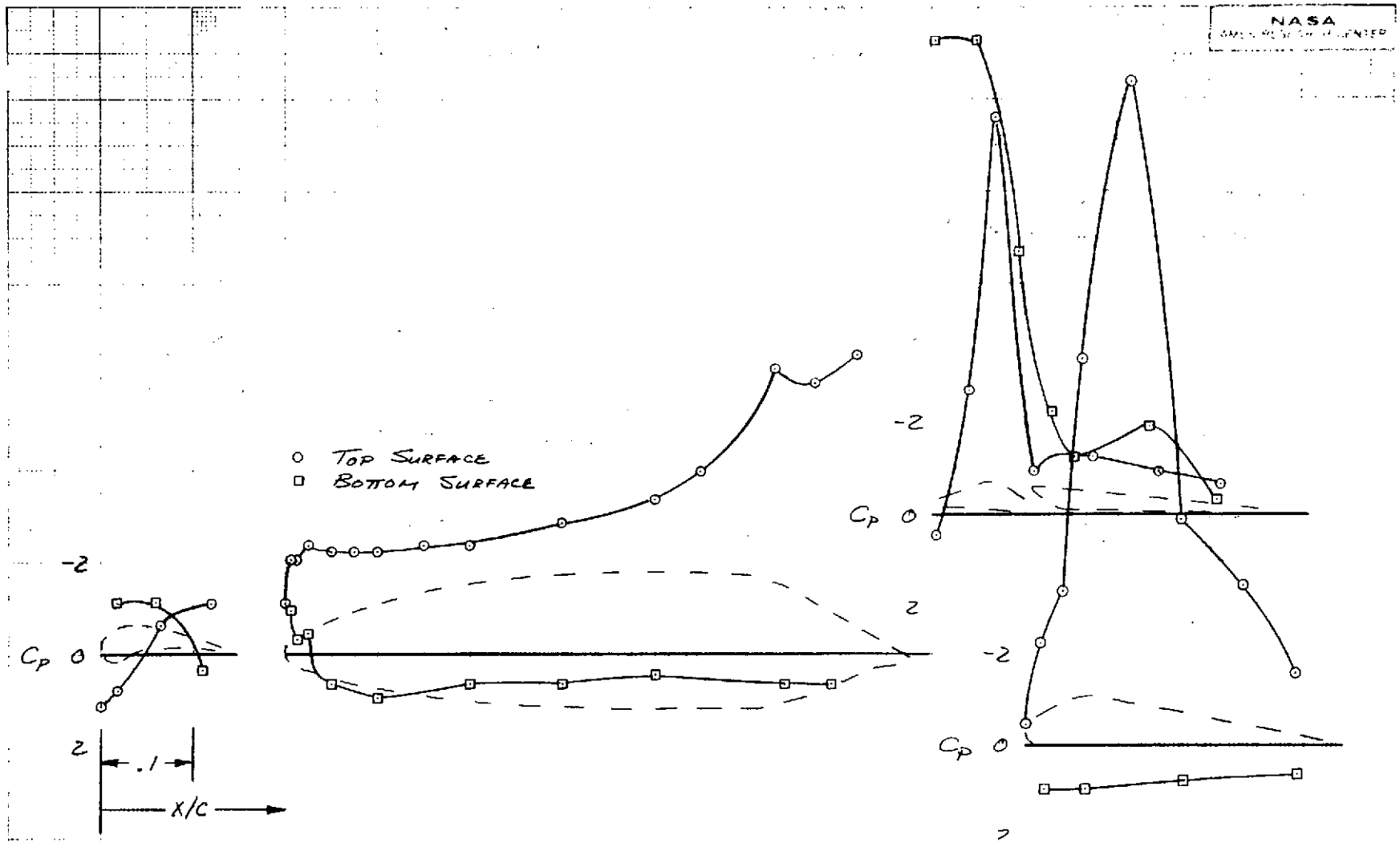

(d) Nozzle 5c, A_e/A_n = 15, Z_f = .15 cm (.06 in), ℓ_f = 2.54 cm (1.0 in).

Figure 38.- Continued.

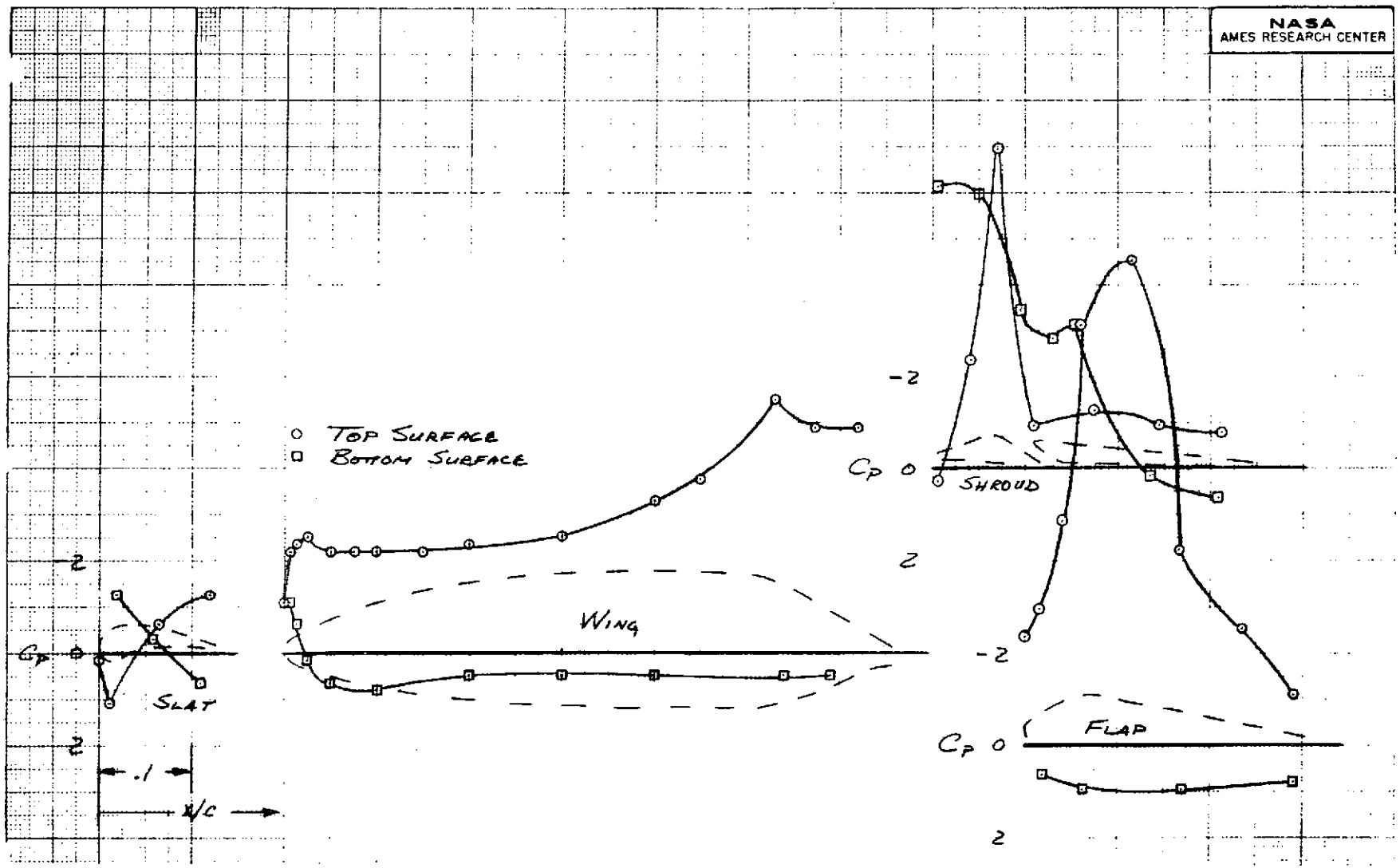

(e) Nozzle 5c, A_e/A_n = 20, Z_f = .79 cm (.31 in), ℓ_f = 5.08 cm (2.0 in).

Figure 38.- Concluded.

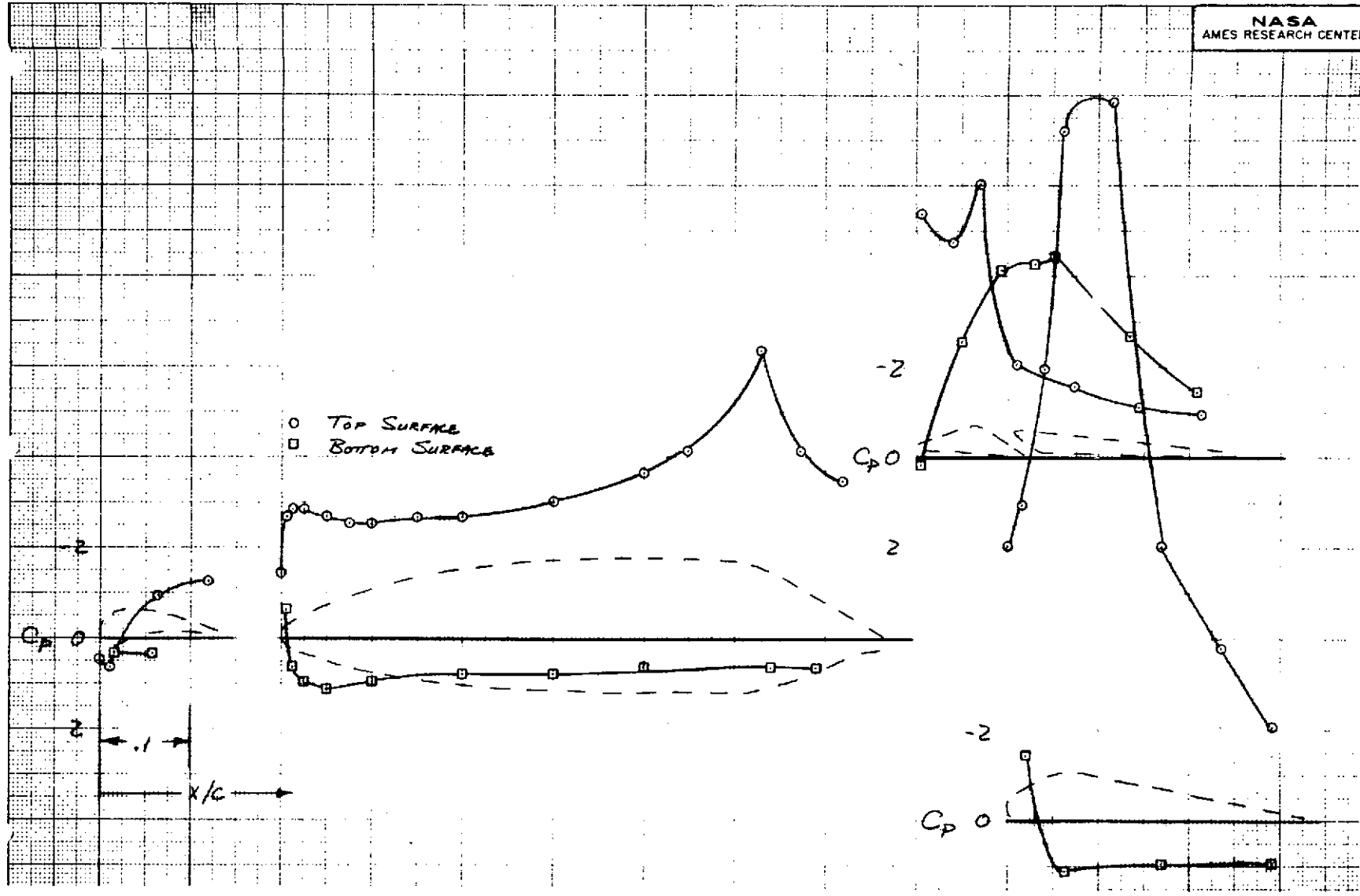

(a) Nozzle 1, A_e/A_n = 15, Z_f = 1.27 cm (.5 in), ℓ_f = 5.08 cm (2.0 in).

Figure 39.- Surface pressure distributions of various configurations at δ_f = 60°; α = 0°, C_{J_n} = 1.5, A_e/A_t = 1.25, ℓ_s = 5.08 cm (2.0 in), PR = 1.53.

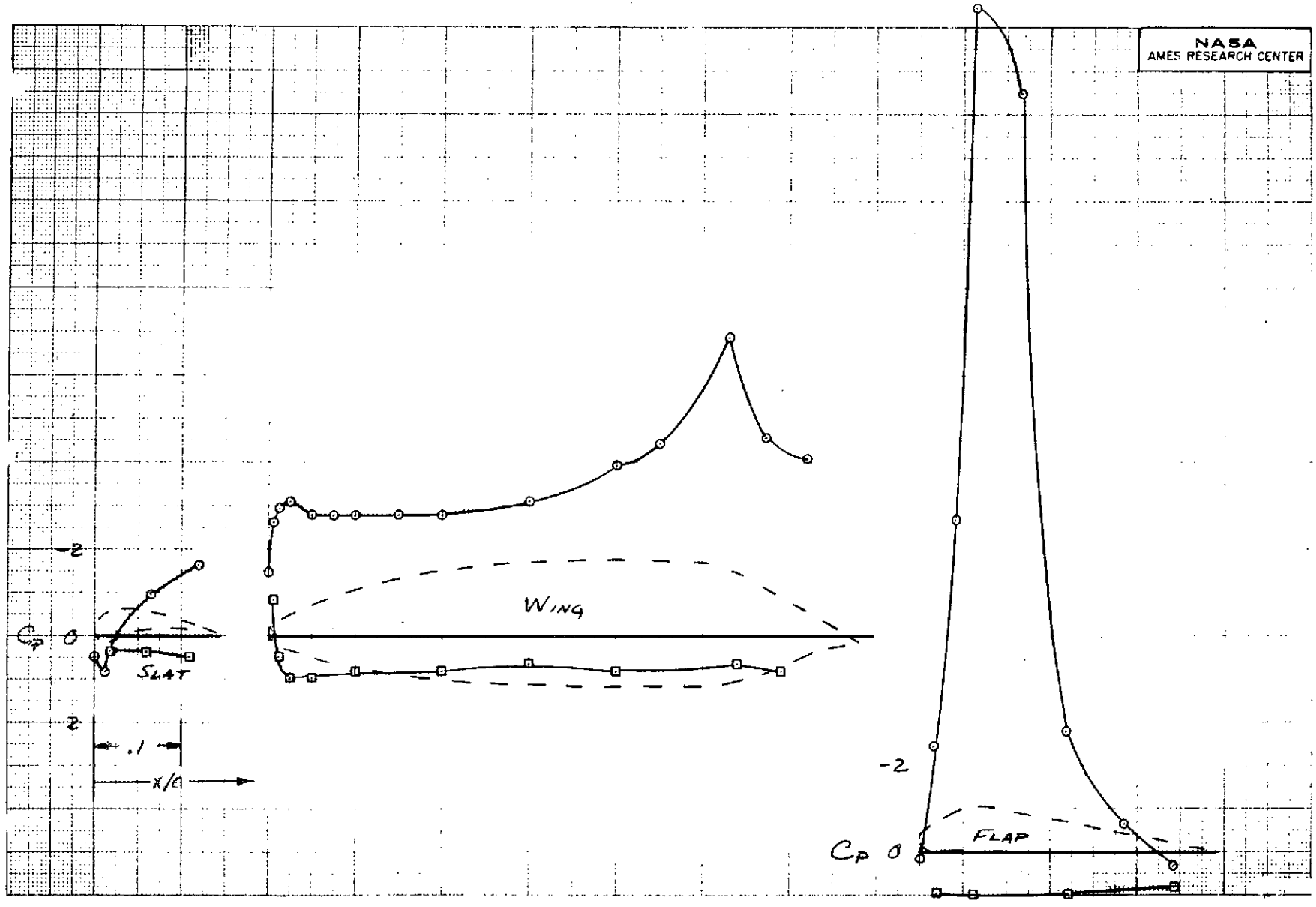

(b) Nozzle 1, shroud off, Z_f = 0, ℓ_f = 5.08 cm (2.0 in).

Figure 39.- Continued.

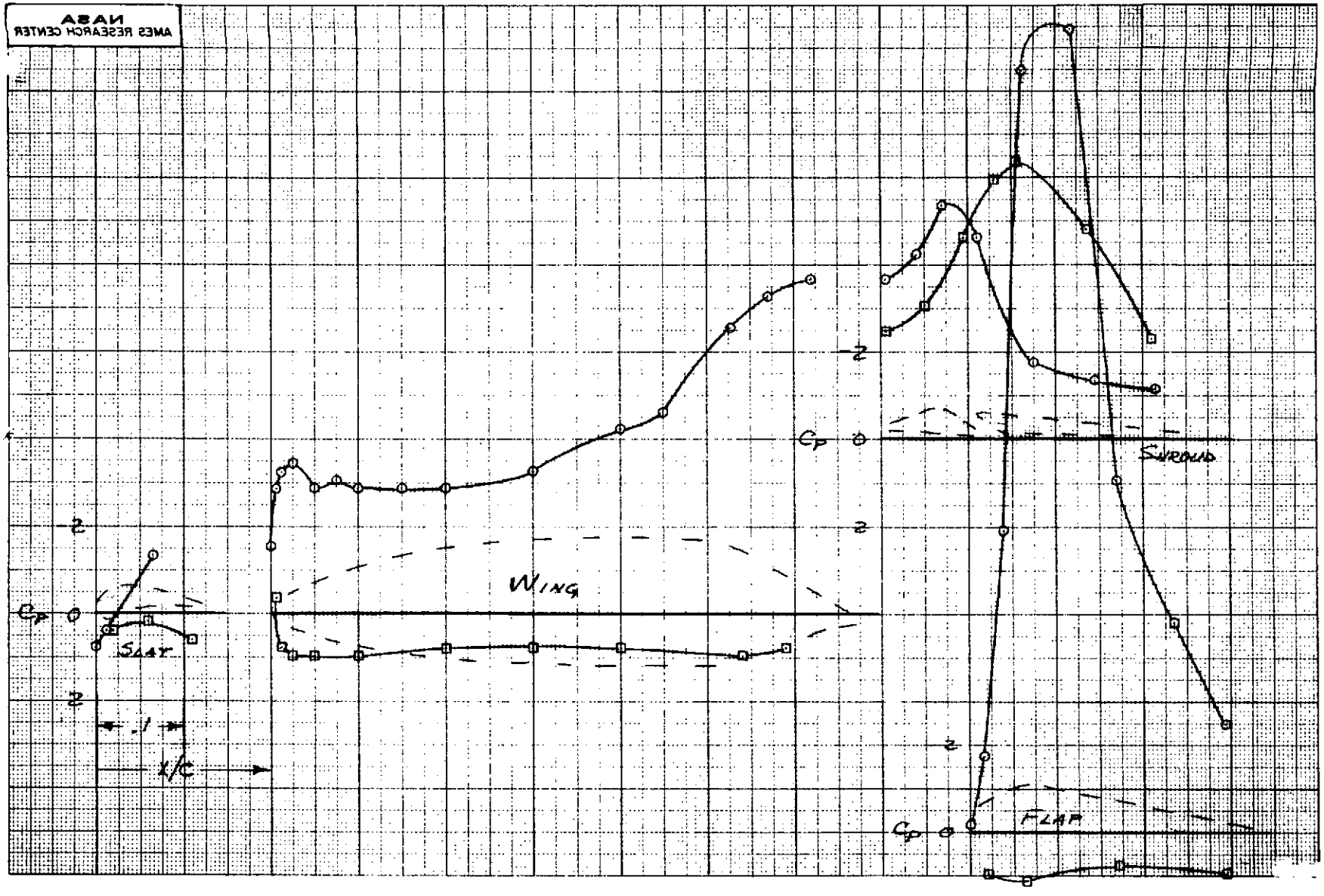

(c) Nozzle 3b, A_e/A_n = 20, Z_f = .15 cm (.06 in), ℓ_f = 2.54 cm (1.0 in).

Figure 39.- Continued.

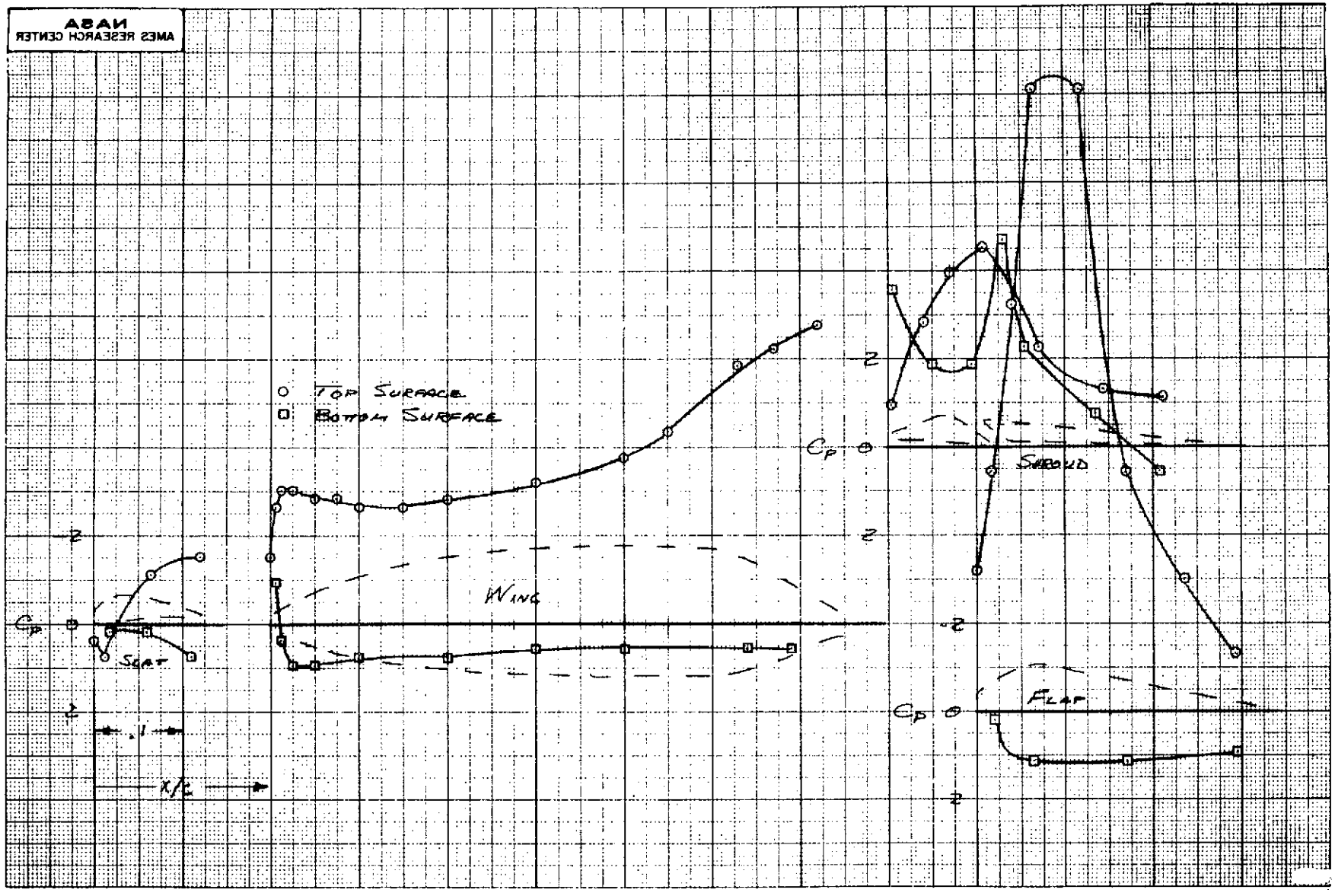

(d) Nozzle 3b, A_e/A_n = 20, Z_f = .97 cm (.38 in), ℓ_f = 5.08 cm (2.0 in).

Figure 39.- Continued.

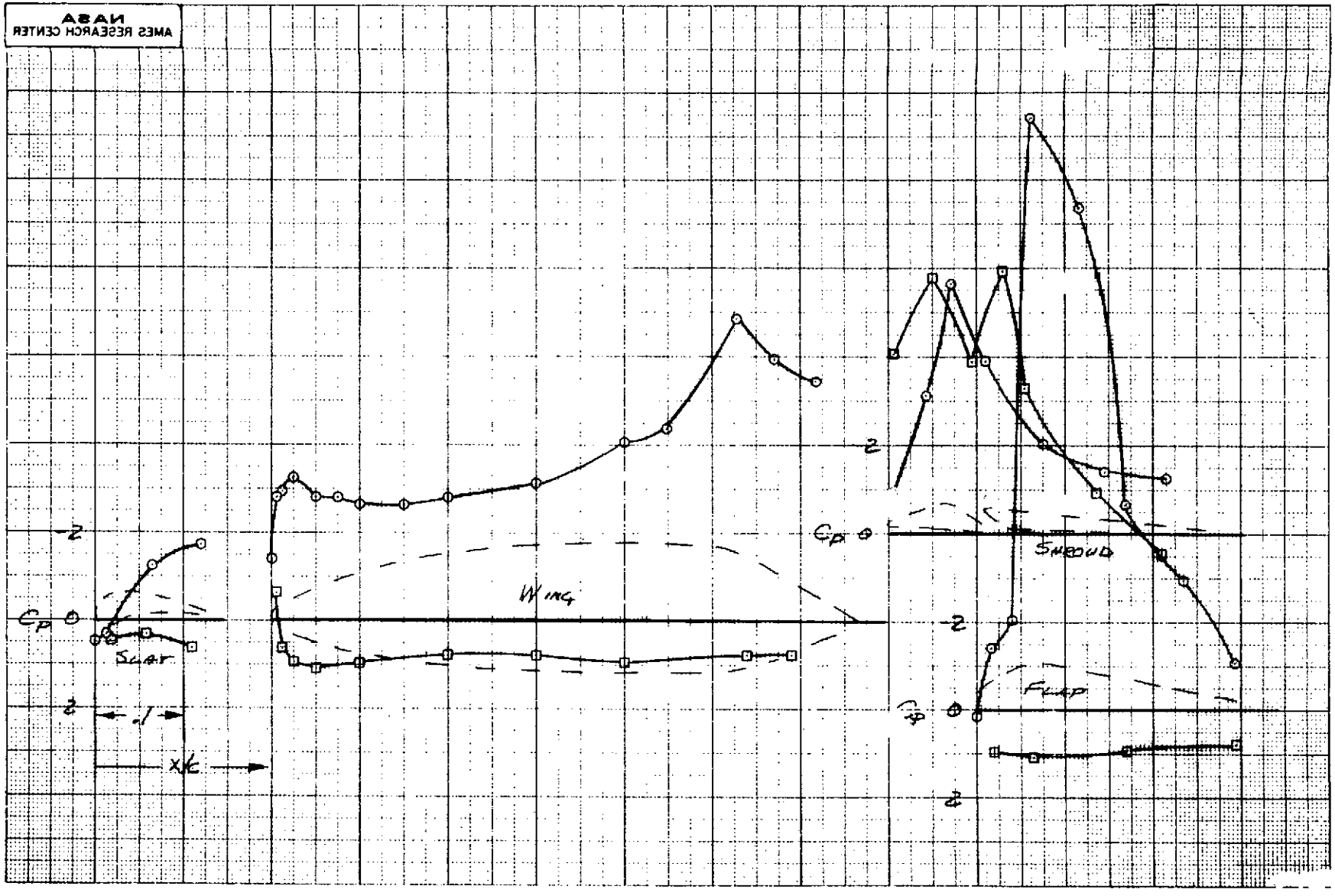

(e) Nozzle 5c, A_e/A_n = 15, Z_f = .15 cm (.06 in), ℓ_f = 2.54 cm (1.0 in).

Figure 39.- Continued.

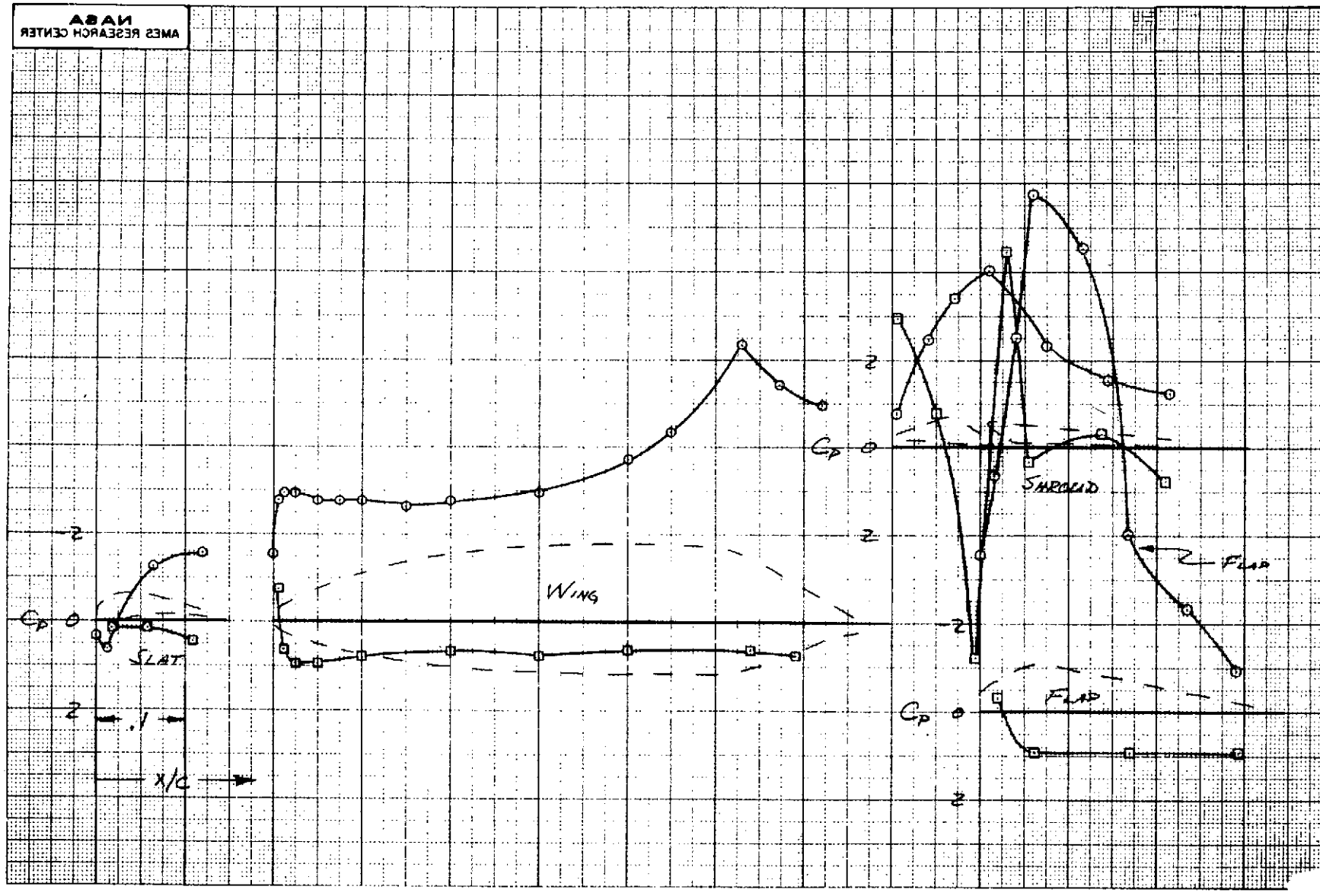

(f) Nozzle 5c, A_e/A_n = 20, Z_f = .79 cm (.31 in), ℓ_f = 5.08 cm (2.0 in).

Figure 39.- Concluded.

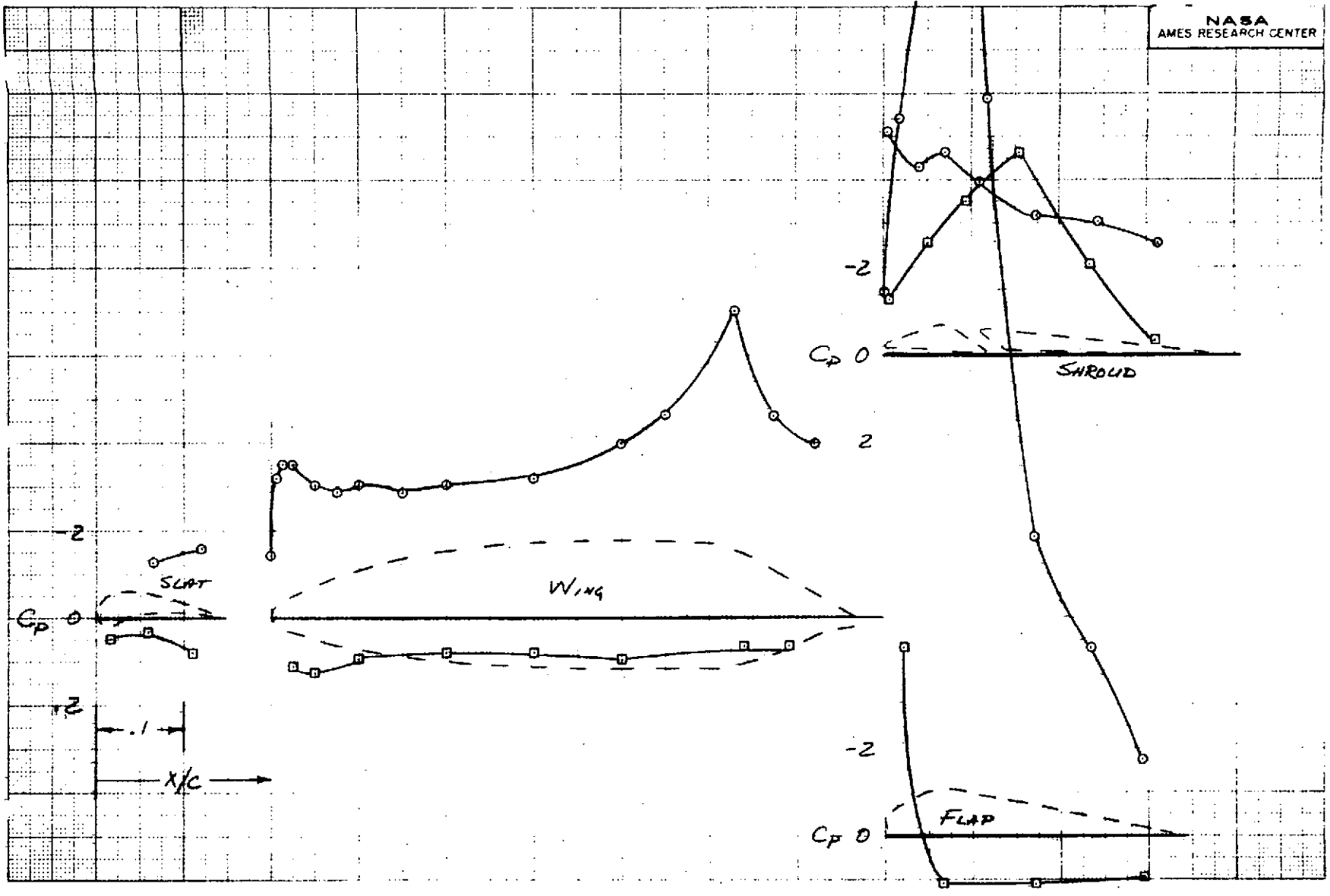

(a) Nozzle 1, A_e/A_n = 15, Z_f = 1.27 cm (.5 in), ℓ_f = 5.08 cm (2.0 in).

Figure 40.- Surface pressure distributions of various configurations at δ_f = 75°; α = 0°, C_{J_n} = 1.5, A_e/A_t = 1.25, ℓ_s = 5.08 cm (2.0 in), PR = 1.53.

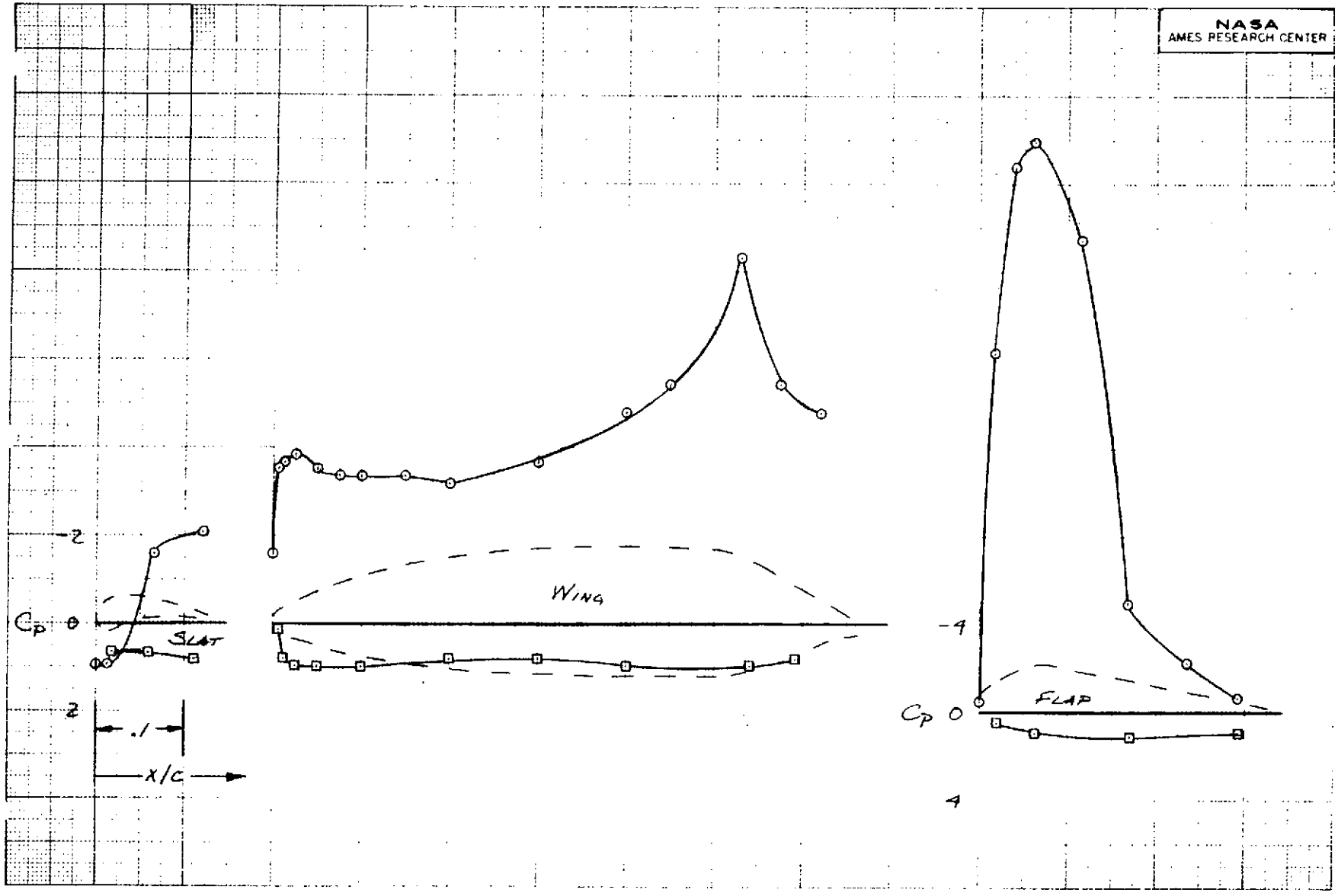

(b) Nozzle 1, shroud off, Z_f = 0, ℓ_f = 5.08 cm (2.0 in)

Figure 40.- Continued.

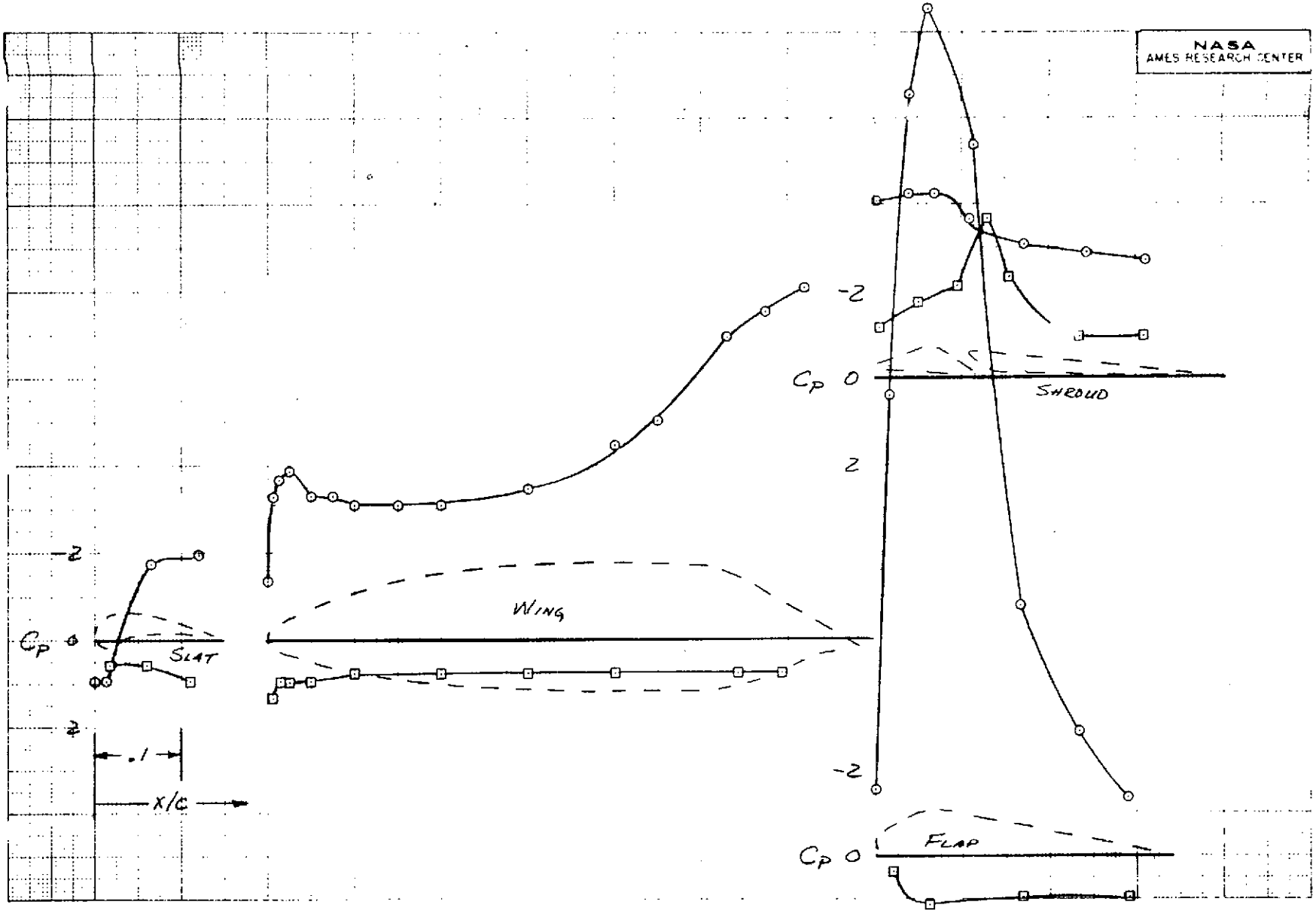

(c) Nozzle 3b, A_e/A_n = 20, Z_f = .15 cm (.06 in), ℓ_f = 2.54 cm (1.0 in).

Figure 40.- Continued.

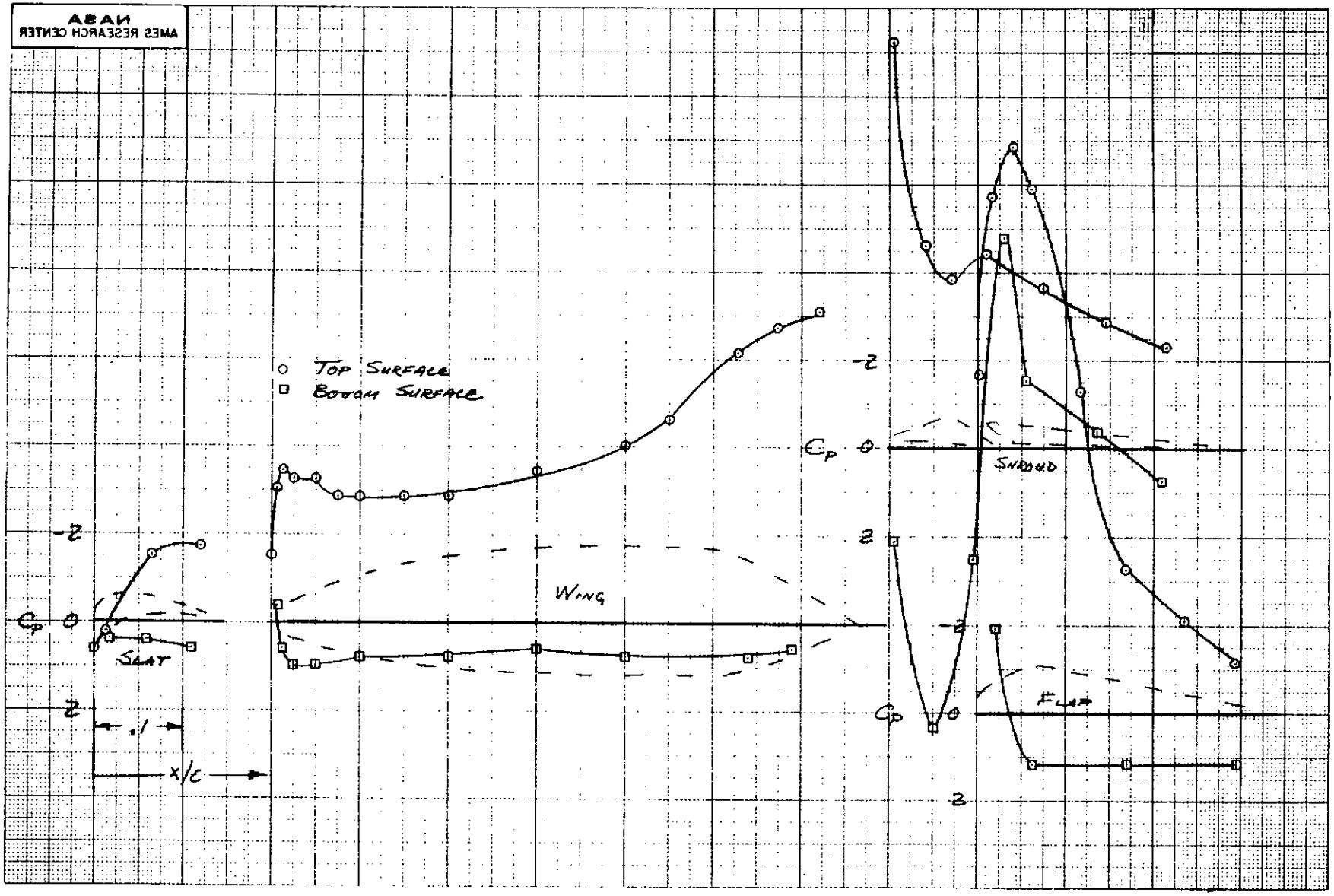

(d) Nozzle 3b, A_e/A_n = 20, Z_f = .97 cm (.38 in), ℓ_f = 5.08 cm (2.0 in).

Figure 40.- Continued.

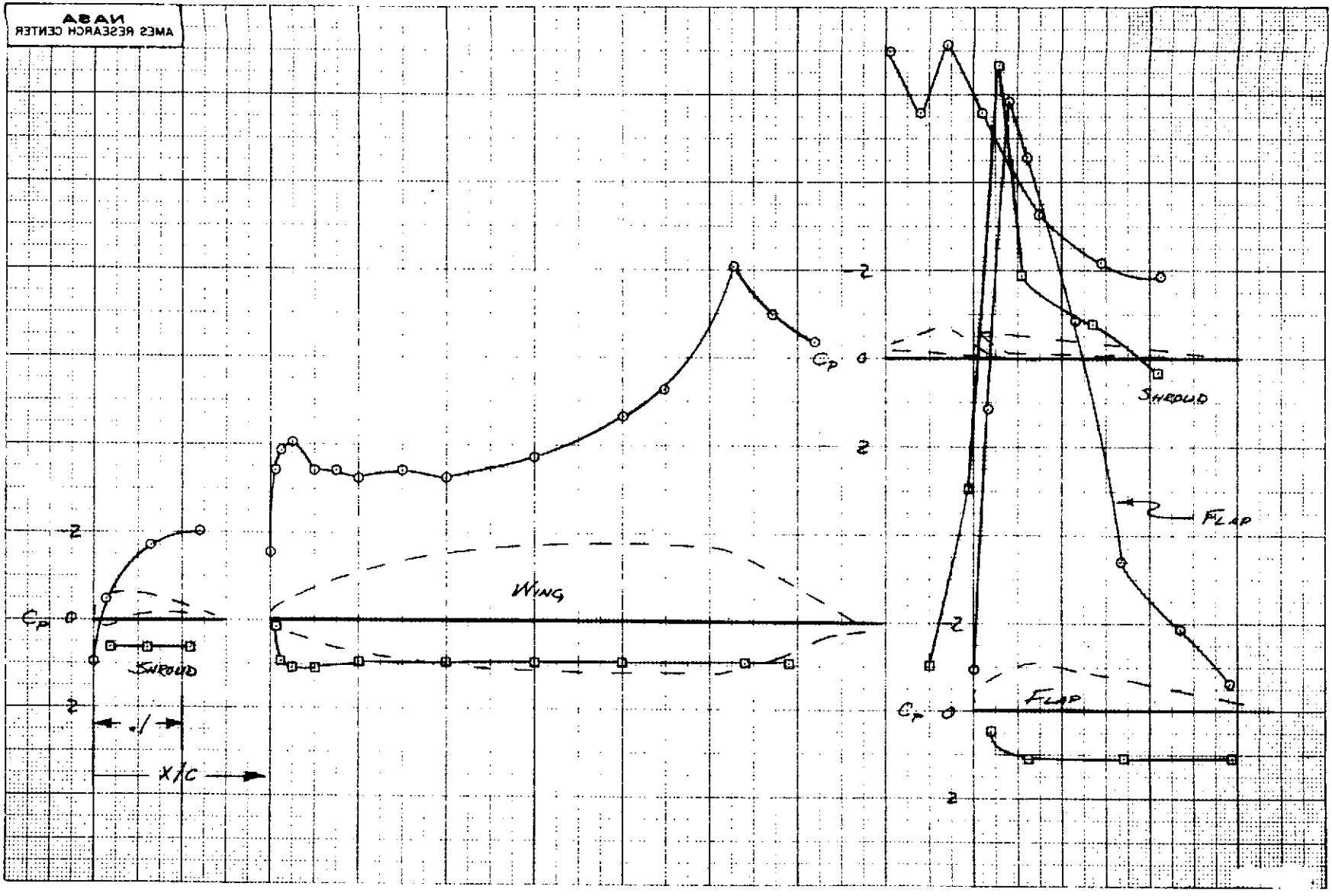

(e) Nozzle 5c, A_e/A_n = 15, Z_f = .15 cm (.06 in), ℓ_f = 2.54 cm (1.0 in).

Figure 40.- Continued.

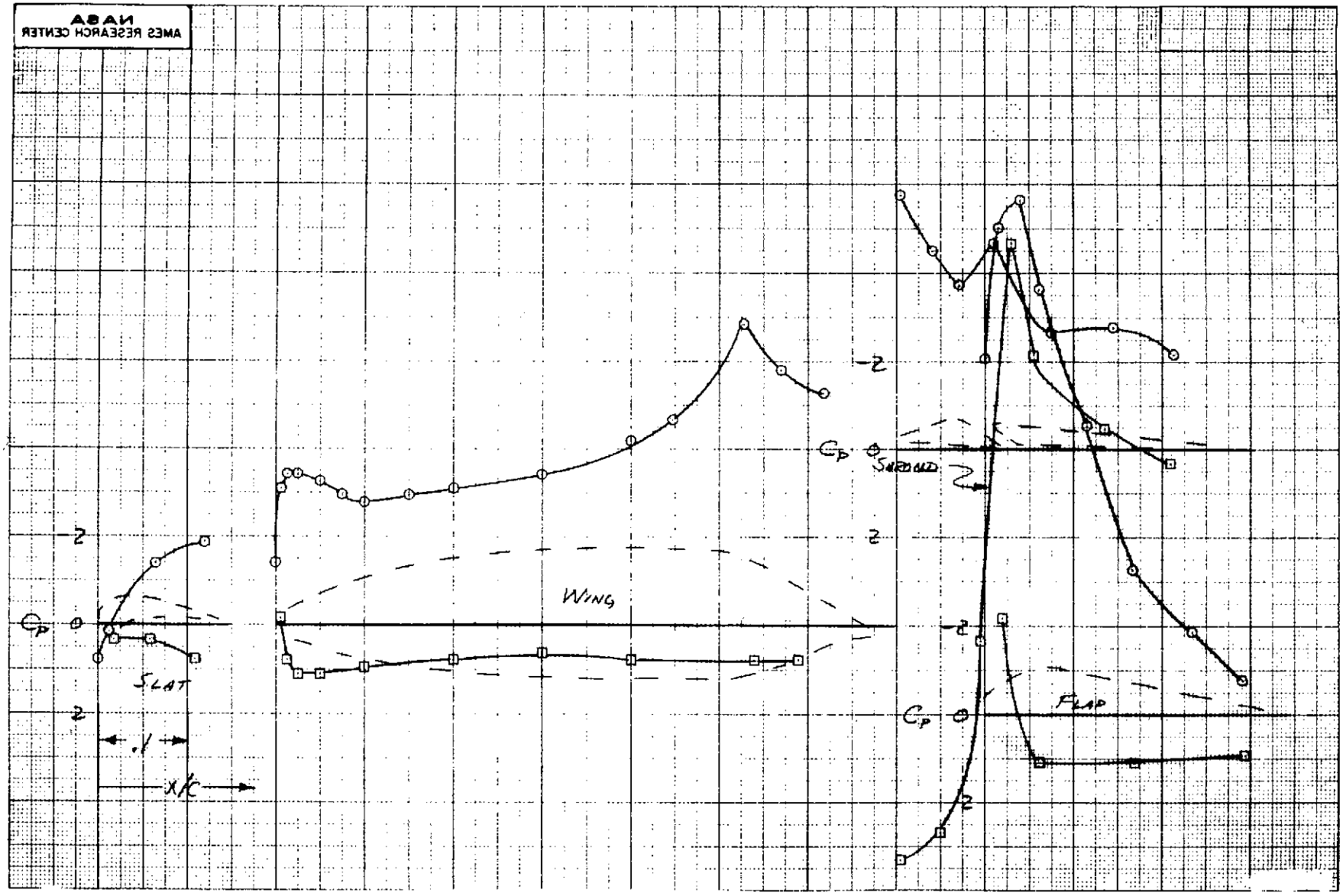

(f) Nozzle 5c, A_e/A_n = 20, Z_f = .79 cm (.31 in), ℓ_f = 5.08 cm (2.0 in).

Figure 40.- Concluded.

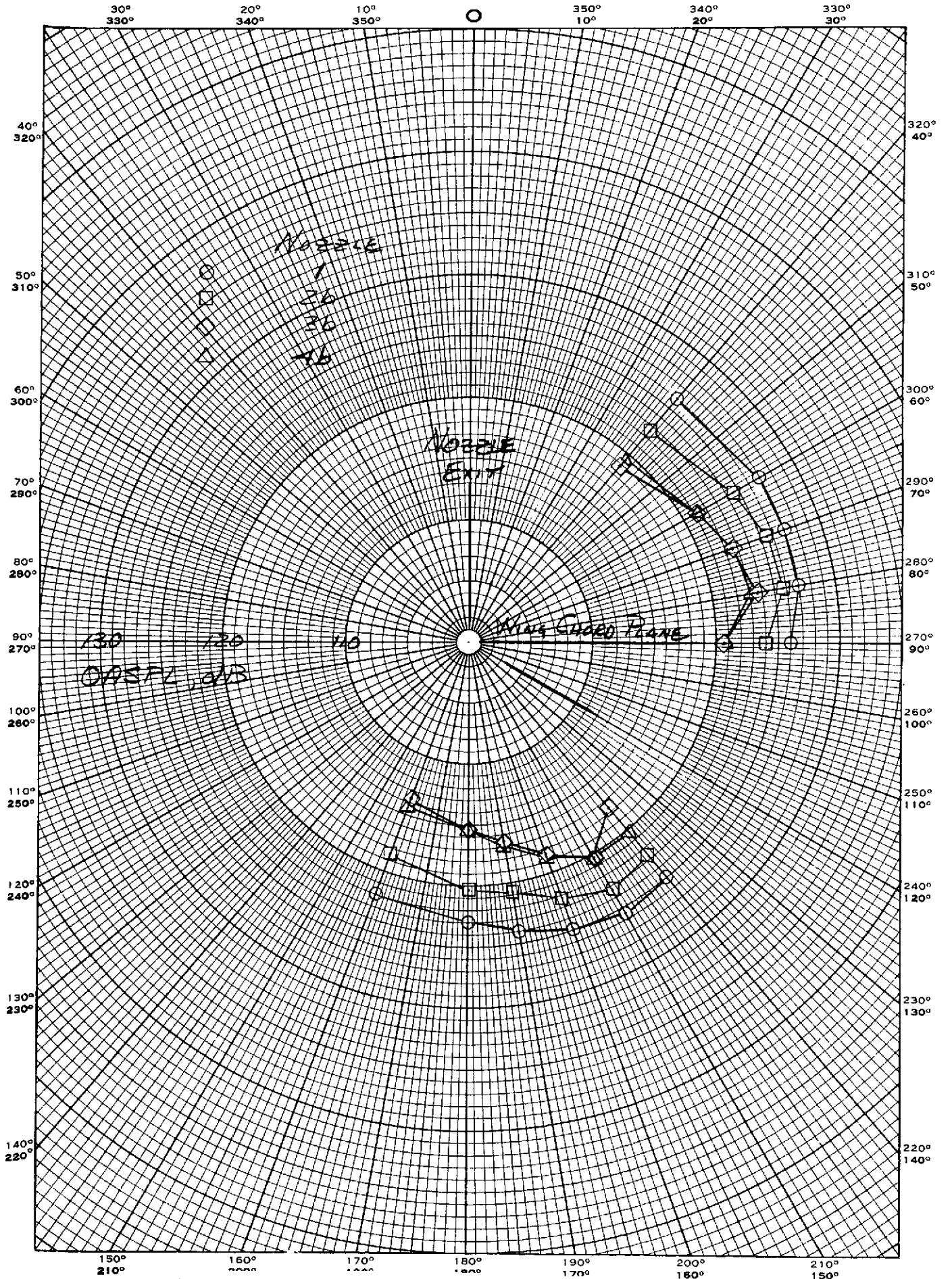

Figure 41.- OASPL directivity for several nozzles; PR = 1.53.

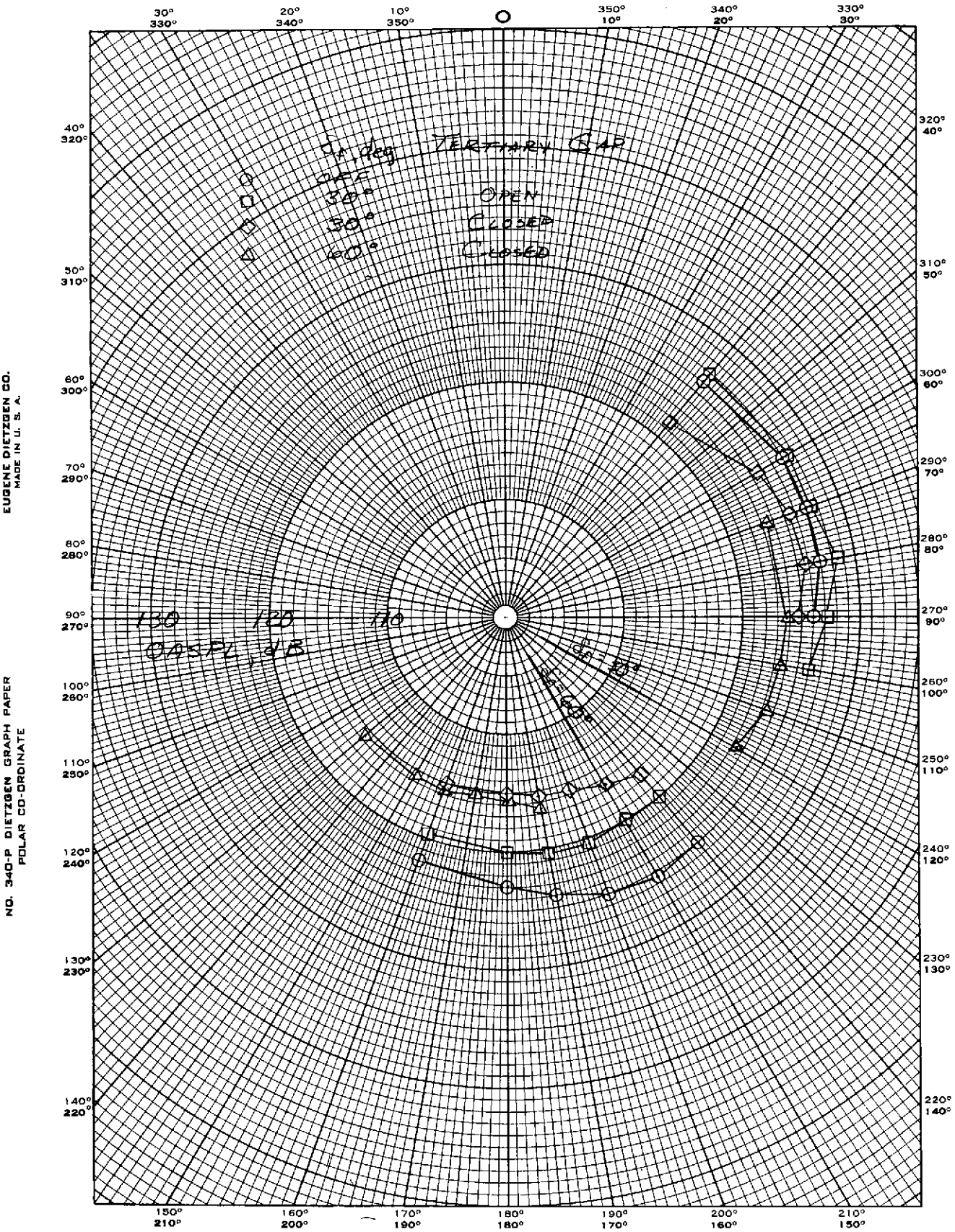

(a) Nozzle 1.

Figure 42.- The effect of a flap (shroud off) on the OASPL directivity for several nozzles; PR = 1.53; tertiary gap open, Z_f = 1.27 cm (.5 in), ℓ_f = 5.08 cm (2.0 in); tertiary gap closed, Z_f = .15 cm (.06 in), ℓ_f = 1.91 cm (.75 in).

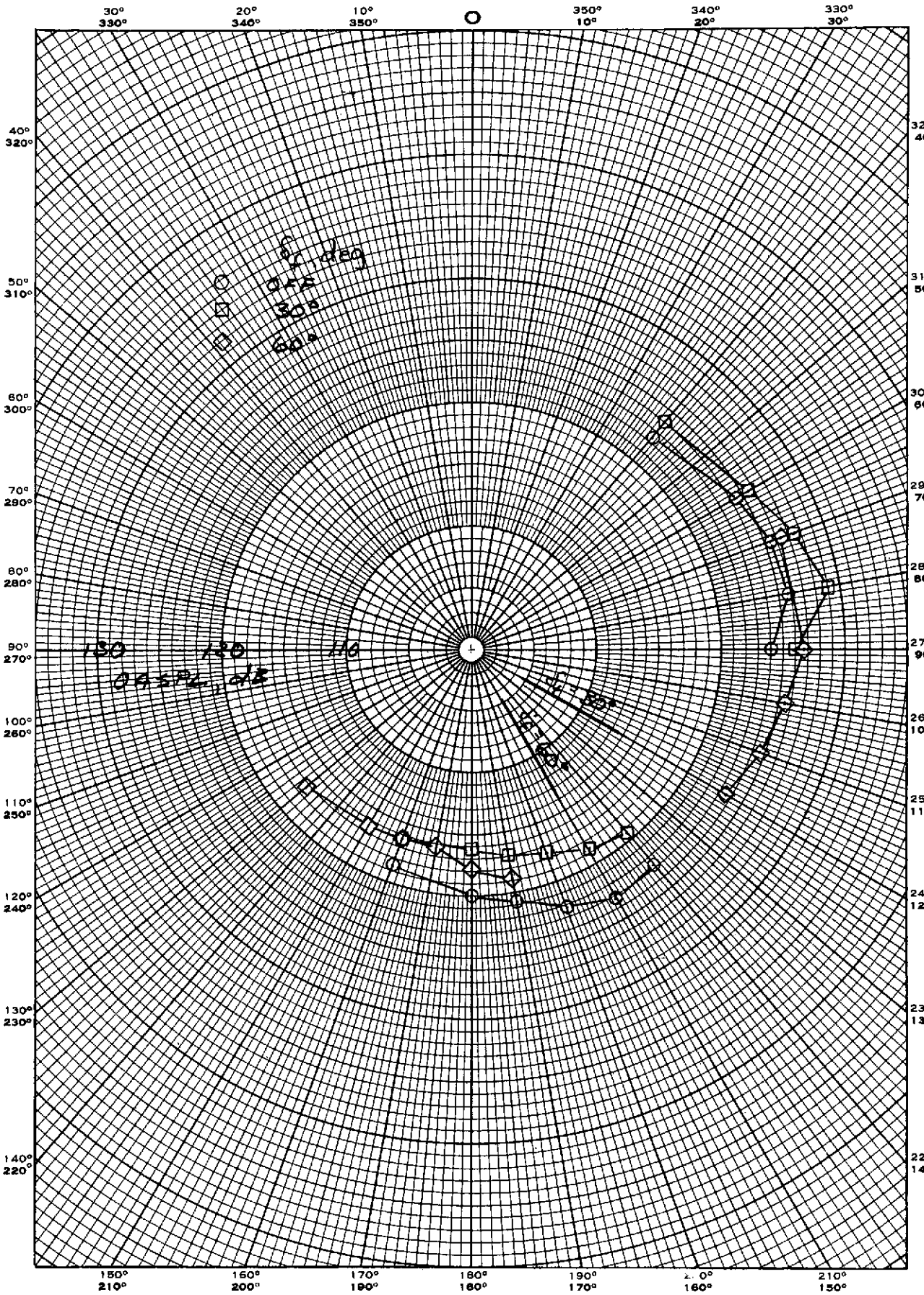

(b) Nozzle 2b, tertiary gap closed.

Figure 42.- Continued.

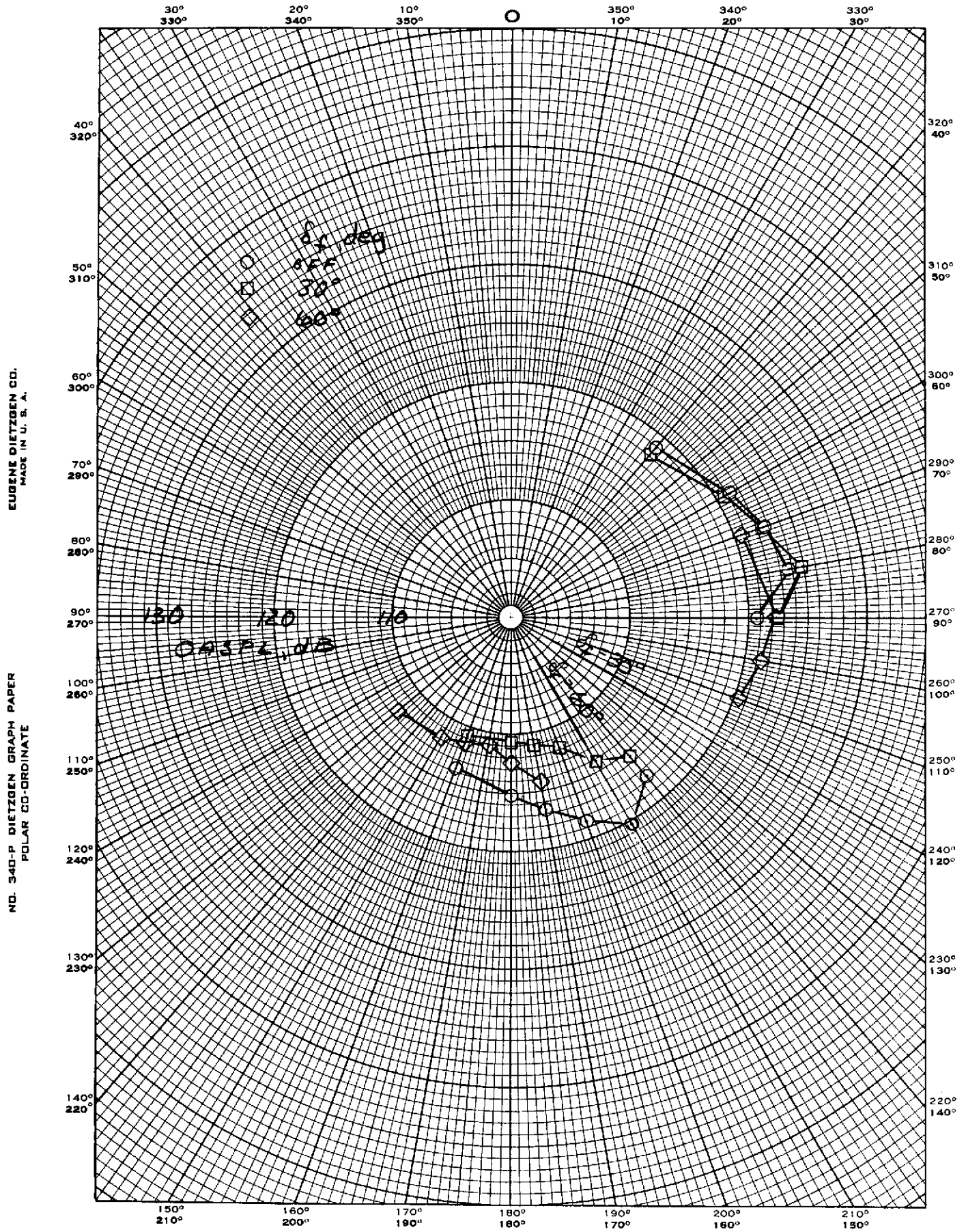

(c) Nozzle 3b, tertiary gap closed.

Figure 42.- Concluded.

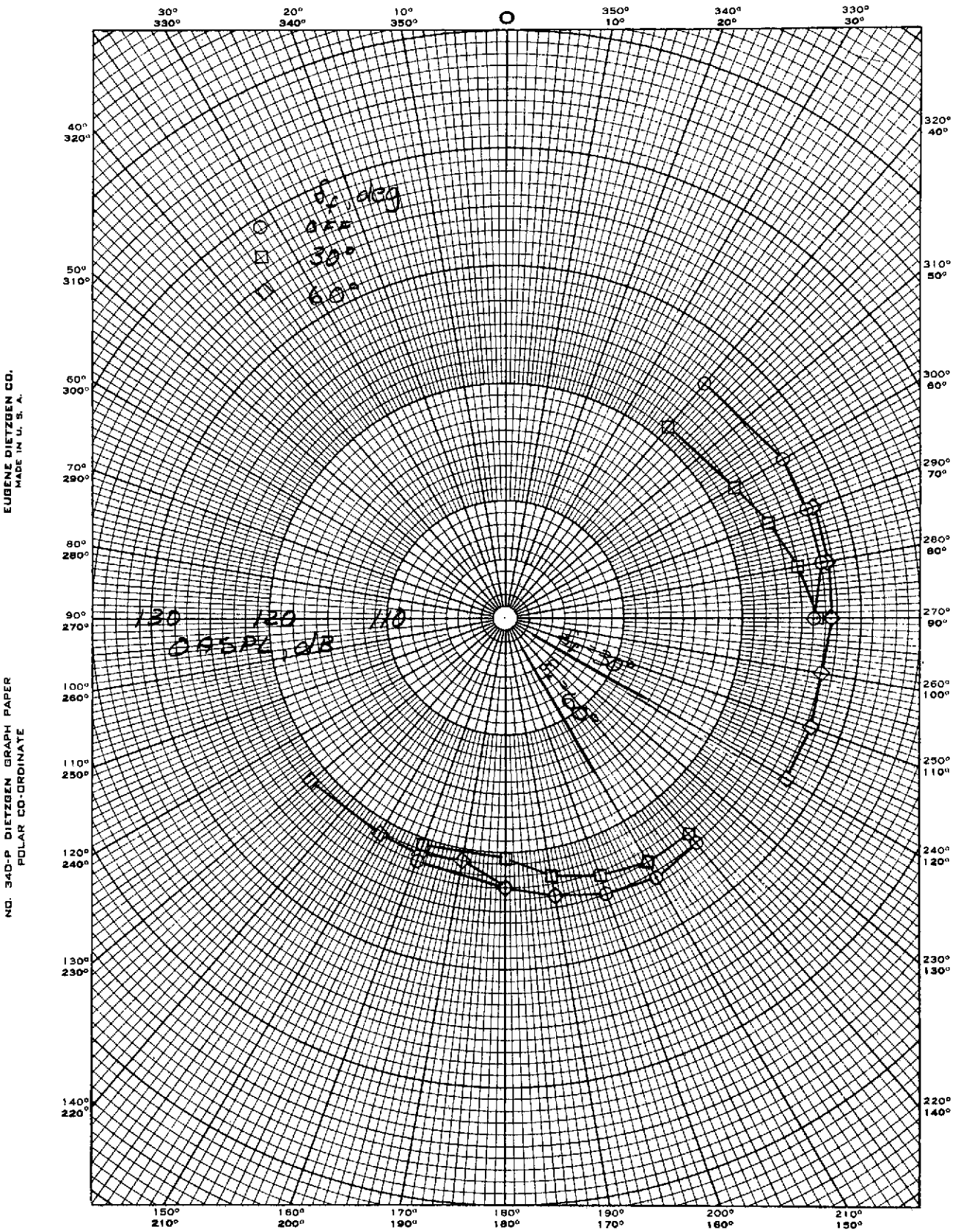

(a) Nozzle 1.

Figure 43.- The effect of an augmentor on the OASPL directivity for several nozzles; PR = 1.53, A_e/A_n = 20, A_e/A_t = 1.25, tertiary gap open, Z_f = 1.27 cm (.5 in), ℓ_f = 5.08 cm (2.0 in).

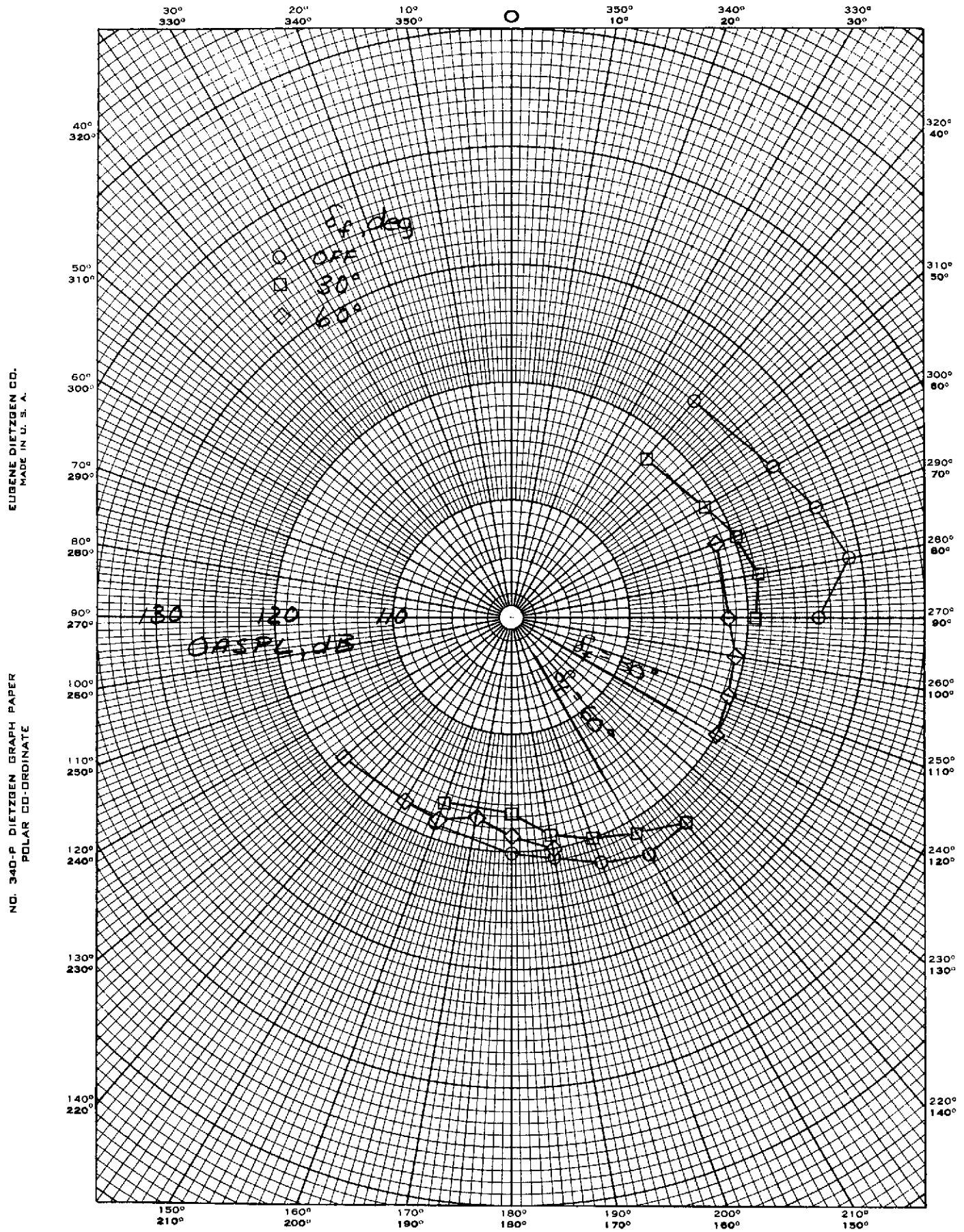

(b) Nozzle 2b.

Figure 43.- Continued.

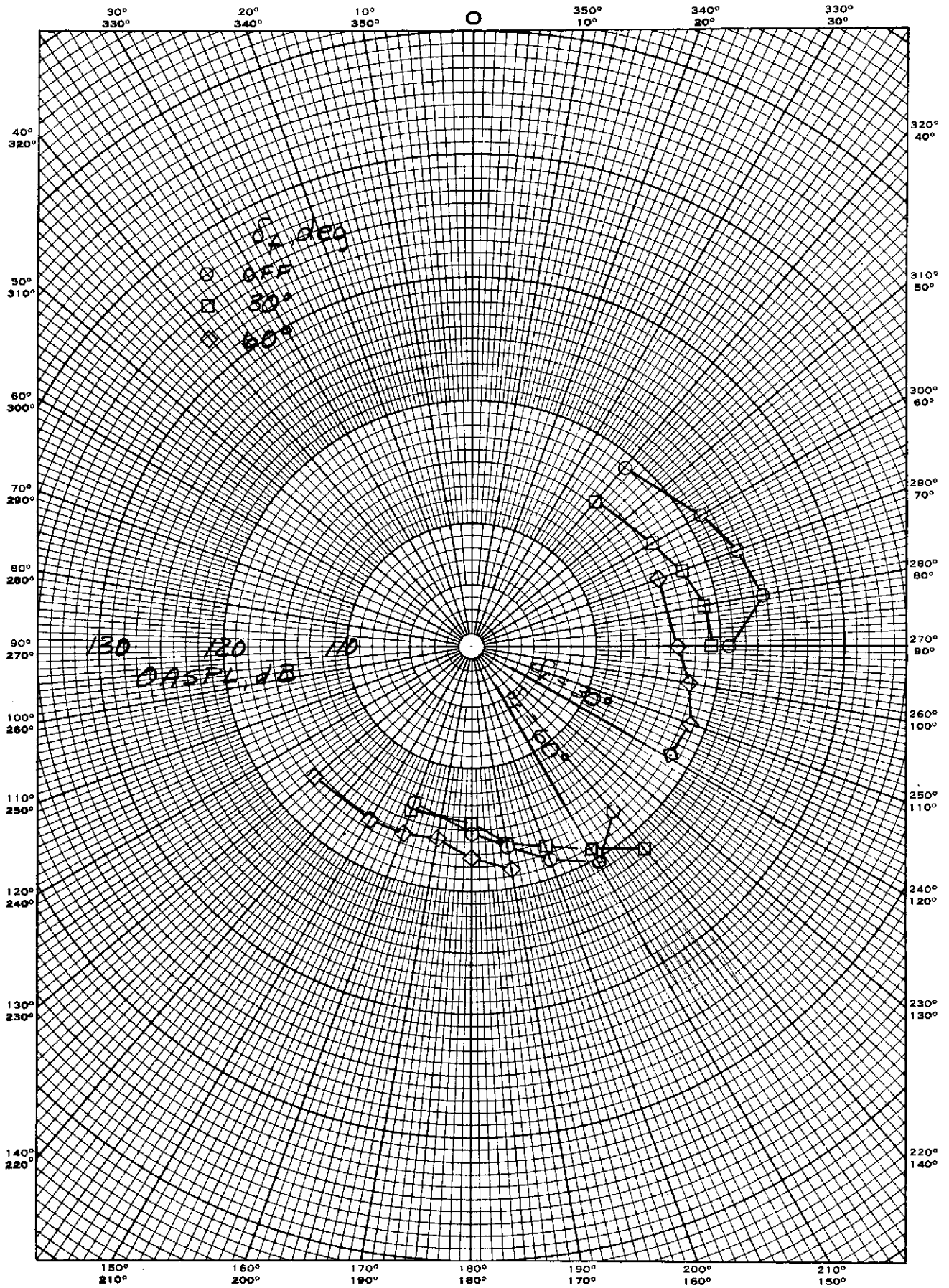

(c) Nozzle 3b.

Figure 43.- Continued.

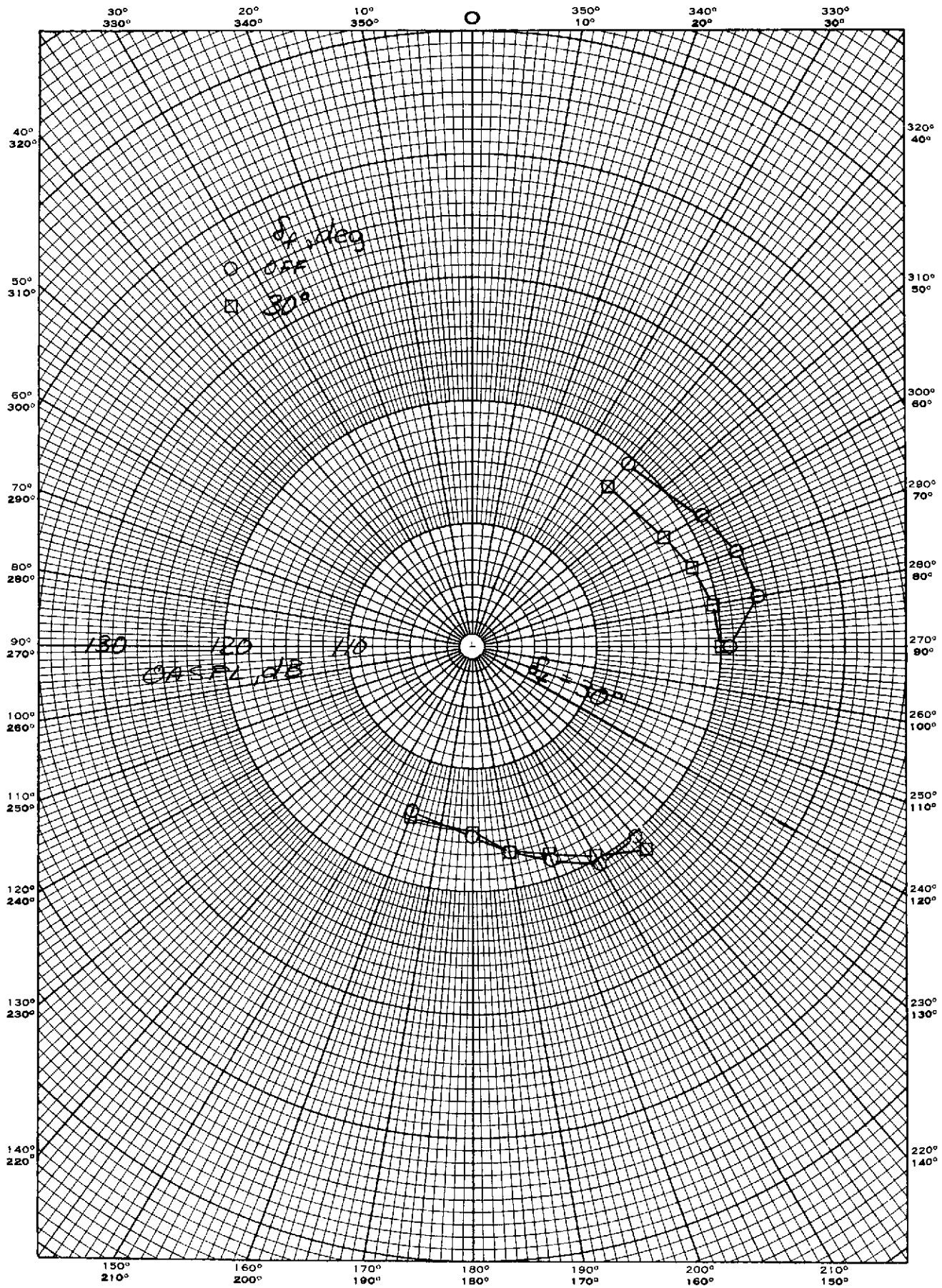

(d) Nozzle 4b.

Figure 43.- Concluded.

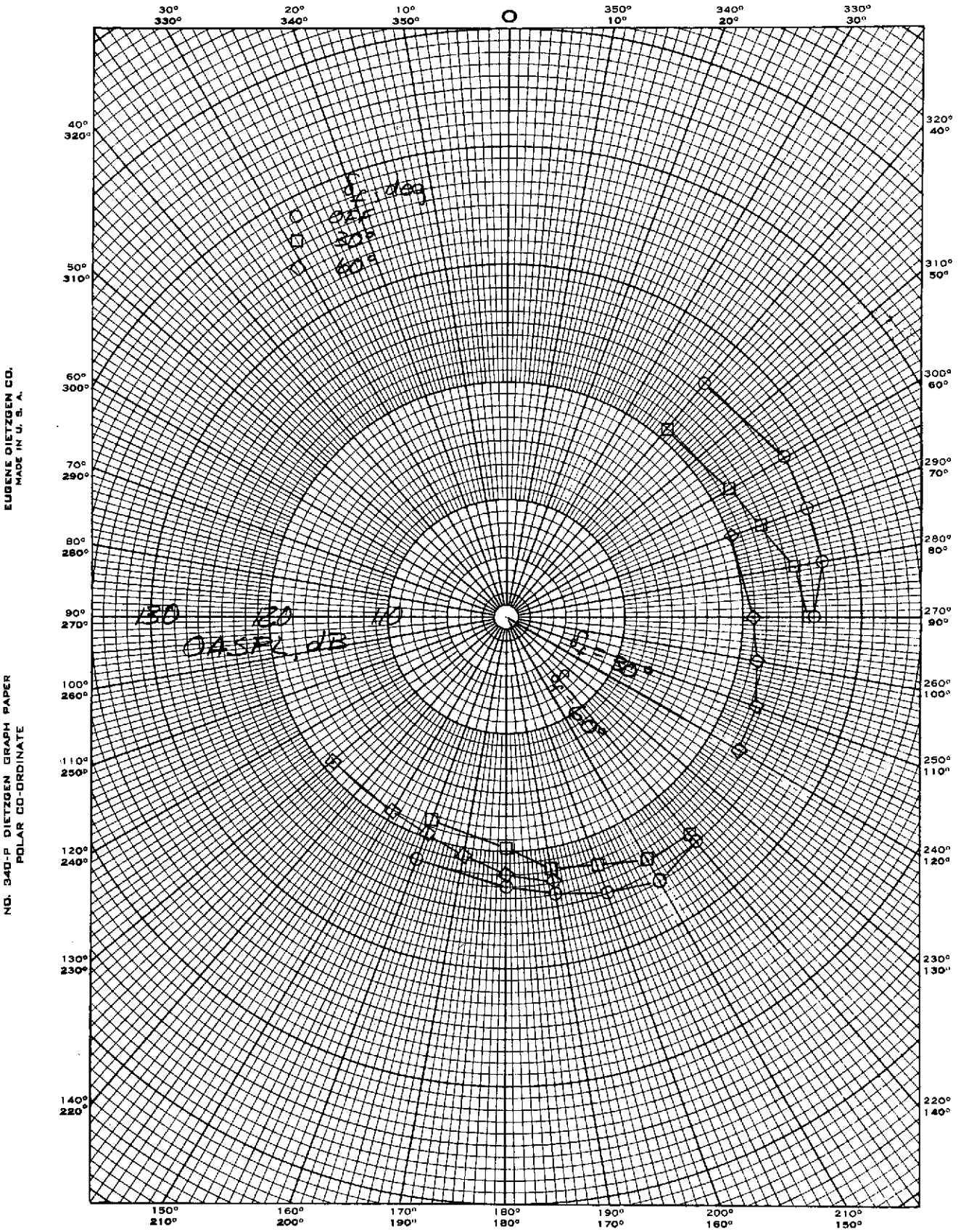

(a) Nozzle 1.

Figure 44.- The effect of an augmentor on the OASPL directivity for several nozzles; PR = 1.53, A_e/A_n = 20, A_e/A_t = 1.25, tertiary gap closed, Z_f = .15 cm (.06 in), ℓ_f = 1.91 cm (.75 in).

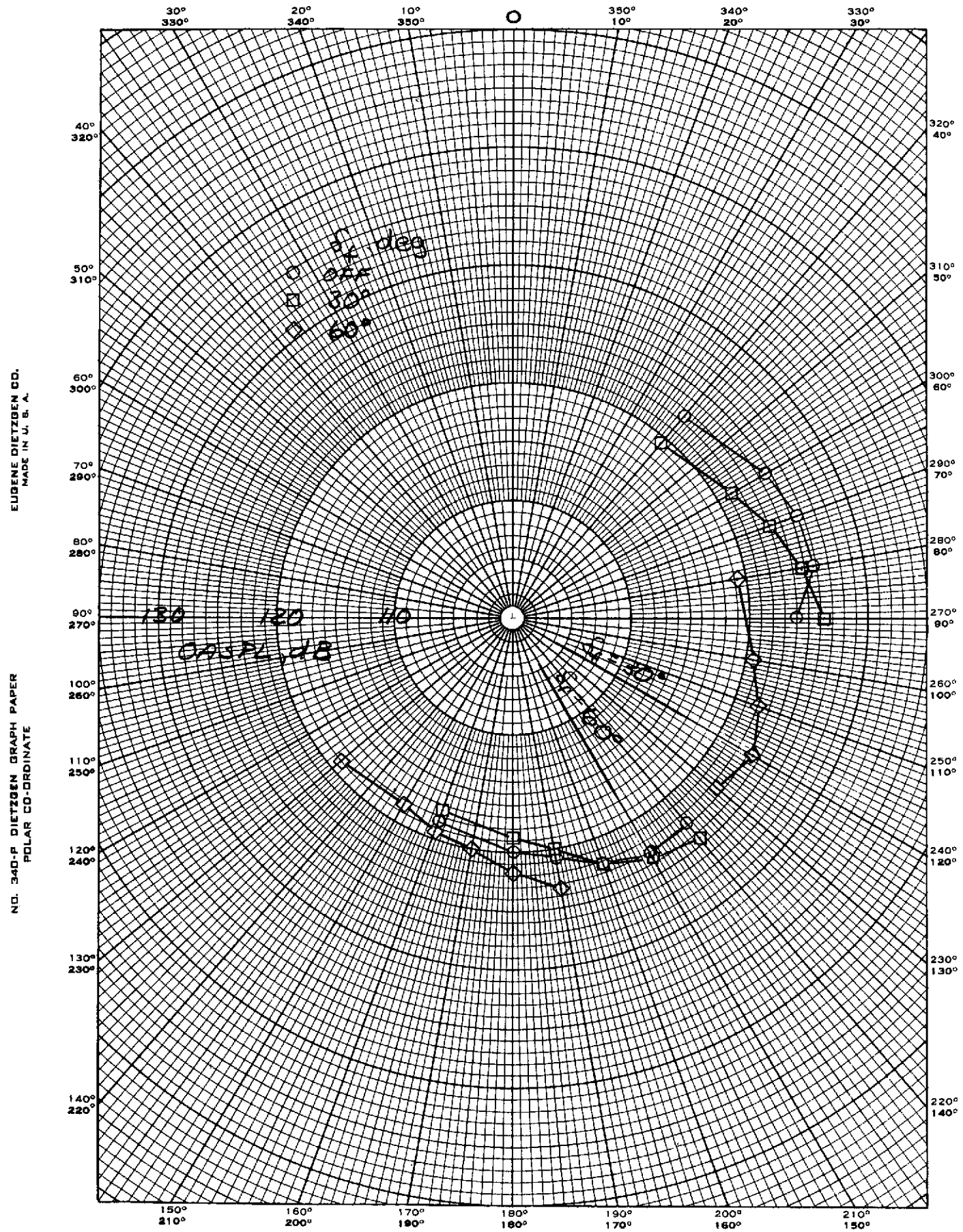

(b) Nozzle 2b.

Figure 44.- Continued.

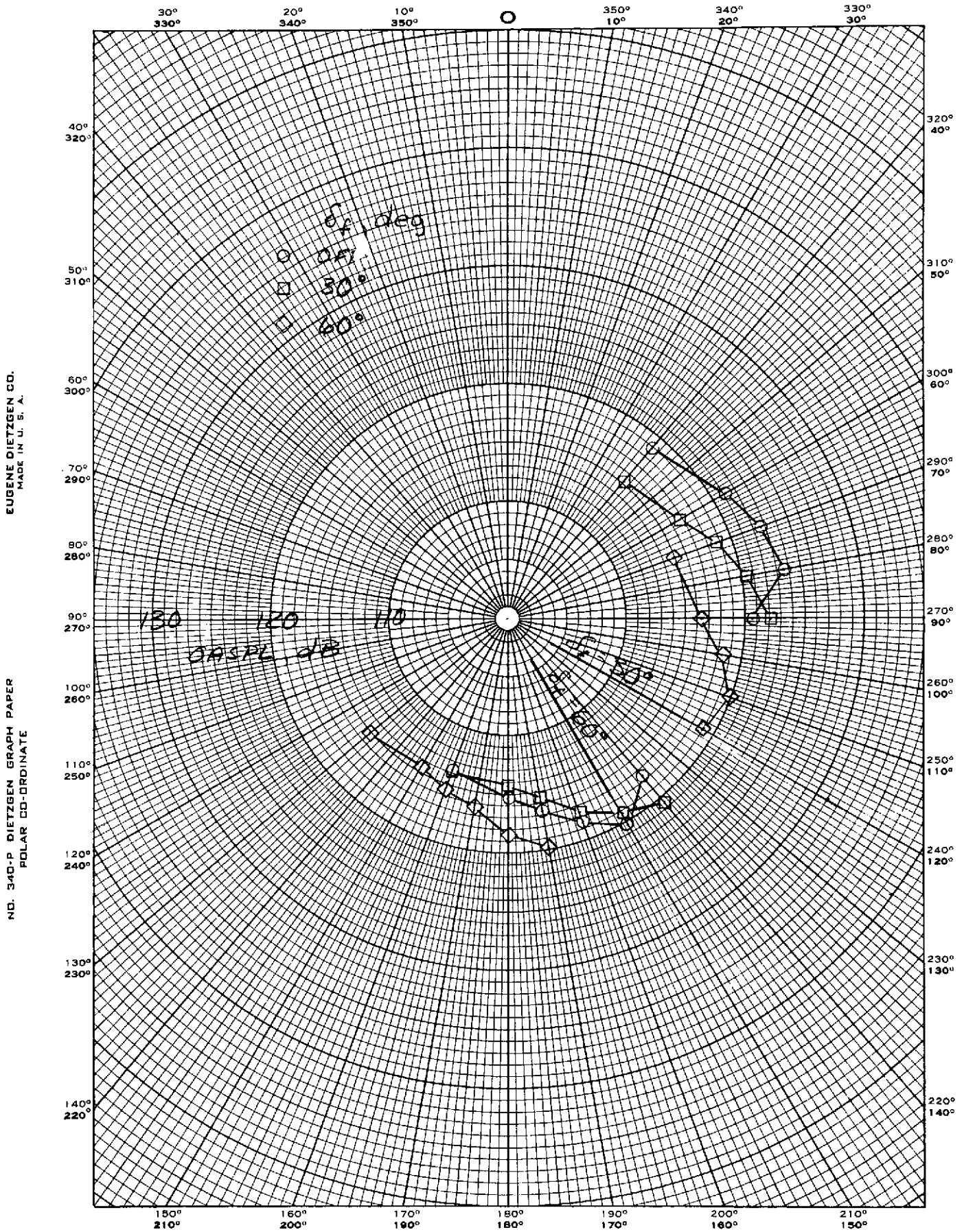

(c) Nozzle 3b.

Figure 44.- Concluded.

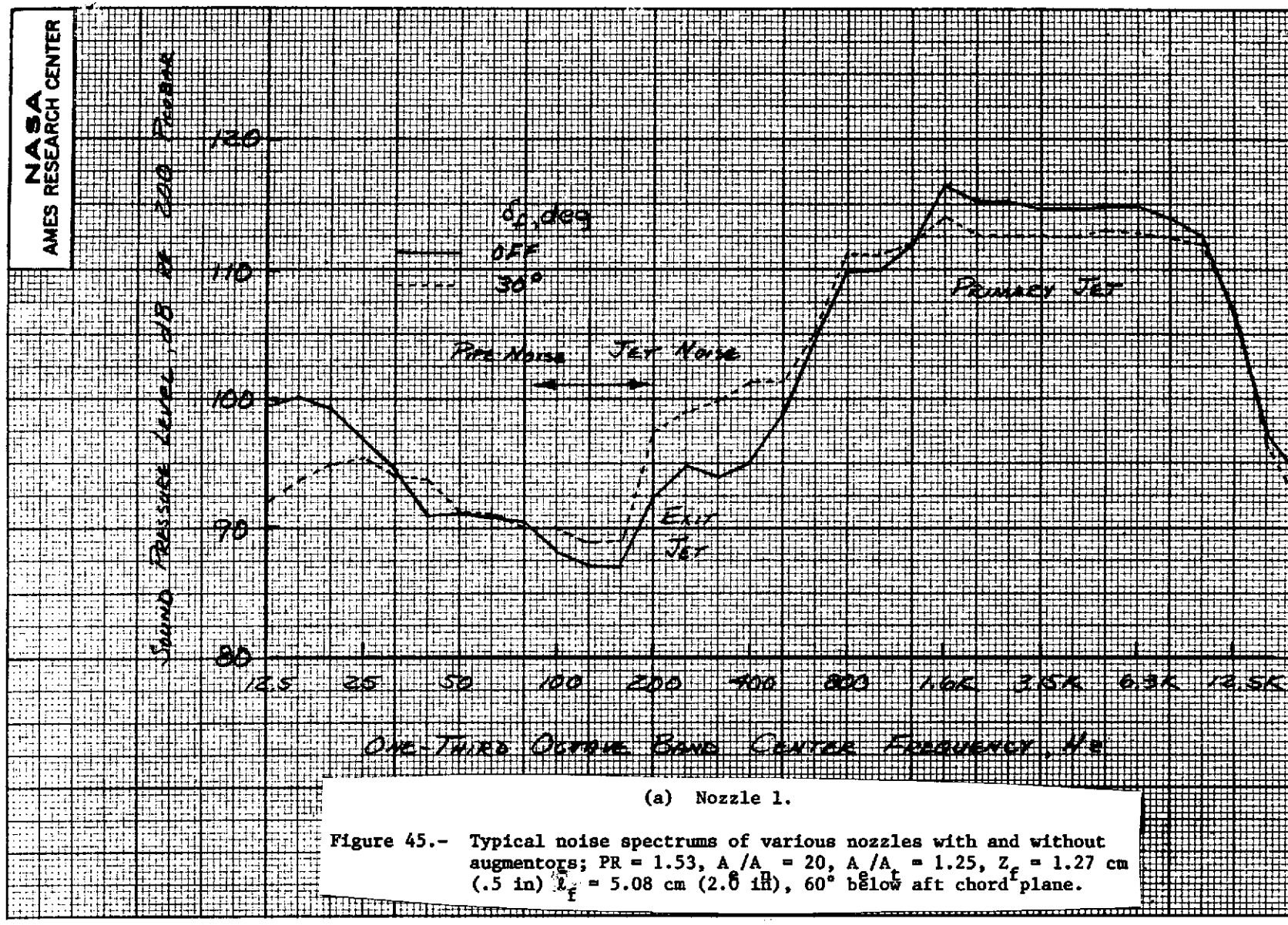

(a) Nozzle 1.

Figure 45.- Typical noise spectrums of various nozzles with and without augmentors; PR = 1.53, A_e/A_t = 20, A_f/A_t = 1.25, Z_f = 1.27 cm (.5 in) ℓ_f = 5.08 cm (2.0 in), 60° below aft chord plane.

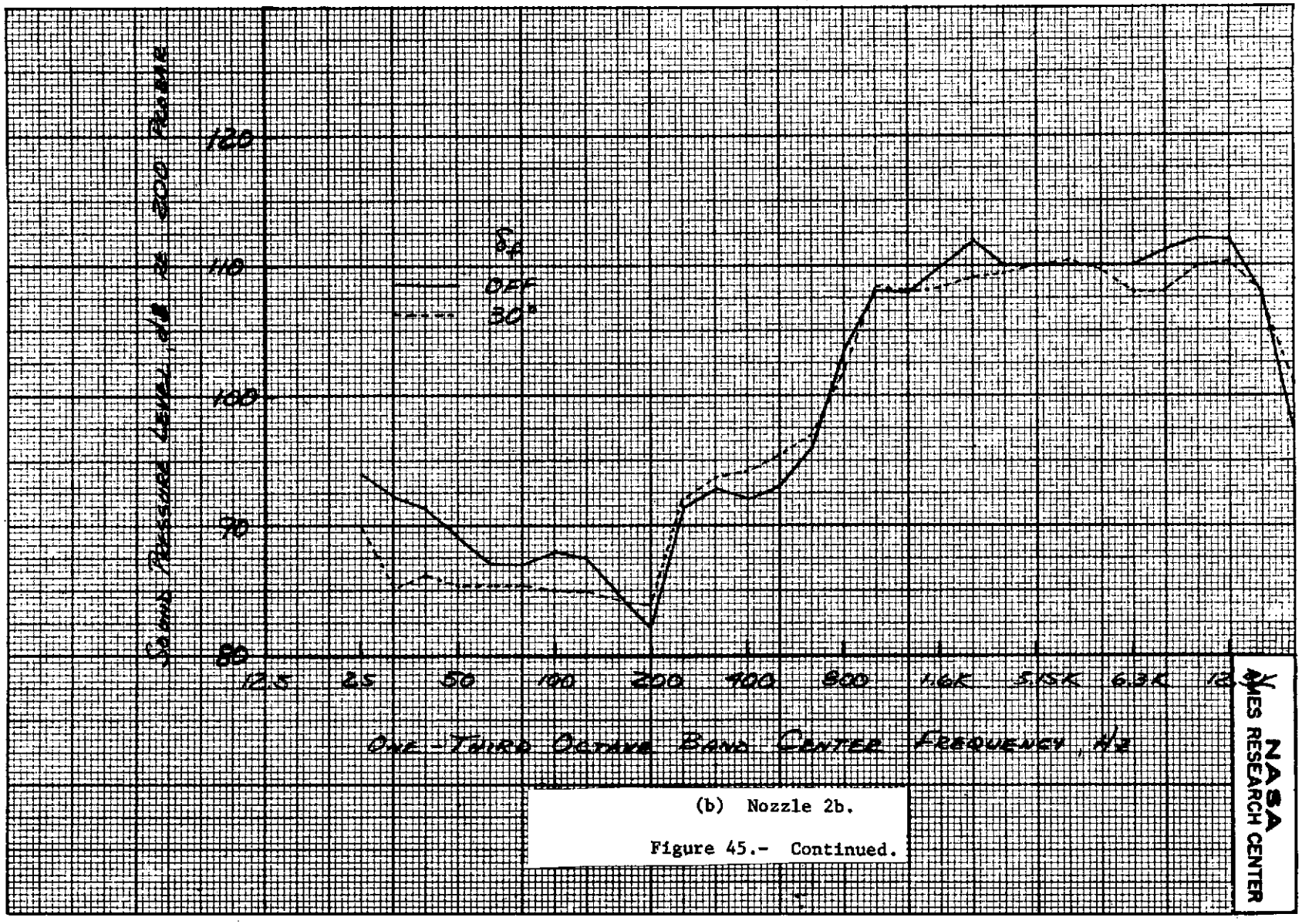

(b) Nozzle 2b.

Figure 45.- Continued.

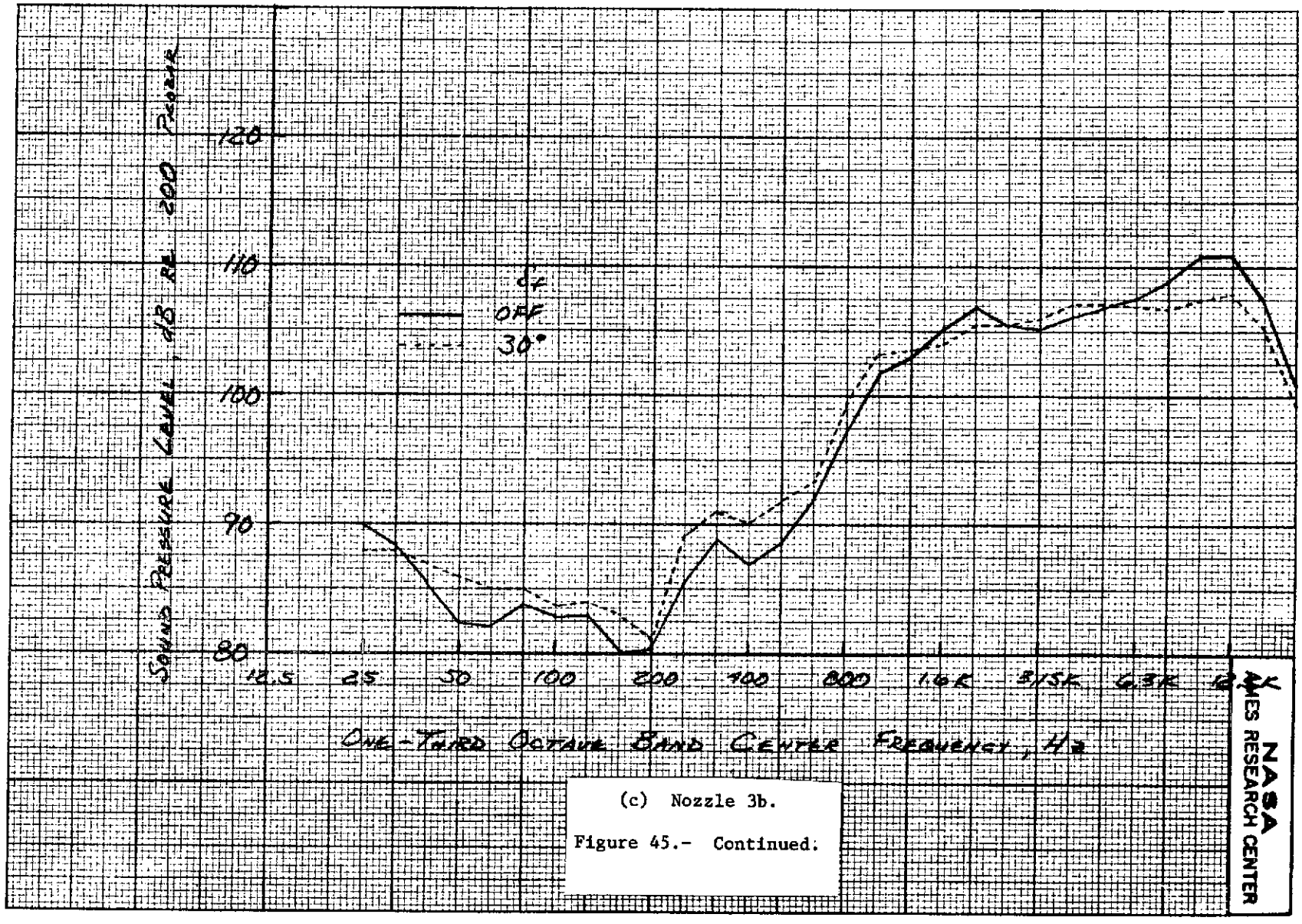

(c) Nozzle 3b.

Figure 45.- Continued.

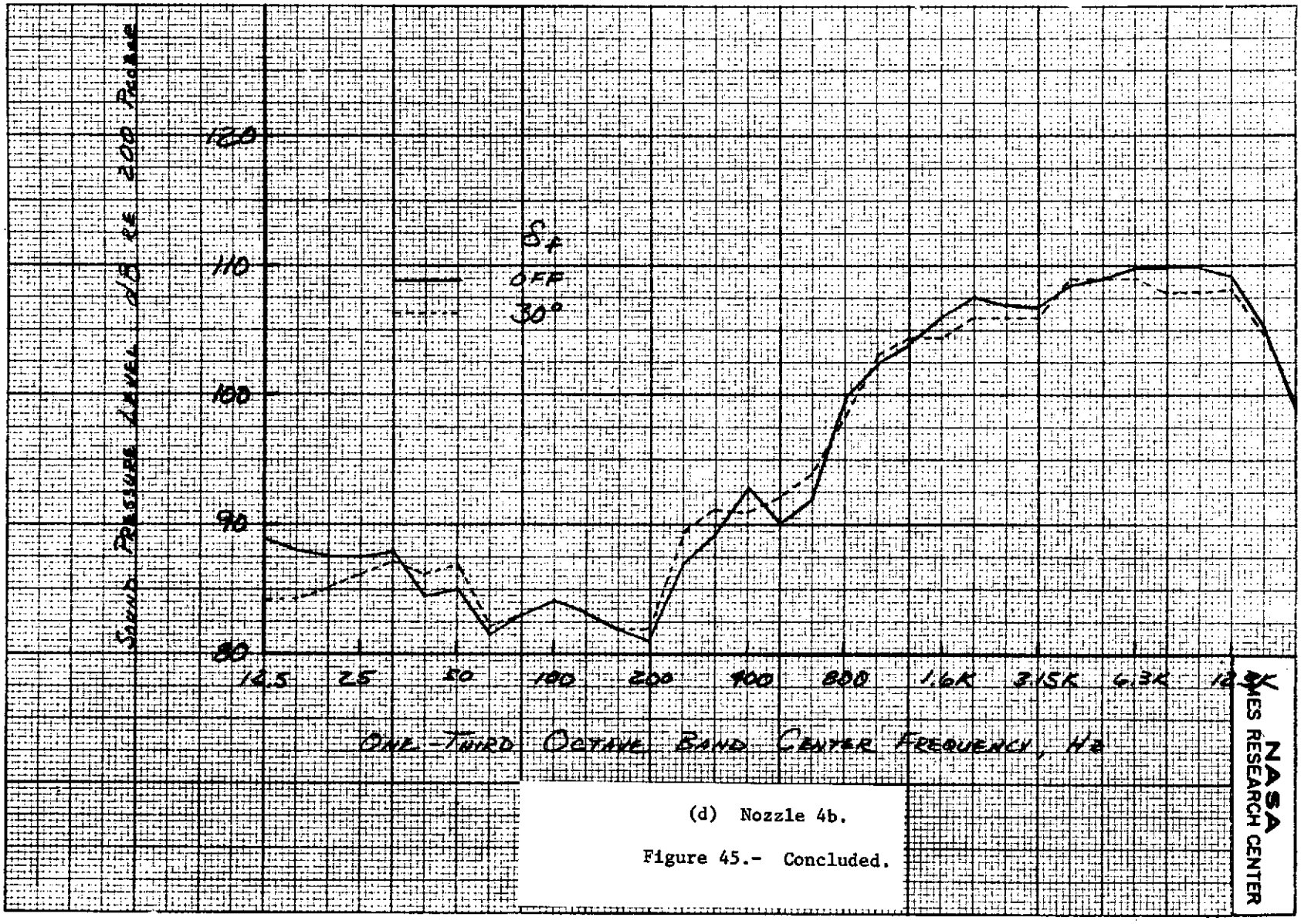

(d) Nozzle 4b.

Figure 45.- Concluded.

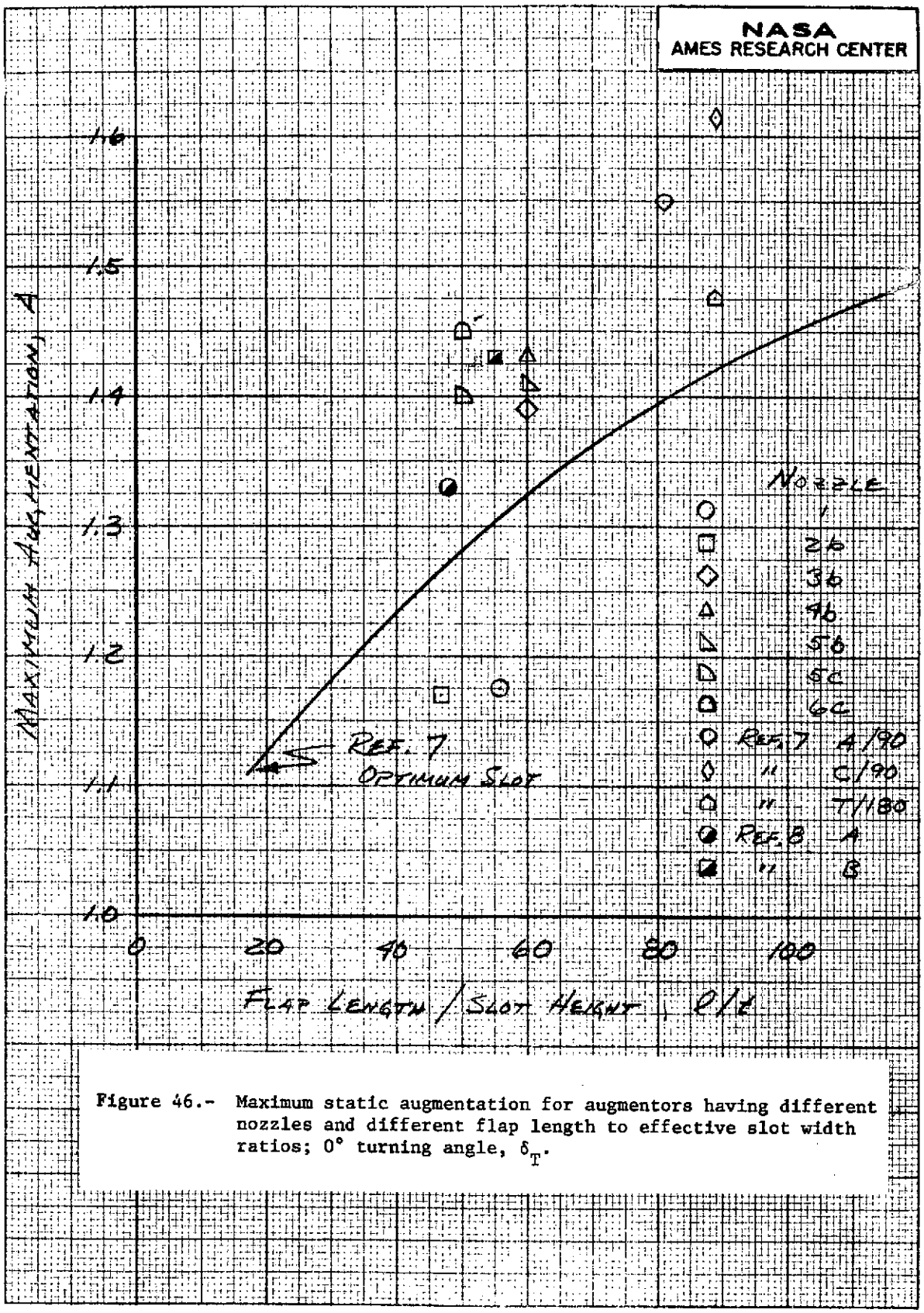

Figure 46.- Maximum static augmentation for augmentors having different nozzles and different flap length to effective slot width ratios; 0° turning angle, δ_T.

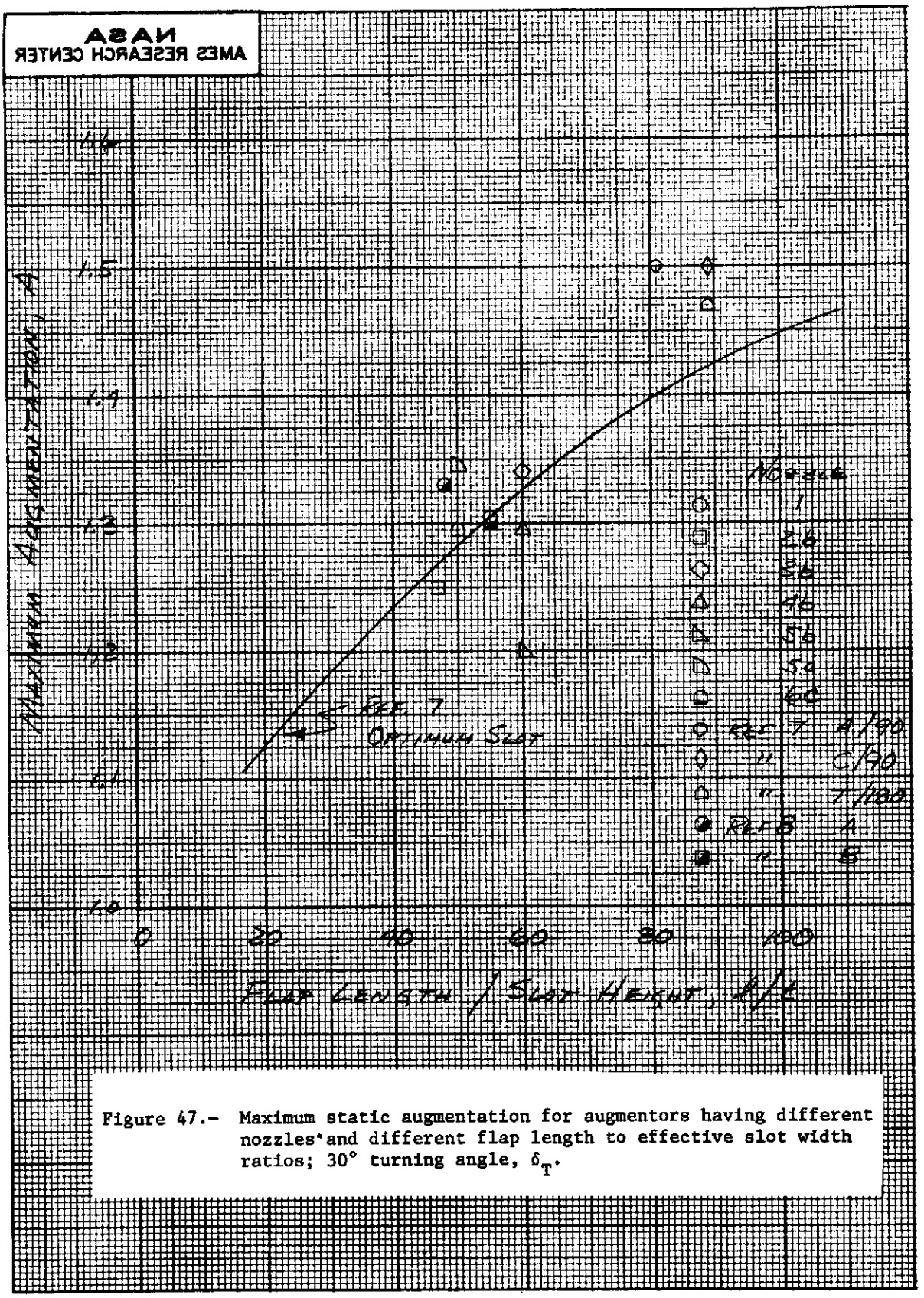

Figure 47.- Maximum static augmentation for augmentors having different nozzles and different flap length to effective slot width ratios; 30° turning angle, δ_T.

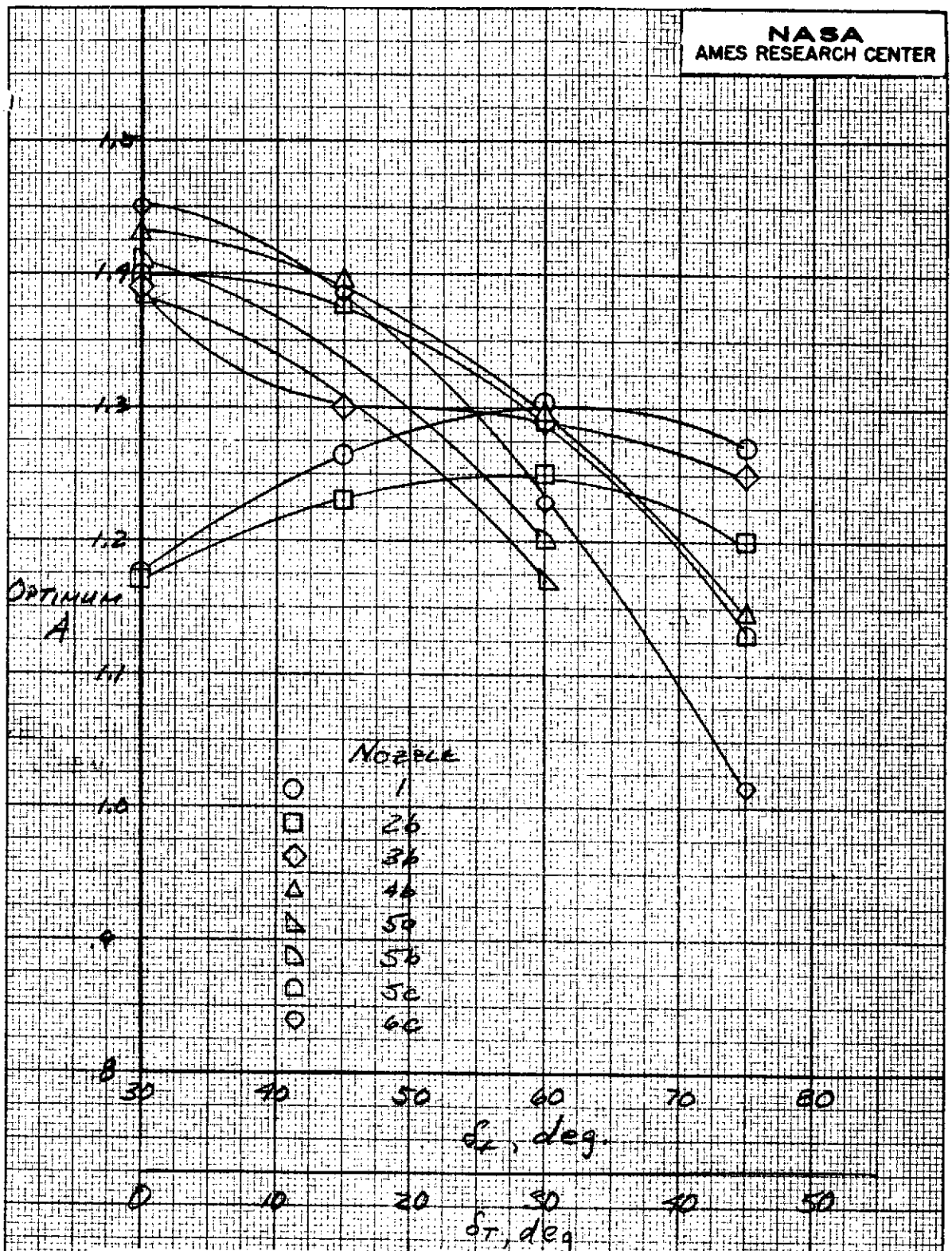

Figure 48.- The effect of flap angle on the optimum static augmentation of several nozzles; tertiary gap open.

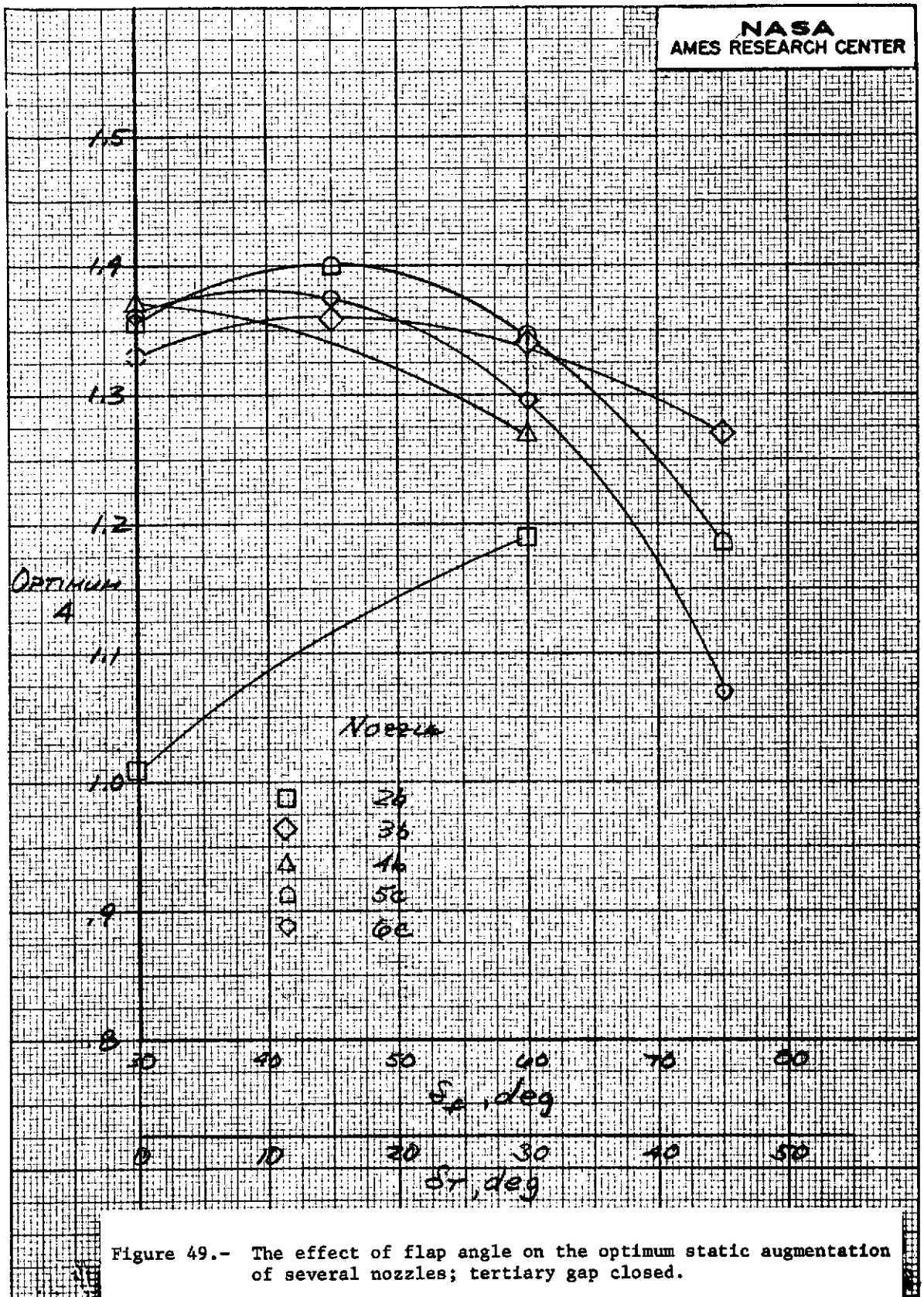

Figure 49.- The effect of flap angle on the optimum static augmentation of several nozzles; tertiary gap closed.

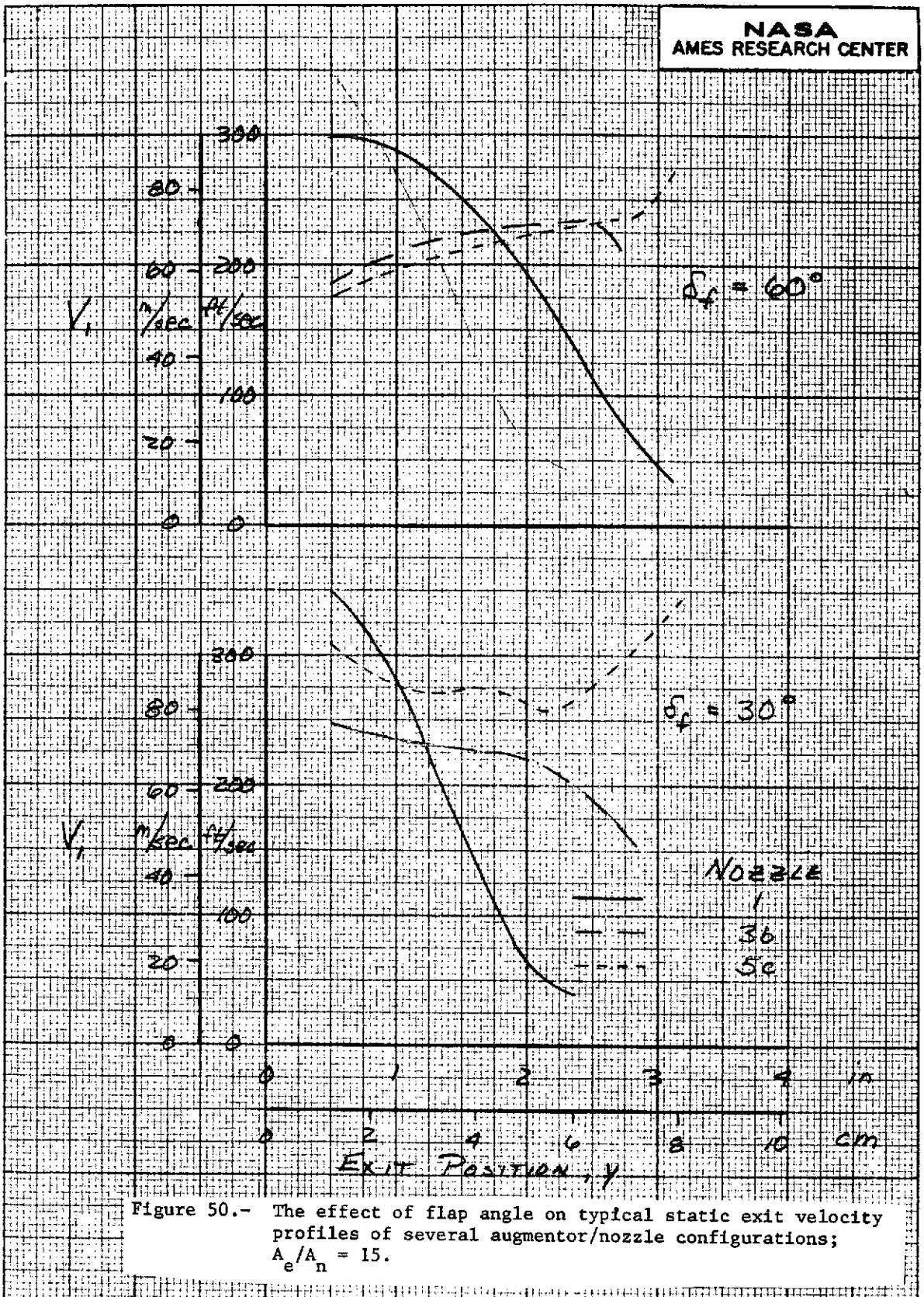

Figure 50.- The effect of flap angle on typical static exit velocity profiles of several augmentor/nozzle configurations; A_e/A_n = 15.

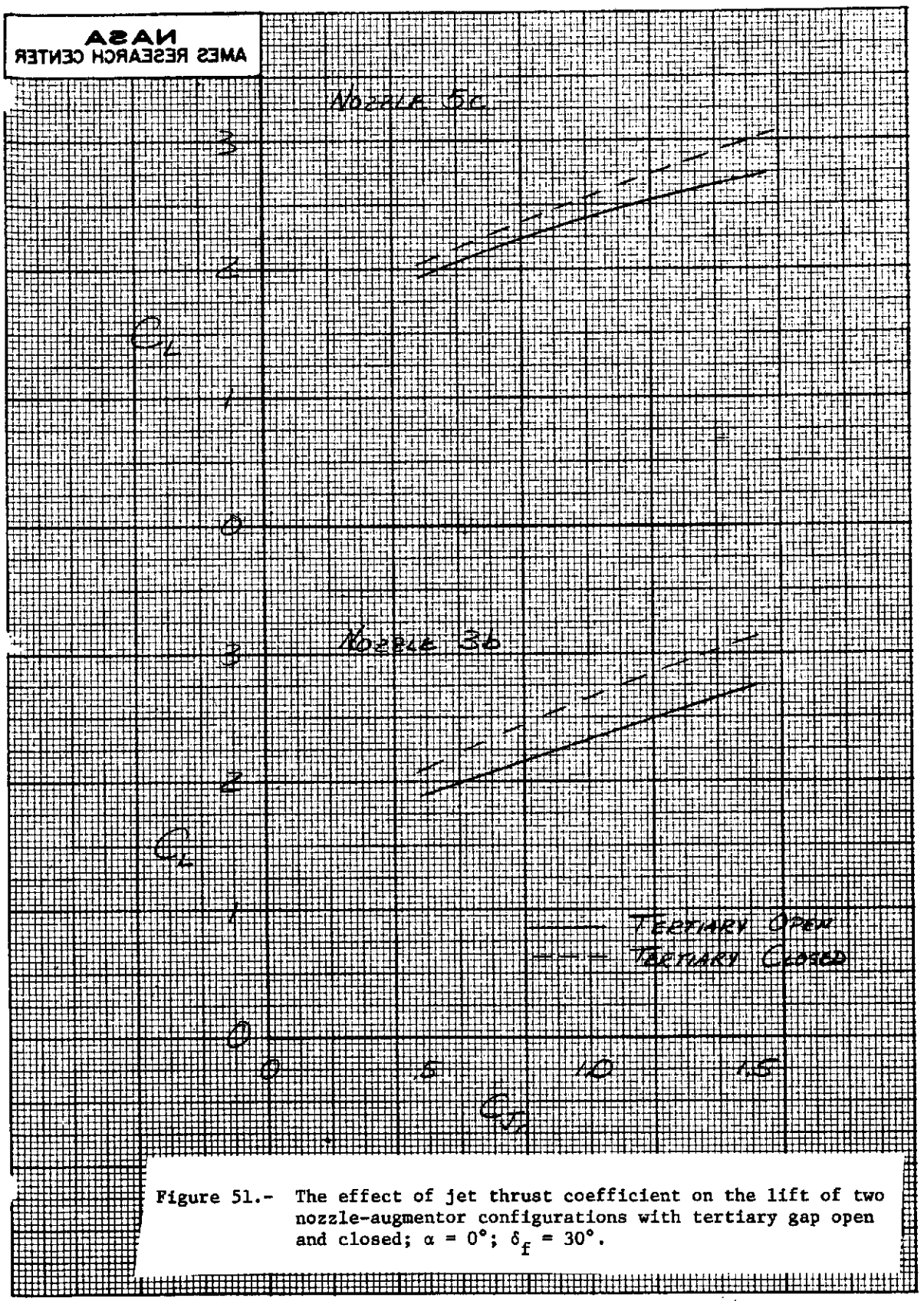

Figure 51.- The effect of jet thrust coefficient on the lift of two nozzle-augmentor configurations with tertiary gap open and closed; $\alpha = 0°$; $\delta_f = 30°$.

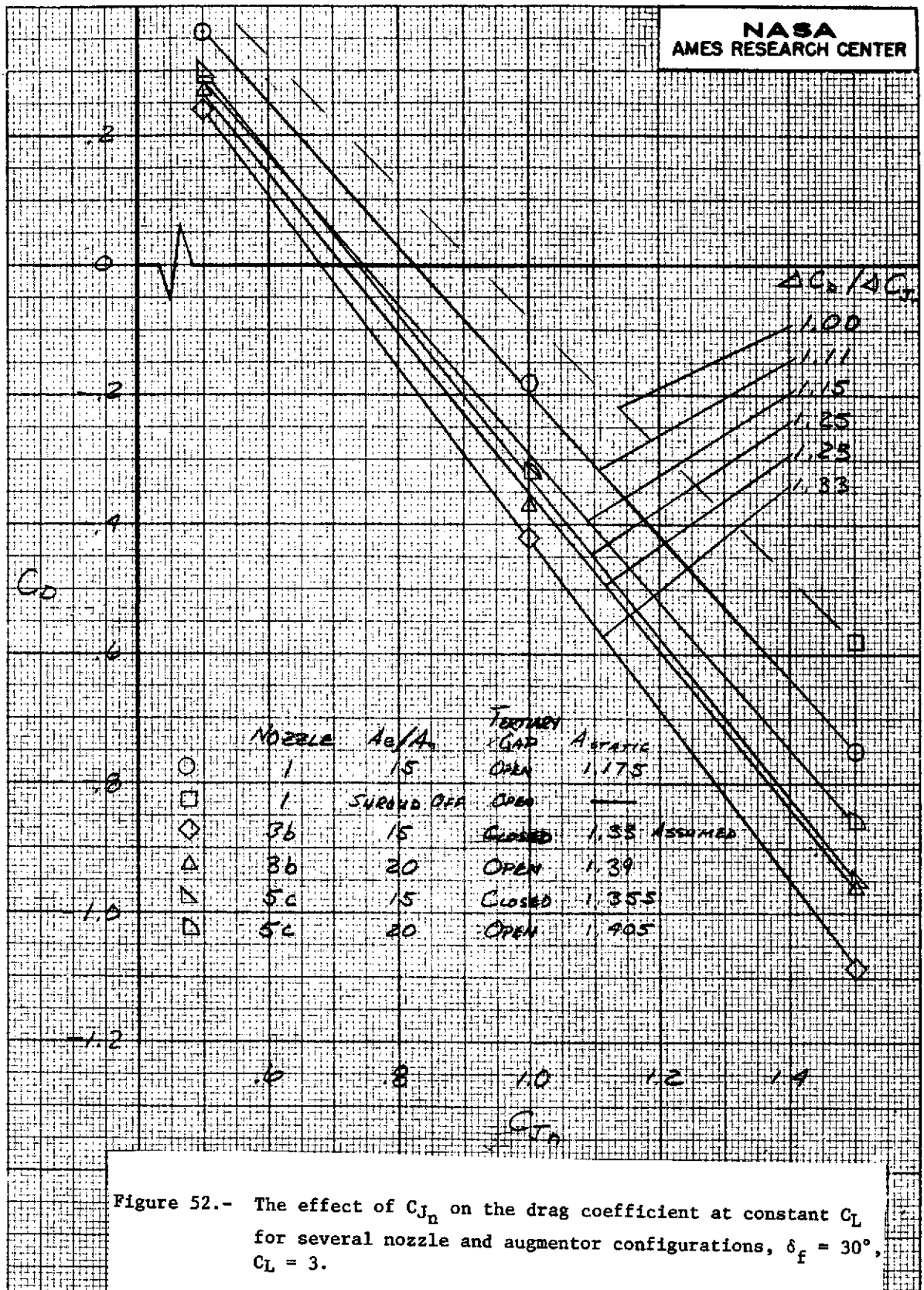

Figure 52.- The effect of C_{J_n} on the drag coefficient at constant C_L for several nozzle and augmentor configurations, $\delta_f = 30°$, $C_L = 3$.

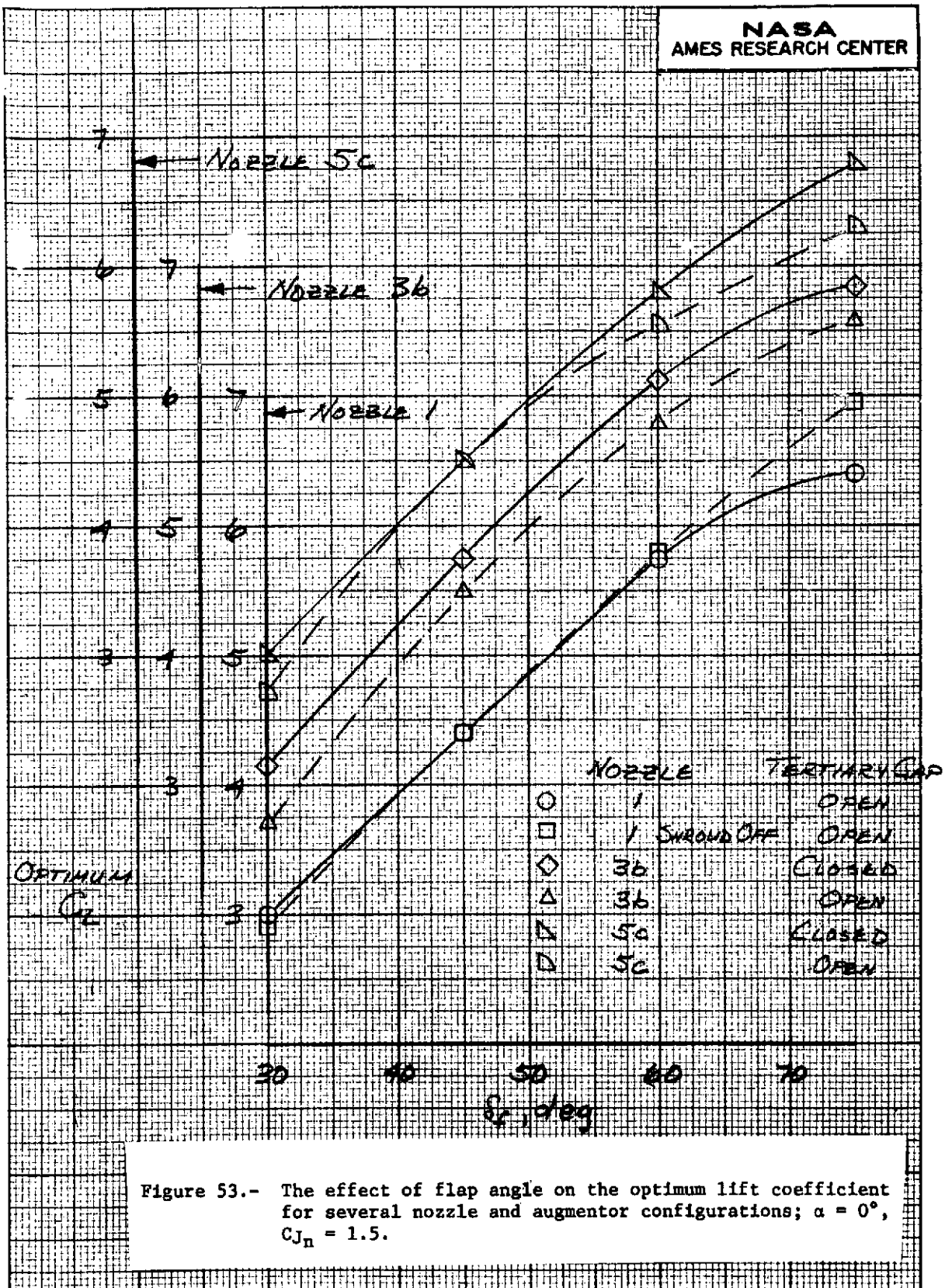

Figure 53.- The effect of flap angle on the optimum lift coefficient for several nozzle and augmentor configurations; $\alpha = 0°$, $C_{J_n} = 1.5$.

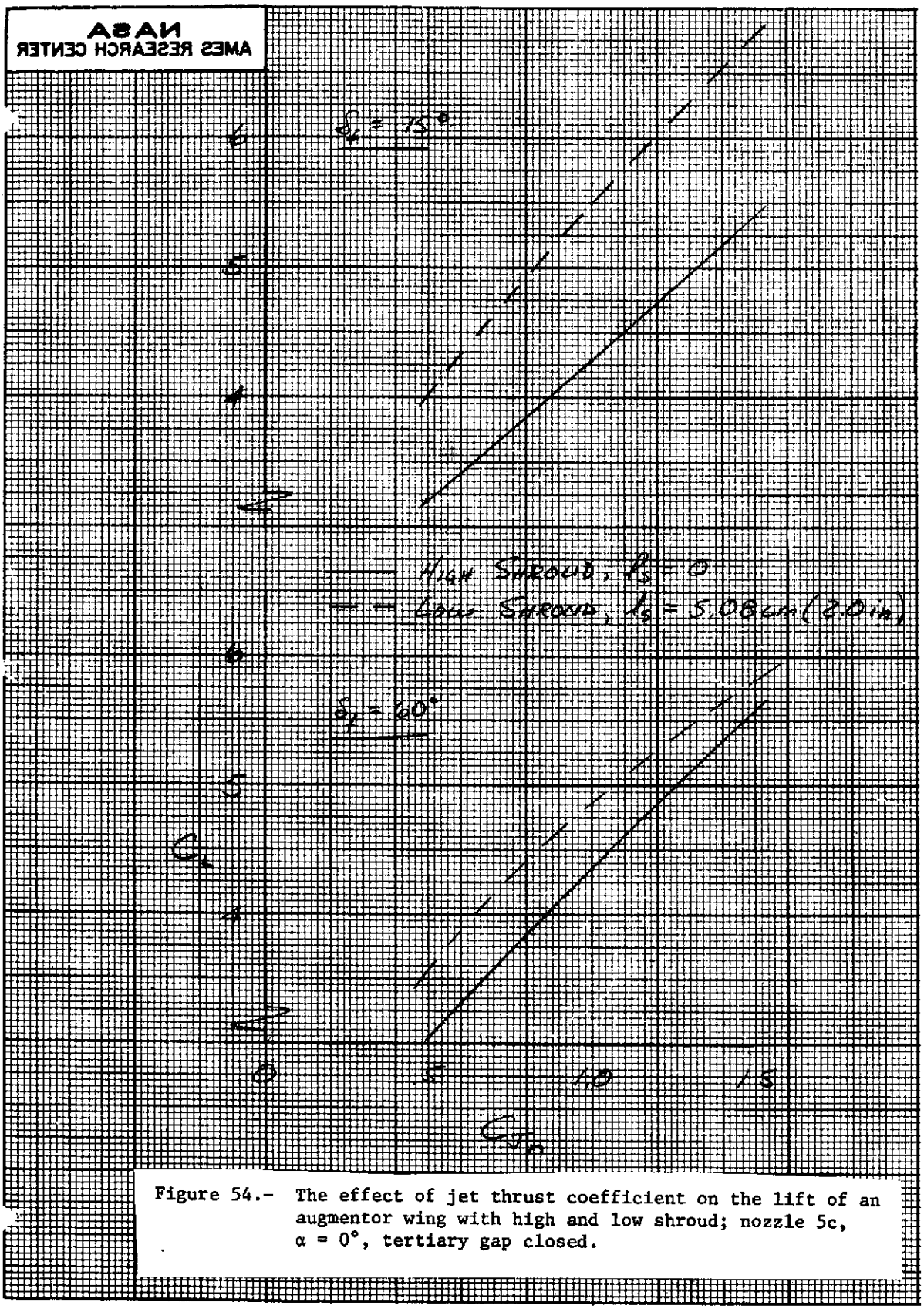

Figure 54.- The effect of jet thrust coefficient on the lift of an augmentor wing with high and low shroud; nozzle 5c, $\alpha = 0°$, tertiary gap closed.

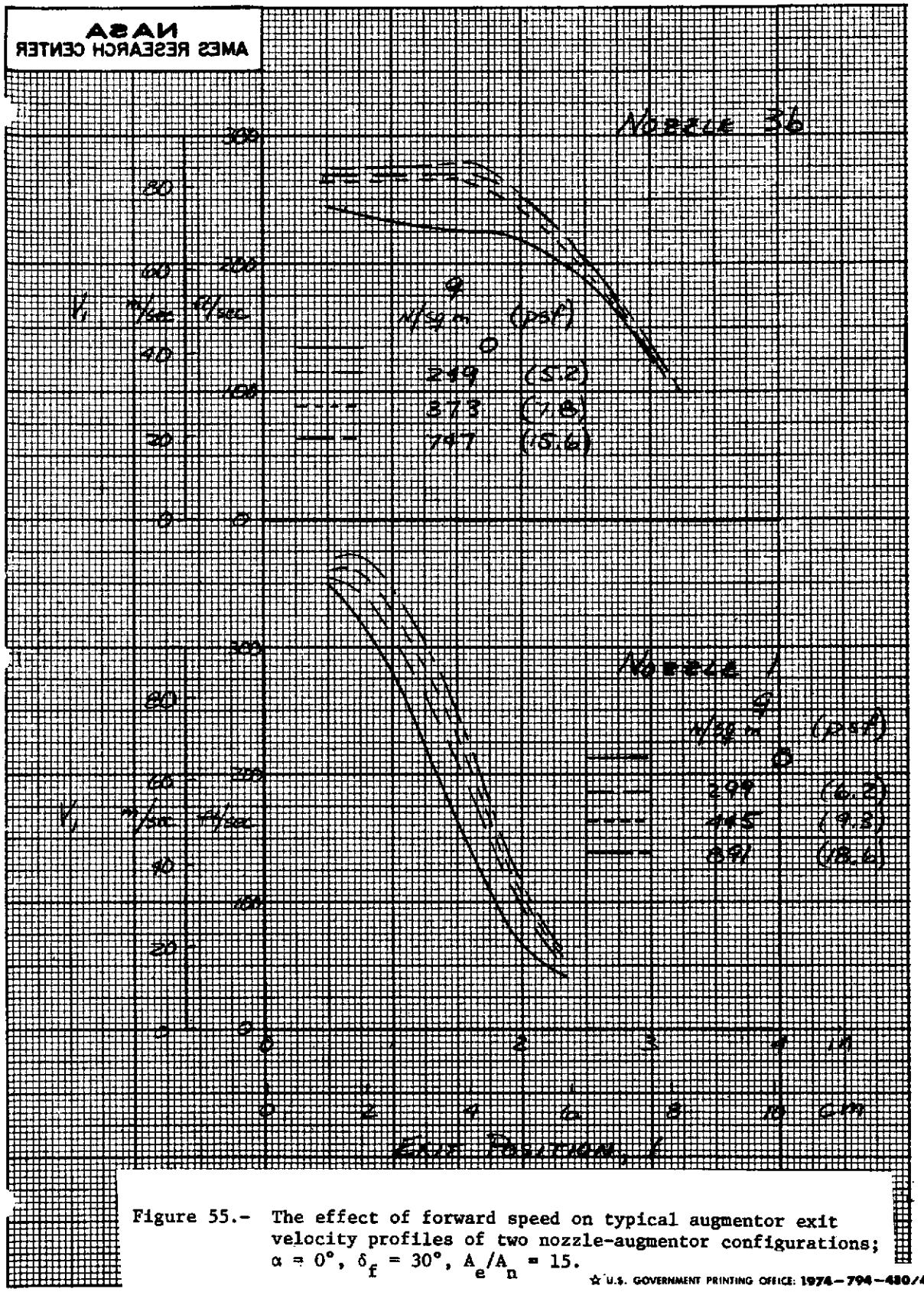

Figure 55.- The effect of forward speed on typical augmentor exit velocity profiles of two nozzle-augmentor configurations; $\alpha = 0°$, $\delta_f = 30°$, $A_e/A_n = 15$.

☆ U.S. GOVERNMENT PRINTING OFFICE: 1974—794—480/4704